NORTHWESTERN UNIVERSITY

Nanostructure Fabrication Using Inorganic Sols and Electron Beam Lithography

A DISSERTATION

SUBMITTED TO THE GRADUATE SCHOOL

IN PARTIAL FULFILMENT OF THE REQUIREMENTS

for the degree

DOCTOR OF PHILOSOPHY

Field of Materials Science and Engineering

By

Suresh Kumar Donthu

EVANSTON, ILLINOIS

December 2007

ABSTRACT

Nanostructure Fabrication Using Inorganic Sols and Electron Beam Lithography

Suresh Kumar Donthu

Dimensionally constrained material systems are at the forefront of current materials research because of their novel and often enhanced physical, chemical and biological properties. The dimensionality effects are pervasive through different classes of materials including ceramics, metals and polymers. Often times dimensionality effects are manifested as internal structure variations in polycrystalline materials. This is evident from some recent reports indicating that "*internal*" microstructural inhomogenities such as grain boundaries and porosity even in dimensionally constrained systems can further enhance their performance metrics such as gas sensitivity, for example. These results, coupled with the maxim that "*microstructure is a material's DNA*" underscore the need for novel approaches to enable tailoring of the "internal" microstructure of constrained nanopatterned systems and their characterization. This dissertation reports one such approach.

We have developed an enabling nanopatterning technique termed as soft-electron beam lithography (soft-eBL) which utilizes liquid precursors (e.g., sol) as the material

source for patterning variety of materials and composites with dimensional control down to 30 nm. Among several advantages, soft-eBL is capable of patterning structures on almost any substrate - single crystals, fragile ultra-thin membranes and insulators. We have exploited these unique attributes of soft-eBL to fabricate nanopatterns of simple and complex functional oxides with defined sizes and shapes. For example, we showed that by controlling the width of ZnO nanopatterned lines on an amorphous substrate, it is possible to define the number of grains per unit line length, such as a beaded (or a bamboo) structure where a single grain spans the entire line width. Using Soft-eBL we were able to demonstrate the effect of dimension, line-width to be specific, on the reduced crystallization rate in ceramic oxide nanostructures. The average grain size in lines was found to be smaller than in thin films prepared in identical conditions.

The dissertation further reports an experimental protocol to fabricate miniaturized gas sensing devices using soft-eBL nanostructures of ceramic oxides. As a part of this work, we have built a set-up in-house to measure the gas sensing properties of active nanostructures at different temperatures. The hydrogen sensing properties of tin oxide lines showed that decreasing line width improves the gas sensing performance. The gas sensing properties of these structures were benchmarked against commercial hydrogen sensor which was also tested under identical conditions. The soft-eBL 1D nanostructures showed better sensitivity and stability compared to commercial hydrogen sensor.

Dedicated to my wife Bavani Balakrisnan and my daughter Aaryaa Donthu who have been a constant source of support through the travails of grad school application and triumphs of thesis completion

ACKNOWLEDGEMENTS

My last fours of graduate school experience at Northwestern have been extremely educational, mind-opening and enjoyable. Many individuals have immensely contributed to this delightful experience and I want to thank here as many of them as possible.

Let me start with the usual suspect, my advisor Prof. Vinayak Dravid. I possibly could not have asked for a better mentor. Simply put, without his support this work would not have been possible. The intellectual freedom and seemingly endless resources he provided were instrumental to this work. His emphasis on “big-picture” thinking and soft-skills had a tremendous impact on my professional development.

The camaraderie and peer-support amongst VPD group members was invaluable especially during the initial trying years. Amongst them, I want to particularly thank my colleague Zixiao Pan who was ever patient to listen to my many crazy ideas and has provided great support during the developmental stages of the project. I want to thank Mohammed Aslam for numerous late night chai trips to devon street and valuable emotional support during the trying times. I also want to thank other group members, Soo-Hyun, Tao, Nasim, Feng, Prad, Ben and Arvind for providing a great group ambience. I want to thank Ann for help with all the administrative work in our group.

I want to thank Kenneth D'Aquila who worked with me during the summer of 2007 on microstructural analysis using TEM. Major portion of this work is reported in chapter 5 of the dissertation. I want to Prof. Lincoln Lauhon for numerous discussions and suggestions. I also want to thank him for providing the photolithography mask. The sensing

devices reported in chapter 6 were made using this mask. I want to thank Warefta Hasan and Ling Huang for helping me with several runs of metal deposition for sensing device electrodes. This was immensely valuable when my only other source went down for repairs for several months towards end of my thesis. I also want to thank Saswati Pujari who was gracious enough run the viscosity experiments within a days request while I was writing the thesis.

Over the last four years at Northwestern I have met several amazing friends and I am sure that many of them will remain my life-long friends. I want to thank my house mate for first two years and collaborator Manish Mundra for teaching me many things not least of them being how to make great “chicken curry”. I also want to thank Prakash Kolli, Nathan Yoder, Rajiv Basu, Brent Fiedler, James Wilson, Robin Koshy and Binoy Shah.

Finally, I thank my wife, Bavani Balakrisnan, for tremendous support, encouragement and understanding. “Thank you for putting up with my crazy schedules and for holding our family together. It is no exaggeration that I would not have achieved this without your support right from grad school application”. I also want to thank my cute little girl, Aaryaa, for teaching me a thing or two about *patience*. She is possibly a better teacher to me thank I am a parent to her.

This work was performed in the EPIC/NIFTI/Keck-II facilities of the NU*ANCE* Center at Northwestern University. The NU*ANCE* Center is supported by NSF-NSEC, NSF-MRSEC, the State of Illinois, and Northwestern University. The research is supported by NSF-NSEC, NSF-MRSEC and DOE-BES programs at Northwestern University.

Table of Contents

ABSTRACT 3

DEDICATION 5

ACKNOWLEDGEMENTS 6

TABLE OF CONTENTS 8

LIST OF TABLES 13

LIST OF FIGURES 14

1. CHAPTER 1 22

1.1 INTRODUCTION 22

1.2 SCOPE OF THE THESIS WORK 25

1.3 GAS SENSORS AND NANOTECHNOLOGY 29

1.4 ORGANIZATION OF THE THESIS 32

2. CHAPTER 2 34

2.1 FABRICATING NANOSTRUCTURES 34

2.2 PATTERNING APPROACHES FOR CERAMICS 35

2.2.1 Focused Ion Beam Lithography 36

2.2.2. Ceramic nanostructures using patterned resists as masks 38

2.2.2.1. Methods of making resist molds 38

2.2.3. Ceramic patterns without resist mold 43

2.2.4. Direct deposition methods 45

2.2.5. Soft Lithography 49

2.3 SUMMARY 57

3. CHAPTER 3 59

3.1 SOFT LITHOGRAPHY FOR ZnO NANOSTRUCTURES 60

3.2 MICROMOLDING IN CAPILLARIES 61

3.3 SOL-GEL SYNTHESIS ROUTE AS AN ENABLER 64
3.3 NEAR-FIELD SCANNING OPTICAL MICROSCOPY (NSOM) 65
3.4. EXPERIMENTAL 69
3.4.1 ZnO Sol preparation 69
3.4.2 PDMS mold fabrication 69
3.4.3 Soft-lithography of ZnO patterns 70
3.4.4 Near field Scanning Optical Microscopy 71
3.4.5 Electron and atomic force microscopy: 71
3.5 STRUCTURAL AND OPTICAL CHARACTERIZATION OF THE ZnO PATTERNS 72
3.6 SUMMARY 88
3.7 LIMITATIONS OF MIMIC AND MOTIVATION FOR SOFT-EBL 88

4. CHAPTER 4 90
4.1 NANOSTRUCTURE FABRICATION BY NANOPATTERNING 91
4.2 DESIRED ATTRIBUTES OF THE NANOPATTERNING SCHEME 92
4.3 SOFT-ELECTRON BEAM LITHOGRAPHY 96
4.4. DETAILS OF THE PATTERNING SCHEME 100
4.4.1: Resists 100
4.4.2: Substrate preparation for patterning 100
4.4.3: E-beam lithography 100
4.5: CAPABILITIES OF SOFT-EBL 106
4.5.1. Example 1: Sub-100 nm ceramic nanopatterns 106
4.5.2. Example 2: Variety of ceramic material-substrate systems 112
4.5.3. Example 3: Patterning onto fragile substrates 115
4.5.4. Example 4: Site-specific patterning of ceramic

nanostructures 126
4.5.5. Example 5: Patterning with polymer solutions 134
4.6 BENCHMARKING SOFT-EBL AGAINST OTHER CERAMIC NANOPATTERNING TECHNIQUES 136
4.7 SUMMARY 139

5. CHAPTER 5 140
5.1 POLYCRYSTALLINE NANOWIRES 141
5.2. WAYS OF IMPROVING MICROSTRUCTURAL STABILITY 143
5.2.1 Effect of secondary phases and dopants 143
5.2.2. Effect of reduced dimensionality 145
5.3. EXPERIMENTAL DETAILS 150
5.3.1. Sol preparation 150
5.3.2. Thin film fabrication 151
5.3.3. 1D Nanostructure fabrication 151
5.3.4. Grain size analysis using SEM and TEM 152
5.3.5. Chemical composition analysis using X-ray Photon Spectroscopy 153
5.3.6 X-ray diffraction 154
5.4. EFFECT OF Pd ON SnO_2 MICROSTRUCTURE 155
5.4.1 Thin films 155
5.4.1a - X-ray Diffraction 155
5.4.1b - X-ray photon spectroscopy 162
5.4.1c - Transmission Electron Microscopy 165
5.4.2 1D nanostructures 167
5.4.2a - Transmission Electron Microscopy 167
5.5. EFFECT OF DIMENSIONALITY ON SnO_2 MICROSTRUCTURE 169

5.6 EFFECT OF DIMENSIONALITY ON
ZnO NANOSTRUCTURES 171
5.7. SUMMARY 177

6. CHAPTER 6 179
6.1 GAS SENSORS 180
6.2 MECHANISM OF GAS SENSITIVITY IN
METAL OXIDE SEMICONDUCTORS 183
6.3 MINIATURISATION OF GAS SENSORS 184
6.4 SOFT-EBL OXIDE NANOPATTERNS AS GAS SENSORS 187
6.5 OBJECTIVES AND OUTLINE OF THE CHAPTER 188
6.6 EXPERIMENTAL 191
6.6.1 Sample Preparation: 191
6.6.2 Gas sensing measurement set up: 198
6.6.3 Gas sensing measurements: 201
6.7 GAS SENSING PROPERTIES OF TIN OXIDE THIN FILMS 202
6.7.1 Experimental 202
6.7.2 Hydrogen sensing performance of undoped tin oxide films 205
6.7.3 Pd doped tin oxide thin films 210
6.8 GAS SENSING PROPERTIES OF SOFT-eBL
NANOSTRUCTURES 217
6.8.1 undoped soft-eBL tin oxide nanostructures 217
6.8.2 soft-eBL nanostructures of tin oxide 3%Pd doped 223
6.8.3 Four-probe measurements of 3% Pd doped tin oxide soft-eBL nanostructures 230
6.9 BENCHMARKING GAS SENSING PROPERTIES
OF SOFT-eBL NANOSTRUCTURES 233

6.10 SUMMARY 238

7. CHAPTER 7 241

7.1 SUGGESTIONS FOR FUTURE WORK 242

8. REFERENCES 247

LIST OF TABLES

No.	TITLE ……..…..…	PAGE
4.1	Comparison of Soft-eBL with other established techniques for *ceramic* patterning ……...…	138
5.1	Average grain size in tin oxide films calculated from diffractograms in figure 5.3a using debye-scherrer equation …….....	156
5.2	Average grain size of undoped and 3%Pd doped tin oxide lines and thin films. Value in parenthesis is the total number of grains counted in each case ……...…	170
6.1	Different classes gas sensors currently available in market. The table is adapted from and other review articles …….	182
6.2	Sensitivities measured in tin oxide films doped with different Pd concentrations. These values are used for the plot shown above ……	213
6.3	Response times measured in tin oxide films doped with different Pd concentrations. These values are used for plot shown above ……...	215
6.4	Sensitivity values measured at different temperatures and H_2 concentrations for 300 nm wide soft-eBL undoped tin oxide lines ……...	222
6.5	Resistivity per line values used for plotting the above graph ……...	227
6.6	Sensitivity values used for the plots in figure 6.21b …….	230
6.7	Resistivity values used for plotting the above graph …….…...	232
6.8	Sensitivities of soft-eBL lines and Figaro TGS 821 sensor measured from figure 6.23 …….....	235

LIST OF FIGURES

NO.	TITLE …….. PAGE
1.1	Two different approaches for realizing miniaturized devices containing nanostructures ……..…… 28
1.2	Schematic diagram of a nanostructure with a) grain size about half of line width and significant dopant segregation to grain boundaries, b) uniform dopant distribution across whole structure and c) without grain boundaries …….……. 32
2.1	Various approaches for making patterns in resists ……..……... 41
2.2	Schematic illustration of a) ink jet printing and b) robocasting ……..... 46
2.3	Ceramic nanostructure fabrication using dip pen nanolithography and sol-gel precursors ……..……... 48
2.4	Making PDMS stamp from casting prepolymer onto master mold …...…. 50
2.5	Adaptation of microcontact printing (μCP) for ceramic patterning ……... 50
2.6	Microtransfer molding (μTP) for patterning ceramics ……..……. 52
2.7	Micromolding in capillaries (MIMIC) for pattering ceramics ……..…. 53
2.8	Classification of various ceramic patterning approaches ……..……. 55
3.1	The basic steps in patterning of ceramics using sol precursors and MIMIC ……..……... 63
3.2	Various modes of NSOM operation. Blue arrow represents excitation signal whereas red arrow represents emitted signal from the sample …… 67
3.3a	Operation of NSOM in “Constant-height” mode …….…….. 68
3.3b	Operation of NSOM in “Constant-amplitude” mode when the cantilever tracks the topography ……. 68
3.4	AFM topographic images a) before and b) after annealing at 550 ^{0}C for 1 h in air. c) SEM image of pattern after annealing. These images

were not taken at same location. d) Room temperature μ-PL spectrum of ZnO patterns showing band-edge emission at 3.28eV and Donor-Acceptor Pair emission below 2.5 eV ……...……..…. 74

3.5 a) Topography and b) NSOM optical images taken in "constant-amplitude" mode. Same scale bar applies to both the images and these images correspond to same location on the sample ……...…. 76

3.6 a) Topography and b) NSOM optical images taken in "constant-height" mode. Same scale bar applies to both the images ……. 78

3.7 a) Topographic and b) NSOM optical images of ZnO patterns obtained in *collection mode* configuration while operating in "constant-height" mode. Same scale bar applies to both images ……..…… 80

3.8 a) NSOM-optical image of ZnO pattern. b) Spectrum collected outside the patterns without long pass filter showing excitation laser at 514.5 nm. c) and d) Spectra collected from two locations on adjacent ZnO lines. e) Spectrum collected between these two ZnO lines. Spectra shown in c-e are collected while using the long pass filter to transmit the resonantly excited photoluminescence from defect-induced bands. Dotted lines are the Lorentzian curve fits to multiple PL bands …. 82

3.9a The relative position of the PL spectra of ZnO patterns on chromaticity scale ……..……. 87

3.9b The optical images of patterns when illuminated with (b) white light, (c) blue light and (d) green light ……...…….. 87

4.1 The four main desired attributes of a scheme for nanofabrication of ceramics ……..…..…… 95

4.2 The major steps in soft-eBL scheme ……..……..... 99

4.3 The effect of solution concentration on lift-off. These SEM images of ZnO patterns are taken after spin coating different sols at 6000 rpm and lift-off (they are not annealed). Bottom row consists of magnified views of the images in front row ……...….. 102

4.4 The effect of pattern density at two different ZnO solution concentrations on effectiveness of lift-off. 6000 rpm spinning speeds

are used in all the cases and the images were taken after lift-off. Bottom row consists of magnified views of the images in front row 103

4.5 Viscosities of various sols studied in this work. Viscosities were measured in stress controlled mode ……..……..….. 105

4.6 High resolution patterning capability of soft-eBL demonstrated through multidimensional patterns of ZnO on oxidized silicon substrates. All the patterns were annealed at 700^{o}C for 20 mins in air expect the patterns in (c) that were annealed at 900 ^{o}C for 5 mins. The patterns were made from 0.1M ZnO sol that was spun at 5000 rpm ……..……..….. 109

4.7 a) Backscattered electron image of ZnO patterns on SiOx/Si substrate heated at 700 ^{o}C for 20 min in air, b) Photoluminescence (PL) image of the patterns shown in (a) collected in illumination mode using NSOM operating in constant height-mode to decouple cross-talk from topography. (c) PL spectra collected on and between ZnO lines ……..……..…… 111

4.8 Versatility of the technique is demonstrated through patterning of different materials on different substrates. a) PZT on Pt, b) PZT on Nb:STO (inset shows the magnified view of one of the squares) and c) ZnO on sapphire ……..…..…..……. 114

4.9 Electron micrographs demonstrating high resolution and generic patterning capability of soft-eBL on an ultra-thin membrane. (a) Bright field (BF) TEM image of ZnO with 6 at% Eu after heating at 150 °C for 5 min in air, (b) BF-TEM image of ZnO pattern after annealing at 700 °C for 1 h in air with the inset showing the diffraction pattern of the structure, (c) Scanning transmission electron microscope (STEM) image of ZnO beaded structure annealed at 900 °C for 5 min in air and (d) ADF-STEM image of cobalt ferrite annealed at 1000 °C in air. The nominal electron probe size during STEM imaging is about 0.7 nm ……...……. 117

4.10 (a) AFM topographic image and (b) Bright field TEM image of Soft-eBL patterned ZnO with 6 at% Eu heated at 150 °C for 5 min, (c) Photoluminescence (PL) image of the patterns annealed at 700 °C for 20 min in air taken with NSOM in collection mode and “constant-height” mode to decouple the topographic information and (d) PL spectra collected from these patterns, outside the patterns and from patterns without Eu. The excitation wavelength is indicated with a dotted vertical line …….. 121

4.11 (a) ADF-STEM image of a soft-eBL-patterned barium titanate nanostructure annealed at 1000 °C for 5 h in air and b) EELS spectra collected across the nanostructure at 10-nm intervals. The nominal electron probe used for these measurements is 1.5 nm. The Ti L2,3 and Ba M4,5 edges identify the chemical nature of the structure. The presence of O K edge outside the pattern indicates that nitride membrane could have been oxidized due to high temperature annealing ……..…..……. 124

4.12 a) ADF-STEM image of ZnO nanopatterns containing 6 at% Eu. EDS maps of (b) Zn-Kα, (c) Eu-Lα and (d) Si-Kα identify the chemical nature of the patterns. The nominal electron probe size during these measurements is 0.7 nm and total collection time for EDS maps is 2 min …….. 125

4.13 (a) Optical image of photolithographically patterned Pt/Ti electrodes. (b) SEM image of ZnO patterns fabricated using soft-eBL between two photolithographically patterned electrodes. (c) SEM image of the same electrode after the second eBL process to form the Pt lines connecting the oxide patterns with photolithography electrodes ….. 128

4.14 (a) BSE image of a microhotplate taken at 60^{o} tilt angle. (b) Schematic of the microhotplate design. (c) Low magnification image of a chip containing four microhotplates. (d) SEM image of ZnO soft-eBL patterns positioned across the Pt electrodes. (e) response of a set of nanolines and a microscale film on a microhotplate to three different methanol concentrations ……... 131

4.15 (a) SEM image of Polypyrrole patterns on SiOx/Si substrate. (b) Topographic AFM image (tapping mode) and cross-sectional profile of the Polypyrrole patterns. (c) CN- ion map taken using SIMS. These images were not taken at same locations ……...…… 135

5.1 SEM images of tin oxide patterns (a) before and (b) after annealing. Atomic force microscope images of the same patterns (c) before and after annealing. The line profiles are shown below each AFM image. The patterns were annealed in air for 1 h at 700 ^{o}C. The average height of the patterns changes from 170 nm before annealing to 100 nm after annealing with a standard deviation of about 6 nm …….. 148

5.2 Schematic representation of the effect of dimensionality on the overall crystallization rate ……. 149

5.3a X-ray diffractograms of SnO_2 thin films with various Pd concentrations ……... 157

5.3b Reference x-ray diffractograms of pure phases ……...…… 157

5.3c Reflectivity curves of SnO_2 thin films with various Pd Concentrations ……..……..... 158

5.4a Scanning Transmission Electron Microscope (STEM) image of SnO_2 line doped with 3% Pd annealed at 700 ^oC for 1 h in air ……..…... 160

5.4b Scanning transmission electron microscope image and EDS maps of Sn and Pd. The EDS spectrum simultaneously collected while generating the maps is also shown above. The measurements were performed with a nominal electron probe size of 1.5 nm and the total collection time is 10 min ……... 161

5.5 X-ray Photon Spectroscopy scans of Sn, Pd, O, and C from three different tin oxide films ……..…..…… 164

5.6 TEM micrographs and the corresponding grain size distribution plots of tin oxide thin films with two different Pd concentrations. The grain size is an average of 340 grains ……...…...…. 166

5.7 TEM micrographs and the corresponding grain size distribution plots of tin oxide line with two different Pd concentrations. The grain size is an average of 190 grains. The width of the line is 100 nm ……...… 168

5.8 SEM images of ZnO thin film and line annealed at 700 ^oC for 20 min in air ……. 171

5.9 Scanning electron micrographs of ZnO lines and thin film annealed at 900 ^oC for 5 mins in air. The plot shows the average grain size in each case ……... 173

5.10 Scanning transmission electron microscopy image of ZnO 1D nanostructure fabricated using soft-eBL and annealed at 900 ^oC for 5 min in air …….. 174

5.11 Beaded structures of ZnO soft-eBL patterns formed after annealing at 900 ^oC in air for 5 min ……..…… 175

6.1 Phenomenological model of reducing gas interaction with n-type

tin oxide ……...…. 186

6.2 SEM image of undoped tin oxide soft-eBL lines and the plot showing the effect of flow rate on hydrogen sensitivity of these lines. Analyte gas is 2500 ppm of hydrogen diluted in nitrogen. Purge gas is synthetic air and the measurements were performed at 200 ^{o}C. The resistance was monitored by applying 5 V bias (or 10^{6} V/m along each line) …….. 189

6.3 "Cross-Marks" at four corners used for alignment during soft-eBL …… 193

6.4 The three step process of making gas sensors using soft-eBL nanostructures. Note that during anneal process in step 2, soft-eBL patterns are not in contact with photolithographically patterned Pt electrodes ……..... 196

6.5 Assembly of chip carrier with sample and contacts before loading into a quartz tube ……...…….... 197

6.6 Schematic of the gas sensing measurement set-up used in this work ….... 200

6.7 Electrode design used for thin film gas sensing measurements. Measurements were performed in two-probe configuration by applying potential across two electrodes, one from each of the opposite batches …….…….……. 203

6.8 (a) SEM image of electrodes on thin film, (b) magnified BSE image (c) corresponding SE image of the thin film and (d) cross-sectional image of the film. Pores are clearly visible in BSE image in (b) ……. 204

6.9 I-V plots of undoped tin oxide film at different temperatures. Bottom plot is the log-log plot of current and voltage (re-plotted from top plot). In this plot intercept is Log(R) where R is the resistance …..... 207

6.10 Response of undoped tin oxide films to 250 ppm of H_2 in N_2 at three different temperatures ……..… 208

6.11a Effect of Pd concentration on temperature dependent resistance of tin oxide thin films. Note that y-axis is in Ln (not Log) scale ……..…. 209

6.11b SEM (SE) images of tin oxide thin films doped with different Pd concentration ……..……... 209

6.12 Response of tin oxide films doped with (a) 0%, (b) 1%, (c) 2% and (d) 3% Pd to 250 ppm of H_2 in N_2 ……...…... 212

6.13 Sensitivity of tin oxide film doped with various Pd concentrations to 250 ppm of H_2 in N_2 at different temperatures. R_{air} is resistance in air before exposure to hydrogen amd R_{gas} is the resistance of the film after 3 hr of exposure to 250 ppm H_2 in N_2 ……..… 213

6.14 Response times of Pd doped and undoped tin oxide thin films to 250 ppm H_2 in N_2 measured at three different concentrations ……..... 215

6.15 SEM image of soft-eBL undoped tin oxide nanostructures together with the Cr/Au electrodes ……...…..… 220

6.16 (a) Linear I-V plots of undoped tin oxide soft-eBL lines at different temperatures and (b) plot of resistivity per line based on measured line dimensions. Note that y-axis is in Ln-scale (not Log-scale) ……. 220

6.17 Response of 300 nm wide undoped tin oxide soft-eBL lines to different concentrations of hydrogen in nitrogen. Measurements were taken at (a) 150 ^oC and (b) 200 ^oC with a flow rate of 1000 sccm. Synthetic air is the purge gas. In each case plot in red shows the response of bare substrate tested under identical conditions and electrode configuration ……. 221

6.18 Response of undoped soft-eBL lines to 250 ppm H_2 in N_2 over two days of continuous testing. The measurements were done at 150 ^oC ……..….. 222

6.19 (a) AFM and (b) SEM images of 200 nm wide soft-eBL lines. (c) AFM and (d) SEM images of 85 nm wide soft-eBL lines. These are tin oxide lines doped with 3% Pd. AFM images were taken in tapping mode and the height profiles were used for measuring line heights whereas widths are measured from SEM images. The wide white horizontal patches are the electrodes. Electrodes are made of 10 nm Ti and 100 nm Pt …….. 224

6.20a I-V plots of 85 nm wide lines taken in two-probe configuration at different temperatures ……...……. 226

6.20b Resistivity per line measured at different temperatures in lines of two line widths. Note that y-axis is in Ln-scale (not in Log-scale) ……. 226

6.21a Response of wider and narrower lines to four different H_2 concentrations measured at 150 ^oC. The measurements were taken by applying 1V bias. Based on the electrode spacing, this equals about 4×10^5 V/m electric field ……..……. 229

6.21b Sensitivity dependence on analyte concentration at two different temperatures between wider and narrower lines ……..… 229

6.22 Comparison between resistivities measured at different temperatures in four-probe and two-probe configuration …….……..… 232

6.23 Response of Figaro TGS 821 hydrogen sensor to different H_2 concentrations tested in our in-house built gas sensing set-up. Response of 85 nm wide soft-eBL tin oxide lines with 3% Pd is shown for comparison ……..…… 234

6.24 Response of Soft-eBL lines to over 200 continuous cycles of exposure-purge. Analyte gas is 2500 ppm H_2 in N_2 and purge gas is synthetic air. The measurements were performed at 200 ^oC ……..... 236

6.25 Response of Figaro Sensor to over 200 continuous cycles of exposure-purge. Analyte gas is 2500 ppm H_2 in N_2 and purge gas is synthetic air. The measurements were performed at 200 ^oC ……..... 237

CHAPTER 1

1.1. INTRODUCTION

Revolutionary advances in materials have always precipitated major life-style changing impact on our society. These advances were in the form of either new materials development (e.g. steel) or a deeper understanding of a materials property followed by the ability to manipulate a material structure, for example, to enhance this property (e.g. heat-treatment of the steel). The recent advances in nanotechnology have empowered us with new tools to fabricate, manipulate and probe materials with sub-micrometer and nanometer dimensions. These dimensions are comparable to the length scales of the fundamental structural unit of a polycrystalline material namely, grain size. At these length scales the contributions from interfaces (grain boundaries, surfaces) would become very significant.

The motivation for this thesis work stems from the numerous examples of materials properties that are sensitive to both external form such as size and shape and internal form namely microstructure. This includes physical, chemical, mechanical and biological properties of materials. Some examples include reduction of melting point with particle size[1, 2], dependence of magnetic microstructure and magnetic behavior of materials on size[3],

catalytic activity dependence on Pt particle size, glass transition temperature dependence on polymer dimensions[4] and the influence of particle size on electrical properties[5]. Endowed with this information, materials scientists are now disposed to develop novel high performance devices/systems not only by developing new materials but also by structural engineering and dimensional control of the known materials.

In addition to the enhancement in materials properties, reduction in materials dimensions also enables fabrication of miniaturized devices containing these structures as functional units. Miniaturization has almost always meant an improved overall performance of the device. The best example is from the field of microelectronics where shrinking materials has produced better product performance in the form of more components per chip, lower power consumption and increased functionality through integration of multiple materials or also known as multiplexing[6]. Another equally ubiquitous example is in the field of digital data storage where ever shrinking individual storage unit has revolutionized the way our society handles information. The scientific and technological significance of materials with small/constrained dimensions or nanostructures led to the development of novel nanostructure fabrication techniques especially in the last two decades. Though the term nanostructure could include any structure with at least one dimension smaller than 100 nm (e.g. nanoparticles-0D, nanorods-1D, nanosheets-2D), scope of this thesis work is mostly restricted to 1D nanostructures.

Over the last decade impressive developments have been made in the synthesis and characterization of 1D (e.g. nanorods, nanobelts, nanowires) nanostructures that are monolithic and single crystalline. These monolithic nanostructures are usually grown by either vapor based techniques such as vapor-liquid-solid (VLS) growth[7-9] or using wet chemistry based techniques using surfactants to promote anisotropic growth[10, 11]. The nanostructures thus fabricated "off-site" are assembled onto a substrate for probing their either individual or collective properties. Probing the performance attributes of individual monolithic nanostructures is a relatively direct route to understanding their theoretical performances as the effect of structural defects such as grain boundaries, whose attributes can be highly process dependent, can be eliminated.

Strategies have been developed to assemble these structures into hierarchical architectures with control over their location on a substrate. This would enable fabricating practical miniaturized devices containing nanostructures and also to probe them individually. Several of these techniques make use of microfluidics, electric or magnetic fields, surface prepatterning, self assembly and templating[12-15]. However these techniques do not yet have precision, pattern density or complexity necessary for many applications. On the other hand, within the context of real world applications such as gas sensors grain boundaries have a beneficial effect. While high surface-to-volume ratio of nanostructures could give high sensitivity the nanostructures do not necessarily have to have either high crystallinity or be single crystalline. In fact, the ability to control internal structure of these

dimensionally constrained systems gives an additional parameter to control and tune their performance in addition to the size control.

The challenges of integrating individual nanostructures into hierarchical architectures and with device circuitry could be overcome by using techniques that enable nanostructure fabrication at specific locations on a substrate (see figure 1.1). Unlike assembling approach, patterning approach involves nanostructures fabrication "on-site" with control on their dimensions, from microns down to several nanometers, and shapes. The site-specific patterning capabilities of some of the nanopatterning approaches allow integration of these nanostructures with predefined device circuitry. Moreover, patterning approach is compatible with, and sometimes necessary to use, high temperature heat-treatment protocols that could have secondary beneficial effect of tuning the internal structure, such as grain size and porosity. Results in chapters 5 and 6 partially support this suggestion.

1.2 SCOPE OF THE THESIS WORK

The major themes of this thesis work are two fold, to understand the how dimension affects the physical properties of materials and to study the effect of dimension on microstructural evolution in dimensionally constrained materials systems. It is of specific interest to understand how materials physical dimensions affect the grain size during

amorphous to crystalline phase transformation of a nanostructure. In order to achieve these goals, developing an approach that can enable fabrication of nanostructures with control on shape and size is required. Therefore the first task is to

a) Develop a generic pattering scheme for fabricating variety of ceramic materials with control on their size and shape. The scope includes validation of the new approach through fabrication and comprehensive characterization of variety of ceramic nanostructures. Towards this goal, a novel nanopatterning approach called as soft-electron beam lithography (soft-eBL) was developed. These structures were thoroughly characterized using variety of techniques including electron microscopy and scanning probe microscopy.

Subsequently, we have attempted to

b) Demonstrate the practical application of the approach through a proof-of-concept miniaturized device with patterned nanostructures as the active elements. A miniaturized gas sensor device containing soft-eBL patterned ceramic oxide nanostructures was fabricated and hydrogen sensing performance was evaluated as an example. The hydrogen sensing properties of nanostructures with different line-widths were measured to

understand the effect of size on gas sensing properties. This is chosen as an example to study the effect of dimension on the materials properties.

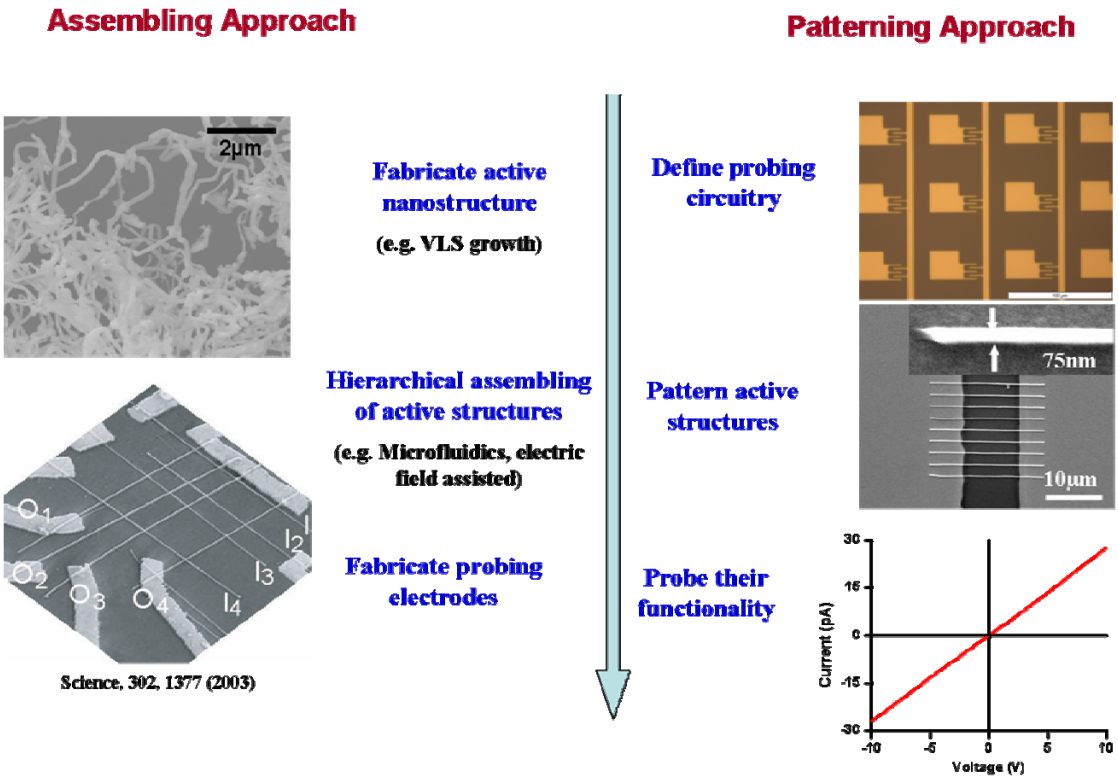

Figure 1.1: Two different approaches for realizing miniaturized devices containing nanostructures

1.3. GAS SENSORS AND NANOTECHNOLOGY

The discovery of first solid state gas sensor using metal oxide semiconductor[16] nearly four decades ago had heralded an unprecedented development in terms of performance and scope of applications[17, 18] for these devices. They are ubiquitous in our everyday life as air quality monitors at household level and as industrial gas monitors at global level. Active sensor element in these devices is a wide band gap semiconductor such as tin oxide (SnO_2), zinc oxide (ZnO) whose conductance is perturbed by chemisorption of either reducing or oxidizing gas molecules on semiconductor surface. On the other hand, over last two decades, research in nanoscience and technology has demonstrated the novel and/or improved properties of materials when their dimensions are reduced. The most direct, far reaching and immediate impact of nanotechnology on society at large appears to be in the field of sensor technology. Because of the high surface to volume ratio afforded by nanostructures and the direct relationship between sensitivity and this ratio, nanostructures are anticipated to show unprecedented sensitivity. Furthermore, as the dimensions of the nanostructures are comparable to the width of depletion layer created by chemisorbed oxygen, their conductivity is very sensitive to the presence of other gas molecules. In addition to performance benefit there could be potential economic savings as the miniaturized active sensor materials require less power for operation.

In spite of widespread application of solid state gas sensors, research and development work in this field remains empirical[19, 20]. An understanding of elementary steps of sensing and influence of structural properties of active sensor material such as crystallinity and grain size on sensitivity is still immature. The four most important measurables of a sensor material performance are sensitivity, selectivity, response time and recovery time. Strategies to improve sensitivity include engineering microstructure of active sensor material, developing new and better sensor materials and using sophisticated measurement techniques such as impedance measurements as opposed to simple DC conductance measurements[21]. The selectivity is usually improved by doping active sensor material with transition metals[22] such as Sb, Pd, Pt etc. On the other hand response time and recovery time are still predominantly optimized by "trial and error" experiments due to the lack of fundamental understanding of these processes.

In order to harness the full potential of superior performance of nanostructures the empirical approach needs to be replaced with a more systematic investigation of sensor material from an integrated structure-property correlation point of view. This is especially important for sensor devices made from nanostructures because fabrication and structural engineering of nanostructures poses new set of material science challenges. For example while the spatial distribution of dopants may not be too critical for performance of a thick film or thin film sensor material, it becomes very important for example in a nanostructure such as a ZnO line with 50nm×50nm cross-sectional area (with 25 nm mean grain size). The

fundamental mechanism perturbing the conductance of such a line due to chemisorption of gas molecules will strongly depend on the structure of the line and structural arrangement of dopants along the line. If the dopants predominantly segregate to grain boundaries (see figure 1.2) this nanostructure would be effectively a heterostructure with spatially modulated dopant concentration and conductance change would be due to schottky barrier height change due to chemisorption of the gas molecules. However a different mechanism similar to gating in field-effect transistor[8] would operate if this nanostructure is a monolithic structure such as a nanowire[23-26] without grain boundaries. This is important because each of these scenarios would require a different set of measurement tools to monitor their conductance. There could be other more fundamental materials science issues relevant to sensor performance such as phase and structural stability and evolution in these nanostructures. Because these structures are spatially constrained, the kinetics of the phenomenon such as grain growth in nanostructures would be different from those in either thin film or bulk. This is important because each of these structures could show different sensor performance.

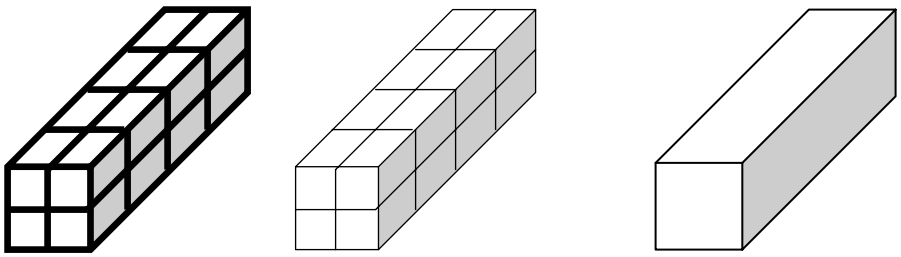

(a) **(b)** **(c)**

Figure 1.2: Schematic diagram of a nanostructure with a) grain size about half of line width and significant dopant segregation to grain boundaries, b) uniform dopant distribution across whole structure and c) without grain boundaries.

The development of a nanofabrication scheme that enables control on size, internal structure and shape of sensing elements is a first step towards our understanding of "structure-property" relations in gas sensors and in the journey towards replacing an empirical optimization approach with a systematic development work in gas sensing research. The work in this thesis aims to contribute to that goal.

1.4 ORGANIZATION OF THE DISSERTATION

Chapters in the dissertation are organized as follows. **Chapter 2** includes a review of various nanopatterning approaches for ceramic materials reported in the literature. Advantages and disadvantages of these techniques specifically for patterning ceramics are

discussed. **Chapter 3** starts with brief background on sol-gel approach and the efficacy of sol-gel route for nanopatterning ceramics. The feasibility of adapting a soft-lithography technique called micro-molding in capillaries (MIMIC) for fabricating ceramic nanostructures using sol-gel precursors is then demonstrated. As an example ZnO nanopatterns that are less than 300 nm are fabricated using MIMIC. The chapter also makes a case for the need to evaluate properties of nanostructures at appropriate length scales by measuring the photoluminescence properties using near field scanning optical microscope. The chapter ends with highlighting the limitations of MIMIC and the need for developing a novel nanopatterning technique called as soft-electron beam lithography (soft-eBL). **Chapter 4** introduces the soft-eBL technique. The unique capabilities of soft-eBL are demonstrated through a series of examples of nanopatterns fabricated on variety of substrates. Results from the studies involving microstructural evolution in constrained material systems or nanopatterns are presented in **chapter 5**. This chapter specifically includes studies of the effect of dopant and dimension on grain size of oxides such as tin oxide and zinc oxide. **Chapter 6** includes the gas sensing performance of oxide nanopatterns fabricated using soft-eBL. The chapter provides the details of gas sensing device fabrication steps and some preliminary hydrogen sensing performance attributes of soft-eBL patterns. The purpose of the chapter is to highlight the application side of the nanopatterning. Finally conclusions from this work and suggestions for future work are presented in **chapter 7**.

CHAPTER 2

2.1 FABRICATING NANOSTRUCTURES

The process of making a functional device containing one or more nanostructures requires several steps including nanostructure fabrication, interfacing nanostructures with other components through wiring and packaging. Nanostructure fabrication can be accomplished with several techniques that can be classified as either “on-site” or “off-site”. “Off-site” fabrication refers to techniques in which nanostructures are synthesized away from the substrates such as chemical solution deposition in a beaker. “On-site” fabrication refers to nanostructure synthesis at controlled locations on a substrate. Nanopatterning is an “on-site” fabrication approach that has a clear advantage over “off-site” fabrication approaches within the context of device fabrication especially when the nanopatterning technique has registry control. This chapter will cover various nanopatterning approaches for ceramic nanostructure fabrication.

2.2. PATTERNING APPROCHES FOR CERAMICS

Patterning of materials in the past has almost exclusively been accomplished with photolithography. Photolithography is the oldest patterning technique whose capability to fabricate smallest feature size is being continually improved through tremendous capital investment by semiconductor manufacturers. Even though this technique is shown to fabricate structures below 100 nm[27, 28], instrumentation required is too specific to semiconductor industry and is too expensive for small companies and research labs. Several novel patterning approaches have been developed particularly over the last two decades as potential alternatives to photolithography. These patterning techniques can be classified in several different ways as either conventional vs unconventional[29], self-assembly vs directed assembly, serial vs parallel or top-down vs bottom-up. Several excellent reviews on patterning of materials[29-33] have been published and it would not be necessary to repeat them here. Instead, the following sections in this chapter will cover various techniques that were demonstrated particularly for patterning ceramic materials. Patterning of ceramic materials poses unique challenges because of their etch resistance and therefore not every technique is capable of patterning ceramics. Techniques that were only used to pattern metals, biomolecules or polymers are not covered unless they were also demonstrated for fabricating ceramic nanostructures. Moreover, if a particular technique was demonstrated for patterning several classes of materials, only the results pertaining to ceramics are highlighted

in this chapter. However, ample references are cited for the benefit of readers interested in other classes of materials.

2.2.1 Focused Ion Beam Lithography

Focused Ion Beam can be used to carve-out nanostructures by milling away material upon exposure to high energy ion beam, usually made up of gallium ions though use of other ions was also reported[34-36]. Several variants of this technique have been developed to fabricate solid state nanostructures. They include direct sputtering away of the material with high energy focused ion beam, localized chemical etching of the material upon interaction of etchant gas with secondary electrons generated by ion beam-sample interaction and wet chemical etching of the ion implanted regions[36-40]. For example Hiramoto et.al.[36, 40] have exploited differential etching capabilities between ion implanted and non-implanted regions to fabricate 30 nm wide grooves in AlGaAs layers and GaAs wires less than 100 nm. Direct milling of various ceramics using FIB was also demonstrated in numerous reports in the literature. However, chemically assisted etching is almost always demonstrated for either metals, metallic alloys or semiconductors such as silicon[41, 42]. Though it was also demonstrated for materials such as SiN_x[43], adaptation of this approach for patterning wider variety of ceramics, oxides for example remains to be demonstrated.

In addition to these subtractive approaches, FIB can also be adapted for additive approaches whereby nanostructures are generated on a substrate by decomposition of a precursor gas by secondary electrons generated from ion-substrate interaction. The secondary electrons could also be generated from electron-substrate interaction instead. This could also lead to (electron) beam induced deposition. However, the secondary electron yield from this type of interaction is much lower and therefore deposition rates are markedly slower than in case of ion beam. The ion/electron beam induced deposition is valuable for applications such as site-specific deposition of metal contacts onto nanostructures[44], fabrication of 3D nanostructures and for protective metal layer deposition during TEM sample preparation.

Overall, the advantages of nanostructure fabrication using FIB technique, either by subtractive or additive approaches, include site-specific capability and high resolution. However, the drawbacks with this technique include undesirable Ga ion implantation, possible structure altering damage to the sample, serial or one-structure-at-a-time nature of the technique, and the limitation of this approach to primarily metal deposition. The reports on ceramic material deposition using FIB are scarce. The refractory nature of ceramics makes them hard to etch though there are several reports of using FIB to mill ceramics[45-48]. However, the amount of structural damage induced by FIB milling and the roughness induced by this approach might be undesirable especially in nanostructures. A recent review article by Tseng[49] is an excellent source for more information on FIB technique.

2.2.2. Ceramic nanostructures using patterned resists as masks

There are broadly two different approaches to fabricating ceramic patterns using resist molds or masks. The resist molds are typically made of polymers but could also be made of inorganic materials as hard masks. The central theme with this approach is to use the resist as a mask to define the size and shape of the final ceramic pattern. The two approaches are, a) define patterns in the polymer resist and deposit ceramic material by chemical/physical vapor deposition or chemical solution deposition routes and b) define the resist patterns and etch the underlying ceramic substrate. Before these two approaches are discussed, various methods by which one can make patterns in resists are discussed.

2.2.2.1. Methods of making resist molds:

The resist materials could be patterned upon exposure to either photons (both UV and x-rays) or electrons. They could also be made using mechanical techniques such as imprinting (nanoimprint lithography). The method of patterning resists using photons is called photolithography while the electron beam lithography (eBL) uses electrons.

a. Photolithography: Photolithography is probably the most common lithography technique that one is aware of. The technique involves exposing a resist coated substrate to a parallel beam of photons through a mask. The resist areas exposed to photons either cross-

link and become insoluble in a developer solution or depolymerise and increase their solubility in the developer solution. The patterned resist layer is then used as mask to either fabricate structure in the underlying substrate by etching or depositing new material from another source. The ultimate resolution one can achieve using photolithography is mainly determined by smallest feature size one can generate in the resist layer. There is a tremendous research activity primarily driven by multi-billion dollar semiconductor industry in continuously reducing this feature size. Even a brief survey of these developments will be unnecessary for this thesis because one can readily access this information even by a cursory literature search efforts.

b. Electron beam lithography (eBL): Unlike photolithography, eBL is a mask-less technique wherein an electron beam is scanned on a resist coated substrate. Depending on the type of resist, exposure to electron beam results in either cross-linking (negative resist) or polymer chain scission (positive resists). Chain scission increases the solubility of resist in a developer solution and therefore resist is removed from the exposed regions. While the main advantages of electron beam lithography are high resolution and registry capability, the drawback is the serial nature of the technique. While the photolithography is a parallel technique, the mask used in photolithography is indeed made using eBL when the feature sizes are less than 500 nm.

c. Nanoimprint lithography: The third and most recent technique for generating patterns in polymer resists is nanoimprint lithography (NIL)[50-52]. In this technique, a hard mold with nanoscale topographic features is pressed into a polymer heated above its glass transition temperature. Upon cooling to temperatures below glass transition temperature of the polymer and removing the hard mold, the features are embossed into the polymer resist. This technique is capable of generating trenches with aspect ratio as high as 10. Several variants of NIL have been developed in the past decade to increase functionality and enhance capabilities. Currently, NIL is capable of generating nanoscale patterns (sub-10 nm) over large area with very high through put. However, like photolithography the mask to generate the master mold requires eBL.

All three lithography approaches discussed above for making resist masks are shown schematically in figure 2.1.

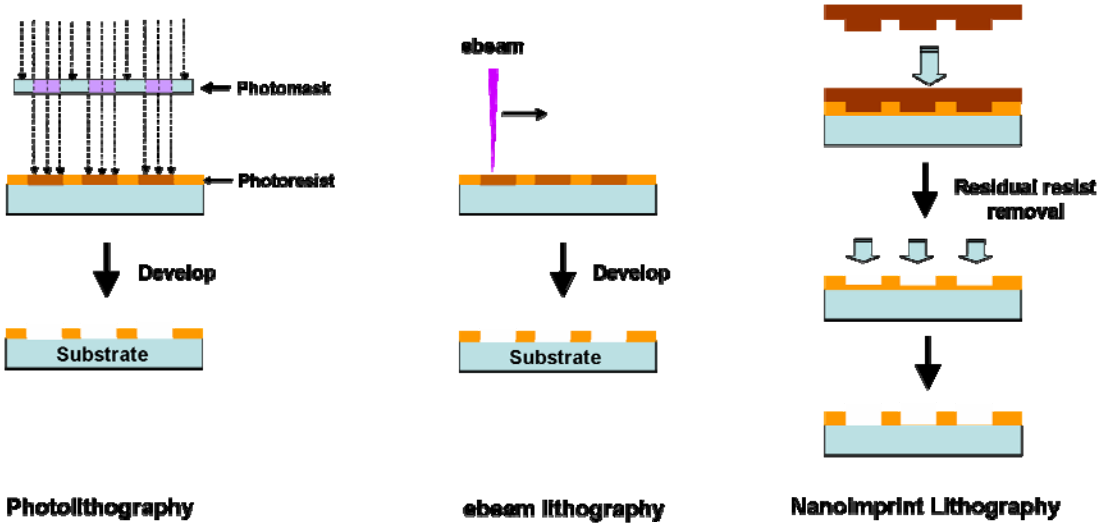

Figure 2.1: Various approaches for making patterns in resists

Once the resists are patterned they could be in turn used as masks to pattern ceramic nanostructures in broadly two different approaches either by adding (additive approach) or removing the material (subtractive). These two approaches are:

a) Define patterns in the polymer resist and deposit ceramic material by chemical/physical vapor deposition or chemical solution deposition routes: This is probably the most straight forward approach amongst the two. In this approach, resist layer is dissolved after the ceramic material deposition to leave the material only in exposed regions. This process is known as lift-off. There are several chemical and physical vapor deposition (C/PVD) routes available for ceramics. PVD techniques include electron beam evaporation, sputtering, pulsed laser deposition and thermal evaporation. CVD techniques involve chemical decomposition of the precursor material on the substrate. The decomposition can be activated by different forms of energy including thermal, laser and plasma. PVD techniques are relatively more benign towards the polymer resists compared to CVD techniques. However, PVD techniques are directional and therefore more difficult to fill high aspect ratio trenches in the resist. Moreover, it is hard to control the stochiometry of the ceramics using PVD techniques and they also typically require high vacuum chambers for material deposition. On the other hand, in the chemical solution deposition (CSD) approach, resist patterned substrates are immersed in a chemical precursor solution and ceramics are deposited either by copious precipitation or selective nucleation on the exposed areas. The advantages of CSD include relatively mild conditions necessary for ceramic deposition,

economical (no sophisticated equipment is necessary) and extremely high crystal quality achievable.

b) Define the resist patterns and etch the underlying ceramic substrate: In this approach, the polymer resist layer is directly spin coated onto a ceramic material and is etched after created openings in the resist. The major disadvantage of this approach is the requirement of ceramic etching. The chemical etching of ceramics is oftentimes difficult, costly and undesirable. Moreover, the severe ceramic etching conditions might also etch the resist material and therefore generation of high aspect ratio structures might require additional process steps.

2.2.3. Ceramic patterns without resist molds

a) Define the patterns using radiation sensitive ceramic resists: An alternative way to using resists as molds to direct ceramic nanostructure growth is to use radiation sensitive ceramic resists. There are several examples of such resists which change their solubility characteristics upon exposure to either photons or electrons. These resist materials contain organometallic precursors and other radiation sensitive molecules that behave similar to regular photoresists used in photolithography. Upon exposure to either UV light, coordination complexes in the resist absorb the radiation and result in formation of metal

complexes that are insoluble in a developer solution. This technique has been demonstrated for depositing variety of metals (Ag[53], Cu[54], Co, Pt, Pd[55], Au[56]), metal oxides (copper oxide[54], silica[57]) and other inorganic material (As_2S_3[58, 59], Si-Ge glass[59]) patterns.

Similar to UV light interaction, inorganic resists can also be designed to be sensitive to electron beam. Exposure to electron beam induces changes in their solubility in a developer solution. In addition, one can take advantage of the high resolution capability of electron beam lithography to generate structures that are much smaller than possible with photolithography. Several reported have recently demonstrated the feasibility of fabricating variety of ceramic (zirconia[60], alumina[61], ZnO[62, 63], titania[64, 65]) patterns as small as 10 nm using electron beam lithography and inorganic resists.

One of the main advantages to using radiation sensitive inorganic resists to fabricate ceramic nanostructures is the absence of any etching step. However, this approach is clearly limited to the films that are sensitive to radiation. Furthermore, the radiation dose (photons or electrons per unit area) required to generate reasonable contrast (solubility difference between exposed and unexposed regions) in inorganic resists is high compared to organic resists. For example, the standard eBL resist, polymethylmethacrylate, can generate very contrast with electron doses as low as 150 $\mu C/cm^2$ whereas titania resists reported by Saifullah et.al[66] required about 300 mC/cm^2 to generate comparable contrast. While direct comparison between these two systems is not entirely appropriate because contrast also

depends on resist thickness, developer solution and radiation energy, it is nevertheless important to realize that inorganic resists usually required several orders of higher doses. This translates into smaller patterning speeds.

2.2.4. Direct deposition methods

The direct deposition methods include those techniques where ceramic material is directly deposited onto the substrate. There are several techniques that can directly deposit ceramic materials at different length scales. These include robotic deposition tools[67, 68], ink jet systems[69, 70], and dip pen nanolithography[71-74]. The ceramic materials could include ceramic powder slurries, ceramic colloidal solutions and sol-gel precursors. Direct write techniques using robotic deposition and ink jet printing involve extruding the colloidal ink through a nozzle and translating the nozzle to generate patterns on the substrate. In a robotic deposition or robocasting technique a continuous filament of the colloidal slurry is deposited onto a substrate while ink jet printing involves deposition of a jet of ink droplets onto a substrate (see figure 2.2).

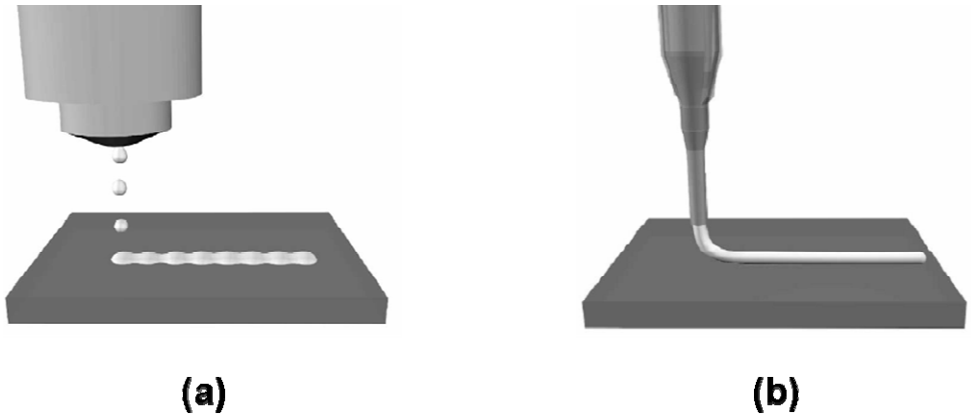

Figure 2.2: Schematic illustration of a) ink jet printing and b) robocasting. Taken from [75]

In ink jet printing, fluid dynamics of droplet formation and spreading of the drop upon impingement with the substrate influence the colloidal ink design. Viscosity, surface tension, and nozzle diameter play important roles in defining the final pattern size. Typically ink jet printing requires low solid content (< 5% by volume) colloidal inks to facilitate consistent drop formation and avoid nozzle clogging. On the other hand robocasting uses high volume content (~ 40-50% by volume) colloidal inks that are extruded through a nozzle by applying pressure. Several variants of ink jet printing and robocasting are reported in the literature under different names. For example, while the variants of robocasting include micropen writing[76, 77] and fused deposition[78], the variants of ink jet printing include hot melt printing[70]. A general over view of the ink jet printing and robocasting can be found elsewhere[79, 80].

The main advantages of ink jet printing and robocasting include the ability to form 3D structures or free-form structures with out requiring any etching steps. However the main drawback of these techniques is the course feature sizes. While these techniques have been demonstrated for depositing free-form structures of variety of ceramic materials (ZnO[81], alumina[82], PZT[68], PNZT[76], hydroxyapatite[83]) the smallest feature size that can be generated using these techniques is at least several tens of microns[80].

An alternative means of depositing ceramic material with high resolution and precision on a substrate is by using dip pen nanolithography (DPN)[71]. This technique uses sol-gel precursor inks that are coated onto an atomic force microscope (AFM) tip. When the ink coated AFM tip is brought within few nanometers of the substrate surface, a spontaneous water meniscus is formed and the ink is transported onto the substrate via this bridge (see figure 2.3). DPN was originally demonstrated for depositing self assembled monolayers and was later adapted by Su .et.al[71] for sol-gel precursors. Surfactants were added to the sol-gel precursors to control the solution viscosity, evaporation rate and hydrolysis rate. Using different sol-gel precursors, variety of ceramic lines (e.g. alumina, titania, ZnO, silica) with widths less than 150 nm were patterned using DPN.

Sol-gel DPN is the high resolution direct deposition method yet reported for ceramic nanostructures. While the high resolution (< 200 nm) ceramic nanostructure fabrication

using DPN and sol-gel precursors is feasible, the technique has challenges with consistency and reproducibility.

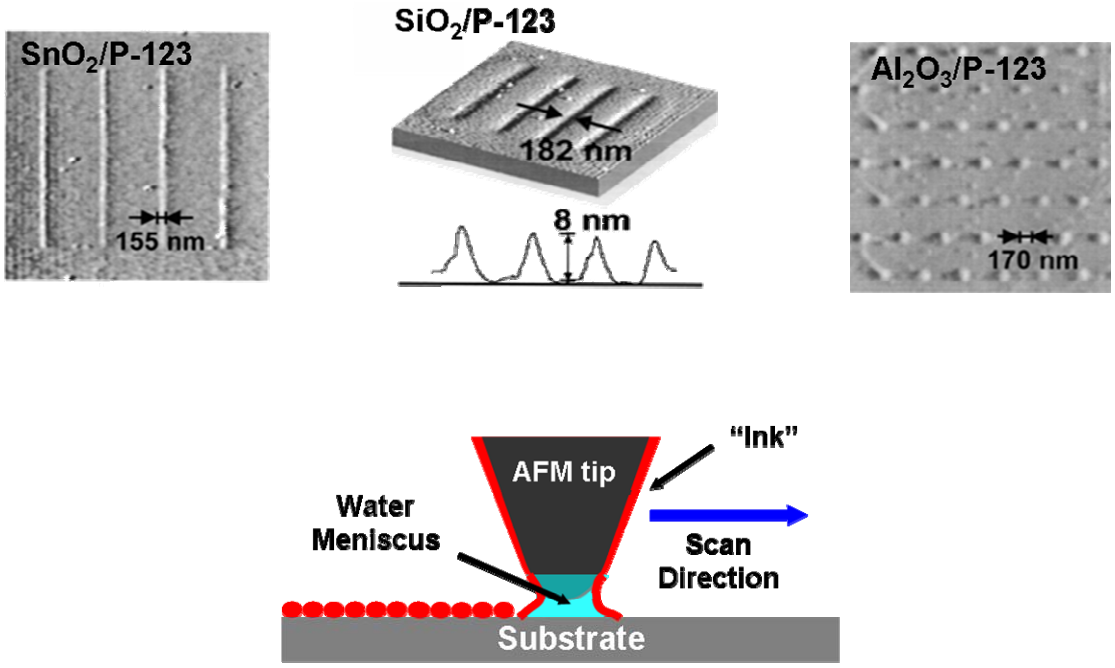

Figure 2.3: Ceramic nanostructure fabrication using dip pen nanolithography and sol-gel precursors. Adapted from [71]

2.2.5. Soft Lithography

Soft Lithography is a patterning concept pioneered by G.M. Whitesides as an inexpensive alternative to photolithography[84-86]. The central element of soft lithography is an elastomeric stamp made of polydimethylsiloxane (PDMS). Several patterning schemes are included under the umbrella of soft lithography and almost every one of these schemes starts with making of PDMS stamp. PDMS stamp is made by pouring the prepolymer of PDMS over a hard master having relief features on its surface (figure 2.4). Upon curing, topographic features from master are transferred to the PDMS stamp. Soft lithography was originally developed for patterning self assembled monolayers and organic polymers. However, it was adapted for patterning ceramic structures. Only the soft lithography techniques demonstrated for ceramic nanostructure fabrication are reviewed here. For a more inclusive review of soft lithography, reader can consult excellent review articles published by Whitesides group[29, 86].

Soft lithography schemes demonstrated for patterning ceramics include micro molding in capillaries (MIMIC), microcontact printing, and microtransfer molding. These techniques are schematically shown in the figure below. The sources of ceramic materials include sol-gel precursors and ceramic powder slurries.

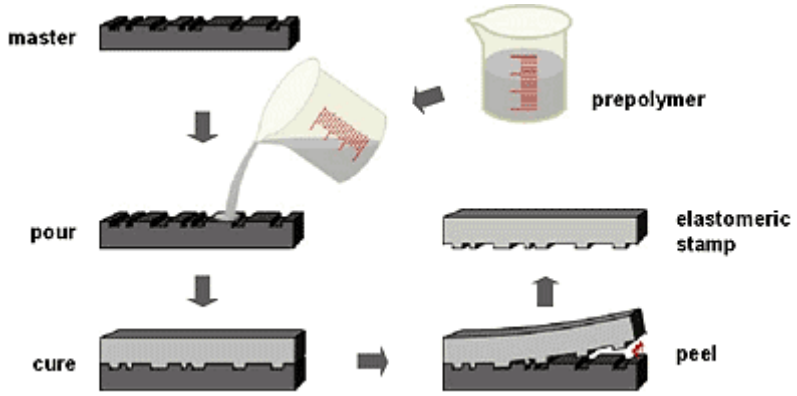

Figure 2.4: Making PDMS stamp from casting prepolymer onto master mold. Image taken from Phillips Research website (http://www.research.philips.com/technologies/light_dev_microsys/softlitho/)

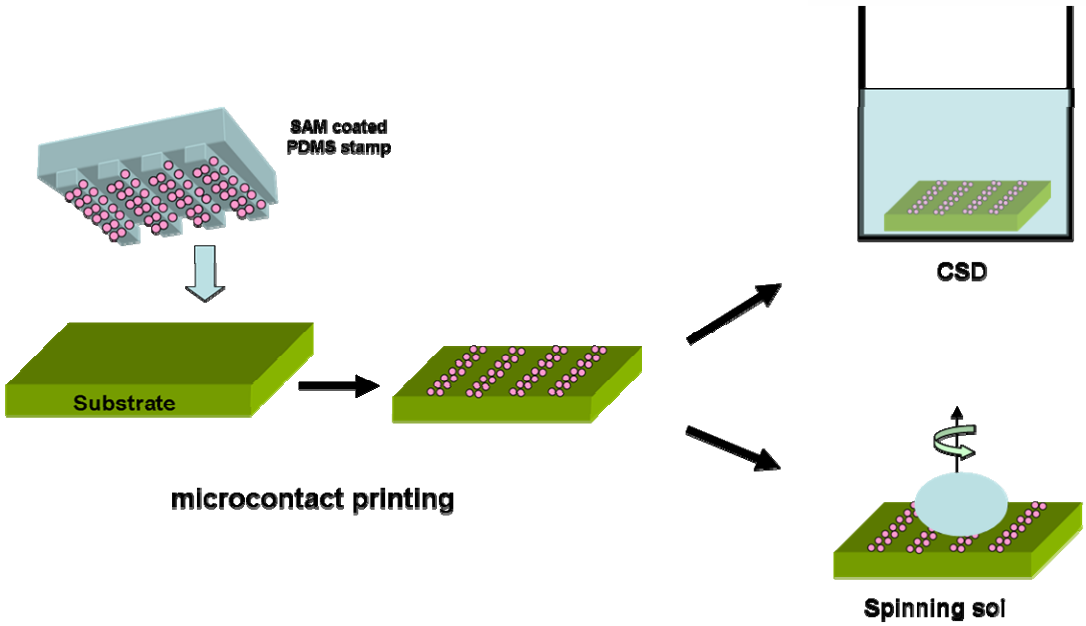

Figure 2.5: Adaptation of microcontact printing (μCP) for ceramic patterning

In microcontact printing (figure 2.5), PDMS stamp is first coated with the solution or ink. Subsequently, ink coated PDMS stamp is placed on a substrate such that relief features on the stamp are in contact with the substrate surface. Upon removal of the stamp, ink is transferred to the substrate due to preferential adhesion of the ink molecules to the substrate. The ink is typically a solution of self assembled monolayer molecules such as octadecanethiol (ODT). These are long alkyl chain molecules with functional end groups with one of the functional end groups having a strong affinity to substrate. For example thiol (SH^-) end groups have a strong covalent interaction with gold. After the transfer of ink onto substrate, the patterns are used as templates for selective deposition of ceramic material from solutions. For example Jeon et.al[87] demonstrated the feasibility of patterning variety of ceramic materials using microcontact printing. They first microcontact printed octadecyltrichlorosilane (OTS) onto substrates such as silicon, sapphire, indium tin oxide (ITO) and then spin coated sol-gel precursors of materials such as $LiNbO_3$ and (Pb, La)TiO_3. Upon subsequent pyrolysis, the ceramic material above OTS had poor adhesion and could be easily removed by wiping with cotton. Using this approach they were above generate $LiNbO_3$ lines as small as 4 μm.

In microtransfer molding (figure 2.6), a layer of ceramic solution is applied on the patterned surface of PDMS stamp and the excess solution is removed by scrapping against a flat surface. A substrate is then placed on top of the solution filled PMDS stamp and entire set-up is heating to temperatures between 60 and 70 ^oC. This solidifies the ceramic solution

and subsequent stamp removal leaves the ceramic patterns or mold on the substrate. This technique has been used to fabricate titania[88, 89], alumina[90] structures with line widths less than 1 μm using appropriate powder slurries. One has to play with the surface energies of the substrate and PDMS mold to promote preferential and reproducible transfer of the ceramic patterns onto the substrate.

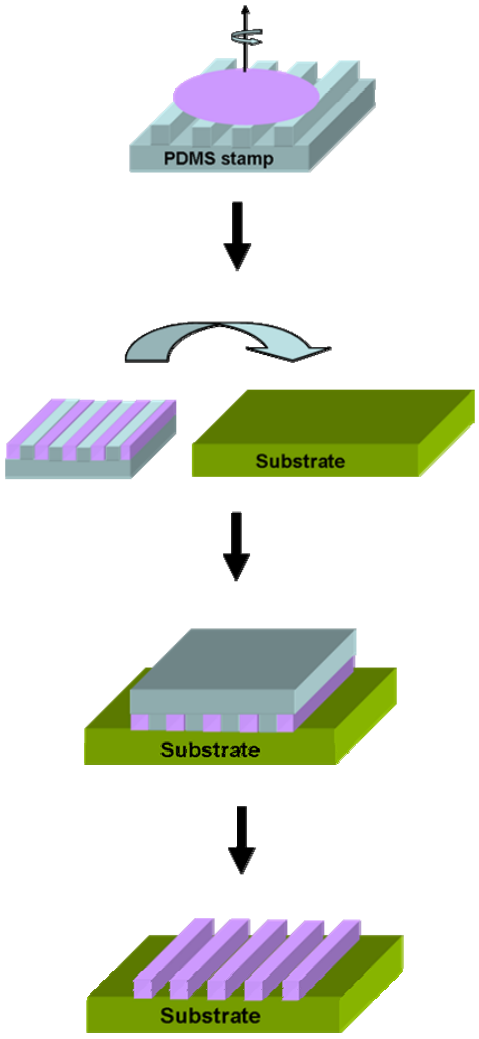

Figure 2.6: Microtransfer molding (μTP) for patterning ceramics

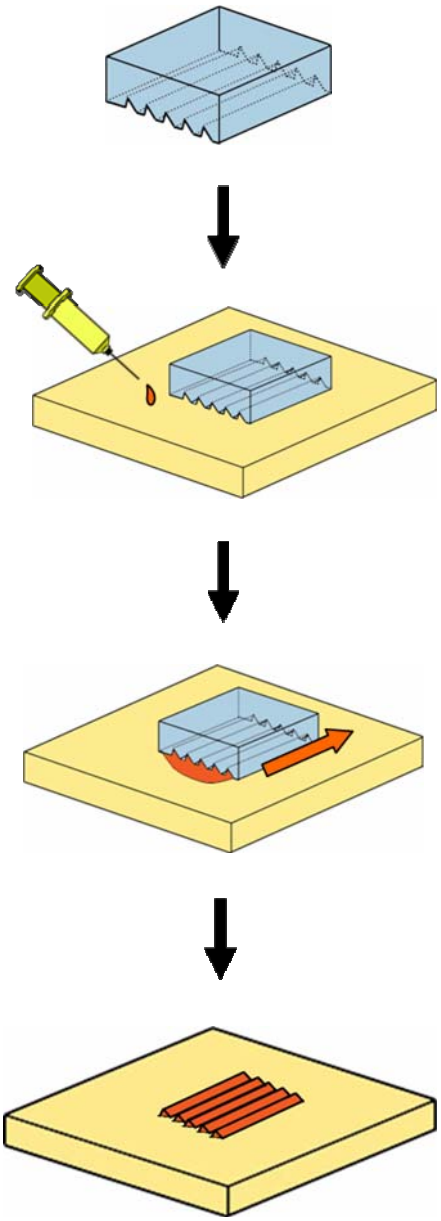

Figure 2.7: Micromolding in capillaries (MIMIC) for pattering ceramics

In micromolding in capillaries (MIMIC) (figure 2.7), the PDMS stamp is placed against a substrate to form a network of interconnected channels. When a low viscosity ceramic solution is placed at the entrance of the channel network, it is quickly sucked into the network due to capillary effect. The entire set-up is heated at slightly above room temperature (~ 60-70 ^{o}C) to remove the solvent from ceramic solution and gelate the structures. Upon removal of the stamp, ceramic structures preferentially adhere to the substrate and the PDMS stamp can be reused. This is by far the most extensively used soft lithography technique for fabricating ceramic structures. Both sol gel precursors and ceramic powder solution have been used in conjunction with MIMIC. For example we have shown[91] used ZnO sols to fabricate 300 nm wide lines on oxidized silicon substrates using MIMIC. Heule et.al[92] have fabricated 10 μm wide tin oxide lines using titania powder and MIMIC. Beh et.al[93] demonstrated the feasibility of using MIMIC to pattern ZrO_2 and SnO_2 starting from their sol-gel precursors. They were also able to fabricate free-standing nanostructures of ZrO_2 and SnO_2 by selective etching of the substrate after MIMIC. This technique was also used to demonstrate functional miniaturized devices such as gas sensors using ceramic powder solutions[94, 95].

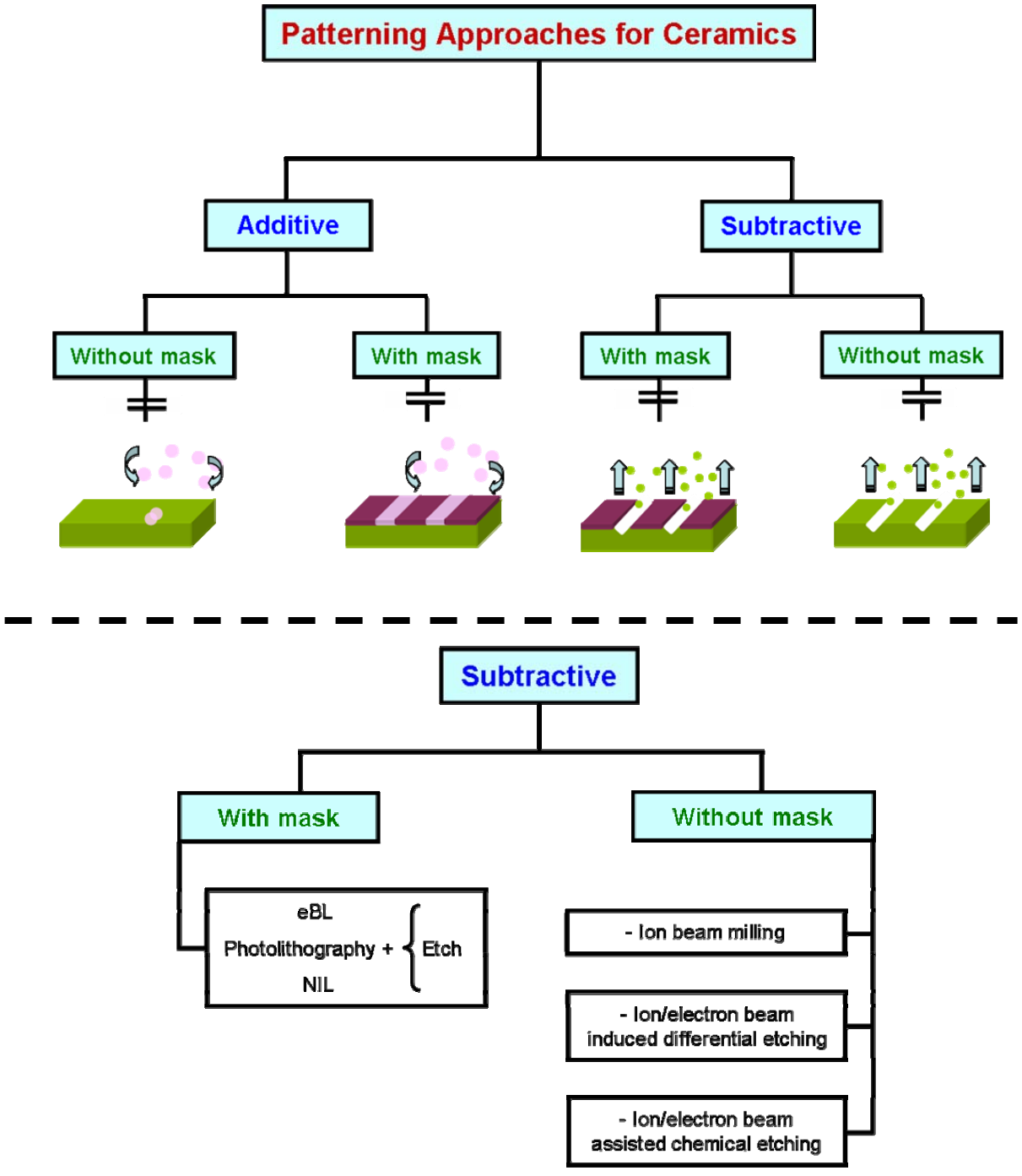

eBL = electron beam lithography, NIL = nanoimprint lithography

Figure 2.8: Classification of various ceramic patterning approaches (continued on next page)

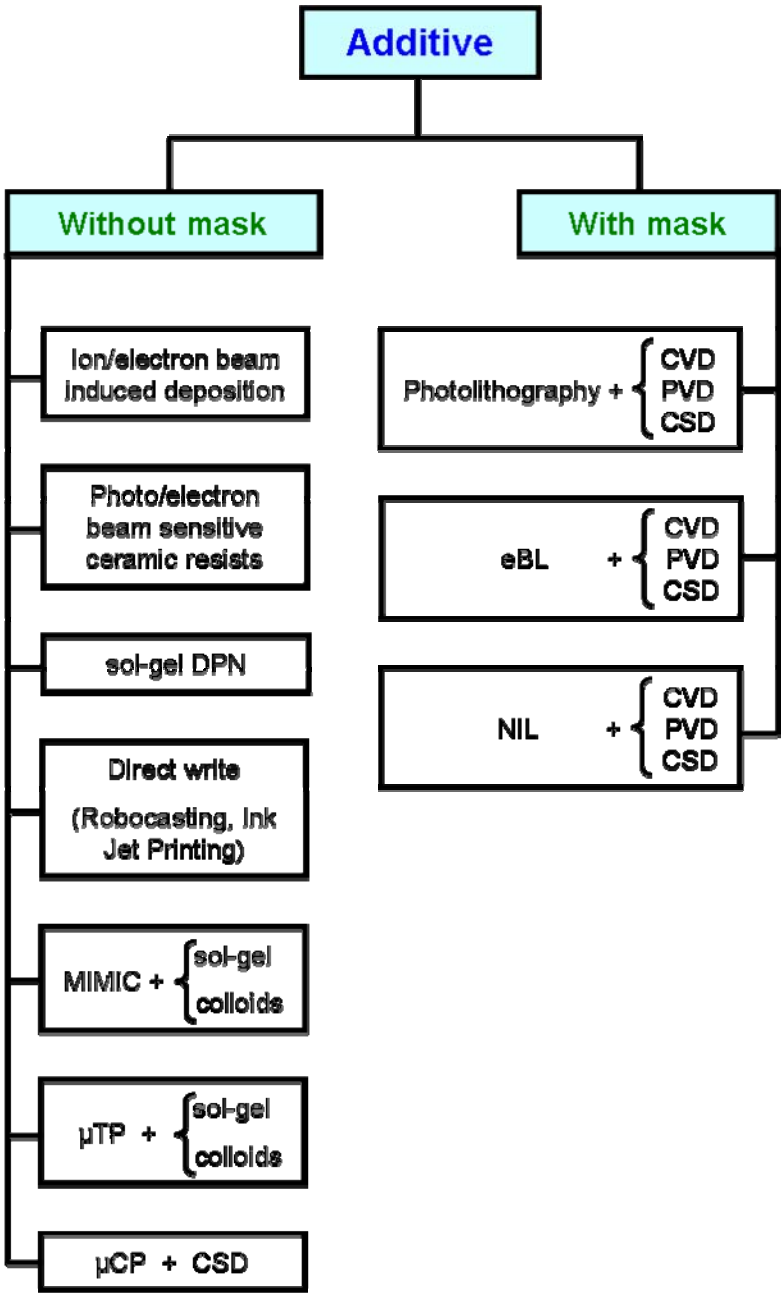

µCP = microcontact printing, µTP = microtransfer molding, DPN = dip pen nanolithography, CSD = chemical solution deposition, C/PVD = chemical/physical vapor deposition

Figure 2.8: Classification of various ceramic patterning approaches (continued from previous page)

2.3 SUMMARY

This chapter has covered most of the permutations and combinations of patterning approaches that have been used for ceramic nanostructure fabrication. Each one of the routes has certain advantages and disadvantages.

The primary desirable attributes of a ceramic patterning approach are high resolution (structures <100 nm) and site-specific capability. While the direct deposition techniques do not have high resolution, most of the soft-lithography techniques do not possess the registry capability. Similarly, while nanoimprint lithography is a high resolution technique it does not have the site-specific patterning capability. Moreover the NIL molds for high resolution patterning have to be in turn made using electron beam lithography. This is particularly inconvenient when one has to make nanostructures at different length-scales and not sure of what length scales one has to work at. Every new pattern design will require a different mold that can be costly and time consuming. For the same reason photolithography is also unattractive. Furthermore, in case of photolithography, fabrication of high resolution patterns will require very expensive equipment such as mask aligners, UV sources and other microfabrication facilities. For these reasons, electron beam lithography (eBL) is attractive. It is a maskless technique and the patterns can be designed in a computer to quickly generate patterns of different shapes and sizes. A modified version of eBL is used in this work.

The myriad of patterning techniques available in literature at first appear overwhelming. It is therefore instructive to classify them to get a better perspective on their broad attributes, advantages and disadvantages. While several authors of review articles on patterning methods have classified them in different ways, the classification in figure 2.8 is particularly useful ceramic patterning approaches.

The variety of patterning techniques relevant for ceramics shown in figure 2.8 suggests that no single technique has all the desirable qualities. This is the main reason why new approaches that are often times a merger of attributes from multiple techniques have been regularly invented. The development of soft-eBL is one such example where the advantages two processes are synergistically combined to develop a facile means of ceramic nanostructure fabrication.

Soft-electron beam lithography (soft-eBL) developed in our group combines the high resolution and site-specific capabilities of eBL with easy formability capability of soft chemistry. This technique is discussed in chapter 4. Prior to that, in the next chapter the advantages of soft chemistry for ceramic nanostructure fabrication and the need for physical property measurement at appropriate length scales are demonstrated.

CHAPTER 3

NEAR-FIELD SCANNING OPTICAL MICROSCOPY OF ZNO NANOPATTERNS FABRICATED BY MICRO-MOLDING IN CAPILLARIES

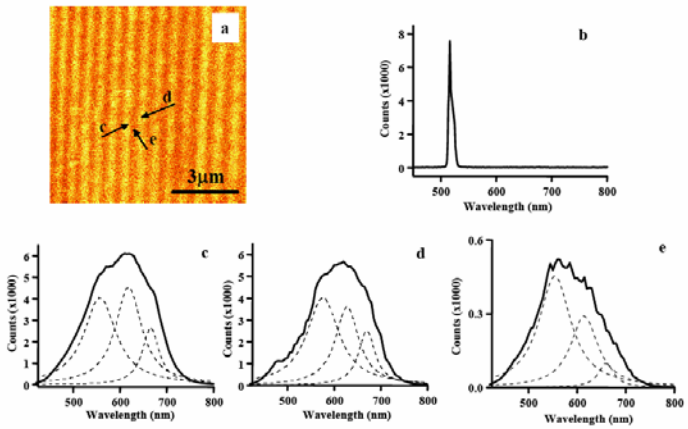

This chapter reports near-field scanning optical microscopy (NSOM) studies of 300 nm wide ZnO nanopatterns fabricated by micro-molding in capillaries technique using a sol-gel route. A protocol to decouple the topography and optical signal collected in NSOM scans and therefore extract the true photoluminescence (PL) properties of the ZnO nanopatterns is presented. The nanoscale spectral mapping shows very broad defect-induced green-yellow-red luminescence bands, at room temperature, when excited with 514.5 nm Ar ion laser. These results demonstrate the significant effect played by the processing conditions and the structural defects on optical properties of ZnO and therefore underscore the need to couple nanoscale physical characterization with functional properties at the same scale.

A part of the work discussed in this chapter is published in: **J. Appl. Phys. 98, 24304 (2005)**

3.1 SOFT LITHOGRAPHY FOR ZnO NANOSTRUCTURES

The potential benefits of miniaturization are the driving forces behind innovation in micro and nanofabrication techniques. The ubiquitous relation between "structure-property-performance" of materials suggests that thorough evaluation of the physical properties of the nanostructures must keep pace with the developments in novel fabrication tools. The motivation for extensive property evaluation of the nanostructures also stems from the size dependent properties observed in several material systems[4, 96-98]. In addition to the dimensions, the properties are also influenced by the fabrication routes even in a bulk material system because of the influence of processing route on microstructure. For example, several papers in the literature report the photoluminescence (PL) peak intensity maximum in zinc oxide (ZnO) not at a single wavelength but at different wavelengths spanning the entire visible spectrum depending on the fabrication process. Photoluminescence (PL) refers to the process of spontaneous photon emission from a material upon illumination with photons of higher frequency. The most widely accepted premise for this strong influence of fabrication routes on optical properties of ZnO is the dependence of concentration of structural defects on deposition technique. In addition, the PL properties of several types of ZnO nanostructures such as nanowires, nanotubes and tetrapods[99-101] have been reported and are shown to be different from ZnO single crystal[102]. The size and processing effect on optical properties of ZnO is the main motivation for the work reported in this chapter.

The primary goals of this chapter are two fold. First, this chapter reports the feasibility of adapting a soft-lithography technique called as micro-molding in capillaries (MIMIC) to large area patterning of ZnO lines with widths less than 300 nm using their sol-gel precursors. The other goal of the chapter is to demonstrate a experimental protocol for extracting the true optical properties of these nanostructures using near field scanning optical microscope. The next three sections will explain the relevant salient features of MIMIC technique, sol-gel processing route and NSOM technique. Subsequently, the main experimental details are outlined followed by the discussion of the results.

3.2 MICROMOLDING IN CAPILLARIES

Micro-molding in capillaries (MIMIC) is a versatile patterning technique with flexibility to pattern variety of materials rapidly over areas in excess of several centimeters[103-106]. This is one of the soft-lithography techniques first proposed by G.M. Whitesides[107] for patterning organic polymers and was subsequently adapted for patterning other materials starting from their liquid precursors/solutions. In this technique, a mold containing a regular array of grooves is pressed against a substrate to form a continuous network of channels. When a low viscosity liquid is placed in contact with this channel network, the liquid spontaneously fills the network due to capillary effect. The mold is most commonly made from an elastomer called poly-(dimethylsiloxane) (PDMS) though other elastomers have also been tested[85]. The mold is fabricated by pouring the mixture of

elastomer and a catalyst (cross-linker) onto a substrate (called master) containing inverse topographic features and curing at moderate temperatures to harden the elastomer. The master is a hard substrate whose topographic features might have been fabricated using standard photolithography. The cured elastomer mold faithfully replicates the topographic features of the master while the master can be reused to generate more replicas. The efficacy of MIMIC depends on several factors including, the mechanical properties and surface roughness of the elastomer mold, surface energy of the mold as well as substrate supporting the patterns, viscosity of the patterning liquid and the chemical resistance of the mold to the patterning liquid. Therefore, adaptation of MIMIC for patterning different materials requires thorough optimization of these parameters and thus might require additional steps depending on the nature of the liquid precursor. In this work, patterning of ceramics, ZnO in specific is achieved using their sol precursors. The main steps in MIMIC adapted in this work for patterning ceramics from sol precursors are shown in figure 3.1.

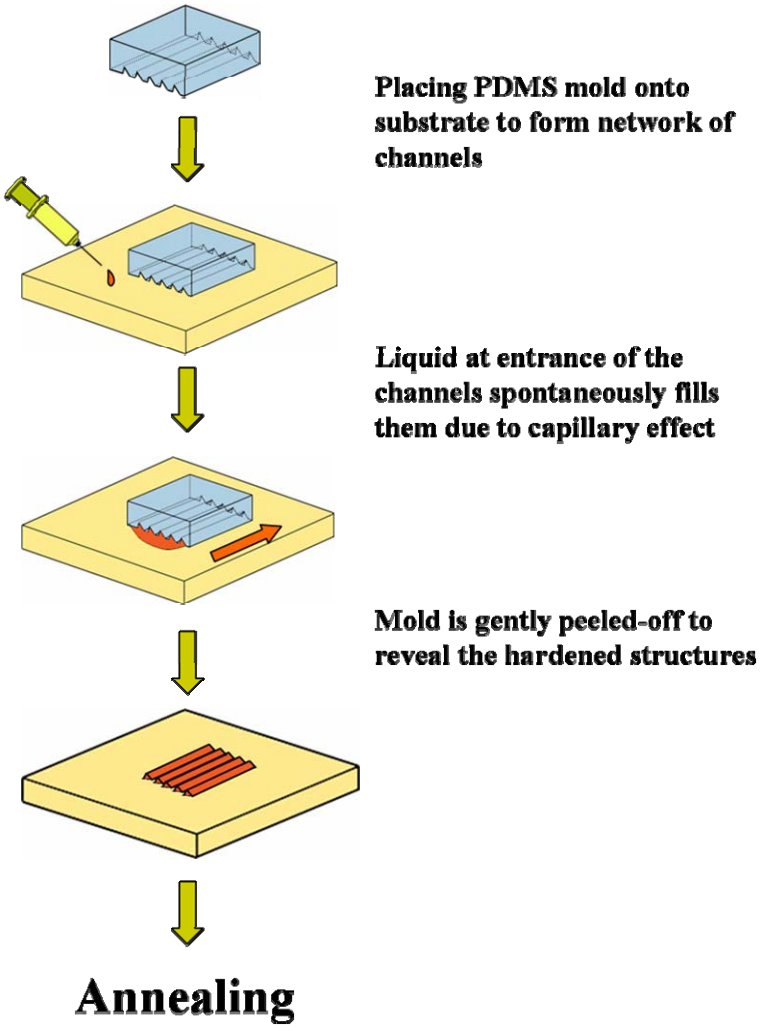

Figure 3.1: The basic steps in patterning of ceramics using sol precursors and MIMIC

3.3 SOL-GEL SYNTHESIS ROUTE AS AN ENABLER

Sol-gel[108] stands for solution-gelation. This is a wet-chemistry process widely used to make inorganic structures such as oxides and glasses that typically involves hydrolysis and condensation of metallo-organic compounds such as alkoxides in a suitable solvent medium. By controlling the rate of hydrolysis and condensation it is possible to tailor the structural integrity of the final structure[109]. This synthetic approach is recognized as an important direction for the rational design and controlled synthesis of a wide range of novel materials in the areas of electronics, photonics and sensors[110-114].

In addition to low working temperatures, sol-gel process has a number of other advantages. These include

1. The precursors are easily purified to high level and contribute to high-purity products that are very important for various device applications.
2. It is possible to achieve a homogeneous and controlled dopant level in sol by using miscible organometallic dopant precursors[115]. This is one of the major driving forces for using this technique extensively for making active chemical sensor elements.
3. Highly porous structures are naturally formed after combustion of the organic matter enabling the final structures with high surface areas and activity[109].

4. Because the precursors are liquids, their physical properties such as viscosity could be easily modified with additives, for example, and cast into complex shapes without the need for machining. This is an important advantage in light of the difficulty in machining ceramics due to their brittle nature.

3.3 NEAR-FIELD SCANNING OPTICAL MICROSCOPY (NSOM)

Near-field scanning optical microscopy is a powerful tool that combines the advantages of scanning probe technology with the optical microscopy. This is emerging as a powerful analytical tool, capable of sub-wavelength spatial resolution that is ideally suited to investigate optical properties of nanostructures[116-118]. Versatility of the NSOM is highlighted by reports investigating varied phenomenon such as photonic block copolymer morphology[119], fluorescence imaging of biological samples[117], imaging of second harmonic generation in ZnO nanowires[120], observation of local ferroelectric phase transitions[121], among many others. With significant technological advances in NSOM tip fabrication and with major advances in instrumentation, NSOM will continue to serve as a valuable tool to probe optical properties of nanostructures.

The technique involves scanning a cantilevered optical fiber, with apertures as small as 50 nm, over a sample surface. The method of operation is similar to tapping mode of operation in atomic force microscopy where the cantilever scans the sample surface in x and

y directions (in-plane of sample) while the cantilever oscillates at much higher frequency in z-direction. During these oscillates the cantilever periodically taps the sample surface. The tapered ends of the fiber are coated with metals such as aluminum to guide the light through the aperture and to achieve high light throughputs (the fraction of light intensity that exits the aperture). It can be shown that when the aperture size is smaller than the wavelength of the light, strongly enhanced fields appear at the vicinity of the aperture. As in scanning probe microscopy, the NSOM tip is scanned very close to the sample surface (within few nanometers) by mounting either the tip or sample on a stage driven by piezo motors. The distance between sample and the tip is maintained by the feedback loop consisting of an optical laser and a position sensitive detector similar to method used in atomic force microscope.

NSOM can be operated in several modes depending on the relative motion of the sample and tip as well as the method of optical excitation of the sample. Figure 3.2 shows the various modes of NSOM operation. In the transmission mode the wave vectors of excitation and emitted signal have the same sign. In the illumination mode, the sample is excited with the light in near field by delivering it through the NSOM tip while the emitted signal is collected in far field usually using normal optical lenses. On the other hand in collection mode the excitation signal is delivered in far field, typically using another optical fiber placed parallel to the sample normal, while the emitted signal from the sample is collected with the NSOM tip in near field. This is a particularly useful mode of operation

when the intensity of the emitted signal from the sample is weak. In addition to these modes of operation NSOM could also be operated in "constant-height" or "constant-amplitude" modes depending on the nature of tip-sample relative motion (Figure 3.3). In a "constant-height" mode, the tip scans sample surface while always maintaining a constant distance between sample and tip. In other words, in this mode the cantilever does not follow the sample topography.

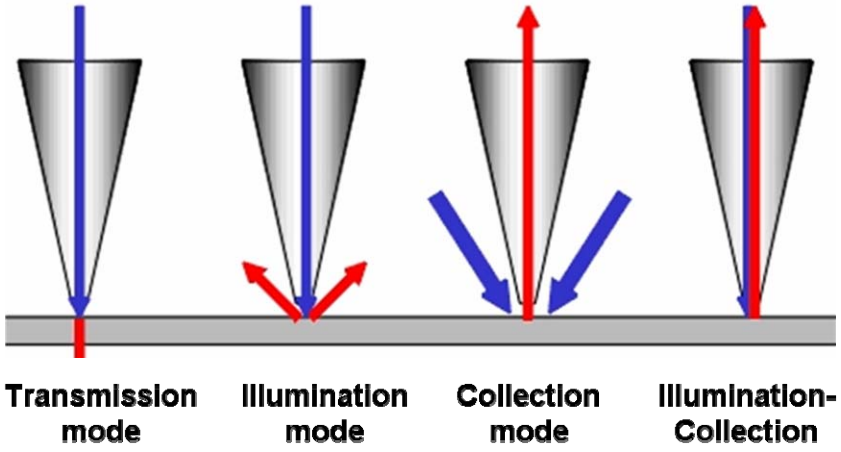

Figure 3.2: Various modes of NSOM operation. Blue arrow represents excitation signal whereas red arrow represents emitted signal from the sample.

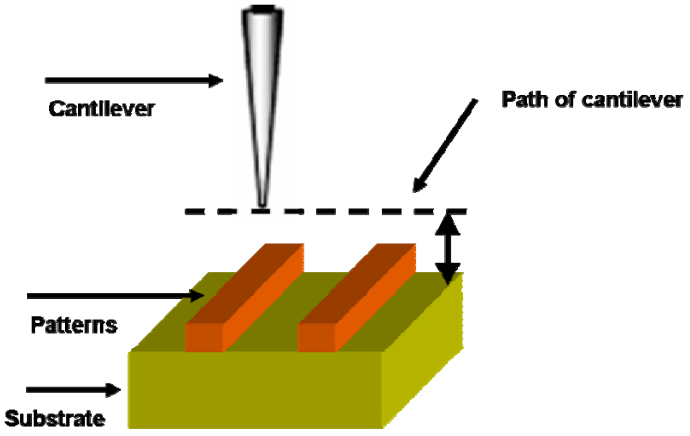

Figure 3.3a: Operation of NSOM in "Constant-height" mode

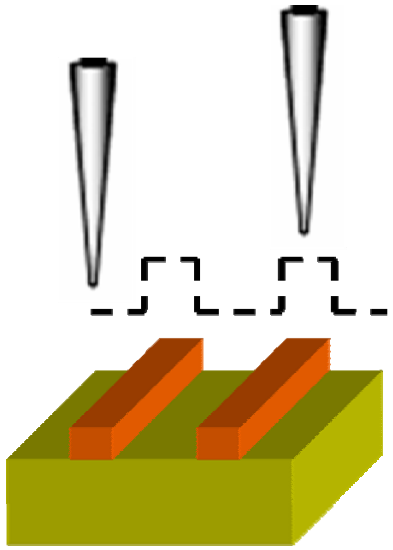

Figure 3.3b: Operation of NSOM in "Constant-amplitude" mode when the cantilever tracks the topography.

On the other hand, in constant amplitude mode the cantilever maintains a constant gap between the sample and tip by following the sample topography. This method is called as constant amplitude mode because the amplitude of oscillation of the cantilever is used as feedback signal for maintaining a constant tip-sample gap, similar to tapping mode of operation in atomic force microscope.

In this work, NSOM is operated in several modes including collection mode, illumination mode, constant height mode and constant amplitude mode. One of the goals of this chapter is to highlight the unique information one can obtain by operating in combination of these modes.

3.4. EXPERIMENTAL

3.4..1 ZnO Sol preparation: Zinc oxide sol was prepared by stirring a mixture of zinc acetate dihydrate (1.54 g), 2-methoxy ethanol (19.6 ml) and ethanolamine (0.4 ml) at 60 ^{o}C for 2 h. This gives a 0.35M ZnO sol that is transparent and remains stable for more than six months when stored in a desiccator. All the sol precursors were purchased from Sigma-Aldrich and used in as received form without further purification.

3.4.2 PDMS mold fabrication: PDMS elastomer mold was made from a mixture of prepolymer and catalyst available under commercial name, Sylgard 184 (Dow Corning Inc.,

Midland, MI, USA). Sylgard 184 is spin-coated on a gold grating (Edmund Optics, 1200 grooves/mm and a glazing angle of 36° 52') to obtain a sub-millimeter thick PDMS mold. After curing at 70 °C for about 10 h, the PDMS film was carefully peeled off from the Au grating (master mold). There are several advantages to using a sub-millimeter thick mold as opposed to a bulk (~cm thick) mold that is typically reported in the literature. First, the thinner mold thickness allows a better conformal attachment, even on a curved surface, of a substrate. Second, smaller thickness will allow a quicker degassing and results in less likelihood of pore entrapment. Third, one can use less mold material.

3.4.3 Soft-lithography of ZnO patterns: After curing, the PDMS layer is carefully peeled-off from the gold grating and placed on top of SiO_x/Si substrate that was previously cleaned sequentially in acetone, piranha (3:1volume ratio of H_2SO_4:H_2O_2) solution at 70 ^oC and DI water. A droplet of ZnO sol placed at the entrance of capillaries quickly fills the channels. The whole substrate was then moved into a vacuum chamber for 2 h to enhance degassing from PDMS stamp and liquid infusion into the channels. The substrate was then slightly heated at temperatures between 60 °C and 70 °C for 2 h to evaporate the solvent. The mold was subsequently peeled-off and the patterns were annealed at 550 ^oC for 1 h in air. After few trial experiments, it was found that oxygen plasma treatment of the mold is not necessary prior to placing it on the substrate and in fact plasma treating of the mold material is often detrimental to patterns. The patterns seemed to preferentially stick to plasma treated mold and peeled off from the substrate.

3.4.4: Near field Scanning Optical Microscopy: Near-field scanning optical microscopy measurements (NSOM) (The MultiView 1000^{TM}, Nanonics Imaging Ltd.) were done in both, illumination and collection modes, using Cr/Al coated cantilevered optical fiber probes with 200 and 300 nm aperture diameter. In both modes, Ar ion laser (λ = 514.5 nm, 10 mW output power) coupled to the optical fiber was used to excite the defect induced luminescent states in ZnO nanopatterns. Images in "constant-amplitude" mode were obtained with the normal force feedback loop to maintain constant tip distance from the surface, while the "constant-height" images were obtained by scanning with feedback mode turned off. NSOM-PL intensity mapping was carried out using an avalanche photodiode (APD) with single photon counting electronics. Specific optical filters were used for efficient detection of reflected or luminescent light from ZnO.

3.4.5: Electron and atomic force microscopy: The patterns were imaged using AFM (Digital Instruments Nanoscope IIIa) operating in contact mode with SiN_x cantilevers of a nominal force constant of 0.05 N/m. SEM images were taken with a Hitachi S4500 equipped with a cold field emission electron gun.

3.5 STRUCTURAL AND OPTICAL CHARACTERIZATION OF THE ZNO PATTERNS

The structural characterization of the ZnO patterns was carried out using AFM and SEM. Figures 3.4a and 3.4b show the AFM topographic images of ZnO patterns taken before and after annealing the patterns at 550 ^{o}C for 1 h in air. The lines appear uniform and remain continuous after annealing. A comparison of AFM cross sectional scans taken before and after annealing showed that the widths of these lines decrease by about 10% to 300 nm where as their height decreases nearly by 50% to about 80 nm. It is possible that most of this shrinkage is accommodated by patterns through generation of porous network when organics in sol are burned away during annealing step. The large shrinkage observed in height compared to width is due to relatively strong silicon-oxygen-metal bonding which is observed when sols hydrolyze on oxide substrates[122]. This results in a relatively larger constraint to reduction in width of the line compared to the height that is virtually unconstrained. However, the results in later chapters show that width of the patterns fabricated from sols using other patterning techniques can also decrease as much as height upon annealing at slightly higher temperatures of 700 ^{o}C. The comparable size reductions in both lateral and normal directions could be due to larger shrinkage stresses generated and higher atomic mobility observed when annealed at high temperatures.

The SEM image of the pattern shown in figure 3.4c confirms the AFM results about pattern uniformity and line continuity. Multiple images taken at several locations indicated that lines are continuous over several tens of microns and no noticeable agglomeration was observed. The widths of these ZnO lines measured from SEM images (280 nm) are consistent with AFM analysis.

In order to ensure that fabricated ZnO nanopatterns are functional in terms of their photoluminescence activity, micro-photoluminescence (μ-PL) measurements were carried out using a Renishaw 2000 micro-PL setup. The room temperature μ-PL spectrum recorded from these patterns with 325 nm excitation is shown in figure 3.4d. The room temperature PL spectrum shows the characteristic near-band edge emission at 3.28 eV and the defect-induced donor-acceptor pair emission bands below 2.5 eV. These results indicate that annealing scheme used in this work is sufficient to produce photoluminescent ZnO nanopatterns. The 2 μm spot size used for measuring μ-PL spectrum is still relatively a macroscopic probing because the sampling area is at least six times larger than the minimum feature size. However, it is desirable to have a characterization tool with spatial resolution better than the minimum feature size in the structure of investigation to probe the uniformity of PL emission within each line. NSOM is ideally suited for this task because it has the spatial resolution necessary to resolve the MIMIC nanopatterns of ZnO.

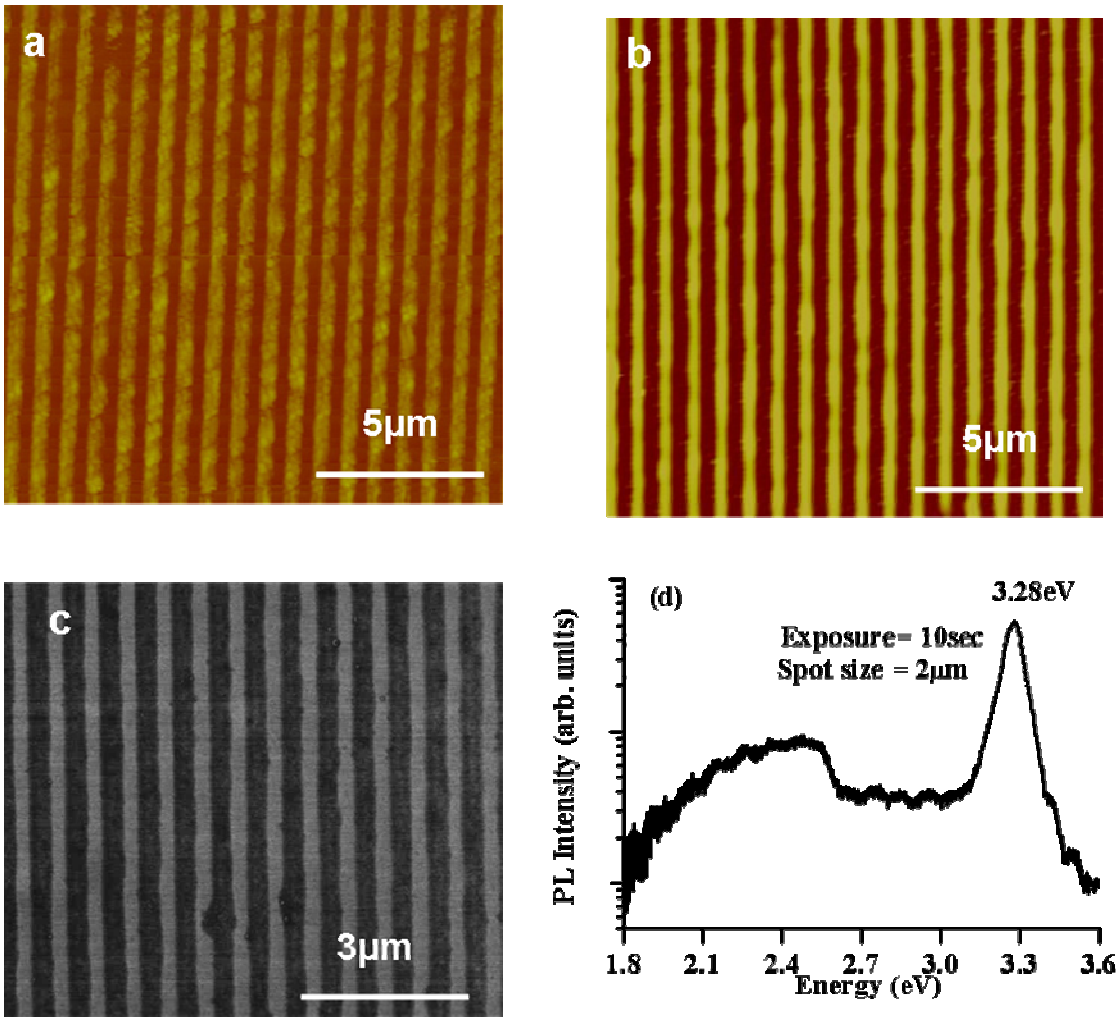

Figure 3.4: AFM topographic images a) before and b) after annealing at 550 ^{0}C for 1 h in air. c) SEM image of pattern after annealing. These images were not taken at same location. d) Room temperature μ-PL spectrum of ZnO patterns showing band-edge emission at 3.28eV and Donor-Acceptor Pair emission below 2.5 eV.

Figure 3.5 shows a set of topographic and reflection NSOM-optical images of ZnO patterns obtained in “constant-amplitude mode” mode. All these images were obtained from the same specimen location by collecting reflection optical signal in far-field (i.e. illumination mode). Figures 3.5a and 3.5b show the topographic and NSOM-optical images obtained in “constant-amplitude” mode. In “constant-amplitude” mode, the cantilevered optical fiber probe scans the sample while maintaining constant amplitude with respect to sample using normal force feedback loop similar to the feedback control used in scanning probe microscopy. Thus, the cantilever closely tracks the surface and generates a topographic image similar to AFM. The average width of ZnO line measured in topographic image in figure 3.5a (370 nm) is slightly larger than that measured using AFM (figure 3.4a) mainly because of the coarse tip (200 nm) used in NSOM experiments compared to the typical radius of pyramidal SiN_x tips (usually < 50 nm) used for contact mode AFM scans. In agreement with AFM measurements, these images show that lines are continuous and optical signal is uniform along each line without any dark spots. Similar to the topographic image collected with AFM (e.g. figure 3.4b), topographic image collected with NSOM probe (figure 3.5a) also shows certain topographical features, possibly individual grains within each line. However, the NSOM-optical image could not clearly resolve the exact dimensions because the aperture diameter is larger than the size of these individual features.

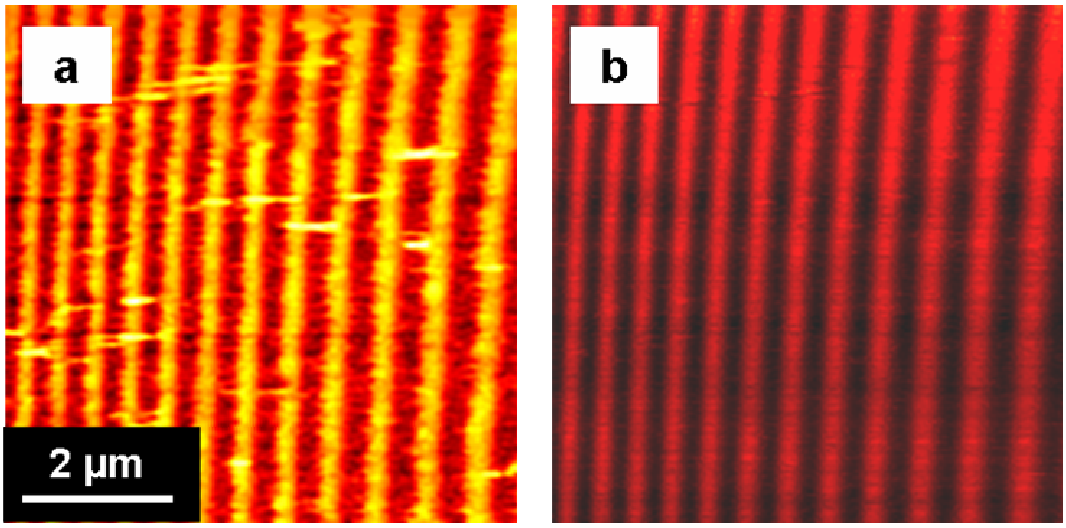

Figure 3.5: a) Topography and b) NSOM optical images taken in "constant-amplitude" mode. Same scale bar applies to both the images and these images correspond to same location on the sample.

The NSOM-optical images taken in "constant-amplitude" mode are known to contain z-motion artifacts in the form of cross-talk between topographic and optical images[123, 124]. This is evident as a strong phase-shift correlation between features in topographic and NSOM-optical images in figures 3.5a and 3.5b. This strong correlation between topographic and optical images makes the origin of optical signal ambiguous. For example, it is not clear if the contrast in NSOM optical image (figure 3.5b) is due to ZnO patterns or an artifact of topography. To decouple the topography and optical signals, the optical and topographic images from the same location were obtained by operating NSOM in "constant-height" mode. In "constant-height" mode, the cantilever is rastered on the sample without engaging it in the feedback control. In this mode, the cantilever is maintained at a constant height from sample while scanning and thus, it does not trace any topographic feature on the surface. The optical images obtained in this mode are therefore free of z-motion artifacts. Figures 3.6a and 3.6b are topographic and NSOM-optical images, respectively, obtained in "constant-height" mode. As expected, topographic image is flat and no contrast is visible because the cantilever is not in feedback control. On the other hand, optical image clearly outlines ZnO nanopatterns, though with a slightly larger line-width than seen in figure 3.5b. In addition, some non-uniformity in the line widths across the image is also evident in figure 3.6b due to limited optical resolution in z-axis. This is an artifact because substrates are often not horizontally flat relative to the cantilever. Thus, while cantilever is scanning the sample at a constant height, one part of the sample might be farther from probe than another part of the sample, giving rise to observed differences in

line-widths. The reduced resolution in figure 3.6b compared to figure 3.5b is due to larger tip-sample separation.

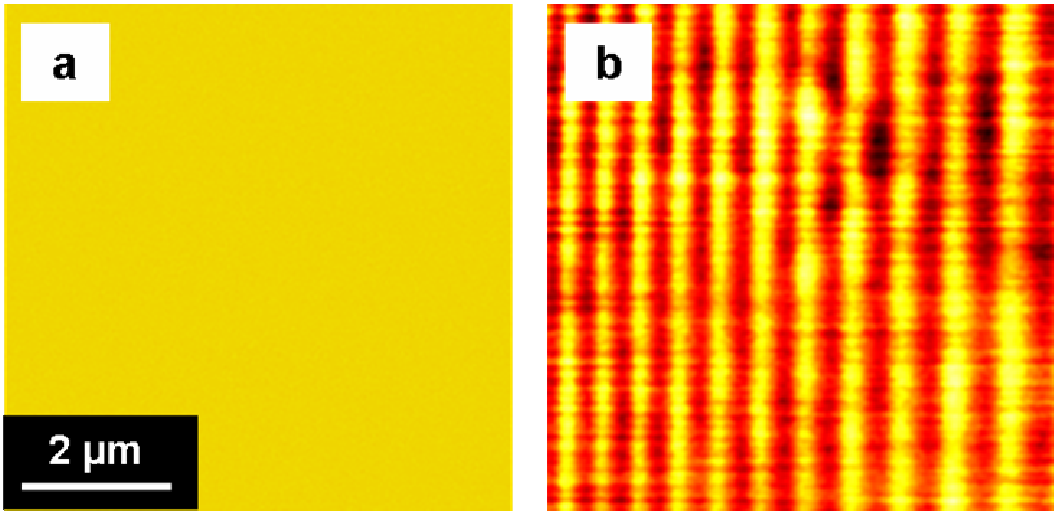

Figure 3.6 a) Topography and b) NSOM optical images taken in "constant-height" mode. Same scale bar applies to both the images.

It has been reported by Hecht et.al[117] that spatial resolution in optical images decreases as tip height above sample surface increases by few nanometers. The optical image in figure 3.6b therefore unambiguously shows that optical signal used to form this image is truly originating from ZnO lines as the cross-talk with topography signal is eliminated. However, the source of contrast in this reflected optical image is not yet clear. There are two possible sources of contrast in scanned NSOM-optical images: a) A difference in refractive index between ZnO lines and SiO_x substrate. In this case, contrast would be simply due to the difference in reflected intensity of excited 514.5 nm light from ZnO lines and oxide substrate between ZnO lines. b) Due to true localized photoluminescence from ZnO lines. One way to identify the actual source of contrast amongst these two choices is to use an appropriate optical filter to cut-off the excitation laser light (i.e. 514.5 nm) because reflected light is predominantly at this wavelength. Therefore, subsequent NSOM images were obtained by selecting an appropriate filter range in the monochromator before signal reached the detector. In addition, these images were obtained in collection mode for efficient signal collection. In collection mode operation, the excitation laser light was delivered to the sample via optical fiber whose axis is parallel to the sample normal. This optical fiber is different from the cantilevered optical fiber probe used to scan and collect optical signal. The optical signal from the sample is then collected with cantilevered probe of a 300 nm aperture diameter and fed via long pass filter to the monochromator with attached avalanche photodiode.

The optical and topographic images of patterns, while operating in “constant-height” mode in collection mode configuration, are shown in figure 3.7.

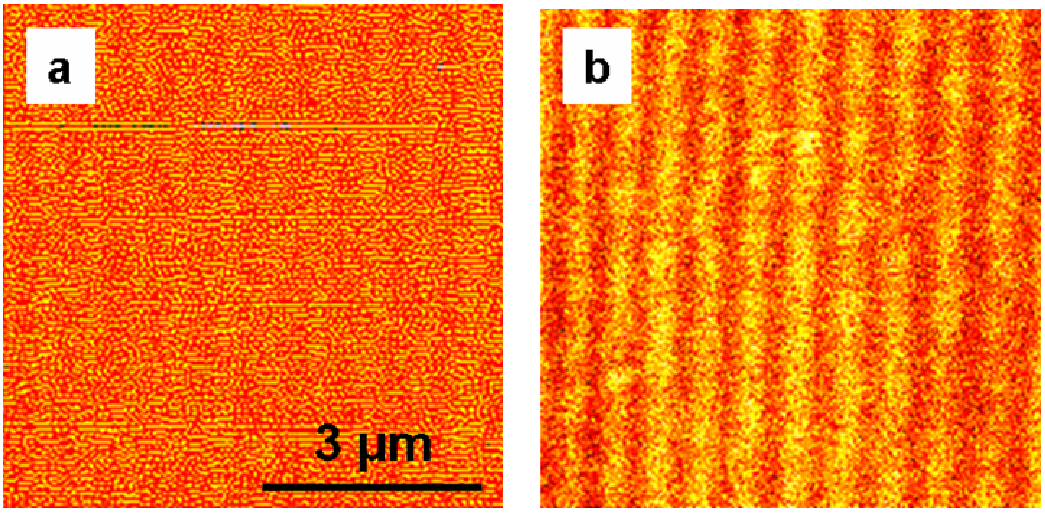

Figure 3.7 a) Topographic and b) NSOM optical images of ZnO patterns obtained in *collection mode* configuration while operating in “constant-height” mode. Same scale bar applies to both images

As expected, this figure shows no pattern features in topographic image (because of constant-height mode operation) whereas patterns are clearly visible in the NSOM-optical image. As indicated earlier, this optical image is formed after filtering the 514.5 nm excitation laser light with a long pass filter. This image clearly shows the spatially resolved PL intensity distribution within ZnO patterns. It was also noticed that maximum photon count in figure 3.7b decreased compared to images in figures 3.5b and 3.6b. The weaker scattered light intensity results in grainier NSOM-PL image. Because a long pass filter is used to form the image shown in figure 3.7b, the contrast in this image cannot be due to difference in simple reflected light intensity from ZnO lines and oxide surface. To further confirm this, spectrum from three different locations on the sample, with and without long pass filter, is collected by positioning the cantilever probe at various locations.

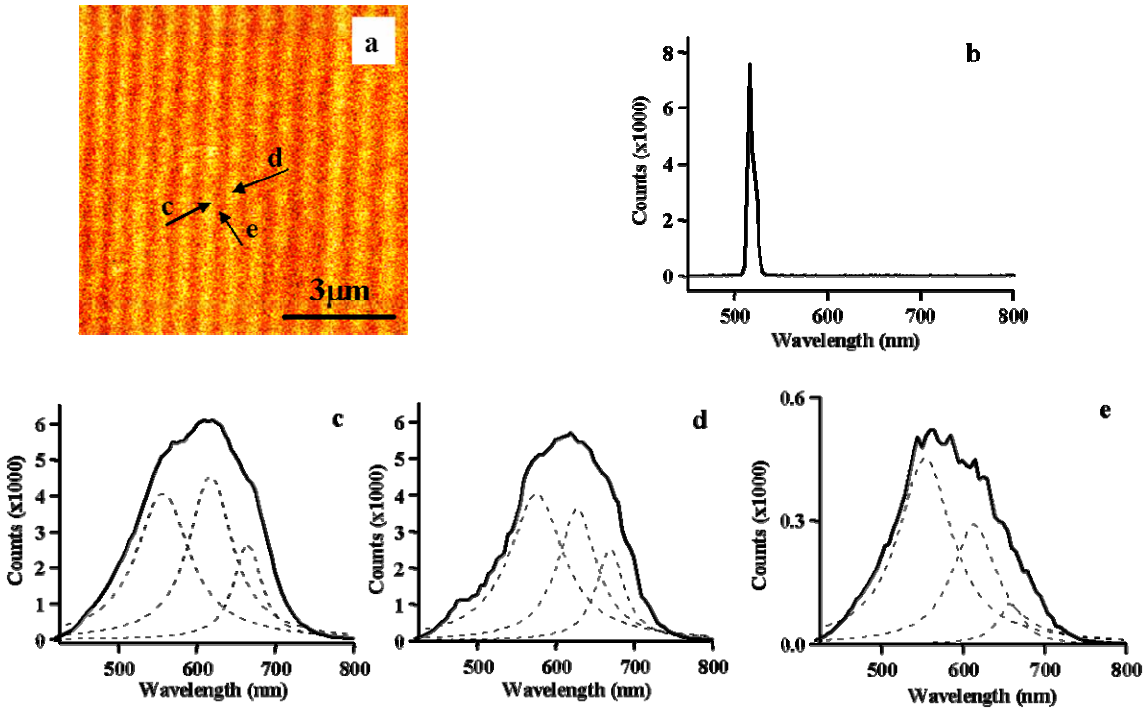

Figure 3.8 a) NSOM-optical image of ZnO pattern. b) Spectrum collected outside the patterns without long pass filter showing excitation laser at 514.5 nm. c) and d) Spectra collected from two locations on adjacent ZnO lines. e) Spectrum collected between these two ZnO lines. Spectra shown in c-e are collected while using the long pass filter to transmit the resonantly excited photoluminescence from defect-induced bands. Dotted lines are the Lorentzian curve fits to multiple PL bands.

Figure 3.8a shows the NSOM-PL intensity image scanned while using the long pass filter prior to collecting the spectra in figure 3.8. The spectrum in figure 3.8b is collected from substrate, but outside the nanopatterns, without using long pass filter. This spectrum shows a single narrow peak at 514.5 nm due to simple reflection from the substrate. As expected for indirect bandgap semiconductor such as Si, no additional emission bands are visible in this spectrum. The spectra in figures 3.8c and 3.8d were collected from two different locations on adjacent ZnO lines while spectrum in figure 3.8e is collected between these two lines. Arrows on NSOM-optical image in figure 3.8a schematically indicate these locations. As the probe aperture diameter (300 nm) is comparable to spacing between lines, some intensity from ZnO lines is also collected in spectrum shown in figure 3.8e. However, the peak PL intensity in this region is an order of magnitude lower when compared to those spectra recorded directly from the ZnO lines. Comparison of spectra in 3.8b and 3.8c (or 3.8d) shows that high pass filter decreases the 514.5 nm laser intensity reaching the spectrometer by almost 80%. However, the most interesting results are evident in spectra shown in figures 3.8c and 3.8d. These spectra show characteristic broad green-yellow emission bands between 520 and 640 nm in addition to the red emission band above 650 nm. These bands are commonly observed in ZnO prepared by different chemical routes and arise due to Donor-Acceptor Pairs (DAP) recombination associated with defect-impurity complexes. It can now be unambiguously concluded from the spectra in figure 3.8 that the signal used to form optical images in these NSOM-optical scans is clearly the PL signal from the 300 nm ZnO nanopatterns and conclude that these patterns are optically active.

It is interesting that the ZnO PL spectra collected from nanopatterns exhibit red emission band unlike most of the reports in recent literature where PL investigation of ZnO films and ZnO nanostructures reveals only green-yellow emission bands between 510 and 640 nm[125-130]. A multiple peaks fitting analysis of the spectrum of figures 3.8c-e depicts that the PL from these ZnO patterns consists of at least three emission bands at approximately 560, 620, and 667 nm (corresponding to 2.2, 2.0, and 1.9 eV, respectively). Highest PL intensity in the near-field is evident at 620 nm. The green-yellow emission bands is usually assigned to one of the donor and acceptor mid band gap defect states such as oxygen vacancies (V_O), zinc interstitials (Zn_i), zinc vacancies (V_{Zn}) or antisite defects (O_{Zn})[131]. Though most of the recent literature contains only report on green-yellow emission bands in ZnO, there are few earlier reports on red emission band and even a near IR emission band at 730 nm (1.7 eV) in ZnO pellets[132-134]. As in the case of green-yellow emission band, the origin of red and near IR emission bands remains an open question. Thus, the source of 667 nm PL band detected from these ZnO nanopatterns is unclear at this time. A concerted look at the vast literature on optical properties of ZnO shows that in addition to the fabrication routes, annealing conditions can significantly affect the PL characteristics. This is not surprising because fabrication route and processing conditions do strongly influence the concentration of various structural defects in a material. These defects are the source of complex PL in ZnO. These therefore indicate that optical properties of ZnO can be potentially tuned to show at a particular wavelength by designing an appropriate annealing treatment protocols. However, it remains a challenge to tailor the PL emission bands in ZnO

spanning the whole visible spectrum through appropriate fabrication routes and processing parameters for potential optoelectronic applications such as polychromatic and white light displays.

In order to emphasize the practical importance of the three PL bands observed in ZnO patterns in this work, these patterns were imaged using a fluorescence microscope. This involved illuminating the sample with light having different wavelengths and collecting the emission signal with a CCD to form the luminescent image of the sample. Figure 3.9 shows these images of ZnO patterns collected in far field using a fluorescence microscope. These images were collected with a CCD at different exposure times because of the difference in emission intensities. Figure 3.9a shows the PL spectrum of the patterns collected using NSOM superimposed with chromaticity scale on the x-axis. Figure 3.9b shows the ZnO patterns fabricated across two gold electrodes imaged by illuminating with white light in a conventional optical microscope. The patterns were annealed in air at 550 ^{o}C for 1 h and agglomeration of the gold electrodes is noticeable in figure 3.9b. A collection time of less than 50 msec is used for obtaining this image. Figure 3.9c shows the image collected by illuminating the sample with blue light (497 nm) and using a collection time of 2 sec. Only the patterns are visible in this image suggesting that they are indeed photoluminescent. The green color of the patterns suggests that when they are illuminated with blue color, the maximum PL intensity is in green color range. This could be the 560 nm peak shown in figure 3.9a. For the similar argument, when the patterns are illuminated with green color

(550 nm) the patterns appear red in color as shown in figure 3.9d. The image in figure 3.9d is obtained using 7 sec collection time. Again, examining the PL spectra in figure 3.9a suggests that when patterns are illuminated with green light, the 620 nm and 667 nm peaks should be excited.

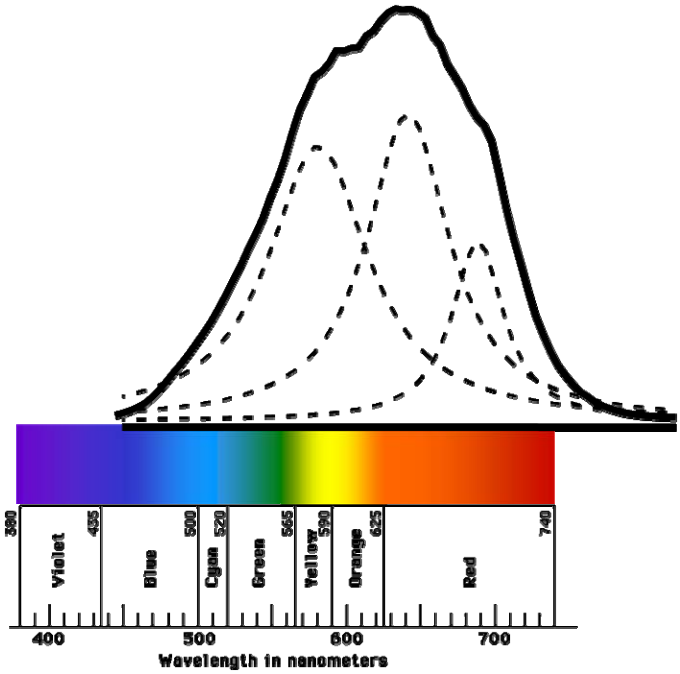

Figure 3.9a: The relative position of the PL spectra of ZnO patterns on chromaticity scale.

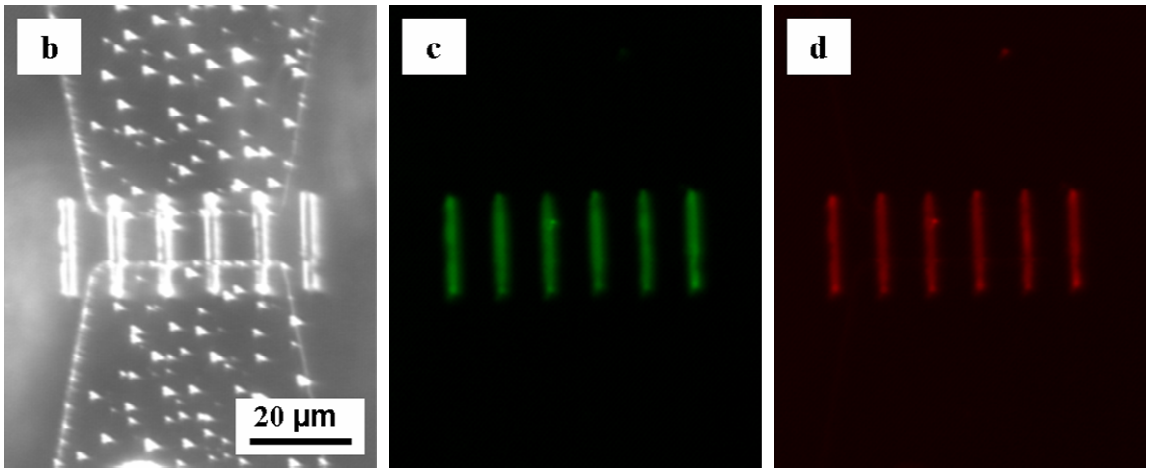

Figure 3.9b: The optical images of patterns when illuminated with (b) white light, (c) blue light and (d) green light.

3.6 SUMMARY

In summary, this chapter shows successful fabrication and characterization of PL properties of 300 nm wide ZnO nanopatterns. The NSOM-PL intensity images represent maps of the defect-induced photoluminescence signal originating from ZnO nanopatterns. These patterns showed significant green-yellow-red emission bands when excited with 514.5 nm laser line, at room temperature. Furthermore, this work demonstrates the capability of micro-molding in capillaries as a patterning technique to fabricate 300 nm wide functional ZnO lines with high spatial density that are continuous on oxide substrates even after annealing at 550 ^{o}C for 1 hr in air. We believe that these results would be useful to understand structure-optical property relationship of nanopatterned wide bandgap semiconductors.

3.7 LIMITATIONS OF MIMIC AND MOTIVATION FOR SOFT-EBL

While the advantages of MIMIC include the ability to pattern variety of materials from their liquid precursors over large areas, there are several limitations with this technique. First, MIMIC has a limited resolution or the size of the smallest feature that can be fabricated. Although MIMIC technique has been used to pattern several materials with feature sizes in micron range[103], reports on fabrication of pattern features in nanometer range using this technique are particularly rare. In fact the 300 nm wide lines of ZnO fabricated in

this work are the smallest ceramic features yet reported using MIMIC. However, there is a clear need for developing techniques with much higher resolution capability especially for ceramics. Second, the MIMIC technique does not have a true site-specific fabrication capability. It is hard to align or place nanostructures at precise locations, between electrodes for example, using this technique. The need for integrating nanostructures into hierarchical architectures and prepatterned device circuitry requires a precise nanostructure positioning capability. The third disadvantage of MIMIC includes the difficulty in patterning different materials in close proximity or the ability to realize multiple nanostructures in close proximity (multiplexing). Multiplexing is a promising method of increasing the functionality of a device by integrating multiple nanostructures each with a different functionality.

The above three requirements have motivated the development of a new nanofabrication technique called as soft-electron beam lithography[135, 136] that is discussed in the next chapter.

CHAPTER 4

SOFT-eLECTRON BEAM LITHOGRAPHY FOR INORGANIC NANOSTRUCTURE FABRICATION

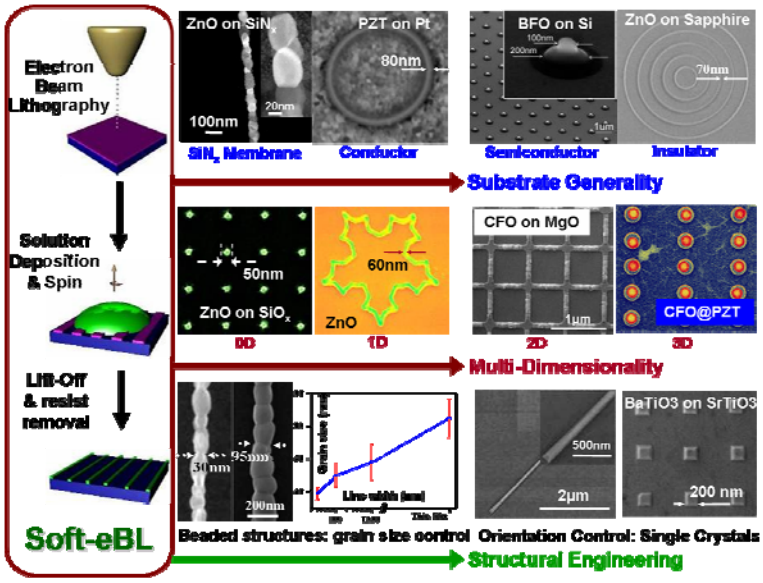

This chapter details the attributes of a novel nanofabrication technique called as soft-electron beam lithography (soft-eBL) and demonstrates the unique advantages of soft-eBL specifically for fabrication of ceramic nanostructures.

A part of the work presented in this chapter was published in **Nano Lett., 5, 1710 (2005) and Small, 2, 274 (2006).** Other parts were presented at **2006 Materials Research Society (MRS) Spring Meeting, 2007 MRS Spring Meeting,** and **3rd International Conference on Materials for Advanced Technologies, Symposium G, Singapore, 2005**

4.1 NANOSTRUCTURE FABRICATION BY NANOPATTERNING

The ability to manipulate materials at nanometer length scales and control dimensions of nanostructures is a prerequisite not only to study novel properties of materials at different length scales but also to realize useful miniaturized devices. Nanopatterning of materials is one approach which enables these dual goals. Functional ceramics such as ferroelectric (e.g., $PbZr_xTi_{1-x}O_3$ - PZT), ferromagnetic (e.g., $CoFe_2O_4$ - CFO) and optoelectronic materials (e.g., ZnO) are very important technological materials for applications such as actuators[137, 138], chemical sensors[139-141], high density data storage[142, 143] and polychromic displays[144-146]. Some of these properties show remarkable size dependency[147, 148] as well as interesting synergistic coupling[149, 150] when materials with different functionalities are positioned in close proximity. The ability to create nanoscale architecture for functional ceramics is a prerequisite for exploring the rich field of ceramic nanotechnology.

While several nanopatterning schemes[71, 151-156] have been developed over the last two decades, techniques that can pattern ceramics under 100 nm resolution are very limited[157]. This is due in part to the refractory nature of ceramics and difficulty in etching such materials[138]. Dip-pen nanolithography (DPN) with sol-gel inks[71] has been employed to generate structures under 200 nm. Another high resolution nanopatterning technique for ceramics is the direct-write using electron beam[66, 148, 158-161]. This involves exposing a spin

coated resist layer consisting of metal-organic compounds and a chelating agent to electron beam. The exposure breaks down the organic components in the resist layer leaving behind a cross-linked inorganic component. Though this technique was shown to generate very fine structures (< 10 nm), it is limited to resists that are sensitive to e-beam and the process typically requires a high electron dose for development of e-beam sensitive inorganic resists. Other patterning techniques based on molding and replication[103, 106, 157] processes generate ceramic structures over fairly large areas and direct-write fabrication techniques such as robotic deposition of polyelectrolytes could generate 3-D ceramic architectures[162, 163]. However, these techniques do not attain true nanometer scale patterning resolution. This motivated the development of a general scheme for fabricating ceramic nanostructures with control not only over their dimensions but also on their location

4.2 DESIRED ATTRIBUTES OF THE NANOPATTERNING SCHEME

Development of the nanopatterning scheme described in this chapter is primarily driven by the desire to have a technique with all of the following attributes (also see figure 4.1):

1. To circumvent the high etch resistance of ceramics, the scheme should not require either wet or dry etching steps. Etching of ceramics is not only difficult due to their refractory nature but also often times it is a costly

affair because of the requirements of expensive equipment such as vacuum systems. Furthermore, etching of ceramics produces roughness at length scales comparable to the nanostructure dimensions and therefore undesirable.

2. The technique should be capable of fabricating solid structures well under 100 nm because the dramatic size dependent phenomena in solid state structures appear at this length scale.

3. The technique should be capable of fabricating structures with control over their location on the substrate. This capability also known as registry or site-specific fabrication capability is very important for integrating the nanostructures into device circuitry. The registry capability is not only crucial for fabricating functional devices out of these nanostructures but also for positioning multiple nanostructures in close proximity to increase the functionality of the device or to multiplex.

4. In order for the technique to be truly generic, it should be capable of fabricating nanostructures of variety of materials on almost any substrate. The substrates used for many ceramic applications range from electrical insulators, conductors, semiconductors, single crystals, polycrystals to amorphous materials. Therefore to maximize potential applications of the

technique it should be capable of fabricating nanostructures on almost any solid substrate.

While most of the recently developed nanopatterning techniques possess at least one of the above attributes, there is no technique that possesses all of the above attributes. While Nano-imprint lithography is capable of fabricating structures less than 10 nm[164], the process requires etching step at some stage of the process to form final structures. The self-assembly approaches while not requiring etching or selective material removal as in lithography, do not possess the registry capability.

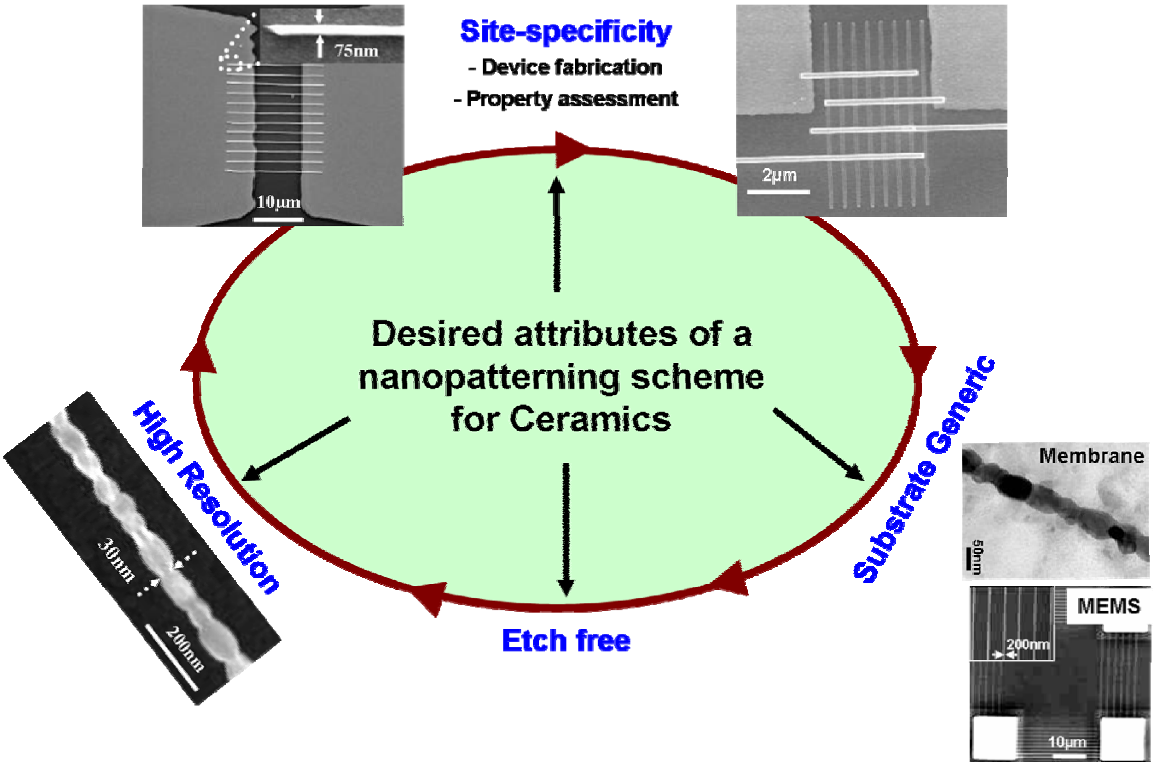

Figure 4.1: The four main desired attributes of a scheme for nanofabrication of ceramics

4.3 SOFT-ELECTRON BEAM LITHOGRAPHY

The soft-electron beam lithography (soft-eBL) technique developed two years ago in our laboratory is a high resolution technique possessing all four of the above attributes. In fact the uniqueness of the technique is the *combination of these capabilities*. Soft-eBL is a hybrid technique in that it synergistically combines the advantages of electron beam lithography (registry, high resolution) with the advantages of soft chemistry (easy formability, etch-less). In this scheme, electron beam patterned polymer resists are used as molds to define the size and shape of the nanostructures and the sol-gel precursors as their material sources.

The critical steps in soft-eBL are shown in figure 4.2 and described below.

1. Spinning ebeam resists: The resist is a sequentially spin coated bi-layer structure with a low molecular weight MMA-MAA[⊕] copolymer at the bottom and a high molecular weight PMMA resist on top. The higher sensitivity of copolymer compared to PMMA results in an undercut and enables excellent lift-off.

[⊕] methyl methacrylate and methacrylic acid

2. E-beam lithography: Resist coated substrates are exposed to electron beam (ebeam) and are developed in an inert solvent (1:3::MIBK:IPA[∅]). Because these are positive resists, ebeam exposure breaks down the polymer backbones through chain scission and increases the solubility in developer solution. After developing the patterns, they are cleaned in oxygen plasma for 30 to 60 sec to remove any residual resist left[165] in the patterned areas and to increase hydrophilicity of the substrate. This is necessary to achieve effective filling of the patterns with sol in the subsequent step. Numerous trials over the course of developing this technique have repeatedly showed that oxygen plasma treatment is absolutely necessary especially while patterning fine structures.

3. Spinning liquid precursors: This is the critical innovative step in the process. Few drops of liquid precursors of interest are dropped onto ebeam patterned substrate and the substrate is spinned to remove the excess liquid. This process step eliminates the need for any additional steps to remove excess sol from the substrate such as either back polishing[166] or reactive ion etching[167, 168].

4. Lift-off: Sol spinned substrates are nominally heated at 150 ^{o}C for 10 mins to remove solvent and promote partial hydrolysis/gelation. Subsequently the substrates are soaked in acetone to dissolve resist and lift-off material from unpatterned areas. Lift-

[∅] methylisobutylketone

off is usually accomplished with the aid of ultrasonication. However, as will be shown later in the chapter, when the ultrasonication is not desirable, optimizing other process conditions could also achieve effective lift-off without sonication.

5. After the lift-off the patterns are usually annealed at high temperature in air to fully decompose the organics and crystallize the structures

It should be noted that the five steps described above are only the main steps. Over the last two years, numerous developments and improvements to soft-eBL process capabilities have necessitated modifications to these basic steps. One of the main goals of this chapter is to highlight these developments through a series of ceramic nanopatterning examples and demonstrate the capabilities of this seemingly simple nanopatterning scheme.

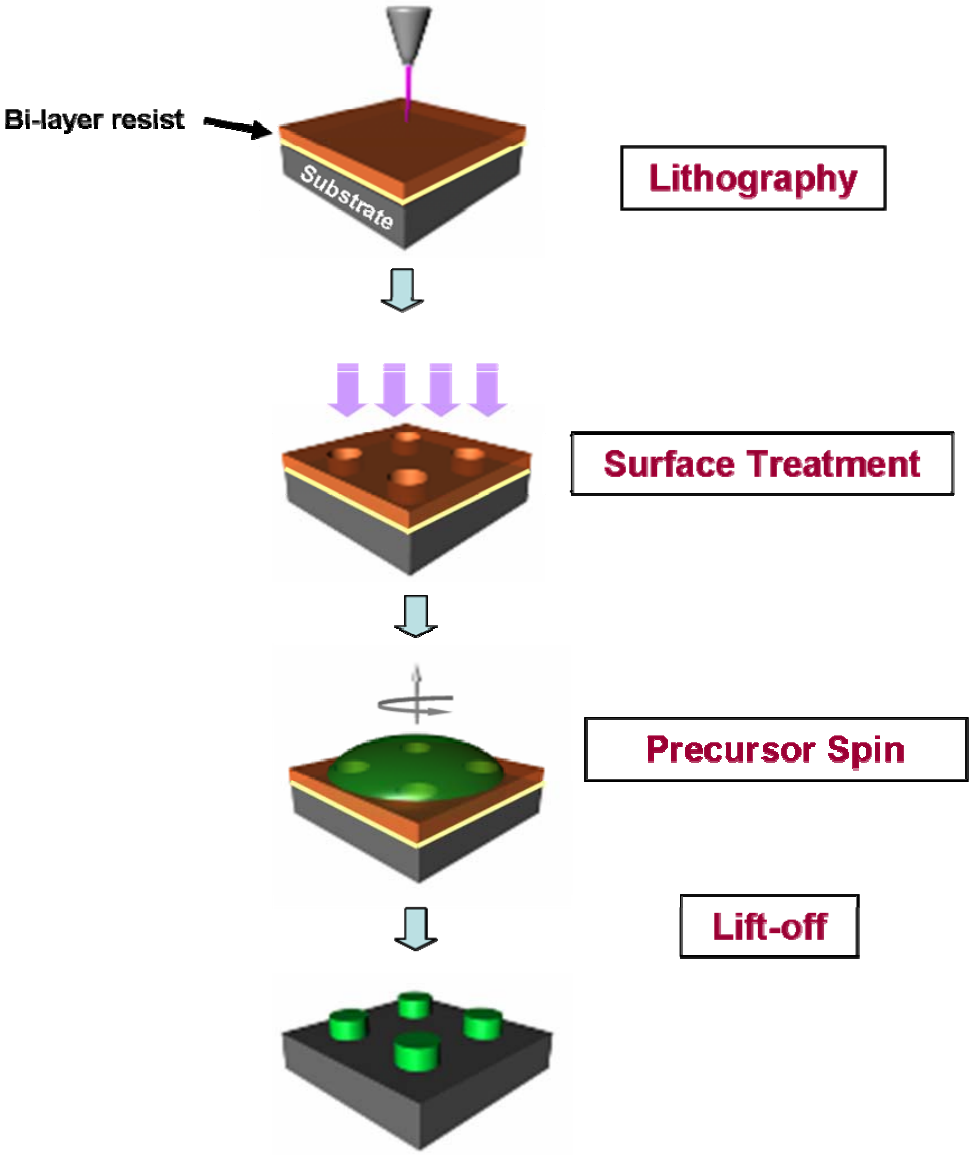

Figure 4.2: The major steps in soft-eBL scheme

4.4. DETAILS OF THE PATTERNING SCHEME

This section contains the experimental details that are common to all examples while the details specific to each example are reported in the relevant sections.

4.4.1: Resists: The e-beam resists MMA-MAA copolymer (MMA(8.5)MAA EL6) and PMMA (950PMMA A3) were bought from MicroChem. These resists were stored in dark bottles covered with aluminum foils to reduce exposure to ambient light. Only these resists were used throughout this project work.

4.4.2: Substrate preparation for patterning: The substrates were thoroughly cleaned in acetone, water and isoproponal prior to spin coating the resists. When wet cleaning is undesirable, substrates were treated with oxygen plasma. Each resist layer is spin-coated at 3000 rpm for 45 sec to give a nominal thickness of about 150 nm (≈ 300 nm of bi-layer thickness). After spin coating each layer, substrate is heated at 175 ^{o}C for 1 min on a hot plate to remove solvent (anisole).

4.4.3: E-beam lithography: E-beam resist coated substrates were subsequently patterned at 30 kV with area doses between 200 - 500 $\mu C/cm^2$ using Quanta 600F (FEI Co.,) which can be operated in variable/high pressure mode for patterning insulating substrates. The same machine is used for subsequent imaging of the patterns. The patterned substrates were then treated with oxygen plasma (75 W, 50 sccm flow rate, 75 mTorr operating pressure). The

plasma treated patterned substrates were immediately used for spin coating solutions. The solutions were spun between 4000 and 6000 rpm for 45 sec and were immediately heated on hot plate for 5 min at 150 ^{o}C. This temperature is chosen because it is above the boiling point of solvent in the spinned solution but well below the glass transition temperature of the resist materials. The choice of the spinning speeds is dictated by the pattern density and the solution concentration. Higher speeds are necessary to achieve effective lift-off when either solutions of higher concentration or patterns of higher spatial density are used. A qualitative understanding of the effect of solution concentration and pattern density can be obtained from figures 4.3 and 4.4. Images in figure 4.3 show that for a given spinning speed and pattern density (1 μm spacing in this case), increasing the sol concentration results in interconnection between adjacent patterns and therefore poor lift-off conditions. On the other hand, images in figure 4.4 show that at a given spinning speed and sol concentration, decreasing the pattern density improves the lift-off conditions. These results show that spinning speed, sol concentration and pattern density are interrelated. Process development for new solutions therefore would require a preliminary trials involving optimization of these parameters.

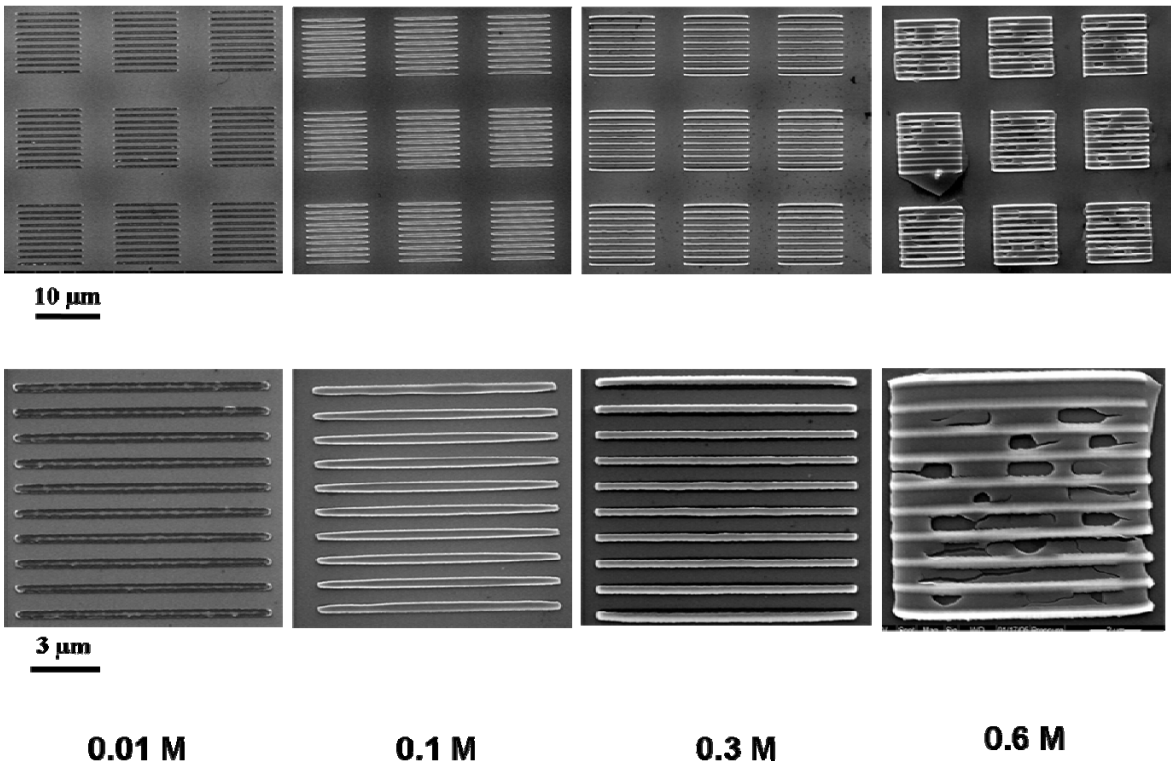

Figure 4.3: The effect of solution concentration on lift-off. These SEM images of ZnO patterns are taken after spin coating different sols at 6000 rpm and lift-off (they are not annealed). Bottom row consists of magnified views of the images in front row.

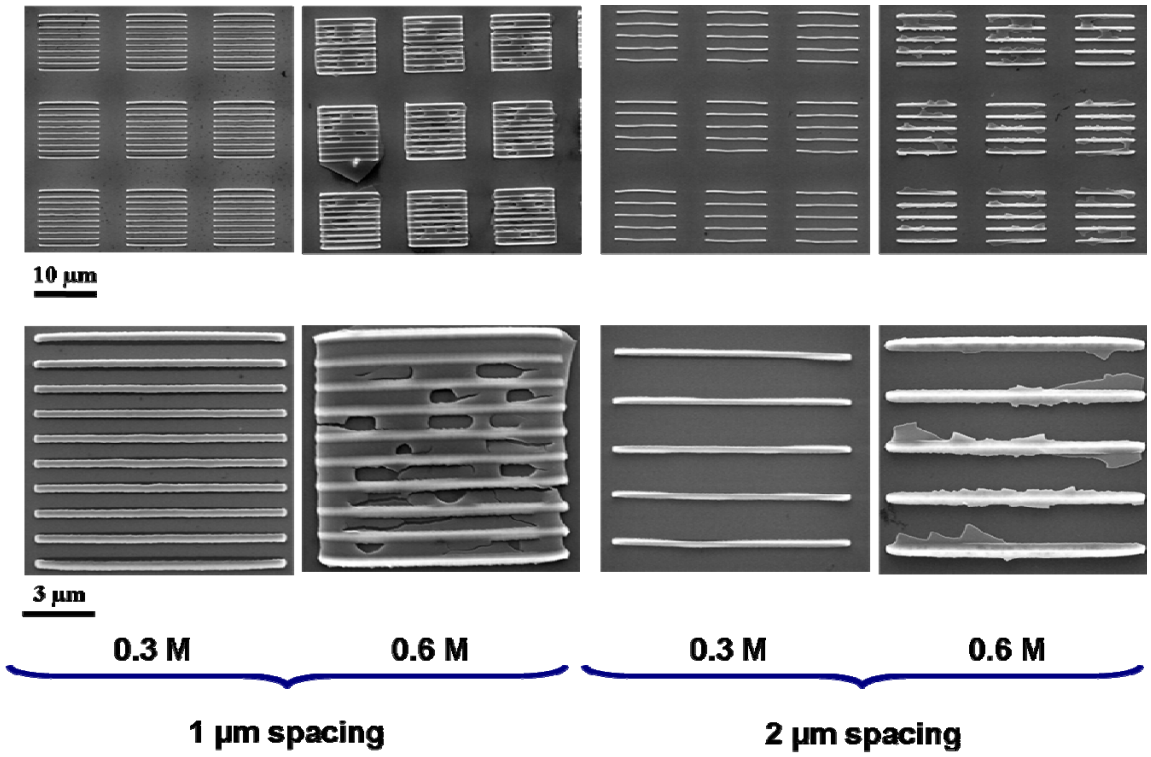

Figure 4.4: The effect of pattern density at two different ZnO solution concentrations on effectiveness of lift-off. 6000 rpm spinning speeds are used in all the cases and the images were taken after lift-off. Bottom row consists of magnified views of the images in front row.

At first it might appear that concentration might affect viscosity and therefore sol viscosity might be a better parameter. However, one has to note that the sols studied in this work are very low in total mass content. Even in 0.6M ZnO sol, the mass content is less than 1%. Therefore all these sols would have similar viscosities. This is confirmed from viscosity measurements shown in figure 4.5. Viscosities were measured using stress controlled rheometer (Par Physica MCR). Viscosities of different solutions and of those with different concentrations were measured. For all the solutions measured, viscosities were found to be close to that of solvent (0.3 Pa.s) and were independent of shear rate above 100 rps (rotations per sec). All these sols, except $BiFe_2O_3$ (BFO) sol, were made using 2-methoxy ethanol as the solvent while acetic acid was used for BFO sol. Please note that during actual soft-eBL process sols were spinned on substrate at rates between 4000 to 6000 rpm (or 67 to 100 rps). Clearly in this range, all sols had similar viscosity values. Therefore the dependence of patterning effectiveness on sol concentration could not be due to viscosity instead it could be related to hydrolysis rate. When the sol is spinned on the substrate, solvent quickly evaporates and sol immediately begins to hydrolyze. This leads to formation of film containing interconnected network of polymerizing metallorganic molecules or a gel network. The continuity of this film would depend on the concentration of the sol.

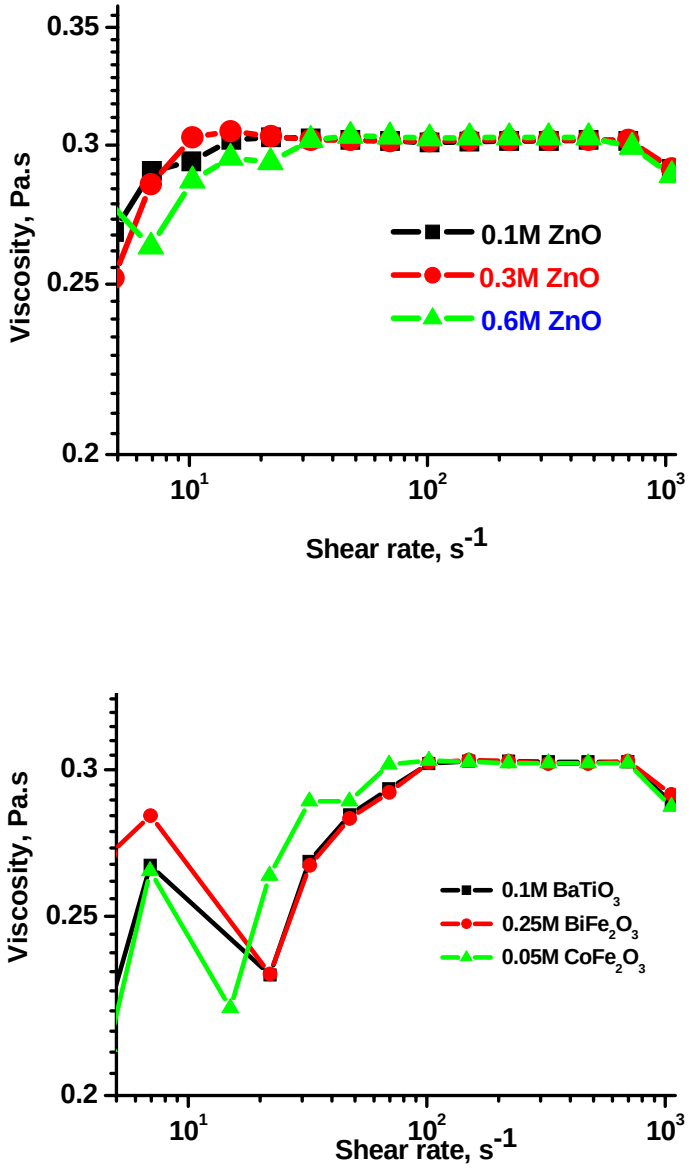

Figure 4.5: Viscosities of various sols studied in this work. Viscosities were measured in stress controlled mode

4.5: CAPABILITIES OF SOFT-EBL

The capabilities of soft-eBL are demonstrated through a series of following examples.

4.5.1. Example 1: Sub 100 nm ceramic nanopatterns

As the sizes and shapes of the patterns are defined by electron beam, soft-eBL is capable of fabricating structures as small as 30 nm. The electron microscopy images in figure 4.6 demonstrate the excellent control possible on ceramic nanostructure size and shape. These SEM images were taken after annealing the patterns at high temperatures to crystallize the structures. The structures were fabricated on silicon substrates with 600 nm thick thermal oxide. The ZnO sol used for these patterns was prepared using chemicals purchased from Sigma-Aldrich and used in as-received form without further purification. In a typical process, zinc oxide sol is prepared by stirring a mixture of zinc acetate dihydrate, 2-methoxy ethanol and ethanol amine at 60 ^{o}C for 2 h. The relative compositions were adjusted so as to give a 0.1M ZnO sol with equimolar ratio of zinc and ethanol amine.

Figure 4.6 demonstrates that soft-eBL is capable of fabricating lines with widths as small as 30 nm. This is possibly the smallest feature size yet reported for ZnO nanostructures fabricated using a patterning approach. The polycrystalline ZnO structure in figure 4.6c is also interesting because the grain size is equal to the line-width. Such structures, also called as beaded-structures, are very interesting structures because the

percolation length of an electron is very well defined in such structures. Also these structures would enable one to decouple the effects of grain boundaries from grain interiors. The microstructural evolution of these structures is discussed in next chapter.

Experiments during the initial stages of soft-eBL development were focused on confirming the chemical identify and functionality of the fabricated patterns. By way of one example, figure 4.7 shows the backscattered electron image, photoluminescent (PL) image and PL spectra from a ZnO pattern. Figure 4.6a shows the backscattered electron (BSE) image of ZnO patterns annealed at 700 ^{o}C in air for 20 mins whereas figure 4.6b shows the PL image of these patterns collected using near-field scanning optical microscopy (NSOM) (MultiView 100^{TM}, Nanonics Imaging Ltd). The PL image was collected in illumination mode using 50 nm diameter tip operating in constant-height mode to decouple the cross-talk from topography signal[91, 123, 169]. This is discussed in more detail in the previous chapter. The patterns were excited using Ar ion laser (λ = 514.5 nm, 10 mW output power) and source signal was filtered from PL signal using a 520 nm longpass filter. The emitted signal is then fed into a Triax 180 monochromator and subsequently to an avalanche-photodiode (APD). Thus the optical image in figure 4.7b unambiguously shows the defect induced emission from ZnO lines and confirms the identity of the patterns. This also shows that the structures are optically active. The PL spectra collected from ZnO line and from a location between lines are shown in figure 4.7c. The spectrum from lines shows a strong peak at 544 nm which is assigned to the defect induced emission from ZnO[127, 128, 170]. As expected this

peak is absent when measured between lines though a small hump could be seen at this value which could be due to proximity of tip to lines.

Though figures 4.6 and 4.7 show only the ZnO nanostructures other ceramic materials could also be fabricated at similar length scales. By the end of this chapter, through a number of examples, fabrication of several technologically important oxide ceramic nanostructures will be demonstrated. The choice of materials seem only to be limited by the availability of suitable liquid precursors

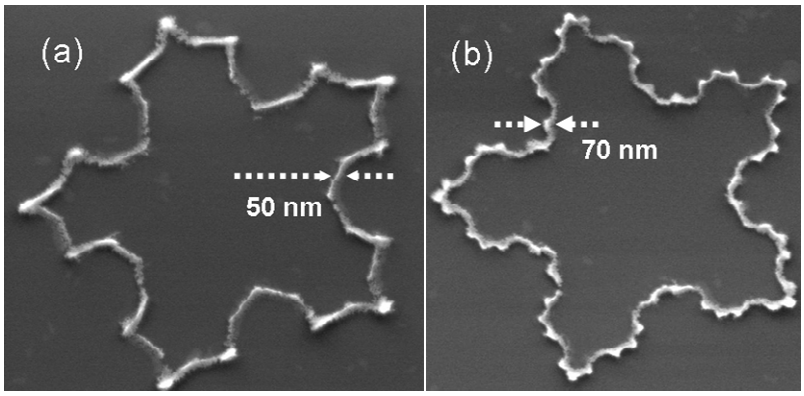

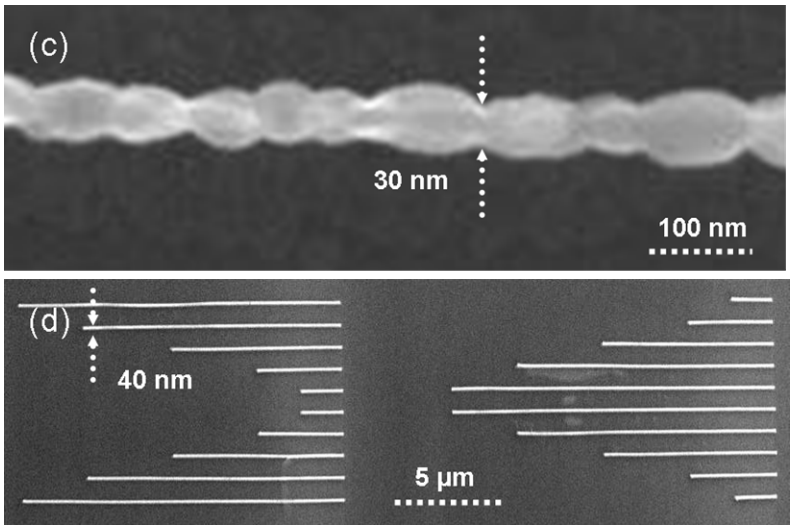

Continued on next page

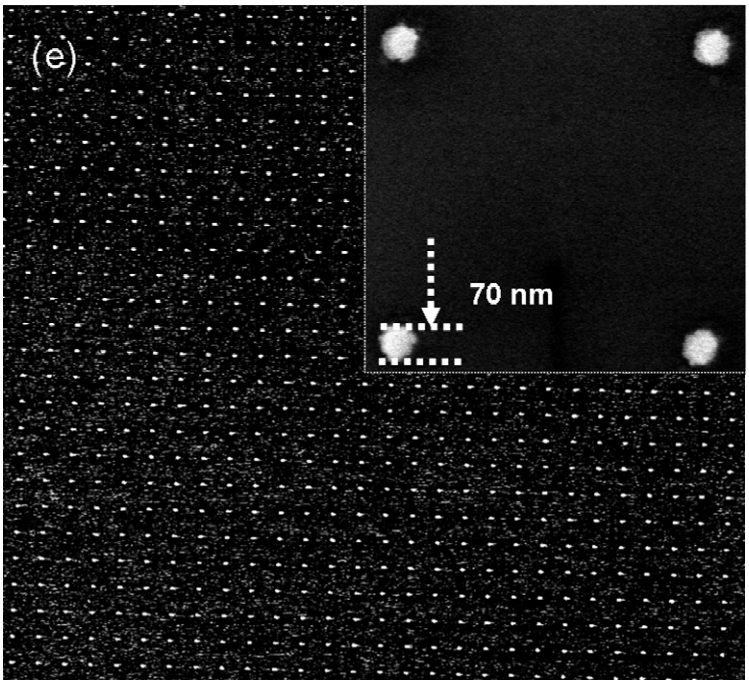

Figure 4.6: High resolution patterning capability of soft-eBL demonstrated through multidimensional patterns of ZnO on oxidized silicon substrates. All the patterns were annealed at 700^{o}C for 20 mins in air expect the patterns in (c) that were annealed at 900 ^{o}C for 5 mins. The patterns were made from 0.1M ZnO sol that was spun at 5000 rpm.

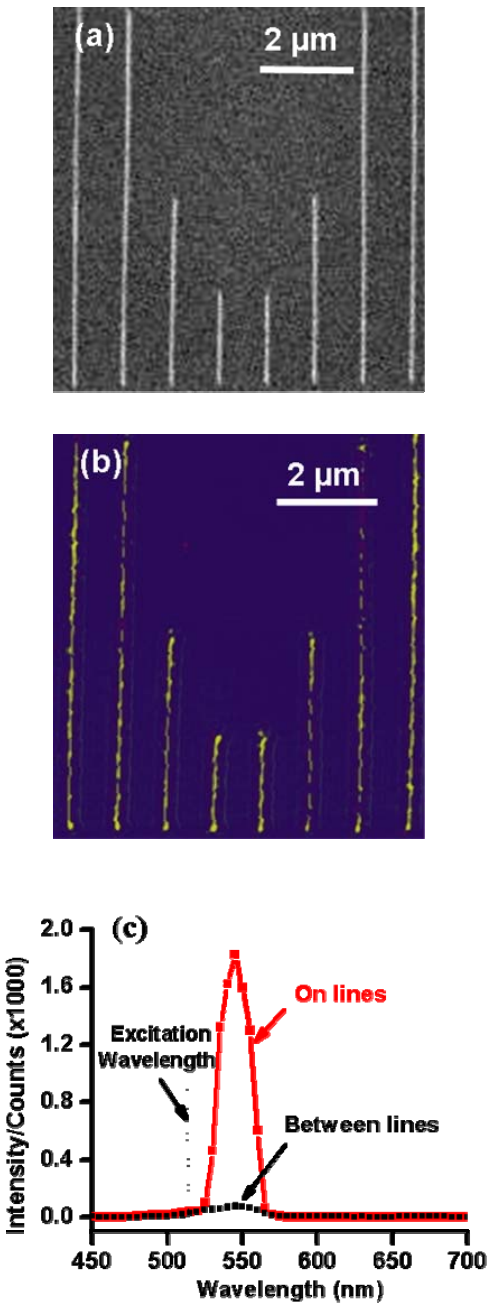

Figure 4.7: a) Backscattered electron image of ZnO patterns on SiOx/Si substrate heated at 700 ^{o}C for 20 min in air, b) Photoluminescence (PL) image of the patterns shown in (a) collected in illumination mode using NSOM operating in constant height-mode to decouple cross-talk from topography. (c) PL spectra collected on and between ZnO lines.

4.5.2. Example 2: Variety of ceramic material-substrate systems

In this example the generic nature of soft-eBL is demonstrated by fabricating ceramic nanostructures on variety of substrates, including electrical conductors, insulators, single crystals and polycrystals. Figure 4.8a shows 80 nm PZT ring structure patterned on $Pt/Ti/SiO_x/Si$ substrate. This is a well known substrate to produce highly textured and device quality PZT films using the sol-gel route. Figure 4.8b shows 500 nm wide PZT square patterns on 1 at% Nb doped strontium titanate (Nb:STO) single crystal substrate. Both these substrates are examples of electrically conducting substrates. Nb:STO substrates had a resistivity of about 3.5 mΩ-cm at room temperature. Transparent and highly stable 0.1M PZT sol used for these experiments was prepared following a recipe reported elsewhere[171, 172]. The patterns in both figures 4.8a and 4.8b were annealed at 600 ^oC for 2 h in air. The height difference at the edges of square patterns in figure 4.8b is a result of undercut due to higher sensitivity of copolymer compared to PMMA.

Figure 4.8c shows examples of fabricating ZnO patterns on another technologically important substrate, sapphire, which is electrically insulating. While pattering on conducting substrates is trivial, it is almost impossible to do eBL on insulating substrates due to severe charging effects when operating in high vacuum mode. However, it is possible to pattern on insulating substrates by backfilling the chamber with water vapor to 1Torr chamber pressure to minimize charging effect[173]. The availability of eBL machines capable of operating at

chamber pressures as high as 1.5Torr therefore enables patterning of structures on any insulating substrate.

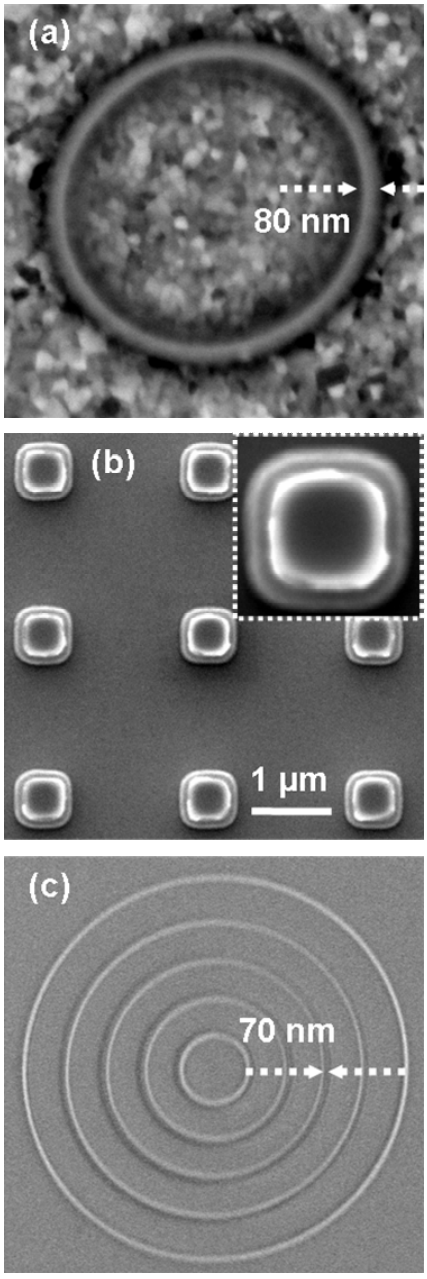

Figure 4.8: Versatility of the technique is demonstrated through patterning of different materials on different substrates. a) PZT on Pt, b) PZT on Nb:STO (inset shows the magnified view of one of the squares) and c) ZnO on sapphire

The results in figure 4.8 demonstrate the applicability of soft-eBL scheme to wide selection of substrate-material systems and highlight the remarkable versatility of the soft eBL approach. These results are particularly interesting from the point of obtaining ceramic nanostructures and possibly single crystalline structures with known epitaxial relationship to appropriate substrate[174-177] and ultimately enabling one to engineer the microstructure of the nanopatterns through a careful choice of substrate and annealing scheme. This has already been demonstrated Pan.et.al[178] through single crystal conversion of variety of ceramic nanopatterns on substrates such as MgO and STO.

4.5.3. Example 3: Patterning onto fragile substrates

In order to demonstrate that one can use soft-eBL scheme on fragile substrates, various nanostructures have been fabricated onto 75 nm thick electron transparent membranes. The motivation for using electron transparent membranes stems from the need for structural characterization of nanopatterns using transmission electron microscopy (TEM) without subjecting them to usual TEM preparation processes such as ion milling and dimpling. These processes could introduce unacceptable levels of damage to the samples that will be particularly unacceptable in case of nanostructures since the amount of damage can constitute a significant percentage of the total nanostructure volume. This section will demonstrate that ceramic nanostructures can be patterned onto electron transparent

membranes and examined using TEM without requiring any post-patterning sample preparation. Therefore it is possible to characterize the patterns in near-pristine condition.

The soft-eBL process steps for working with membranes are slightly different and are explained in section 5.3.3 of the next chapter. Figure 4.8 shows the examples of ceramic nanostructures fabricated at variety of length scales, dimensions and shapes onto 75 nm thick SiN_x membranes. Figure 4.9a is a bright-field TEM image of 40 nm wide ZnO lines prepared from a 0.1-M ZnO precursor sol containing 6 at% Eu. The lower magnification image highlights the large area patterning capability of soft-eBL on these membranes. Figure 4.9b is a bright-field image of a ZnO pattern that is crystallized by annealing at 700 ^{o}C in air for 20 min. The samples were annealed by introducing them into a furnace set at 700 °C (i.e., up-quenching), and then removing them from the furnace after 20 min. The samples were subsequently let to cool in laboratory ambient conditions. The diffraction pattern in the inset corroborates the crystalline nature of the pattern and can be indexed to the Wurtzite structure of ZnO. Figure 4.9c is an annular dark field scanning transmission electron microscope (ADF-STEM) image of a single ZnO line annealed at 900 °C for 5 min to generate a single-grain-wide structure, also called a “beaded structure”. The diffraction patterns taken at multiple locations on one grain confirm that a single grain spans the entire thickness of the line as in a bamboo structure. Figure 4.9d shows an ADF-STEM image of CFO nanodots with 50 nm diameter separated by about 500 nm, demonstrating the high resolution and spatial density achievable by this process.

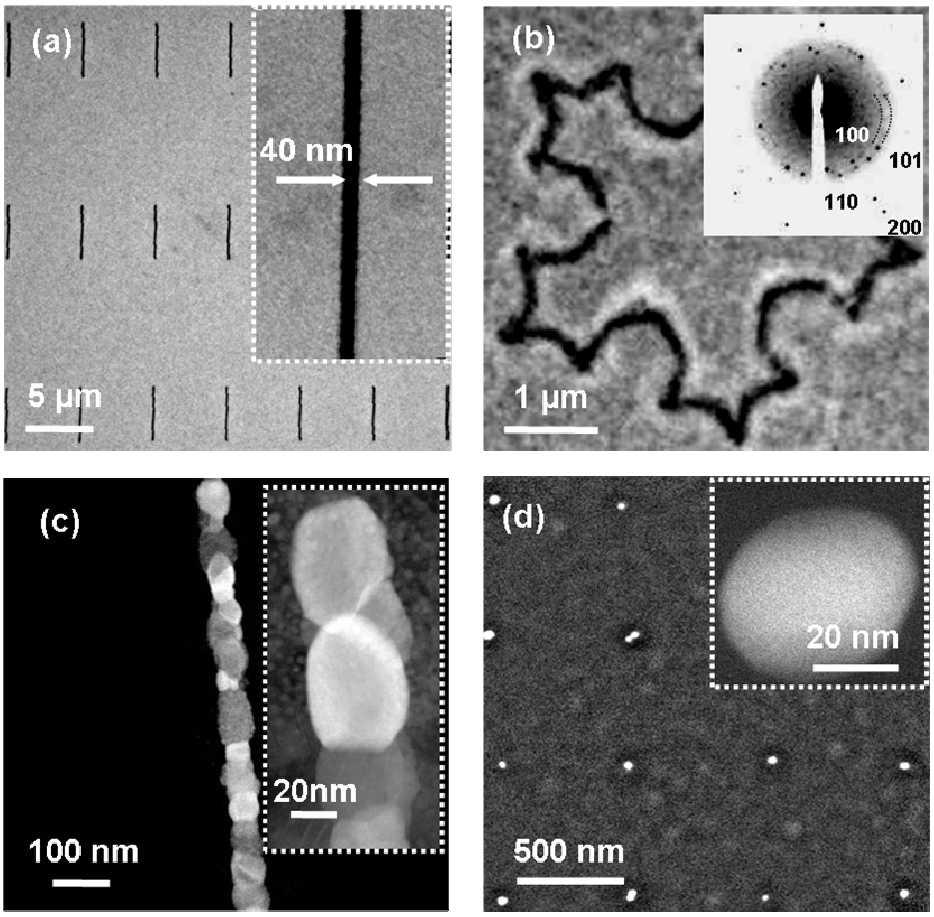

Figure 4.9: Electron micrographs demonstrating high resolution and generic patterning capability of soft-eBL on an ultra-thin membrane. (a) Bright field (BF) TEM image of ZnO with 6 at% Eu after heating at 150 °C for 5 min in air, (b) BF-TEM image of ZnO pattern after annealing at 700 °C for 1 h in air with the inset showing the diffraction pattern of the structure, (c) Scanning transmission electron microscope (STEM) image of ZnO beaded structure annealed at 900 °C for 5 min in air and (d) ADF-STEM image of cobalt ferrite annealed at 1000 °C in air. The nominal electron probe size during STEM imaging is about 0.7 nm.

All the samples discussed in figure 4.9 were imaged by directly loading the patterned membranes into the microscope without subjecting them to additional sample preparation steps. The results in this figure therefore show that the membranes with nanostructures can withstand the rigors of thermal treatment and the soft-eBL patterning process, underscoring their effectiveness as ideal test-beds for fabrication and structure-property evaluations of nanostructures.

Next it is shown that a given membrane with soft-eBL fabricated nanostructures can be characterized by a variety of techniques to extract complementary structural, chemical and electronic information, as well as functional attributes. For example, Figure 4.10 shows nanostructures of ZnO with 6 at% Eu probed with three different characterization techniques: TEM for internal structure evaluation, atomic force microscopy (AFM) for surface morphology evaluation and near-field scanning optical microscopy (NSOM) for photoluminescence (PL) property measurements. Figure 4.10a shows the 3D topographic image of the patterns between the lift off and annealing steps, obtained using an AFM operating in tapping mode, whereas figure 4.10b shows the bright-field TEM image of the same pattern. Comparison with corresponding images obtained after annealing at 700 °C for 20 min in air showed that the pattern height decreases by nearly 40% due to densification and removal of the organic moiety during annealing. Such large volume shrinkages are not unique to the membrane substrate, and these values are comparable to the shrinkage values observed in soft-eBL fabricated ceramic nanostructures on several other substrates. Indeed,

shrinkage of this magnitude is not uncommon for ceramic nanostructures prepared via a sol-gel route, as can be found in several reports in the literature [33, 105]. However, such large shrinkage in thin films usually leads to cracking, whereas high surface-to-volume ratios of 1D and 0D nanostructures, as in the present case, can effectively dissipate shrinkage stresses and therefore maintain their structural and morphological fidelity to remain monolithic. The patterns were annealed at 700 °C for 20 min prior to the optical measurements and their PL images, obtained using NSOM (MultiView 100, Nanonics Imaging Ltd)†, are shown in figure 4.10c. The PL image was obtained in "collection mode" using a 100-nm diameter tip operating in constant-height mode to decouple the topographic information[91]. The patterns were excited with an Ar-ion laser (λ = 488 nm, 10 mW output power) and the source signal was filtered using a 520-nm long-pass filter. The emitted signal was then fed through a Triax 180 monochromator to an avalanche photodiode (APD) to form the optical image using PL emission with wavelengths above 520 nm. The PL spectra collected from one of these nanostructures and from a location between the structures are shown in figure 4.10d. The PL spectrum from the nanostructure has a peak centered at about 628 nm, which is absent when observed between the patterns. The small hump could be due to the proximity of the probe tip to the adjacent patterns. The PL band from the pattern can be assigned to the frequently reported $^5D_0 - {}^7F_j$ (j =1, 2, 3 and 4) transitions[179-181] of Eu ions doped in ZnO. In a separate experiment we patterned similar size nanostructures of ZnO without Eu onto a different membrane and annealed them at 900 °C for 5 min in air. The PL spectrum from these undoped ZnO nanostructures with an asymmetric peak at about 570 nm is also shown in

figure 4.10d for comparison. While the annealing treatment for undoped and doped patterns is not identical, comparison of their PL spectra is still valuable. Comparison of the PL spectra from Eu-doped and undoped ZnO nanopatterns not only shows the clear red shift in the PL spectrum of doped ZnO but also a slightly narrower PL peak for the doped sample.

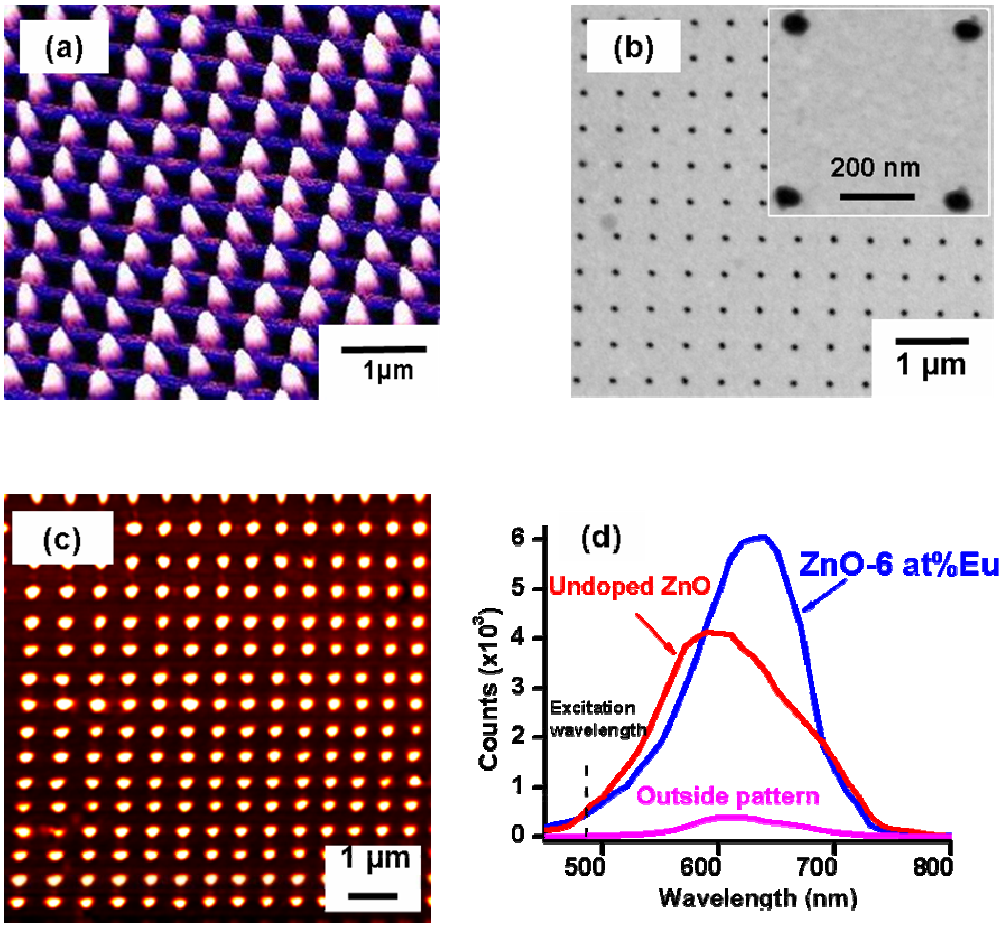

Figure 4.10: (a) AFM topographic image and (b) Bright field TEM image of Soft-eBL patterned ZnO with 6 at% Eu heated at 150 °C for 5 min, (c) Photoluminescence (PL) image of the patterns annealed at 700 °C for 20 min in air taken with NSOM in collection mode and "constant-height" mode to decouple the topographic information and (d) PL spectra collected from these patterns, outside the patterns and from patterns without Eu. The excitation wavelength is indicated with a dotted vertical line.

The broad PL peak in undoped ZnO is usually associated with structural defects such as oxygen vacancies and zinc interstitials[127, 128, 170]. The strong and narrower red emission peak from the Eu-doped sample shows not only the $^5D_0 - {}^7F_j$ transitions of Eu ions but also indicates a reduced concentration of structural defects[180, 182] because of the difference in the oxidation state of Eu and Zn ions. This suggests the possibility of using rare-earth doping as a means to enhance and tailor the optical properties of ZnO nanostructures.

In addition to the structural information, the chemical identity of the patterned nanostructures is also important. The chemical nature of the soft-eBL patterned nanostructures on membranes was investigated using electron energy loss spectroscopy (EELS). EELS is a powerful technique in which the energy loss of an electron through inelastic scattering with the specimen is analyzed to assess the electronic structure of the specimen [[183-185]]. Figure 4.11a shows ADF image of a barium titanate (BTO) nanostructure patterned on a 75 nm thick membrane, and figure 4.10b shows the point-by-point analysis of EELS spectra taken across this BTO nanostructure at 10 nm intervals. The relative intensity variations in the Ti L_{23} edge and Ba M_{45} edges originate from the thickness variation of the nanostructure across the diameter. Even after an extended, high-temperature anneal (1000 °C for 5 h in air), the membrane and the structure retain their integrity. The spectra clearly identify the constituent elements of the nanostructure. However, the presence of oxygen within and outside the nanostructure indicates that the membrane is oxidized when annealed at 1000 °C. The results in Figure 4.11 demonstrate the feasibility of performing

localized chemical analysis on soft-eBL patterned nanostructures on a membrane without requiring any sample preparation for electron microscopy.

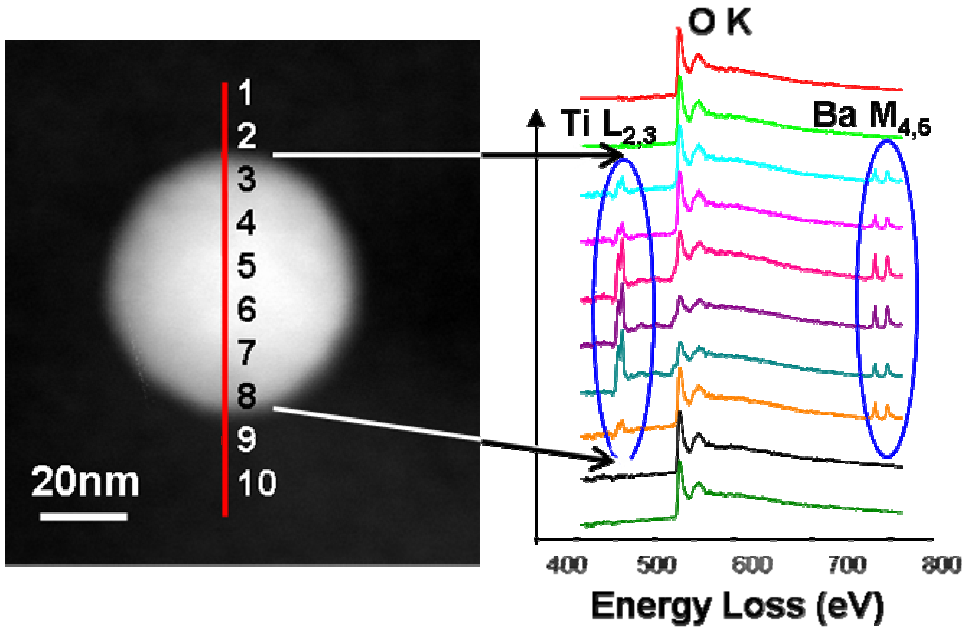

Figure 4.11: (a) ADF-STEM image of a soft-eBL-patterned barium titanate nanostructure annealed at 1000 °C for 5 h in air and b) EELS spectra collected across the nanostructure at 10-nm intervals. The nominal electron probe used for these measurements is 1.5 nm. The Ti L2,3 and Ba M4,5 edges identify the chemical nature of the structure. The presence of O K edge outside the pattern indicates that nitride membrane could have been oxidized due to high temperature annealing.

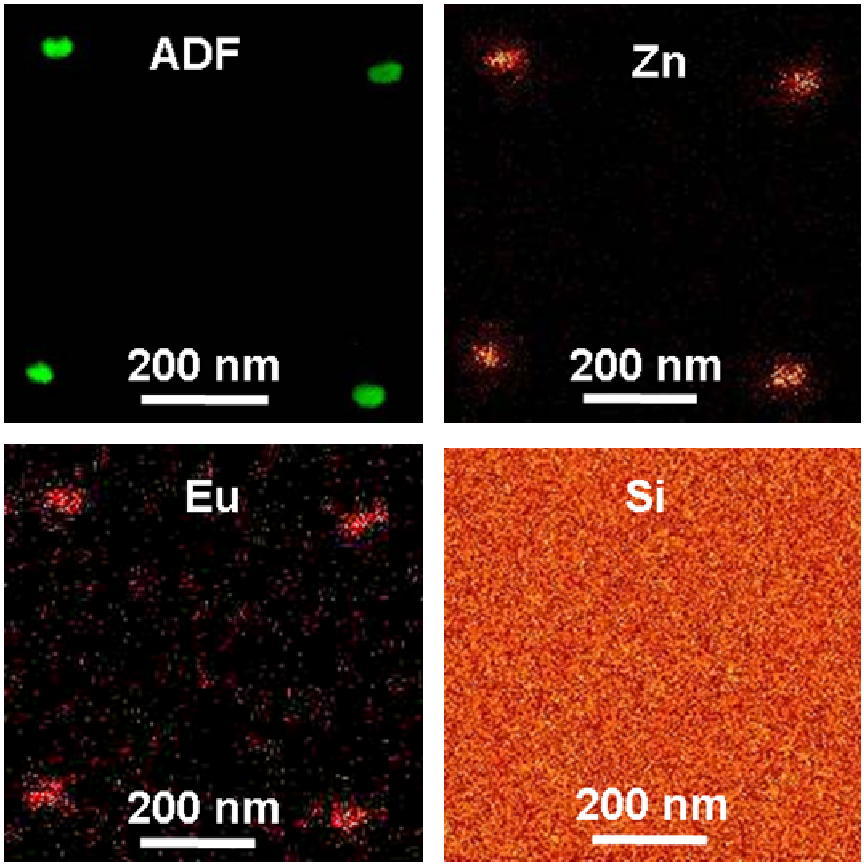

Figure 4.12: a) ADF-STEM image of ZnO nanopatterns containing 6 at% Eu. EDS maps of (b) Zn-Kα, (c) Eu-Lα and (d) Si-Kα identify the chemical nature of the patterns. The nominal electron probe size during these measurements is 0.7 nm and total collection time for EDS maps is 2 min.

This capability can be extremely valuable to study the chemical heterogeneity in a composite patterned nanostructure, for example, where conventional TEM sample preparation procedures could induce unacceptable levels of damage. Figure 4.12 shows another example of an analytical electron microscopy technique, energy dispersive spectroscopy (EDS), used to identify the chemical nature of the Eu-doped ZnO nanopatterns. This result too demonstrates the feasibility of elemental mapping and chemical analysis of soft-eBL patterned ceramic nanostructures without requiring additional sample preparation.

4.5.4. Example 4: Site-specific patterning of ceramic nanostructures

One of the final goals of patterning is to integrate nanostructures into device architecture and fabricate functional miniaturized devices. This requires the ability to position nanostructures at specific locations on a substrate such as between electrodes. The site-specific capability of soft-eBL is demonstrated by two examples, a) by fabricating ZnO and SnO_2 nanostructures between photolithographically platinum electrodes on a silicon substrate and b) by position nanostructures of these oxides on microhotplates (micro-electro-mechanical-system devices with embedded heaters and probing circuitry). Figure 4.13 shows the first example. The photolithographically patterned Pt electrodes are shown in figure 4.13a. Platinum layer thickness is 100 nm and a 10 nm thick Ti layer is present the Pt layer to promote the adhesion of electrodes to oxide substrates. After photolithography, ZnO patterns were fabricated using soft-eBL between electrodes by aligning the entire pattern

with the aid of alignment marks located at the corners. Figure 4.13b shows the SEM image of ZnO patterns after soft-eBL and annealing at 700 ^{o}C for 1 h in air.

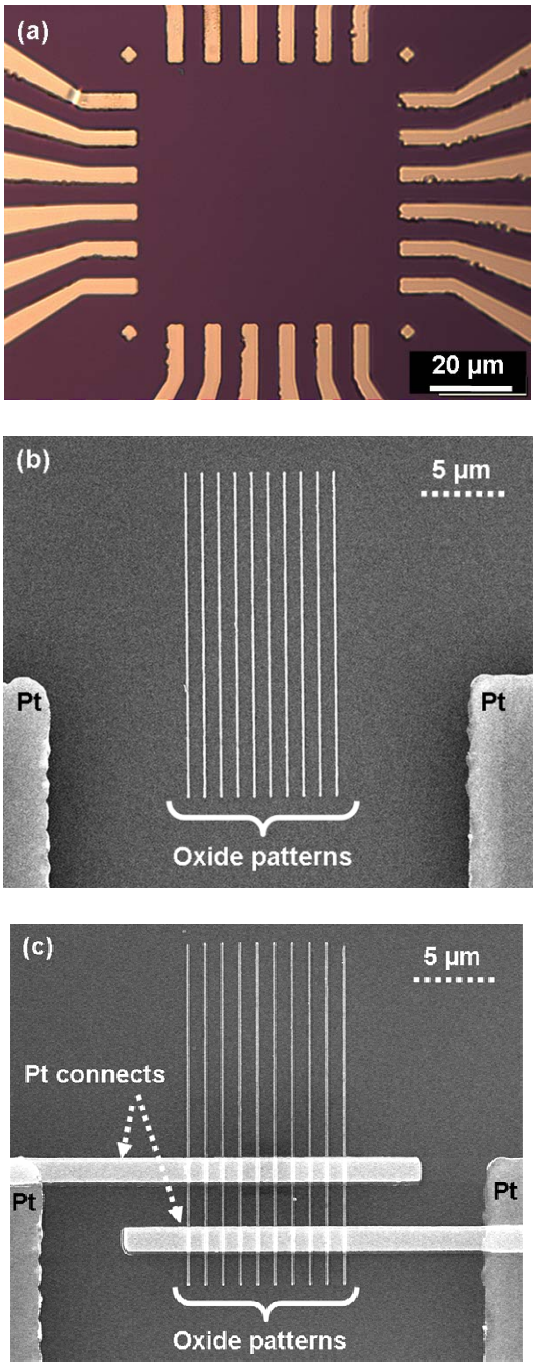

Figure 4.13: (a) Optical image of photolithographically patterned Pt/Ti electrodes. (b) SEM image of ZnO patterns fabricated using soft-eBL between two photolithographically patterned electrodes. (c) SEM image of the same electrode after the second eBL process to form the Pt lines connecting the oxide patterns with photolithography electrodes.

It was found that 100 nm of Pt with 10 nm of Ti underlayer is sufficient to prevent agglomeration of the electrodes when the soft-eBL patterns are annealed at 700 ^{o}C. Subsequently, the samples were patterned a second time using eBL to define the contact lines connecting oxide patterns with the photolithography electrodes as shown in figure 4.13c. These structures were then mounted into a chip carrier, wire bonded and loaded into a gas sensing measurement chamber. The details of gas sensing results are discussed extensively in chapter 6. The goal of this section is only to demonstrate the feasibility of site-specifically fabricating the ceramic nanostructures.

As another example, ZnO soft-eBL patterns were fabricated on microhotplates. Microhotplates are extensively used in the research field of miniaturized gas sensors. One limitation of current gas sensor technology is the large power consumed in operating a sensor element at several hundred degrees above ambient temperature. Fabricating sensor elements on microhotplates (MEMS devices that contain an embedded heater and probing circuitry) can reduce the power requirements due to their low thermal mass. Furthermore, if the sensor material is also nanostructured, there can be additional advantages (beyond increased sensitivity) in terms of quicker response and recovery times that are typical of these nanostructures. However, placing nanostructures on the microhotplates can be challenging. It is shown here that soft-eBL can pattern nanostructures of ZnO gas sensing materials onto several fragile microhotplate substrates in an array. Figure 4.14a shows a backscattered electron image of a microhotplate with Pt contact pads while the schematic of

the hotplate cross-section and low magnification SEM image of the chip containing four hotplates are shown in figures 4.14b and 4.14c respectively.

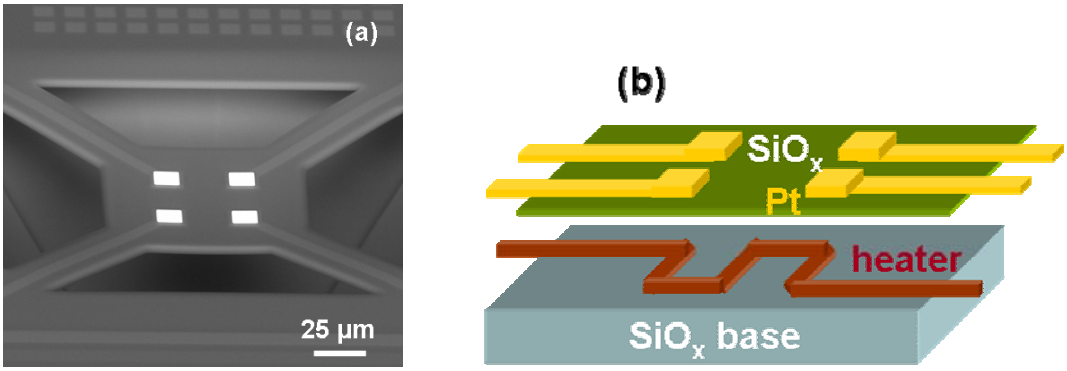

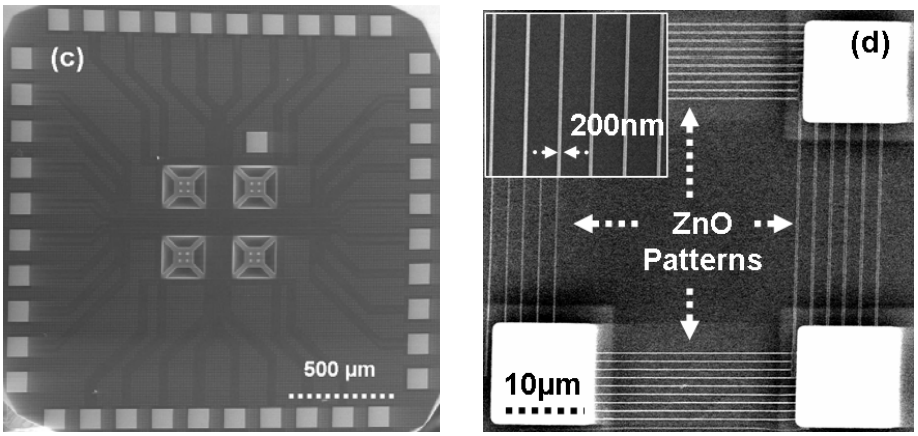

Continued on next page

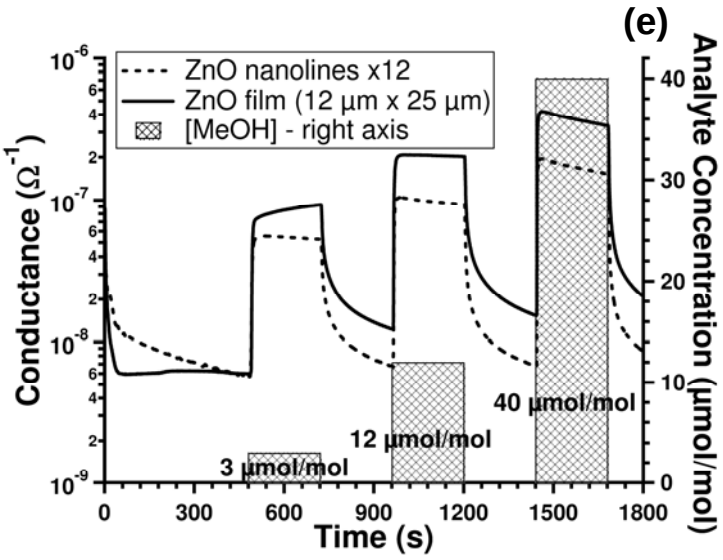

Figure 4.14: (a) BSE image of a microhotplate taken at 60^{o} tilt angle. (b) Schematic of the microhotplate design. (c) Low magnification image of a chip containing four microhotplates. (d) SEM image of ZnO soft-eBL patterns positioned across the Pt electrodes. (e) response of a set of nanolines and a microscale film on a microhotplate to three different methanol concentrations.

This microhotplate is a suspended, multilayer square plate that is about 4 μm thick with an embedded poly-silicon heater. The details of the microfabrication and unique capabilities of the microhotplate are published elsewhere[186, 187]. Soft-eBL patterned ZnO lines that are 200 nm wide and 30 μm long contacting Pt contact pads are shown in Figure 4.14d. After deposition, the soft-eBL patterned ZnO lines are annealed at 495 °C in air using the embedded heater. The fabrication steps are similar to those involved in patterning onto nitride membranes described earlier. The responses of these patterns to various concentrations of methanol at 495 °C are shown in figure 4.14e. The sensor response level, defined as the ratio of the change in conductance due to methanol exposure to the conductance in air ($\Delta G/G_0$) was found to be ≈ 8 at 3 μmol/mol and ≈ 22 at 40 μmol/mol of methanol in zero-grade dry air. The response times were less than 10 s, whereas the recovery time was less than 2 min. The response and recovery times (time for the measured conductance to change from $0.1\Delta G$ to $0.9\Delta G$) are comparable to those reported in the literature for ZnO nanorods and nanowires, which are single crystalline structures [164, 179, 188], while the nanolines in figure 4.14d are polycrystalline. This shows that quick response and recovery are not necessarily unique only to nanorods and nanowires. While positioning nanorods and nanowires into device architecture is a challenge, soft-eBL can fabricate nanostructures with similar dimensions and position them site-specifically in a seamless manner. It must be emphasized that though the response of only ZnO lines are shown, the soft-eBL technique is generic enough to fabricate nanostructures of diverse ceramic material composites onto these microhotplates, using appropriate solution precursors.

4.5.5. Example 5: Patterning with polymer solutions

While the majority of the work in this thesis used sol-gel precursors to fabricate ceramic nanostructures, polymeric solutions were also shown to be compatible with soft-eBL technique. Polypyrrole, a popular conducting polymer, nanostructures were patterned using dilute solutions of polypyrrole on SiO_x/Si surface. Polypyrrole in 3% water was received as a black solution with proprietary organic acids from Sigma-Aldrich. This solution was further diluted to 1:3 ratio of polypyrrole to water and was used for patterning. Figure 4.15a shows the SEM image of polypyrrole patterns with different line-widths and spacing. Inset in this figure shows a section of the pattern with 190 nm width. The 3D AFM topographic image and cross-sectional profile of a section of this pattern is shown in figure 4.15b indicating that the height of the lines is uniform. In order to confirm the chemical identity of these patterns, ion maps were taken using secondary ion mass spectrometer (SIMS) (PHI TRIFT III, Physical Electronics, USA). Figure 4.15c shows the SIMS CN^- ion maps of section of the pattern, which is consistent with the presence of polypyrrole. The poorer resolution of the patterns in SIMS ion map is partly due to coarser Ga ion probe size (~300nm). This further validates that the soft eBL approach is not only applicable to inorganic solutions but also to organic solutions. The soft eBL approach would be extremely valuable for patterning polymers because similar to ceramics etching polymers to generate nanostructures is otherwise very difficult.

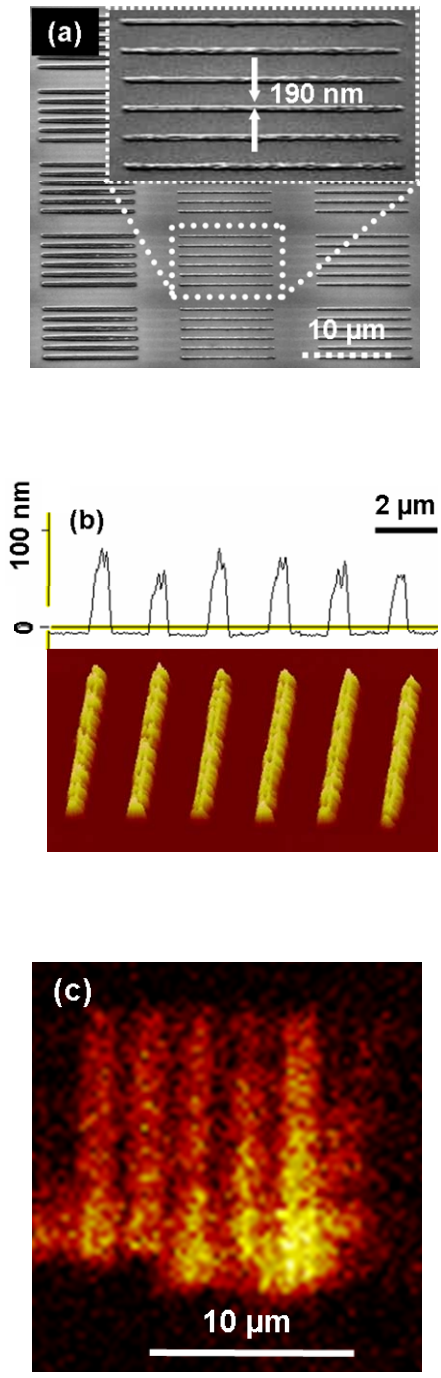

Figure 4.15: (a) SEM image of Polypyrrole patterns on SiOx/Si substrate. (b) Topographic AFM image (tapping mode) and cross-sectional profile of the Polypyrrole patterns. (c) CN- ion map taken using SIMS. These images were not taken at same locations.

4.6 BENCHMARKING SOFT-EBL AGAINST OTHER CERAMIC NANOPATTERNING TECHNIQUES

This chapter demonstrated a versatile nanopatterning approach suitable for a broad range of material-substrate systems. There are several advantages to this approach. First, the types of materials that can be patterned seem only to be limited by the availability of appropriate solution precursors that are compatible with e-beam resists, such as ceramic and polymer solutions. Second, because of the use of high sensitive e-beam resists such as PMMA for patterning, there is a distinct advantage over "direct-write" eBL of e-beam sensitive inorganic resists[66] that typically require high electron doses which translates into lower patterning speeds. In addition, spin coating is not only a low-cost process but also a high throughput process. Lastly, by spinning the solution, the need for any subsequent etching steps which might be undesirable especially for ceramics and organic materials is eliminated. There is a prior report by Shimada et.al[189] who have demonstrated a scheme to pattern nanostructures of ferroelectrics combining eBL and solution precursors, similar to this soft-eBL. However, their scheme required etching ferroelectric material before dissolving e-beam resist. Recently Xia et.al[190, 191] have also reported patterning nanostructures of silica particles using interference lithography and spin coating. Thus combining a high resolution patterning technique such as eBL with a low cost process such as spin coating has considerable potential for generating nanostructures using not only solution precursor but also colloidal solutions.

It is instructive to benchmark soft-eBL against other techniques demonstrated for patterning ceramic materials. Table 4.1 lists the various ceramic nanopatterning techniques.

Table 4.1: Comparison of Soft-eBL with other established techniques for *ceramic* patterning

Patterning Technique	Resolution	Etch-free	Site-specificity	Material-Substrate generality	Remarks	Specific Advantages
Photolithography[192]	20 nm	No	Possible	Yes, but not on fragile substrates∗	Mask fabrication with high resolution features needs electron beam lithography	High through put
Nano Imprint Lithography (NIL)[164]	20 nm	No	Possible			High through put
Soft-Lithography[91]	300 nm	Yes	No	Yes		Economical
Soft-eBL[193]	30 nm	Yes	Yes	Yes		Ideal for exploratory research in a lab setting
Dip Pen Nanolithography (DPN)[71]	140 nm ⊗	Yes	Yes	Yes		
Direct Write[194]	~ 100 μm	Yes	Yes	No		3D structures possible

∗ Fragile substrates: Ultra thin (electron transparent) membranes, microhotplates
⊗ Though the technique is capable of higher resolution, this value corresponds to the demonstrated resolution for patterning *ceramic* material.

4.7 SUMMARY

Soft-eBL is a highly versatile nanopatterning approach for fabricating variety of ceramic and organic nanostructures with controlled dimensions and locations. The approach synergistically combines the advantages of e-beam lithography and wet chemistry. The efficacy of soft-eBL is demonstrated through a series of examples of ceramic nanostructure fabrication. The advantages of soft-eBL include

1. *High resolution:* Ceramic structures as small as 30 nm could be routinely fabricated
2. *Registry capability:* Ceramic nanopatterns could be positioned at specific locations on the substrate such as across electrodes to facilitate property assessment and miniaturized device fabrication
3. *Material-Substrate generality*: Almost any ceramic nanostructure, subject to availability of a relevant liquid precursor, could be patterned onto a variety of substrates including insulators, single crystals, MEMS structures and electron transparent membranes
4. *Etch-free:* Because the technique uses liquid molecular precursors as sources, it does not require any etching steps.

In addition to demonstrating the above attributes through examples, the chapter also included experiments designed to identify chemical nature and functionality of fabricated nanostructures. This entailed the use of a combination of analytical and measurement techniques such as TEM, STEM, Analytical TEM, SIMS, NSOM and gas sensing performance assessments.

This chapter will be concluded with the following proposal. The soft-eBL technique consists of two major steps; one involving fabrication of resist molds on a suitable substrate and the other involving spinning of liquid precursors. While the resist molds are fabricated with eBL in this case, in future one could envision fabricating them using other high resolution patterning techniques such as nanoimprint lithography in order to harness the additional advantage of high throughputs.

CHAPTER 5

EFFECT OF Pd DOPING AND DIMENSIONALITY ON GRAIN SIZE OF SOFT-eBL INORGANIC NANOSTRUCTURES AND THIN FILMS

This chapter primarily discusses the effects of Pd doping and the dimensional constraint on the microstructural evolution during annealing of thin films and lines synthesized by sol-gel route. The results in this chapter demonstrate that a) 3% Pd doping can decrease the grain size by as much as 60% in tin oxide films, b) the reduced dimensionality in case of 1D nanostructures or lines compared to thin films decreases the grain size and c) the effect of Pd doping and dimensional constraint are not additive. The chapter also highlights the means of generating single grain wide nanostructures or "beaded-structures". These results are supported by structural and chemical characterization of both lines and thin films using TEM, SEM, XPS and XRD. It is argued that the soft-eBL is an enabling technique for controlling the grain size in inorganic 1D nanopatterns.

A part of the work discussed in this chapter is published in: **Adv. Mat., 19, 125, (2007)** and another part submitted to **IEEE Transactions in Nanotechnology**

5.1 POLYCRYSTALLINE NANOWIRES

The last decade has witnessed an explosion of research activity in fabrication and characterization of single crystalline one-dimensional (1D) nanostructures such as nanowires, nanorods and nanobelts [139, 195-198]. The high surface area to volume ratio of these structures makes them an obvious choice for potential applications involving surface/interface phenomena, such as gas-solid interactions in gas sensing and catalysis [199]. The lack of grain boundaries in these nanostructures is proposed as one of their attractive attributes especially for above room temperature applications such as gas sensors. At the usual gas sensors operating temperatures, between 300 ^{o}C and 700 ^{o}C, the structural instability due to grain growth and dopant segregation leads to loss of sensing performance with time in the case of polycrystalline sensing elements. This leads to a common problem known as base-line drift that requires periodic calibration of the sensor. Notwithstanding, the literature on gas sensors is replete with reports [200-202] suggesting a strong correlation between sensitivity and grain size of the sensing element. Higher sensitivity is generally associated with a smaller grain size especially when the diameter of the grain is comparable to the depletion layer thickness. Though the reports in literature are based on measurements conducted on polycrystalline bulk samples, without rigorous control on the grain size distribution, it is clear that structural defects such as grain boundaries and porosity are beneficial from the point of sensitivity and incorporation of these inhomogenities into the monolithic 1D nanostructures might further enhance their sensitivity. There is already some

evidence suggesting the superior sensing performance of polycrystalline nanostructures. Xia et.al [119] have recently reported sensing performance of polycrystalline SnO_2 nanowires. These polycrystalline SnO_2 nanowires showed sensitivity (change in the resistance normalized to base resistance) of about 4 when exposed to 20 ppm of carbon monoxide (CO) and a sensitivity of about 3 when exposed to 500 ppm of hydrogen (H_2) at room temperature. These results are superior to CO and H_2 sensing performance of either polycrystalline bulk, single crystalline bulk[203, 204], single crystalline whiskers[205], thin film [206-208] or single crystalline 1D nanostructures [24, 209, 210] of SnO_2 reported in the literature. For example, the best CO sensing performance of SnO_2 nanobelts reported [24] to date required operating at temperatures as high as 400 ^oC to notice a sensitivity of about 2 when exposed to 250 ppm of CO. This suggests the potential of polycrystalline nanostructures (nanowires) as excellent sensors. Nevertheless, measurements by Xia et.al were also performed on a film of nanowires by drop casting the solution of polycrystalline nanowires on top of electrodes. Therefore their results are not only ensemble average performance of millions of polycrystalline nanowires and grains but also the overall resistance measurements are unreliable because of weak contacts between nanowires. Therefore the overall resistance change observed in their measurements upon exposure to analyte gas could arise not only from the change in resistivity of individual nanostructures but also due to the change in contact resistance between individual nanostructures. Since the contacts between the individual nanostructures are not reliable (these nanostructures were not annealed to form reliable contacts) their performance could deteriorate with time. It is

therefore important to test polycrystalline nanowires with more reliable contacts and configuration in order to evaluate their performance. Fabrication of individual polycrystalline lines with well defined dimensions, separation and position is possible with the nanopatterning techniques such as soft-eBL. One of the goals of this chapter is to demonstrate such a capability of soft-eBL. In addition to unreliable inter-nanowire contacts one also needs to evaluate the structural stability of polycrystalline nanostructures for example against grain growth. There are several strategies one could employ to improve the structural stability of polycrystalline nanostructures and one of them is to impose dimensional constraint. The other goal of this chapter is to demonstrate the feasibility of using such a strategy on soft-eBL patterned structures.

5.2. WAYS OF IMPROVING MICROSTRUCTURAL STABILITY

5.2.1 Effect of secondary phases and dopants

It is clear from literature that smaller grain size is beneficial for gas sensing performance. However, the problem with smaller grains is their instability due to grain growth. There are several strategies one can pursue in reducing the grain growth kinetics and therefore improve the microstructural stability. One such strategy is to incorporate secondary phases and dopants that pin the grain boundaries. Transition metals such as Pd are commonly added to gas sensing materials such as tin oxide to improve their gas sensing properties. These dopants are often added in concentrations in excess of their solubility limit

and therefore could precipitate as second phase particles. The second phase inclusions reduce the grain growth by making it harder for grain boundaries to pull away from the inclusions. This is a common strategy used for grain refinement in metallic alloys and similar strategy could be applied in case of ceramics used as gas sensors. In addition to acting as grain growth inhibitors, secondary phases and dopants could also have other beneficial effects such as acting as catalysts for gas-solid interactions and improving the selectivity (ability to preferentially detect a certain gas over other gases) of gas sensors. While these secondary phases and dopants might be beneficial for thick film and bulk sensor elements, there might be undesirable side-effects in the case of nanostructures. For example, while the distribution of these secondary phases and dopants might not be too critical for the performance of a bulk sensor element, it becomes very important in case of a nanostructure such as a tin oxide line with 50 nm × 50 nm cross-sectional area (with 10 nm average grain size). The segregation of dopants at length scales comparable to the line dimensions and the effect of line dimension on segregation kinetics can result in the non-uniformity in line-to-line performance and ultimately lead to poor reliability of the sensors made from these lines. Moreover the segregation at length scales comparable to the nanostructure dimensions leads to significant compositional non-uniformity and therefore difficult to assess the dimensional effect on the overall sensor performance.

5.2.2. Effect of reduced dimensionality

An alternative strategy for reducing the grain growth kinetics in a pure phase is to reduce the dimensionality. Solid state crystallization is a type of phase transformation that involves nucleation of a crystalline phase in an amorphous matrix and growth of these nuclei (grain growth) until the entire amorphous matrix is transformed into the crystalline phase. Therefore, the total crystallization rate depends on both the nucleation rate as well as the grain growth rate though it is often times difficult to observe these two processes individually. Both these processes are thermally activated with characteristic activation energies. Any external parameters such as volumetric stresses that affect these activation energies will ultimately affect the crystallization rate and thus the final grain size. It is well known that crystallization rates measured on bulk samples (three-dimensional, 3D case) are noticeably higher than those measured on thin films (two-dimensional, 2D case) for a given material system [211-215]. This is usually explained considering the reduced grain growth due to dimensional constraint. The growth of crystalline phase nuclei is truncated upon impingement with neighboring nuclei in a 3D case, whereas in 2D case they are in addition truncated upon impingement with free surfaces. This results in overall reduction in the crystallization rate. This argument could be further extended to 1D case (lines) where growth will be truncated in lateral dimension in addition to the thickness dimension as in thin film case.

The effect of reduced dimensionality on the overall crystallization rate is two fold. The reduction of dimensionality (3D case versus 1D) leads to increased surface to volume ratio. The nucleation of crystalline phase in case of sol-gel structures leads to the generation of stresses due to large volume shrinkages. Figure 5.1 shows the dimensions of tin oxide patterns measured using scanning electron and atomic force microscopes before and after annealing at 700 ^{o}C for 1 h in air. Line-widths are measured using SEM images while heights are measured from AFM line profile. Based on the measured dimensions before and after annealing one can infer that the patterns experience roughly 60% volume shrinkage upon annealing. The dimensional changes observed in these patterns are typical of the large volume shrinkages observed in sol-gel materials upon annealing. The volume shrinkages are mostly associated with combustion of organics. Please note that the inorganic solid content at typical concentrations used for sol-gel synthesis is very low. For example 0.1M tin oxide sol has tin ionic content of less than 1%. Such low mass contents lead to large volume shrinkages upon annealing. While such large volume shrinkages can lead to cracking in bulk system, one can take advantage of them in case of nanostructures for example to generate extremely fine pore network or to modify the grain growth kinetics as explained below.

Since surfaces are effective sinks for stresses, the reduced dimensionality would promote nucleation and leads to large nucleation density. On the other hand reduced dimensionality can reduce the grain growth rate for the reasons explained in the previous paragraph (truncation at additional surfaces). This is schematically shown in figure 5.2. The

increased nucleation density and reduced grain growth rate will therefore result in finer grain size. This also means that the microstructure of 1D nanostructure is more stable against grain growth than bulk samples.

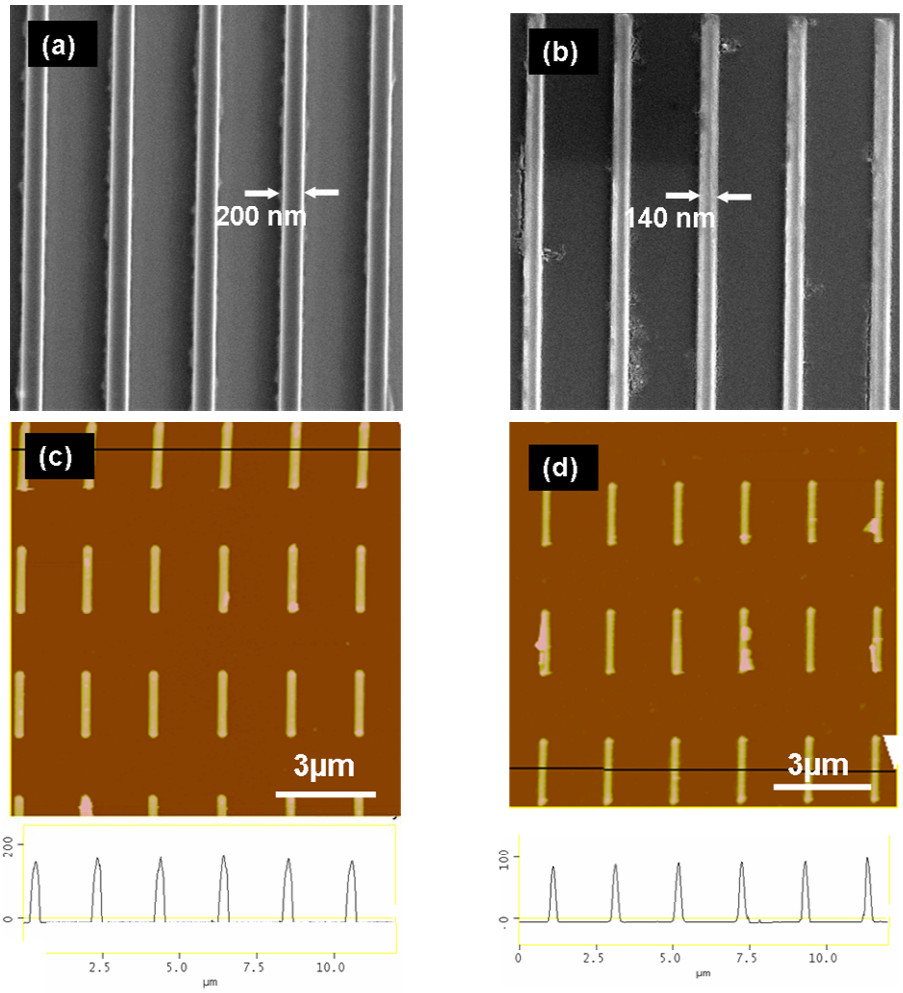

Figure 5.1: SEM images of tin oxide patterns (a) before and (b) after annealing. Atomic force microscope images of the same patterns (c) before and after annealing. The line profiles are shown below each AFM image. The patterns were annealed in air for 1 h at 700 ^{o}C. The average height of the patterns changes from 170 nm before annealing to 100 nm after annealing with a standard deviation of about 6 nm.

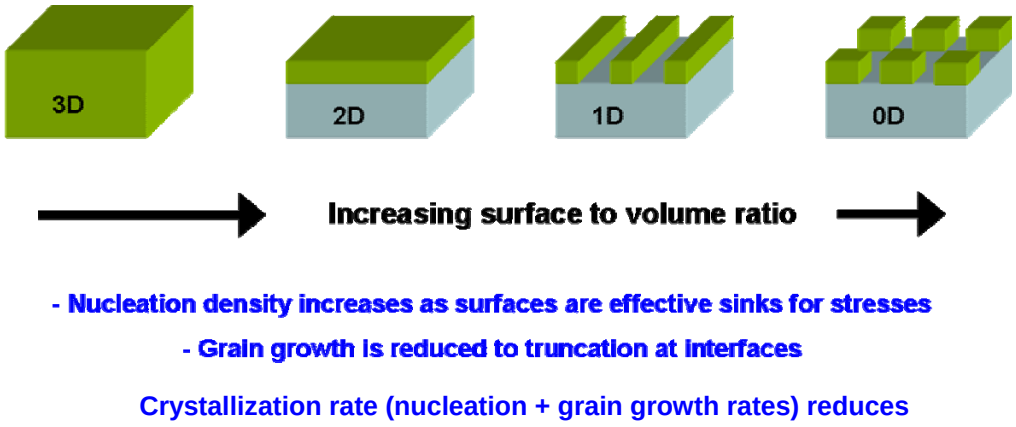

Figure 5.2: Schematic representation of the effect of dimensionality on the overall crystallization rate

This chapter will explore two routes of stabilizing the microstructure of sol-gel derived thin films and nanostructures, namely by doping and reducing the dimensionality. The results will include specifically the effect of palladium on grain size of tin oxide thin films and the effect of line width on the grain size of tin oxide and zinc oxide.

5.3. EXPERIMENTAL DETAILS

5.3.1. Sol preparation

All the chemicals were purchased from Sigma-Aldrich and used without further purification. Undoped and Pd doped tin oxide sols were prepared from their respective acetate precursors. All the sols were prepared inside fumehood without rigorous control on the ambient humidity. Undoped sol was prepared by dissolving equimolar ratio of tin (IV) acetate and ethanolamine in 2-methoxy ethanol by continuous stirring at 90 ^{o}C for 1 h. While stirring the solution, beaker is covered with a layer of paraffin film to reduce the amount of solvent loss. Ethanolamine is a chelating agent that controls the hydrolysis rate of tin acetate whereas 2-methoxy ethanol is the solvent. Palladium doped sols were prepared in the same manner except for the addition of required amount of palladium acetate. Zinc oxide sols were prepared by mixing zinc acetate precursor with the same chelating agent in the same solvent as those used for preparing tin oxide sols. Zinc oxide sols were also prepared in the similar manner as those of tin oxide sols except that stirring was done at 60 ^{o}C for 1 hr. After preparation, all the sols were filtered through a 400 nm average pore size PTFE

membrane to remove any residues. Subsequently the sols were stored in air-tight glass bottles and were kept in a dessicator at room temperature. This ensured that the sols were stable (no visible precipitation) up to at least six months.

5.3.2. Thin film fabrication

Thin films were prepared by spin coating at room temperature and heating on a hotplate at 150 ^{o}C for 5 min to gelate the films. Substrates were spin coated multiple times to achieve desired film thickness. (It is important to cool the substrate to room temperature before spin coating the next layer in order to achieve uniform coating). Prior to spin coating the sol, substrates were sequentially cleaned in acetone, water and isoproponal (IPA) for 10 min in each solution. Typically a 0.1M tin oxide sol spin coated 5 times at 1000 rpm resulted in a film thickness of about 80 nm after annealing in air at 700 ^{o}C for 1 hr.

5.3.3. 1D Nanostructure fabrication

The nanostructures of tin oxide, palladium doped tin oxide and zinc oxide were prepared using soft-eBL technique on silicon nitride membranes. Please refer to previous chapter for experimental details on soft-eBL process. The silicon nitride membranes are 50 nm thick and are electron transparent. The nitride membranes were chosen as substrates for nanostructures because it enabled ready structural characterization using transmission electron microscope (TEM) without requiring any sample preparation. There are several differences in the soft-eBL patterning process using membranes compared to patterning onto

bulk substrates. First, as the membranes are fragile and would not survive the sonication process during lift-off, patterning density was reduced (about 10 μm separation between adjacent patterns) to allow clean lift-off without sonication (Quick lateral movements of the membrane inside acetone solution was effective in achieving clean lift-off). Second, the as-received membranes always tend to be hydrophobic and therefore are treated with oxygen plasma for about 30 sec prior to spin coating the electron beam resists. The wet chemical treatment of the membranes is kept to a minimum to reduce the probability of damage to the membranes. Third, because of low density of backscattered electrons, the electron doses necessary for effective exposure are at least twice as high as those used for bulk substrates.

5.3.4. Grain size analysis using SEM and TEM

Transmission electron microscopy was used to measure the grain size in thin films and patterns of both doped and undoped tin oxide. Conventional bright field images at multiple locations were taken on each sample. Grain size measurements were performed by adjusting the intensity thresholds of the micrographs using digital micrograph software and manually counting the diameter of grains chosen randomly. The reported grain size values were an average of over 300 grains. Scanning electron microscopy was used to measure the grain size of ZnO thin films and patterns. Since the ZnO grains were clearly discernible with SEM and a single grain spans entire film and pattern thickness, grain sizes measured using SEM are a reliable measure of the true grain size in these structures.

5.3.5. Chemical composition analysis using X-ray Photon Spectroscopy

X-ray Photon Spectroscopy (XPS) was used to measure the chemical composition of undoped and Pd doped tin oxide thin films. After annealing the thin films in air, they were immediately loaded into XPS chamber to minimize any spurious organic contamination from laboratory environment. X-ray Photoelectron Spectroscopy (XPS) analyses were performed with an Omicron ESCA probe, which was equipped with EA125 energy analyzer. Photoemission was stimulated by a monochromated Al K_α radiation (1486.6 eV) operating at 300 W power. A low-energy electron flood gun was employed for charge neutralization. Survey and high-resolution scans were collected using pass energies of 50 and 25 eV respectively. High resolution scans were performed to collect the core level spectra of Sn 3d, Pd 3d, O 1s and C 1s. Binding energies of spectra were referenced to the C 1s binding energy set at 284.8 eV. The Pd concentration with respect to Sn was calculated by using the following equation:

$$C_{Pd/Sn} = \frac{I_{Pd^{3d3/2}} S_{Sn^{3d5/2}}}{I_{Sn^{3d5/2}} S_{Pd^{3d5/2}}} \qquad (5.1)$$

where $I_{Pd^{3d3/2}}$ and $I_{Sn^{3d5/2}}$ are integrated intensities under Pd $3d^{5/2}$ and Sn $3d^{5/2}$ core level spectra, $S_{Pd^{3d5/2}}$ and $S_{Sn^{3d5/2}}$ are the sensitivity factors for the corresponding core levels (available as standard tables).

5.3.6 X-ray diffraction

X-ray diffraction measurements were performed to identify the phase and to measure the grain size in Pd doped and undoped tin oxide thin films. Due to the small sample sizes and therefore small scattering volumes of patterns (1D nanostructures), x-ray diffraction was not used for them. Phase identification in thin films was achieved by performing scans in thin film geometry. In this geometry, x-rays strike the sample at glancing angles (~0.4 deg) and the detector scans the 2θ values. Prior to taking thin film scans, x-ray reflectivity measurements were performed to measure the film thickness as well as the critical angle. Critical angle refers to the angle at which x-rays just about penetrate the sample and specular reflection begins to reduce. The critical angle for tin oxide films studied in this work was found to be about 0.8 deg. Therefore thin film scans were performed at a glancing angle of 0.4 deg (half the critical angle).

The grain size is calculated using the standard Debye-Scherrer equation:

$$B = \frac{0.9\lambda}{t\cos\theta} \qquad (5.2)$$

where B is the width of x-ray peak at half maximum, λ is the x-ray wavelength and t is the grain size. This equation does not account for the instrument broadening and therefore the values measured by this technique are lower than the true grain size values. However, this error would be of similar magnitude for all the samples and therefore be irrelevant when

comparing the relative grain sizes between samples. It is important to note that the above equation only gives the through thickness grain size and not the grain size in-plane. In other words, the grain size of columnar grains measured using this equation would equal the film thickness.

All the x-ray diffraction measurements were performed at room temperature using Rigaku ATXG diffractometer operating at 50 kV and 240 mA with filtered (for K_β) Cu K_α radiation. The measurements were taken at 0.7 deg/min scan rate.

5.4. EFFECT OF Pd ON SnO_2 MICROSTRUCTURE

5.4.1 Thin films

5.4.1a – X-ray Diffraction: The x-ray diffractograms and reflectivity scans of tin oxide thin films are shown in figure 5.3a and 5.3c respectively. Figure 5.3b shows the standard x-ray diffractograms of pure phases for reference. All the samples were annealed in air at 700 ^oC for 1 h. All the peaks in figure 5.3a correspond to the tetragonal SnO_2 phase and there is no evidence for presence of either SnO, PdO or Pd_2O phases. While the absence of PdO and Pd_2O peaks could be due to low Pd concentration, the absence of SnO peaks indicates that SnO_2 is the major phase. The grain sizes measured from these diffractograms are shown in table 5.1 below. The grain size calculated is the average of values measured from three peaks corresponding to (110), (110) and (200) reflections in figure 5.3a. It can be

clearly seen from table 5.1 that increasing Pd concentration monotonically decreases the grain size by as much as 60% upon 3 at% Pd. Moreover comparison of relative intensities of XRD peaks in figure 5.3a with those of standard peaks in figure 5.3b shows that films are preferentially textured with (110) parallel to substrate normal. It is also interesting that the relative intensities of the XRD peaks is independent of Pd concentration suggesting that Pd has minimal effect on their texture. Therefore the main effect of Pd doping appears to be on grain size and possibly on porosity.

Table 5.1: Average grain size in tin oxide films calculated from diffractograms in figure 5.3a using debye-scherrer equation

at %Pd	Ave. Grain size (Å)
0	113
0.5	81
1	71
2	52
3	43

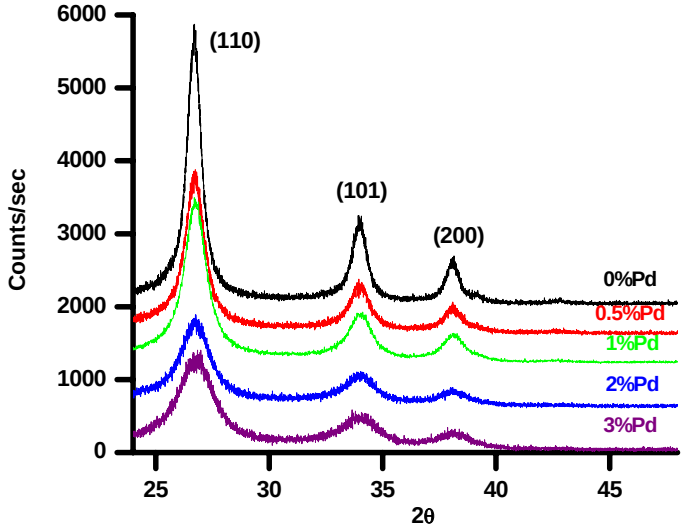

Figure 5.3a: X-ray diffractograms of SnO_2 thin films with various Pd concentrations

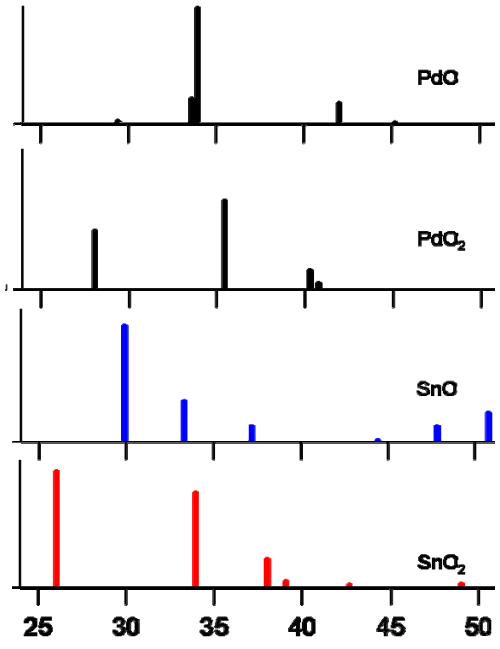

Figure 5.3b: Reference x-ray diffractograms of pure phases

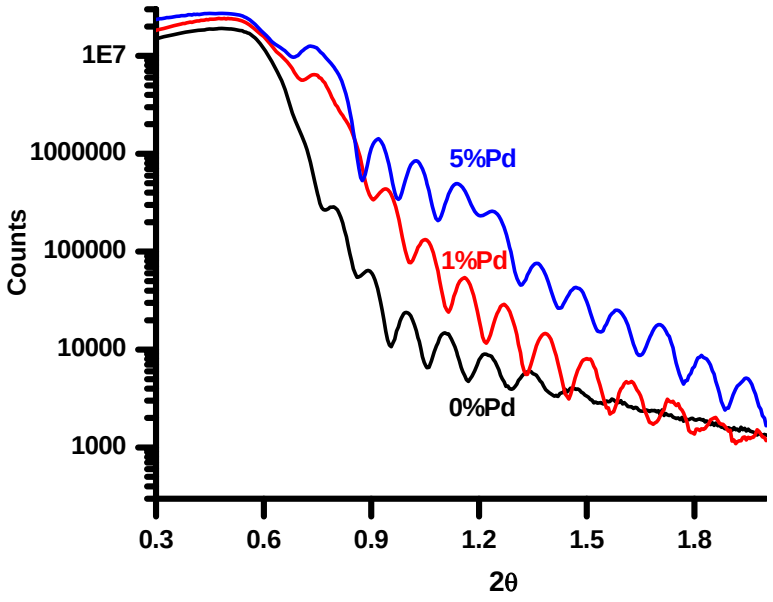

Figure 5.3c: Reflectivity curves of SnO_2 thin films with various Pd concentrations

For a 3 at% Pd the grain size decreases by more than 60%. This demonstrates the significant effect of Pd on reducing the over all crystallization rate resulting in smaller grain size. There are several reports in literature demonstrating the similar grain growth retarding effect of Pd[216] and other dopants[202, 217-224] in SnO_2. While there is no conclusive experimental evidence for the location of Pd, it is possible that Pd either segregates to SnO_2 grain boundaries or forms second phase particles (such as palladium oxides). In either case SnO_2 grain boundaries could be pinned during high temperature annealing process resulting in a smaller grain size. Analytical TEM studies in this work indicated that Pd does indeed form Pd-rich clusters whose dimensions are comparable to tin oxide grains. The analytical TEM studies refer to the energy dispersive spectroscopy (EDS) maps taken in scanning transmission electron microscope mode (STEM). In STEM mode, electron beam is scanned on the sample and the intensity of element specific x-rays are collected. These intensity maps indicate the spatial distribution of the elements. Figure 5.4a shows the STEM image of a line of tin oxide doped with 3%Pd while figure 5.4b shows the EDS intensity maps of Sn and Pd elements, collected in STEM mode. These lines were fabricated on nitride membrane and were not subjected to any additional sample preparation techniques such as ion milling that might otherwise modify the structure. While the palladium map clearly shows the clustering of Pd, comparing the electron image with the EDS maps, it is not clear if there is any preferential segregation of Pd to grain boundaries because the cluster size is bigger than the grain size. Moreover there is no grain boundary decoration of Pd is obvious from Pd EDS maps. This could be mostly due to the limited spatial resolution of the technique

compared to the grain size. While the grain size is about 5 nm, the electron probe is 1.5 nm. Improving spatial resolution by reducing probe size is difficult because of the longer collection times that would be necessary and the associated spatial drift would be significant over such long collection times.

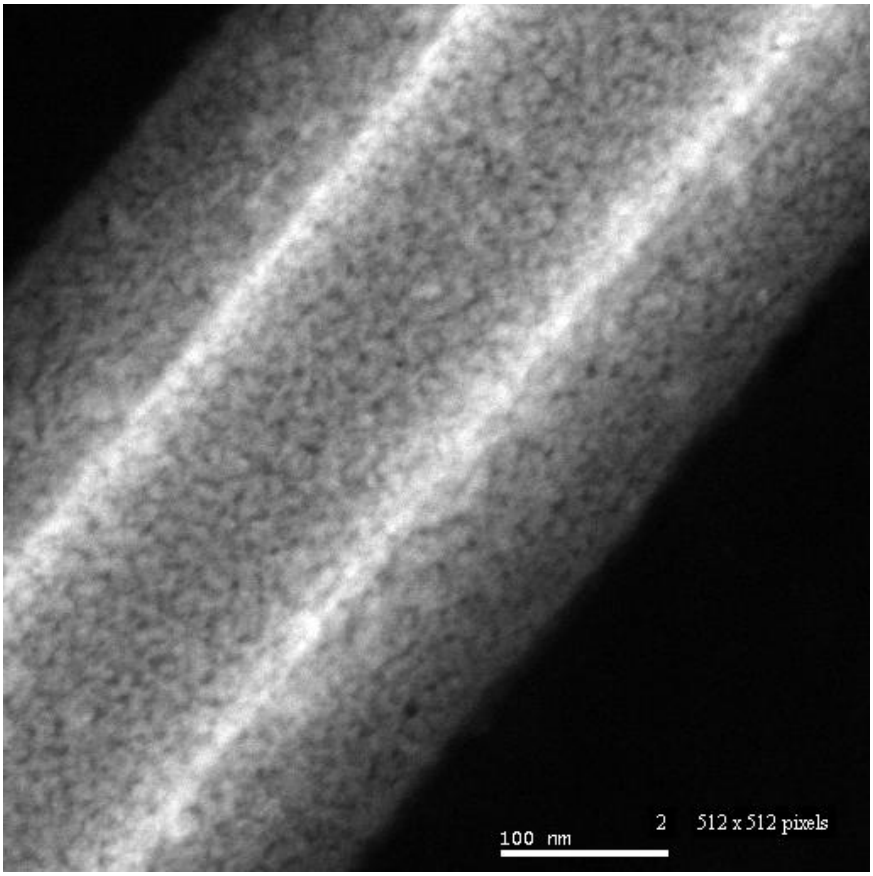

Figure 5.4a: Scanning Transmission Electron Microscope (STEM) image of SnO_2 line doped with 3% Pd annealed at 700 ^{o}C for 1 h in air

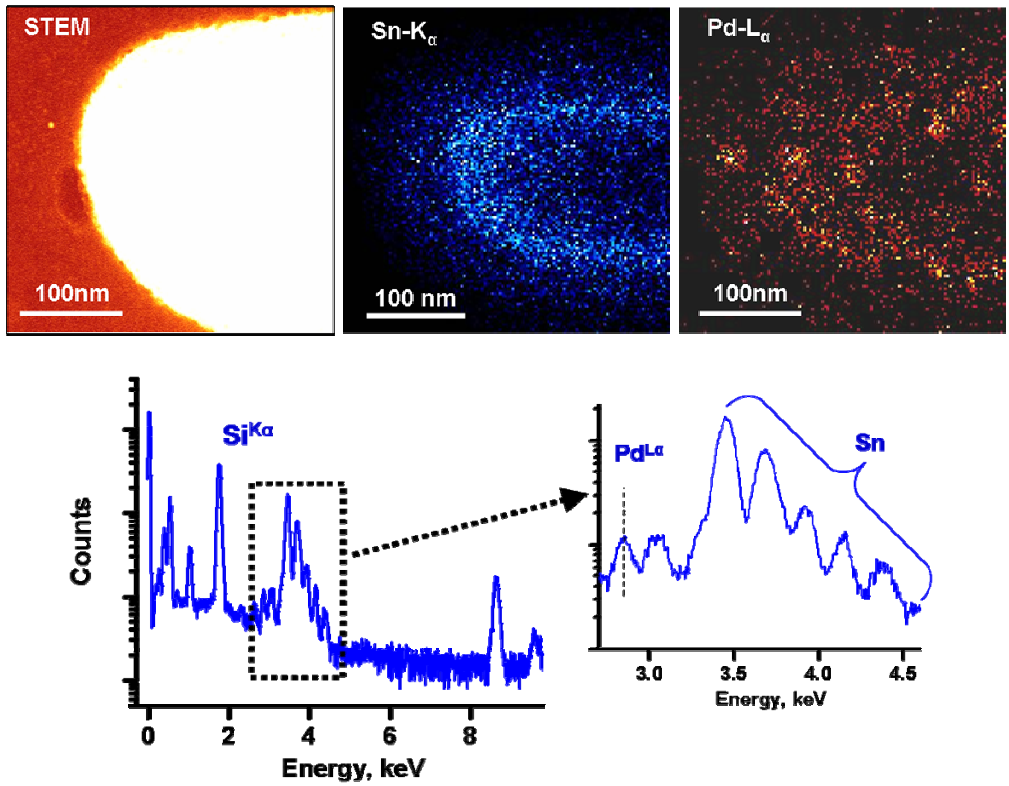

Figure 5.4b: Scanning transmission electron microscope image and EDS maps of Sn and Pd. The EDS spectrum simultaneously collected while generating the maps is also shown above. The measurements were performed with a nominal electron probe size of 1.5 nm and the total collection time is 10 min.

The x-ray reflectivity measurements in figure 5.2b are used to calculate the film thickness using the following approximate equation:

$$d = \frac{\lambda}{2\Delta\theta} \qquad (5.3)$$

where d is film thickness, λ is x-ray wavelength and Δθ is the spacing of adjacent reflection fringes in radians. Figure 5.2b shows that Δθ is similar for all the films and therefore are of similar thickness. Using equation 5.3, the thickness of these films is calculated to be approximately 80 nm. As will be shown in the subsequent sections in this chapter and later chapters, the thickness of lines fabricated using soft-eBL is also comparable to this value. Therefore comparison is made between lines and films of similar thickness. The only difference between these structures is their width.

5.4.1b X-ray photon spectroscopy: The high resolution XPS scans of Sn, Pd, O and C taken from tin oxide films with different Pd concentrations are shown in figure 5.5. These films were annealed in air at 700 ^{o}C for 1 h. Using equation 5.1, the ratio of O to Sn is calculated to be 1.4 in all three tin oxide films and therefore suggest that surface is oxygen deficient SnO_2.

The XPS technique is a surface sensitive tool because of the short escape distance (~ 10 nm) of the photoemitted electrons. Therefore the concentration values measured are

characteristic only of the surface and do not necessarily represent the bulk of the sample. This is the main reason for the difference between XRD and XPS results. The XPS results indicate that tin oxide film surface is oxygen deficient and O:Sn ratio of 1.4 suggests that surface consists of 50% SnO and 50% SnO_2. Moreover, the asymmetry in the O 1s peak suggests the presence of oxygen ions with two different binding energies, possibly corresponding to SnO and SnO_2 phases. There are several reports in the literature reporting an oxygen deficient tin oxide surface even after annealing at high temperature[225, 226]. The sub-stochiometric surface places a significant role in the gas sensing performance of tin oxide.

The Pd to Sn ratios calculated from figure 5.5 are 0%, 0.9% and 2.8%. There values are very close to the expected values based on starting sol formulations. XPS measurements were taken on three different samples cut from same initial substrate for each sol composition. The variation between these three measurements is less than 10% of the values reported above.

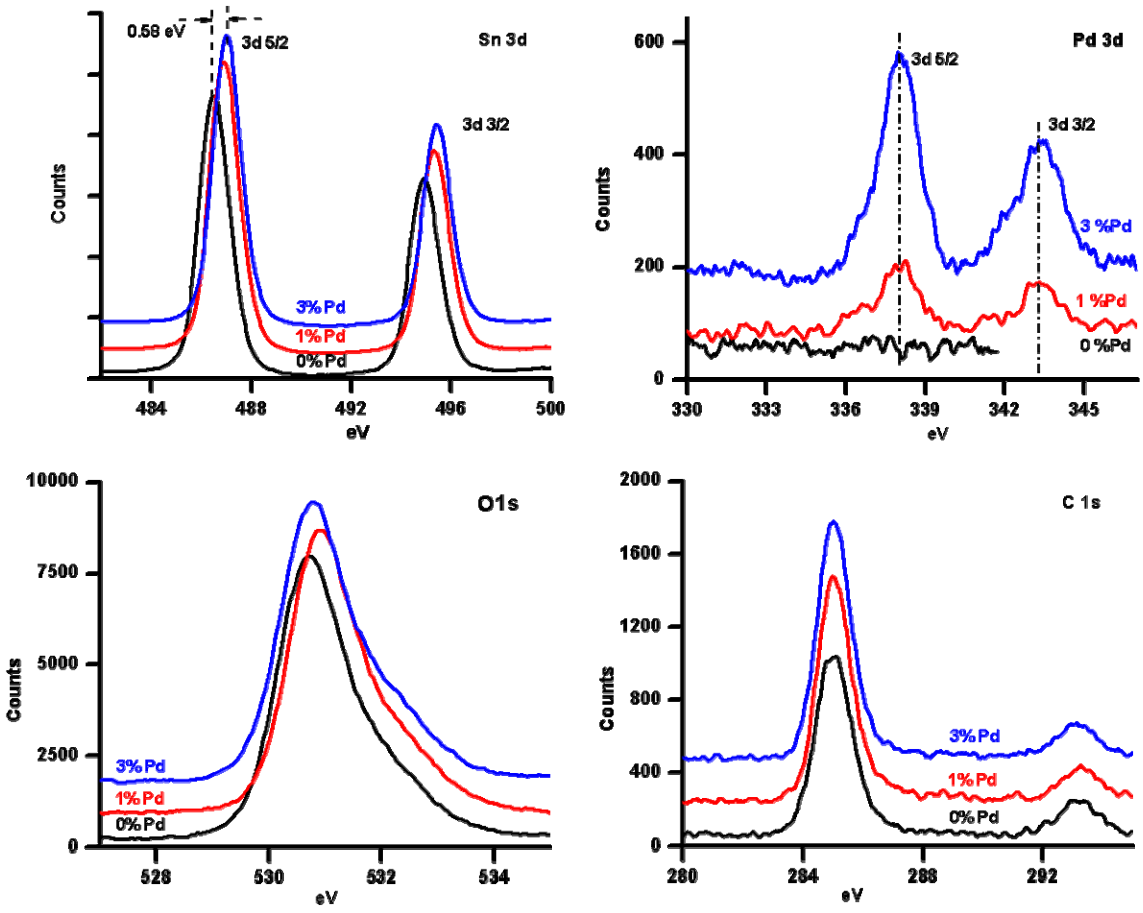

Figure 5.5: X-ray Photon Spectroscopy scans of Sn, Pd, O, and C from three different tin oxide films

5.4.1c Transmission Electron Microscopy: The transmission electron micrographs of tin oxide thin films with two different Pd doping concentrations are shown in figure 5.6. These films were annealed in air at 700 ^{o}C for 1 h. This figure also shows the grain size distribution plots of these samples. Grain size distribution analysis was performed by counting about 340 grains from multiple micrographs taken at different locations on each sample to get a good statistical average. Clearly, Pd doping decreases the grain size in tin oxide and these results support the XRD results presented earlier in the chapter. Based on a slightly smaller standard deviation in doped sample, it appears that Pd doping also gives a narrower grain size distribution in addition to smaller grain size.

Comparison of grain size values measured using TEM and XRD are clearly different. While the undoped sample grain size as measured by TEM is about 14 nm, XRD measurements indicate a value of about 11 nm. For a 3% Pd doped samples, these values are 8 nm (TEM) and 4 nm (XRD). A constant difference in XRD and TEM grain size values (about 3 nm) at different Pd concentrations indicate that the differences in these values are primarily due to the error in neglecting instrument broadening in XRD measurements.

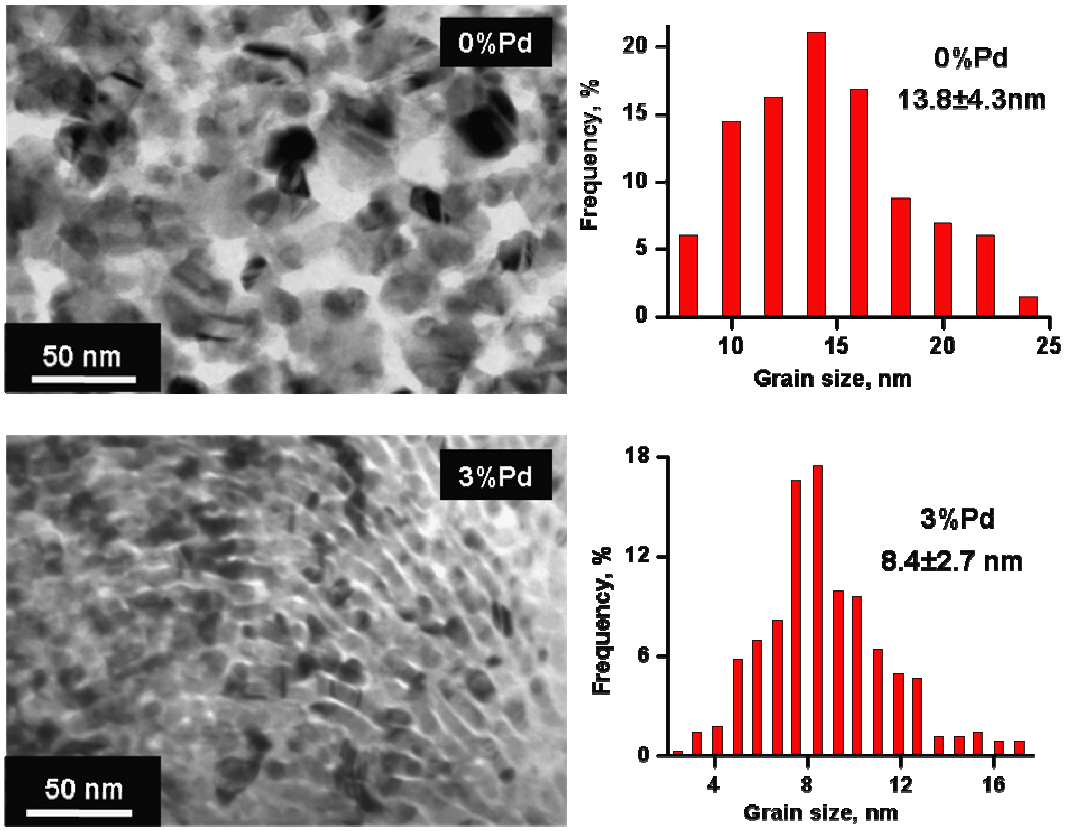

Figure 5.6: TEM micrographs and the corresponding grain size distribution plots of tin oxide thin films with two different Pd concentrations. The grain size is an average of 340 grains.

5.4.2 1D nanostructures

5.4.2a - Transmission Electron Microscopy: 3% Palladium doped and undoped tin oxide 1D nanostructures or lines are fabricated using soft-eBL technique on 50 nm thick SiN_x membranes. These lines are prepared using the same sols that are used for making thin films and annealed in the same manner as the thin films. Figure 5.7 shows the TEM micrographs of the lines and the corresponding grain size distribution plots. Width of the line in each case, as measured from their TEM micrographs, is about 100 nm. There are two interesting observations one can make from the grain size distribution plots in figure 5.7. Firstly the effect of Pd on average grain size and the grain size distribution is minimal. Both the 0% Pd and 3% Pd doped samples show an average grain size of 5.6 nm with similar standard deviation values. Secondly, the average grain size of lines is much smaller than either doped or undoped films shown in figure 5.6. For example while the average grain size in undoped tin oxide thin film is about 14 nm, the average grain size in 100 nm wide undoped tin oxide line is about 60% smaller or is only about 6 nm. It is important to note that the height of the line, measured using atomic force microscope, is about 70 nm whereas the thickness of the film as measured using x-ray reflectivity technique is of comparable value of about 80 nm (< 13% difference). Furthermore, the sol and the annealing conditions used for both films and lines were the same. Therefore, the differences in grain sizes of lines and film appear to be solely due to the differences in line widths. Therefore, dimensionality has a significant effect on the overall crystallization kinetics.

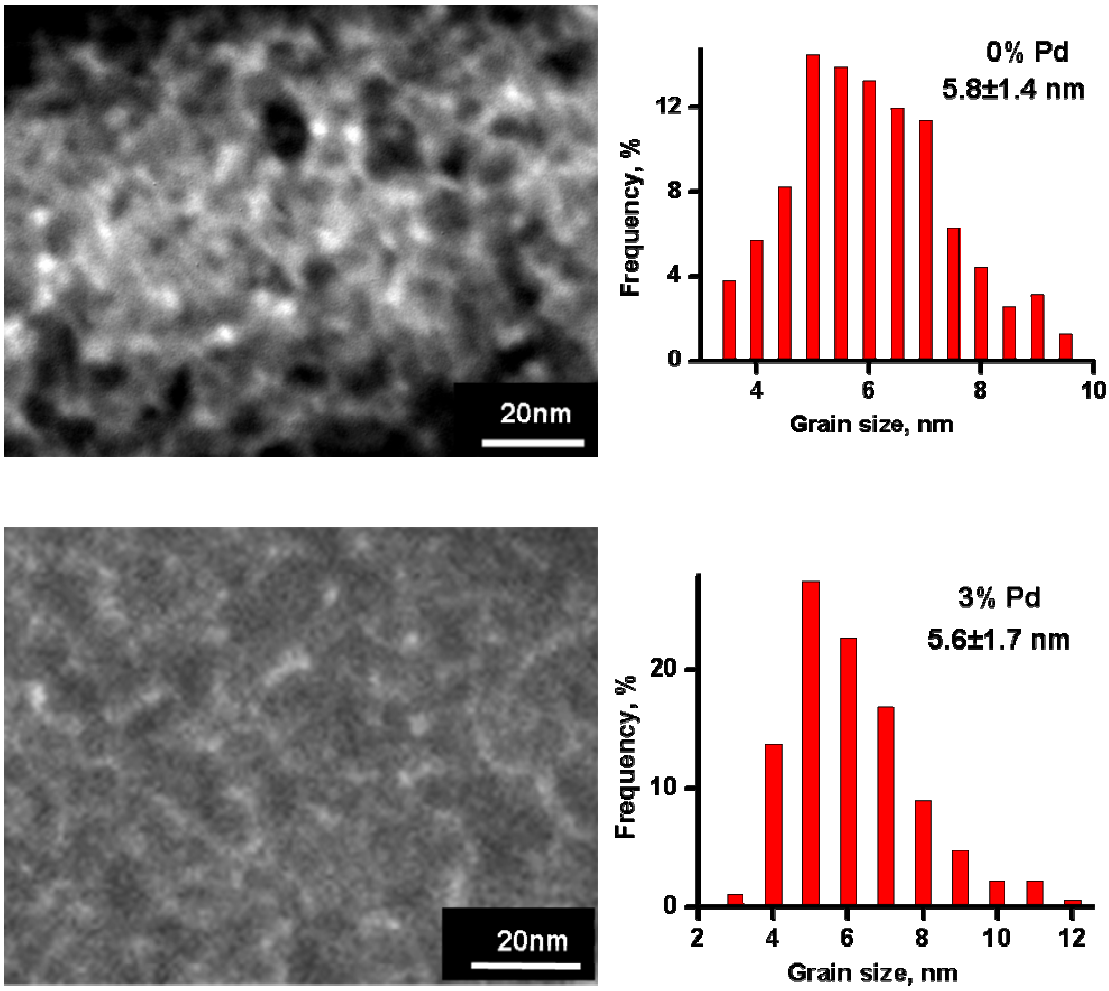

Figure 5.7: TEM micrographs and the corresponding grain size distribution plots of tin oxide line with two different Pd concentrations. The grain size is an average of 190 grains. The width of the line is 100 nm.

5.5. EFFECT OF DIMENSIONALITY ON SnO_2 MICROSTRUCTURE

To investigate the effect of dimensionality on average grain size, 3%Pd doped and undoped tin oxide lines with two different widths were fabricated onto SiN_x membranes. The average grain size measured in each of these samples is shown in table 5.2 below together with the values measured in thin films. These values for lines indicate that irrespective of doping concentration and line width the average grain size is of similar value. This value is smaller than the grain size found in thin films of both concentrations. Also the effect of dimensionality is clear when one compares the grain size in thin film and lines at both the concentrations. It is apparent that while the Pd concentration has an effect on grain size in thin films, it has no significant effect on the grain size in either 100 nm or 200 nm wide lines. This can be explained as follows: The effect of both decreased dimensionality as well as Pd doping is to reduce the grain size. However, both these effects are *not synergistic*. In case of thin films, the effect of Pd is clear. On the other hand in case of lines, the effect of reduced dimensionality dominates and has similar effect in both 100 nm and 200 nm wide lines. To possibly see the effect of line width on grain size, one needs to prepare lines with widths much larger than 200 nm. The absence of any synergistic effect from Pd doping therefore leads to similar grain size in both 100 nm and 200 nm wide lines but much smaller grain size than thin films.

Table 5.2: Average grain size of undoped and 3%Pd doped tin oxide lines and thin films. Value in parenthesis is the total number of grains counted in each case.

Concentration of Pd	Thin film	100nm line width	200nm line width
3%	8.4 ± 2.7 nm (340)	5.6 ± 1.7 nm (260)	5.3 ± 1.6 nm (240)
0%	13.8 ± 4.3 nm (350)	5.8 ± 1.4 nm (158)	6.4 ± 1.3 nm (128)

In summary, the following conclusions can be drawn from the above results:

1. Doping with Pd reduces the grain size of tin oxide films. 3% doping can reduce the grain size by as much as 60% in thin films as measured using x-ray diffraction technique.
2. Reducing the dimensionality also reduces the grain size in tin oxide irrespective of doping concentration.
3. The effects of Pd doping and reduced dimensionality are not additive.

5.6 EFFECT OF DIMENSIONALITY ON ZnO NANOSTRUCTURES

ZnO is another important wide bandgap semiconductor that is extensively used for gas sensing applications. The effect of dimensionality is also studied in this material system. These studies were also motivated by the initial observation of smaller grain size in 1D soft-eBL patterns compared to thin films. Figure 5.8 shows the SEM images of ZnO film and patterns annealed at 700^{o}C in air for 20 mins. While the thin film shows the average grain size to be about 80 nm, the grain size of line is not discernible in case of 1D pattern/line.

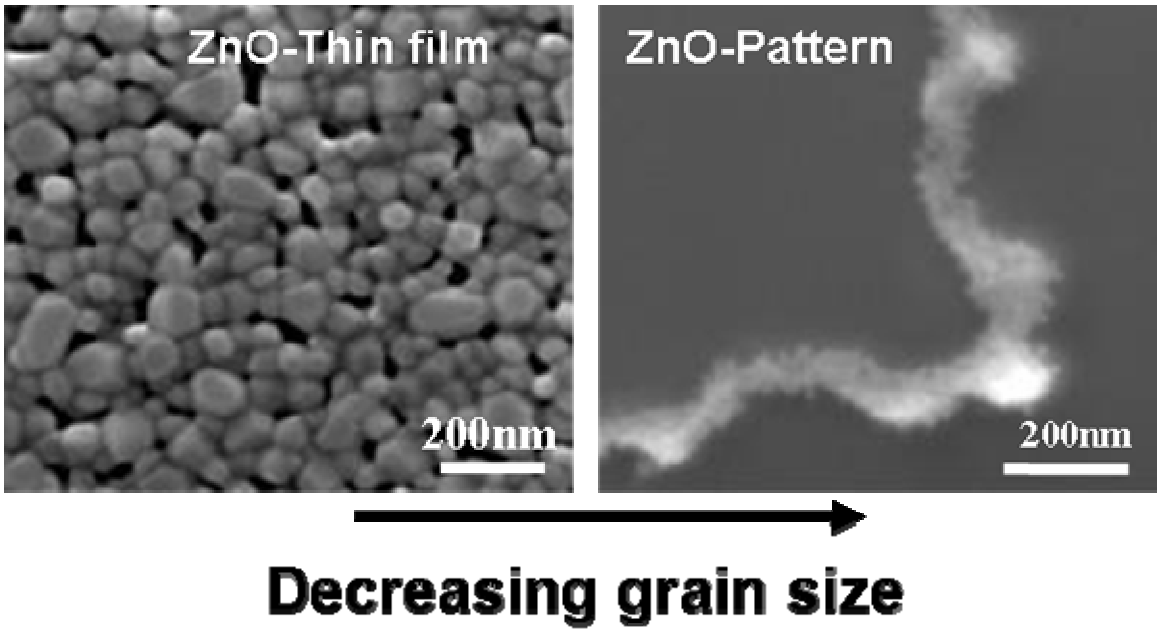

Figure 5.8: SEM images of ZnO thin film and line annealed at 700 ^{o}C for 20 min in air

To further investigate the effect of dimensionality on microstructure, ZnO lines with different widths were fabricated on oxidized silicon substrates using the soft-eBL technique. Figure 5.9 shows the SEM images of different ZnO lines and thin film annealed at 900 ^{o}C in air for 5 mins. The samples were annealed by upquenching (introduced into furnace when it is has reached the annealing temperature). This figure also shows the plot of grain size in each case measured from an average of about 80 grains.

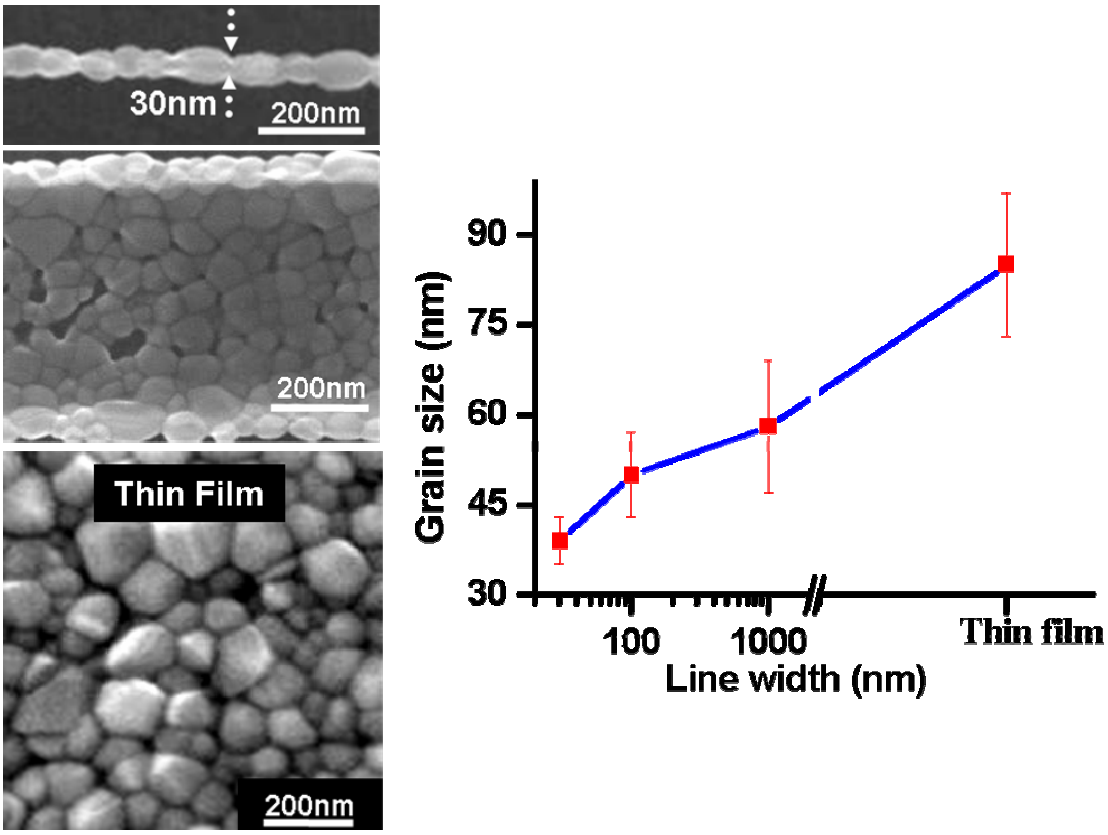

Figure 5.9: Scanning electron micrographs of ZnO lines and thin film annealed at 900 ^{o}C for 5 mins in air. The plot shows the average grain size in each case.

The cross-sectional images (obtained by imaging the tilted samples) showed that these lines are of single-grain height and therefore columnar in nature. This is also confirmed by scanning transmission electron microscopy (STEM), as seen in figure 5.10 below.

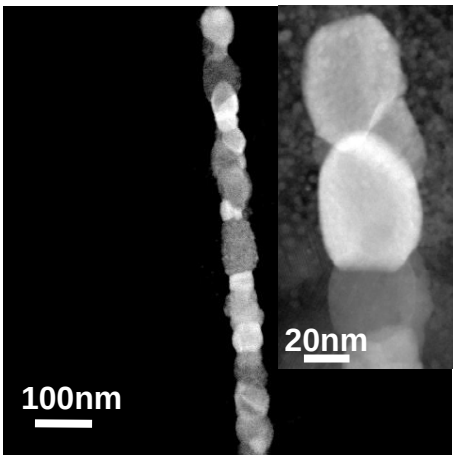

Figure 5.10: Scanning transmission electron microscopy image of ZnO 1D nanostructure fabricated using soft-eBL and annealed at 900 ^{o}C for 5 min in air

From the measurement of line-dimensions before and after annealing it was noticed that the line-width decreases by about 30% where as line height decreases by about 50%. This corresponds to roughly 65% volume shrinkage. While such large volume shrinkages are not uncommon for structures fabricated using solution precursors [105, 227], it is remarkable that these structures accommodate such large volume changes and yet retain continuity between neighboring grains up to several microns along each line as evident in figure 5.11.

The large volume shrinkage observed during annealing of these structures can have a significant effect on their over crystallization rate. Typically strain energy associated with volume shrinkage during crystallization increases the activation barrier for nucleation because transforming system has to overcome that much more energy.

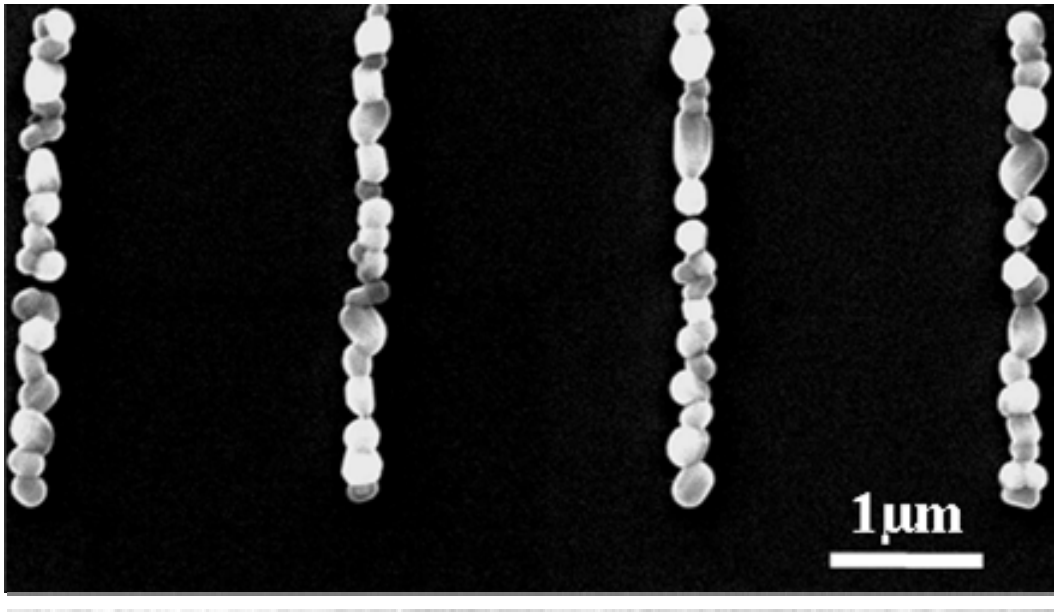

Figure 5.11: Beaded structures of ZnO soft-eBL patterns formed after annealing at 900 ^{o}C in air for 5 min.

Prior to annealing, patterns are in amorphous gel state containing large amounts of organic components. During annealing, volatile components are removed and gel transforms from an amorphous state to a crystalline state. In a simplified case, it can be shown [228] that volume shrinkage, ε, during solid state phase transformation creates an elastic strain energy:

$$\Delta g_{el} = \left[\frac{2\mu(1+\nu)}{9(1-\nu)}\right]\varepsilon^2 \qquad (5.4)$$

where μ is shear modulus and ν is poisson ratio.

Inserting an approximate value [229] of 50 GPa for μ and 0.25 for ν, results in roughly 63 kJ/mol of Δg_{el} for 65% volume shrinkage (density of ZnO is taken as 5.7 g/cm^3). This value is comparable to the typical activation energies (220 kJ/mol) reported for grain growth in bulk ZnO [230]. It can therefore be argued that free surfaces may have significant impact on crystallization rate because the elastic stresses can be readily dissipated at these surfaces [231, 232]. As the line-width decreases, free surface area to volume ratio increases and this may result in a higher nucleation density (number of nuclei per unit volume). It can be argued that the nucleation density in 1D case is higher than that in 2D case because of the higher surface area to volume ratio in the former case. The higher nucleation density and reduced grain growth rate due to truncation at surfaces as well as upon impingement with neighboring grains would give smaller grain size in lines compared to the thin film. This can qualitatively explain the results shown in figure 5.8.

5.7. SUMMARY

The following are the main conclusions from this chapter:

1. Pd doping in tin oxide decreases the grain size. 3% Pd doping can reduce the overall grain size by as much as 60% in tin oxide films annealed at 700 ^{o}C for 1 h in air

2. The effect of dimensional constraint in reducing the overall crystallization rates of sol-gel films and nanostructures is demonstrated in two different material systems, namely ZnO and SnO_2. Reducing the line width decreases the grain size and under appropriate annealing conditions, the grain size will equal the line-width. The reduced crystallization kinetics and the associated smaller grain sizes in constrained systems have some useful practical implications, especially for sensors. The conventional gas sensors are operated at high temperatures (> 300 ^{o}C) and their performance degrades with time. This degradation is referred to as drift which is most commonly associated with changes in microstructure of the sensor element due to elevated temperature operation. The reduced crystallization kinetics in the polycrystalline nanostructures could mean that they might be more

stable at high temperatures as demonstrated by the gas sensing results in the next chapter.

3. The effects of Pd doping and reduced dimensionality are not additive. The dimensionality effect appears to dominate in tin oxide lines with widths less than 200 nm.

4. In addition to the reduced crystallization rates demonstrated in constrained systems, this chapter also reported means to fabricate “beaded-structures” or single grain wide lines. Since one can control the initial line-width while designing the pattern, it is possible to control the grain size of the pattern with an appropriate annealing treatment. Moreover, beaded-structures will be ideal samples for unambiguous evaluation of the role of grain boundaries on transport and related properties in functional device structures because of the well defined percolation length of the electrons in these structures. Furthermore, the grain boundaries are perpendicular to the length of the lines in beaded structures. Such a configuration could be stable against grain growth and provide superior reliability in their performance for high temperature applications as observed in bamboo structures of other device materials [233, 234].

CHAPTER 6

MINIATURIZED GAS SENSING DEVICES CONTAINING SOFT-EBL OXIDE NANOSTRUCTURES

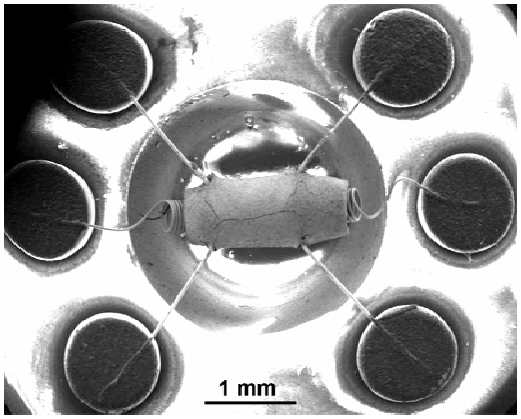

Commercial Hydrogen Sensor (Figaro TGS 821)

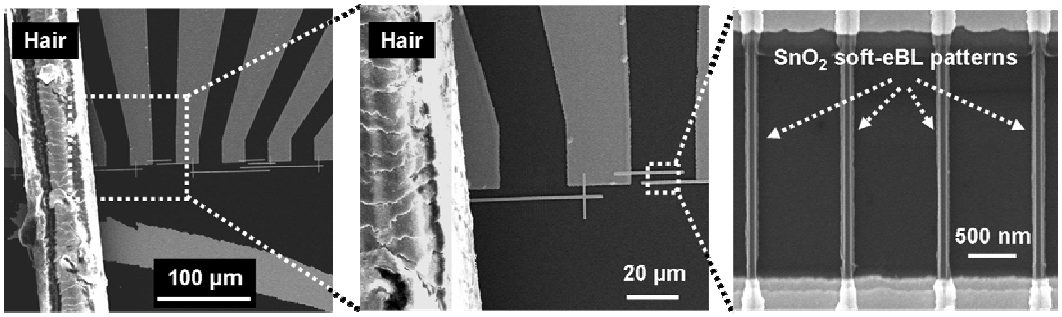

Sensor device with soft-eBL nanostructures

This chapter describes an in-house built gas sensing set-up and the gas sensing performance of soft-eBL oxide nanostructures. The motivation is to provide an application perspective of soft-eBL patterned nanostructures.

6.1 GAS SENSORS

The United States gas sensors market is about US $500 millions in 2004 and it is expected to grow at about 8.5% in 2008[235]. If this is not motivating enough consider that everyday we take in about 20-30 Kg of air compared to about 1 Kg of solid food and 3 Kg of liquid food. We should therefore expect our air to have same quality standard as our food and drink. There is therefore tremendous incentive for developing gas sensors that are faster, cheaper, more sensitive and reliable. The word "sensor" perhaps induces the same perception in scientists and engineers across every discipline though none of them might agree on a single definition. Sensor can be defined as an active structure whose measurable property changes upon interaction with a molecule in the external ambient. Within the context of this chapter, the scope is further restricted to sensors interacting with rarefied or gaseous external ambient and therefore to gas sensors. Depending on the measurable property, gas sensors can be broadly classified into five categories[236] namely electrochemical, infrared, catalytic (pellisters), mass sensitive and conductometric (polymers and metal oxides) sensors.

Electrochemical sensors measure either the change in nerst-potential (potentiometric) on an electrode or the diffusion current in electrolyte (amperometric) upon interaction with gas. The catalytic sensors detect combustible gases that interact with the catalyst particles. The catalysts typically are highly dispersed noble metals such as Pt, Pd, Rh, on an alumina

substrate. The temperature change upon combustion of the gas is detected as a change in resistance of an embedded Pt coil. While the catalytic sensors consume large amounts of power and are restricted to combustible gases, electrochemical sensors are expensive. Mass sensitive devices measure the change in a physical property that is associated with mass change due to gas adsorption. For example, surface acoustic wave devices measure the change in frequency of acoustic wave launched on a piezoelectric substrate surface upon gas adsorption while cantilever based sensors detect change in amount of cantilever bending upon analyte adsorption[237, 238]. The optical sensors depend on the change in optical properties of the sensor element upon gas adsorption. The conductometric sensors measure the change in conductivity upon adsorption of the gas molecules. These are based on either metal oxide semiconductors or conducting polymers. These five broad classes of sensors are shown in table 6.1 with a brief explanation and appropriate references.

Metal oxide semiconductor based conductometric sensors have a rich history of applications since their discovery in 1962[16]. A recent comprehensive review by Eranna et.al[239] details the multitude of gases that can be detected using these materials. In the current thesis work, conductometric sensors based on metal oxide semiconductors are used for detecting the reducing gases such as hydrogen (H_2) and carbon monoxide (CO).

Table 6.1: Different classes gas sensors currently available in market. The table is adapted from [240] and other review articles[17, 239, 241, 242]

Sensor class	Sensor material	Mechanism
Electrochemical[243]	Potentiometric[244]	Nerst-potential of an electrode against a reference is measured
	Amperometric[245]	Diffusion limited current across an electrolyte
Mass sensitive	Surface Acoustic Wave devices (SAW)[246-248]	Resonant frequency or phase of acoustic wave change
	Quartz microbalance[249-252]	
	Cantilever sensors[237, 238]	Cantilevers bend due to adsorption of gas molecules
Catalytic	Dispersed catalysts on a substrate[253, 254]	Temperature change due to combustion of molecules
Infrared [255]	Fluorescence[256]	Change in fluorescence
	Surface Plasmon Resonance[257, 258]	Change in surface plasmon resonance from interaction of gas molecules with evanescent electromagnetic wave
Conductometric	Metal oxide semiconductors[239]	Change in the electrical conductivity
	Polymers[259-261]	

6.2 MECHANISM OF GAS SENSITIVITY IN METAL OXIDE SEMICONDUCTORS

Among the metal oxides, tin oxide is the most widely used material and probably the most studied material[262] for gas sensing applications. The stochiometric SnO_2 is a wide bandgap (3.6 eV) semiconductor that is insulating at room temperature. However, tin oxide surface is almost always oxygen deficient (also see XPS results in previous chapter) and therefore shows n-type semiconducting behavior. When tin oxide is exposed to air, oxygen adsorbs on the surface by capturing the electrons from the oxide. Depending on the temperature[263, 264] oxygen on tin oxide surface is found to be either in O_2^-, O^- or O^{2-} ionic form. The chemisorbed oxygen localizes the electrons creating an electron depletion layer just below the surface. Width of this depletion can range between 10-100 nm depending on the temperature and electron concentration.

A reducing analyte molecule such as CO reacts with the chemisorbed oxygen to form CO_2 and release electrons back to the oxide. Macroscopically this results in conductivity increase. This is schematically shown in figure 6.1 and as equations 6.1a and 6.1b below.

$$\frac{1}{2}O_{2,g} + \alpha e^- + S \leftrightarrow O_S^{-\alpha} \qquad (6.1a)$$

$$CO_g + O_S^{-\alpha} \rightarrow CO_{2,g} + \alpha e^- + S \qquad (6.1b)$$

In addition to the above phenomenological model one has to consider the effects of materials structural information such as porosity, grain size and crystallographic texture on sensor performance. Furthermore, these oxide materials are often doped with transition metals (e.g. Pt, Sb, Pd, Rh etc.) to enhance their sensitivity to particular gases. However, doping has a secondary influence of altering materials structure (grain size, porosity). This interrelation between various structure-altering phenomena together with the poor understanding of their effect on overall sensor performance are the main reasons for the lack of predictive sensor development work.

6.3 MINIATURISATION OF GAS SENSORS

All the processes shown in figure 6.1 are thermally activated phenomena meaning that their reaction kinetics are temperature dependent. In order to attain appreciable rates, the sensors are operated at high temperatures. In commercial sensors, this is usually accomplished by either screen printing heating wires on the backside of the substrate or by putting the substrate inside a heating coil. In either case it leads to large power consumption in the range of few hundreds of mW to Watts. Miniaturizing sensors will reduce power requirements because of their low thermal mass[186]. Miniaturization will also allow integration of multiple sensing elements to improve the overall device selectivity. This is a concept called “electronic-nose” that mimics the biological olfactory system. An array of individual sensors (analogous to taste buds in mammalian nose) with only partial individual

selectivity produces an unique signature when exposed to the analyte gas. By processing the data using sophisticated statistical mathematics or artificial neural network algorithms, one can significantly enhance the selectivity. This concept is gaining tremendous attention and is considered to be the next major development in the field of sensor research and developmet[265-267]. Miniaturization of sensors is necessary to realize “electronic-nose” and 1D oxide nanostructures either single crystalline or polycrystalline will almost surely play an important role towards this goal.

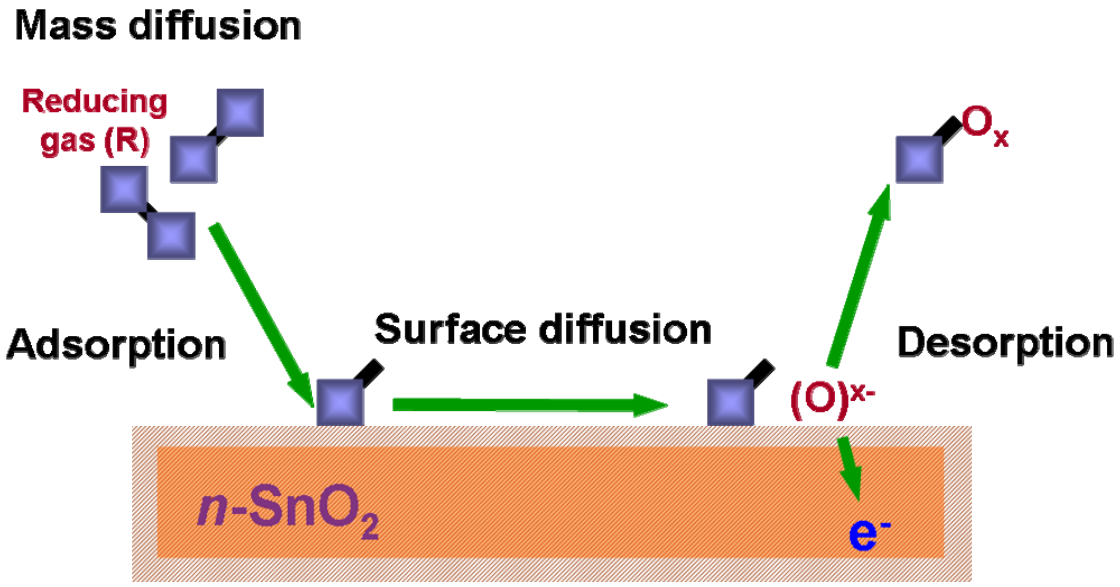

Figure 6.1: Phenomenological model of reducing gas interaction with n-type tin oxide.

6.4 SOFT-EBL OXIDE NANOPATTERNS AS GAS SENSORS

1D nanostructures such as nanorods and nanowires have attracted a lot of attention from gas sensor research community because they are single crystalline and possess large fraction of surface with respect to volume. Gas sensing performance of oxide 1D nanostructures have been reported by several groups over the last few years. Comini et.al[24] have reported the CO and NO_2 sensing properties of SnO_2 nanobelts, Law.et.al[23] have demonstrated the UV assisted NO_2 sensing of SnO_2 and Li et.al[25] have reported sensing properties of In_2O_3 nanowires. While the focus of all the gas sensing studies on 1D single crystalline nanostructures till now has been just to demonstrate their sensing capability, the reports on benchmarking their performance against other structural forms of oxides such as thin films or even polycrystalline 1D nanostructures are scarce. This is partly because the techniques used for making 1D single crystalline nanostructures are not readily suitable for making thin films. Since synthesis routes affect structure and structure in turn affects their gas sensing properties, it is important to realize that sensing performance comparison is only appropriate between structures made in same manner. In this chapter, soft-eBL oxide nanopatterns of different dimensions were fabricated and their gas sensing performances are evaluated. The gas sensing performances of thin films made from same sols and annealed with the same heat-treatment protocol are also measured.

6.5 OBJECTIVES AND OUTLINE OF THE CHAPTER

The vast literature on gas sensors shows that their development is predominantly empirical and often times performed in a "trial-and-error" method. This is because of the vast number of process parameters, which are almost impossible to control, that can affect their performance. The process variables refer to sample preparation conditions and they play a huge role on sensing performance because process variables can have a tremendous effect on materials structure. In addition to the process variables, even the conditions under which the gas sensing measurements are performed can have a huge effect on their sensing performance. Parameters such as electrode spacing[268-270], electrode design[269, 271, 272] (interdigitated vs regular opposing electrodes) and flow-rate of the gases can have an effect on their performance. For example, plot in figure 6.2 shows the hydrogen sensing performance of tin oxide lines at 200 ^{o}C when exposed to 2500 ppm of hydrogen diluted in nitrogen at two different flow rates. The individual flow rates of hydrogen, nitrogen (carrier gas) were adjusted so as to maintain the same concentration but different overall flow rates. The purge gas is synthetic air and its flow rate is set at either 100 sccm or 1000 sccm in each case to match the flow rate of analyte gas. This plot clearly shows that sensitivity (fractional change in resistance) is dependent on overall flow rate even though all the other parameters are identical. The plot shows that sensitivity increases by an order of magnitude, from about 3 to 30, upon increasing the flow from 100 sccm to 1000 sccm. The higher sensitivity at

larger flow rates is due to smaller stationary layer formed on the surface and is consistent with several reports in literature.

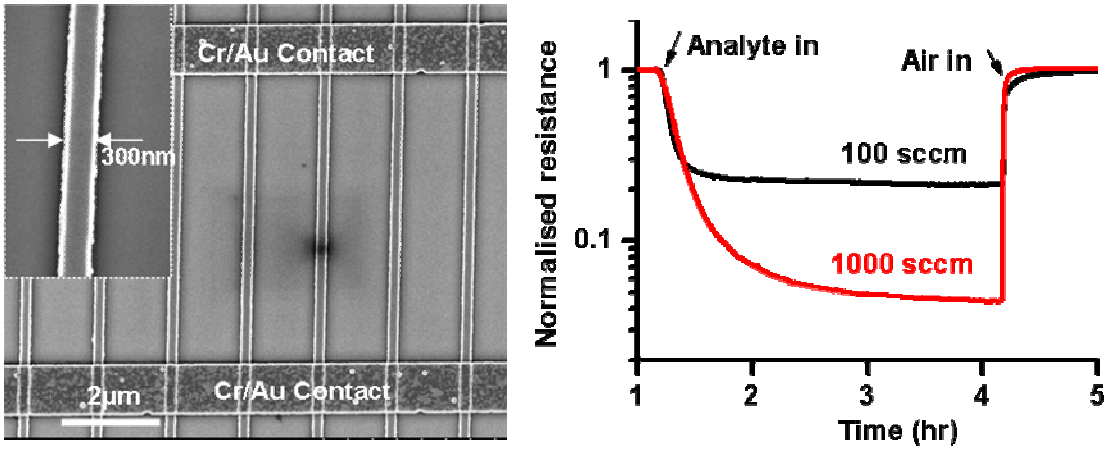

Figure 6.2: SEM image of undoped tin oxide soft-eBL lines and the plot showing the effect of flow rate on hydrogen sensitivity of these lines. Analyte gas is 2500 ppm of hydrogen diluted in nitrogen. Purge gas is synthetic air and the measurements were performed at 200 ^{o}C. The resistance was monitored by applying 5 V bias (or 10^{6} V/m along each line)

The large parametric space means that sensor optimization is not only tedious but also there can be variation in performance between samples from the same batch. Even more importantly, this makes the comparison between the gas sensing performances reported in different articles in literature, even for the same material prepared in similar conditions, almost impossible. This is also accentuated by the fact that there are no standard set of guidelines for gas sensor testing protocols like in measuring the mechanical properties by ASTM standards. For all these reasons, it is imperative that one be careful while comparing the gas sensing measurements with literature values for benchmarking purposes. In this chapter, when comparing our gas sensing results with literature data every effort is made to highlight the differences in measurement parameters between the two.

The main objective of this chapter is to demonstrate the application side of soft-eBL by fabricating gas sensing devices and characterizing their sensing performance attributes. It is not our goal at this stage to optimize the sensor for best performance though it could be part of our group's future work. Towards this goal, an in-house gas sensing set-up was built, a gas sensing device fabrication protocol was developed and hydrogen sensing attributes of tin oxide soft-eBL nanostructures, as an example, were characterized. The next section contains thorough details of sample fabrication, gas sensing set-up and other pertinent experimental parameters. The subsequent sections report some hydrogen sensing measurements from thin films and soft-eBL nanostructures of tin oxide and tin oxide doped with Pd.

6.6 EXPERIMENTAL

6.6.1 Sample Preparation:

Oxidized silicon substrates with 500 nm thick thermal oxide are used throughout this work for gas sensing measurements. The main stages of making the gas sensing device are as follows:

a. Photolithography of electrodes: After thorough cleaning of substrates (10 min each in acetone, water, IPA[♣]) they were spin coated with AZ1518 positive photoresist. The substrates were then exposed to UV light through a mask (chrome coated sodalime glass). Substrates were then developed in AZ400K solution that is diluted with water in 1:3 (vol/vol) ratio. The developed substrates were left to dry in air and were then cleaned with oxygen plasma for about 1 to 2 min. (The oxygen cleaning step was necessary to remove any undeveloped photoresist. This also ensured good bonding of aluminum wires in the final wire bonding step). The substrates were then loaded into an electron beam evaporator system to deposit 10 nm Ti and 5 nm Au films sequentially without breaking vacuum between the two metal deposition steps. This deposition step is immediately followed with a deposition of 100 nm Pt layer in a sputter coater. (This two step process was necessary because we did not have an electron beam evaporator for Pt deposition and a sputter coater

[♣] IPA: Iso Propyl Alcohol

capable of depositing multiple materials without breaking vacuum. The thin Au film protected Ti layer from oxidation while transporting the samples to sputter coater from evaporator). Substrates were then soaked in acetone solution to dissolve the photoresist and lift-off metal outside the pattern area. Preliminary experiments showed that 10 nm Ti, 5 nm Au and 100 nm Pt tri-layer structure is stable against agglomeration up to temperatures as high as 700 ^{o}C for 1 hr in air.

b. Soft-eBL of oxide nanostructures: The photolithographically patterned substrates were spin coated with electron beam resists (MAA-MMA copolymer and PMMA) at 3000 rpm to give nominal total resist thickness of about 300 nm. The substrates were then patterned using electron beam lithography. Prior to exposing to electron beam, substrates were aligned using the markers at the four corners of the batch of 32 electrodes (figure 6.3 below). After writing with electron beam, substrates were developed in MIBK solution diluted with IPA in 1:3 (vol:vol) ratio and oxygen plasma cleaned for about 30 to 60 sec. Subsequently, substrates were spin coated with oxide sols, heated on hotplate at 150 ^{o}C for 5 min and soaked in acetone to dissolve ebeam resist and lift-off material. All the gas sensing measurements were done on tin oxide and Pd doped tin oxide samples. Tin oxide and Pd doped Tin oxide sols were made from their acetate precursors in the manner described in earlier chapters.

The samples were then annealed in air typically at 700 ^{o}C for 1 hr to crystallize the soft-eBL patterned oxide structures. It is important to note that during this annealing process, soft-eBL made oxide structures are not in contact with photolithographically made Pt electrodes. This is necessary to avoid any possible diffusion of Pt into oxide structures at high temperatures. Doping with Pt can significantly modify the gas sensing properties of oxide nanostructures.

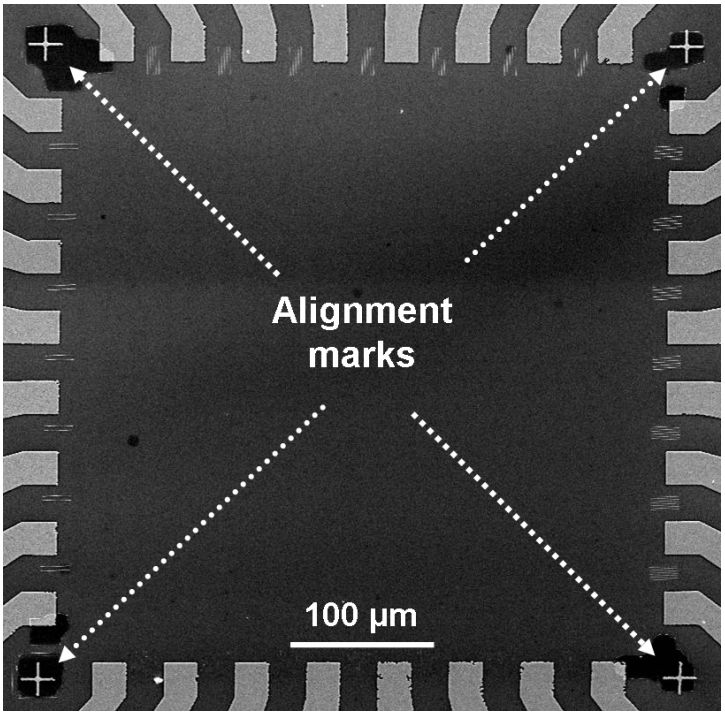

Figure 6.3: "Cross-Marks" at four corners used for alignment during soft-eBL

c. eBL of contact electrodes: Soft-eBL patterned and annealed samples were then spin coated with ebeam resists and patterned a second time. Again after an initial alignment step, lines connecting the soft-eBL patterns and Pt electrodes were written using ebeam. Subsequently, samples were developed, oxygen plasma cleaned and loaded into ebeam evaporator and sputter coater to deposit 10 nm Ti, 5 nm Au and 100 nm Pt. After dissolving ebeam resist in acetone, samples were cleaned in IPA and loaded onto a ceramic chip carrier.

The three main steps discussed above are shown schematically in figure 6.4. The patterned samples were loaded onto a 40 pin ceramic chip carrier (Global Chip Materials LLC., Rancho Cordova, CA, USA) after placing a few dots of TEM epoxy glue on the backside of the sample with a toothpick. Heating this assembly at 150 ^{o}C for 1 hr in air is not only sufficient to hold the sample in place for subsequent measurements but also could also be removed with minimal damage if necessary. After gluing the sample to chip carrier, electrodes on sample and leads on chip carrier are connected with Al[♣] wire using a wire bonder (West Bond Inc., Anaheim, CA). Aluminum wire was found to be better than Au wire because one could use lower ultrasonic power while wire bonding with Al. This often created less damage on the sample such as puncturing through the oxide layer or peeling-off of electrodes as happened when wire bonding with large ultrasonic power necessary with Au wires. Appropriate leads of the chip carrier are then connected to Keithley 4200 SCS data

[♣] The Al wire is in fact an alloy of Al and 1% Si

acquisition system through kapton coated copper wires and copper clips. Even though the insulating Kapton coating was stable up to 150 ^{o}C, these wires were dressed with alumina beads to avoid shorting and ensure easy handling of the thin wires. Copper clips were covered with teflon tape to prevent any shorting upon accidental contact between different clips.

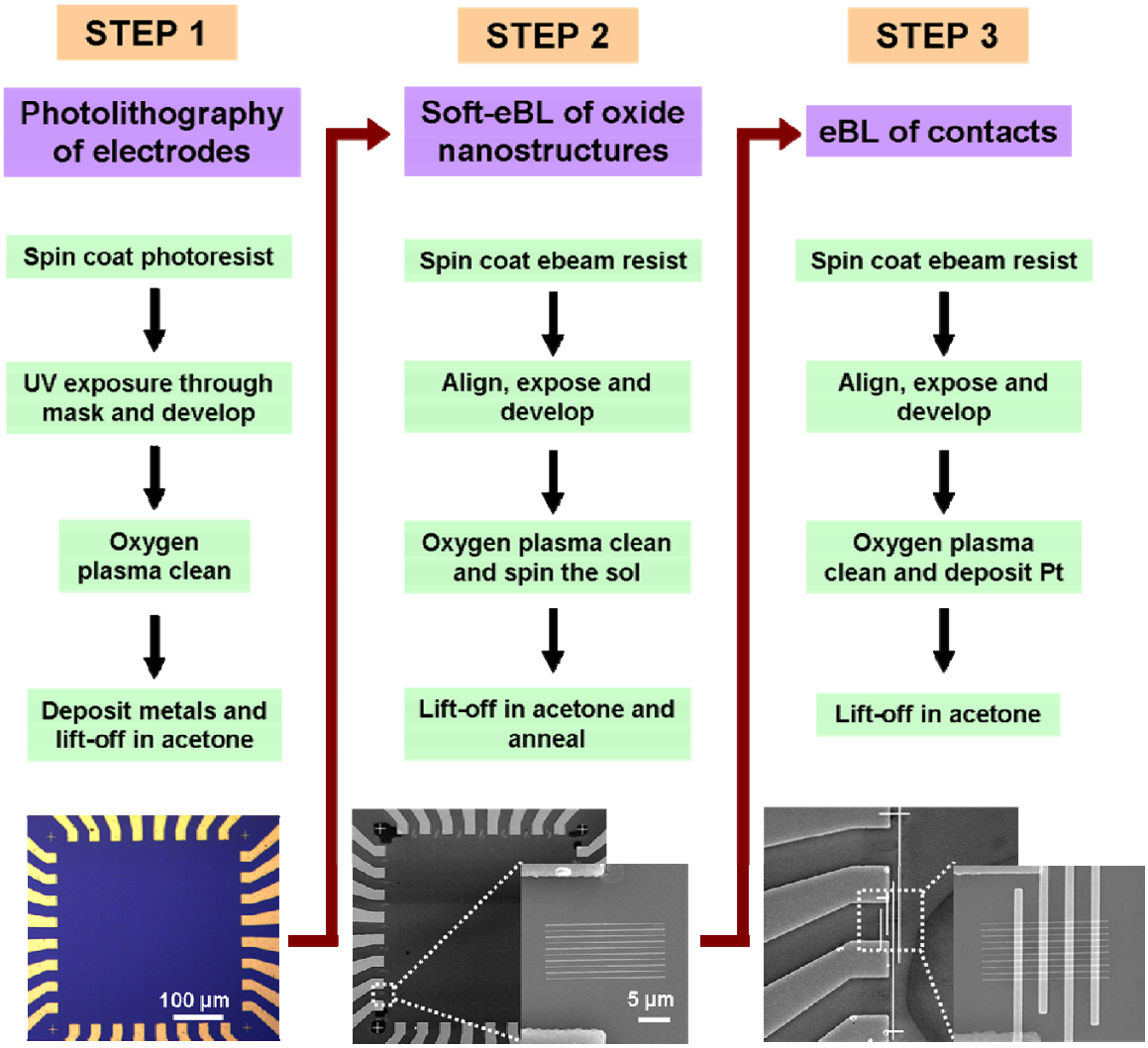

Figure 6.4: The three step process of making gas sensors using soft-eBL nanostructures. Note that during anneal process in step 2, soft-eBL patterns are not in contact with photolithographically patterned Pt electrodes.

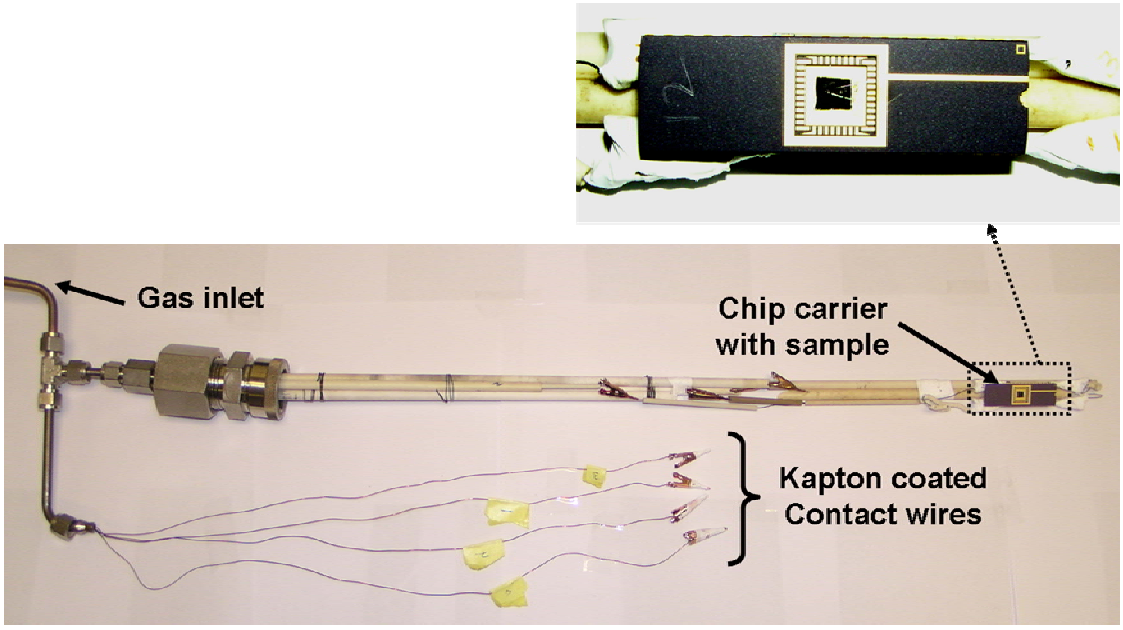

Figure 6.5: Assembly of chip carrier with sample and contacts before loading into a quartz tube

6.6.2 Gas sensing measurement set up:

All the gas sensing measurements were performed using a system built in-house. It consisted of three main modules: Gas delivery system, sample holding unit and data acquisition module.

a. Gas delivery module: This includes gas cylinders, mass flow meters with multichannel gas controller, multiplexer/multifunction switch and custom designed software. The gas cylinders of both analyte and carrier gases with certified purity levels were directly purchased (from Airgas specialty gases, Chicago, USA) and sequential dilution was performed to attain the required analyte concentrations. The gases from cylinders were fed into mass flow controllers (MKS Instruments) interfaced with model 647B multi gas controller (MKS Instruments) and a personal computer running customized software based on LabVIEW (version 7.1, National Instruments). In addition to these basic units, the gas delivery module also consisted of an optional multiplexer unit. This is a 40 channel switch (34980A/34921A, Agilent Technologies) that can read 40 different resistances with 100 channel/sec scanning rate. The multiplexer unit will be useful for future work on electronic nose that involves simultaneous measurements from multiple sensors.

The set-up has a total of 4 mass flow meters. Two of them had a range of 0 to 100 sccm[♣], one with 0 to 1000 sccm and the last with 0 to 5000 sccm range. All of them were certified by the manufacturer to be accurate within 0.1%. The lower range mass flow meters were connected to analyte gases whereas higher range mass flow meters were connected to nitrogen (diluent and carrier gas) and dry air (purge gas).

b. Sample holding unit: The sample is placed in a quartz tube that is part of a tube furnace unit. Though the furnace can go up to temperatures as high as 1200 ^{o}C, most of the sensing measurements were conducted at temperatures less than 250 ^{o}C. The quartz tube has two outlets (gas inlet and outlet) and one of them is also an outlet for the electrical wires that connected sample in the tube with the measurement computer outside. Any unwanted gas leaks at the outlets were sealed with a silicone elastomer. A photograph of the sample holding unit is shown in figure 6.5.

c. Data acquisition module: All resistance measurements during sensing experiments were obtained using a Keithley Model 4200-SCS unit. The high input impedance (> 10^{16} Ω) and accurate low current sourcing of Keithley 4200-SCS is capable of measuring high resistance values (> 10^{9} Ω). Resistances of many of the samples in this study were within that range.

♣ sccm = standard cubic centimeter per minute

A schematic of the entire gas sensing set-up including the three modules is shown in figure 6.6.

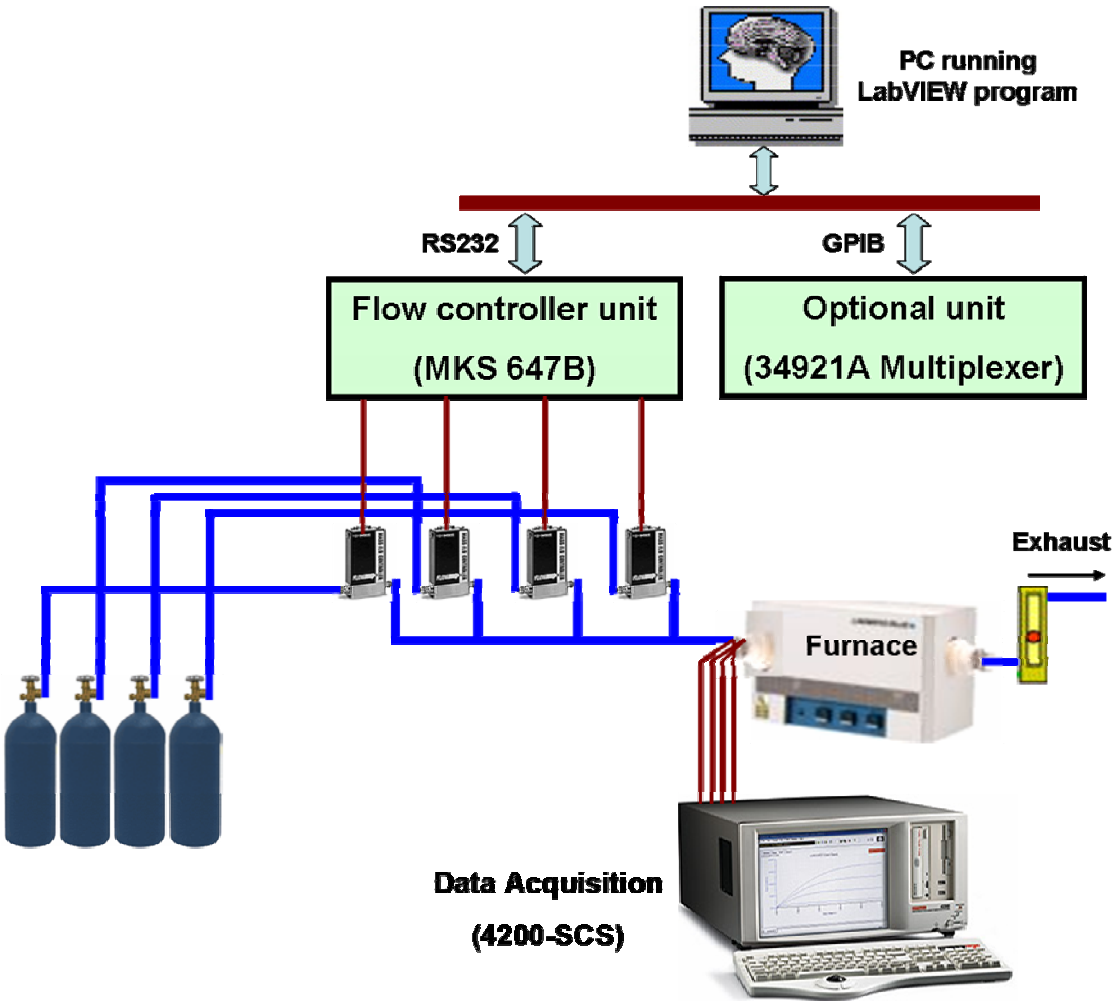

Figure 6.6: Schematic of the gas sensing measurement set-up used in this work

6.6.3 Gas sensing measurements:

All the gas sensing measurements were done at 1000 sccm flow rate. Prior to actual measurements, furnace was heated to the required temperature and sample was left at this temperature with the purge gas (air) flowing while continuously monitoring the sample resistance. Once the resistance is stabilized (usually 1 to 2 hr depending on temperature and sample history), the exposure and purge cycles are initiated while continuously monitoring the sample resistance. The total volume of the test chamber (including quartz tube and piping) is about 400 ml. Therefore at 1000 sccm, the test chamber will be completely purged in less than half a minute. This is much less than the response and recovery times observed for almost all of the samples in this study.

6.7 GAS SENSING PROPERTIES OF TIN OXIDE THIN FILMS

This section will cover the hydrogen sensing properties of undoped and Pd doped tin oxide thin films. The main goals of these experiments are to validate the set-up and generate data to benchmark the performance of soft-eBL nanostructures.

6.7.1 Experimental: Films were prepared by spin coating doped and undoped tin oxide sols. Sols were prepared using their acetate precursors and details of sol preparation are discussed in chapter 4. Thermally oxidized Si (100) substrates with 500 nm thick oxide are spin coated with 0.1M sols five times at 1000 rpm. After annealing at 700 ^{o}C for 1 hr in air, film thickness was found to be about 80 nm as measured using x-ray reflectivity technique. The substrates with annealed thin films were then patterned with electrodes using photolithography. Electrodes consisted of electron beam evaporated 10 nm and 100 nm thick Ti and Au layers respectively. Figure 6.7 shows the electrode design used for these measurements. (This is different from one used for soft-eBL nanostructures). Samples were then mounted onto ceramic chip carriers, wire bonded with Au wires and loaded into the gas sensing set-up shown in figures 6.5 and 6.6. All the thin film gas sensing measurements were done in two-probe configuration with electrode spacing of about 70 μm and each electrode width of about 5 μm.

Analyte gas was hydrogen diluted with nitrogen (UHP grade) while purge gas was synthetic air. Prior to measurements, samples were stabilized at a particular temperature for about an hour while continuously purging with air before each measurement. Current-Voltage (I-V) plots were taken before gas sensing measurements.

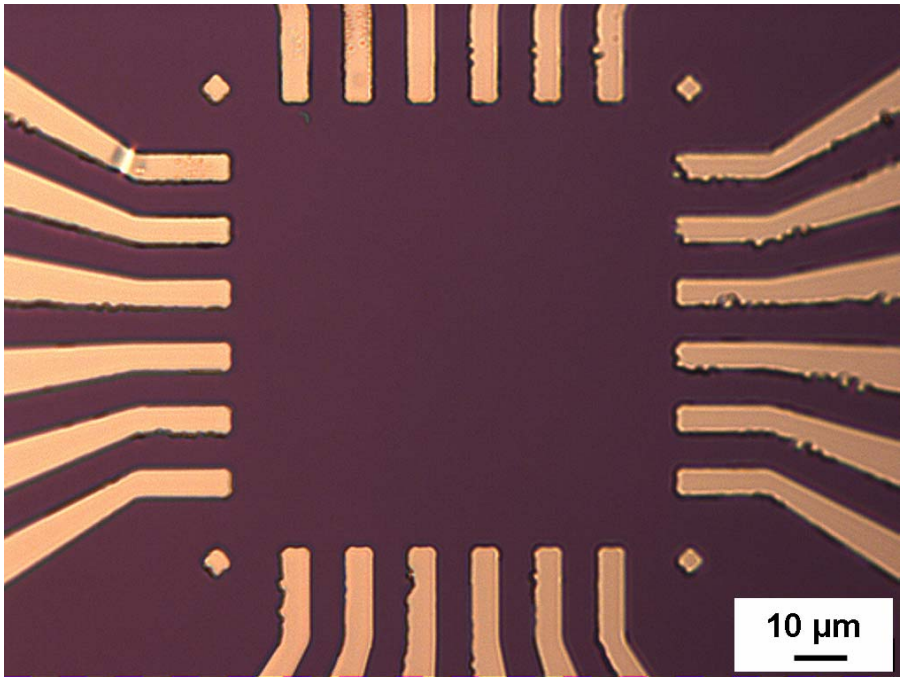

Figure 6.7: Electrode design used for thin film gas sensing measurements. Measurements were performed in two-probe configuration by applying potential across two electrodes, one from each of the opposite batches.

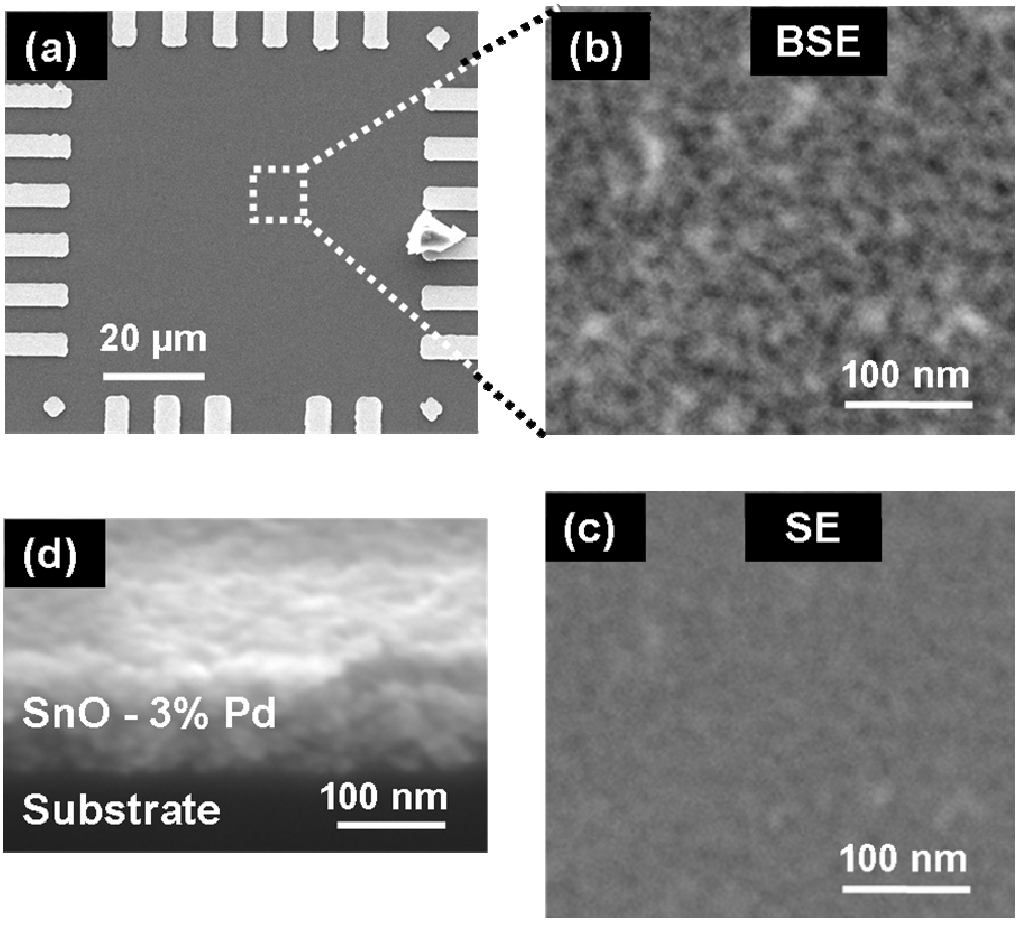

Figure 6.8: (a) SEM image of electrodes on thin film, (b) magnified BSE image (c) corresponding SE image of the thin film and (d) cross-sectional image of the film. Pores are clearly visible in BSE image in (b).

Prior to gas sensing measurements, films were characterized using scanning electron microscope. Figure 6.8 shows the plan-view and cross-sectional SEM images of tin oxide thin films doped with 3 at% Pd. Pores in thin film are clearly visible in back scattered electron (BSE) plan view image. The TEM and XRD results of these films reported in the previous chapter showed that grain size is about 8 nm.

6.7.2 Hydrogen sensing performance of undoped tin oxide films

The I-V plots of undoped tin oxide thin film at four different temperatures are shown in figure 6.9. In the entire sweep range of -5V to 5V, the I-V plots at all the temperatures are linear suggesting that contacts are ohmic. As expected for a semiconductor, resistance decreased with increasing temperature from about 340 kΩ at 75 ^{o}C to about 8 kΩ at 150 ^{o}C.

The response of undoped tin oxide film to 250 ppm of H_2 in N_2 is shown in figure 6.10. As expected for n-type semiconductor resistance decreases upon interaction with hydrogen (reducing gas). Molecular hydrogen dissociates on the tin oxide surface and reacts with oxygen ions. This reaction releases electrons back to tin oxide and therefore resistance decreases. Resistance is normalized with the resistance before exposure to hydrogen at each temperature. Sensitivity, response time and recovery time are the three most common measurables used to evaluate a sensor performance. For the work here, sensitivity is defined as the ratio of resistance in air (R_a, base resistance) to that in gas (R_g), response time as the

time it takes for the resistance to decrease by 90% and recovery time as the time it takes to recover 90% of the resistance before exposure. Based on these definitions, sensitivity of this sample to 250 ppm of H_2 in N_2 is measured to be about 55, 50 and 23 at 150 ^oC, 125 ^oC and 100 ^oC respectively. The response times are 7, 29, 80 mins at 150 ^oC, 125 ^oC and 100 ^oC respectively.

Upon purging with air, resistance increases very quickly initially but saturates eventually. At 100 ^oC, it does not recover back to 90% of its base resistance even after purging for 3 hr. This might translate into a baseline drift if the sample exposed to repeated exposure and purge cycles. These results show that undoped tin oxide film is sensitive to 250 ppm of hydrogen even at 100 ^oC. However, it is desirable to operate at temperatures >100 ^oC in order to realize larger sensitivity, shorter recovery and response times. Usually there is a temperature above which the sensor performance starts to degrade again and thus there is an optimum operating temperature. While the optimum temperature for undoped sample is not found in our experiments, the next section shows optimum temperature for Pd doped samples is < 150^oC.

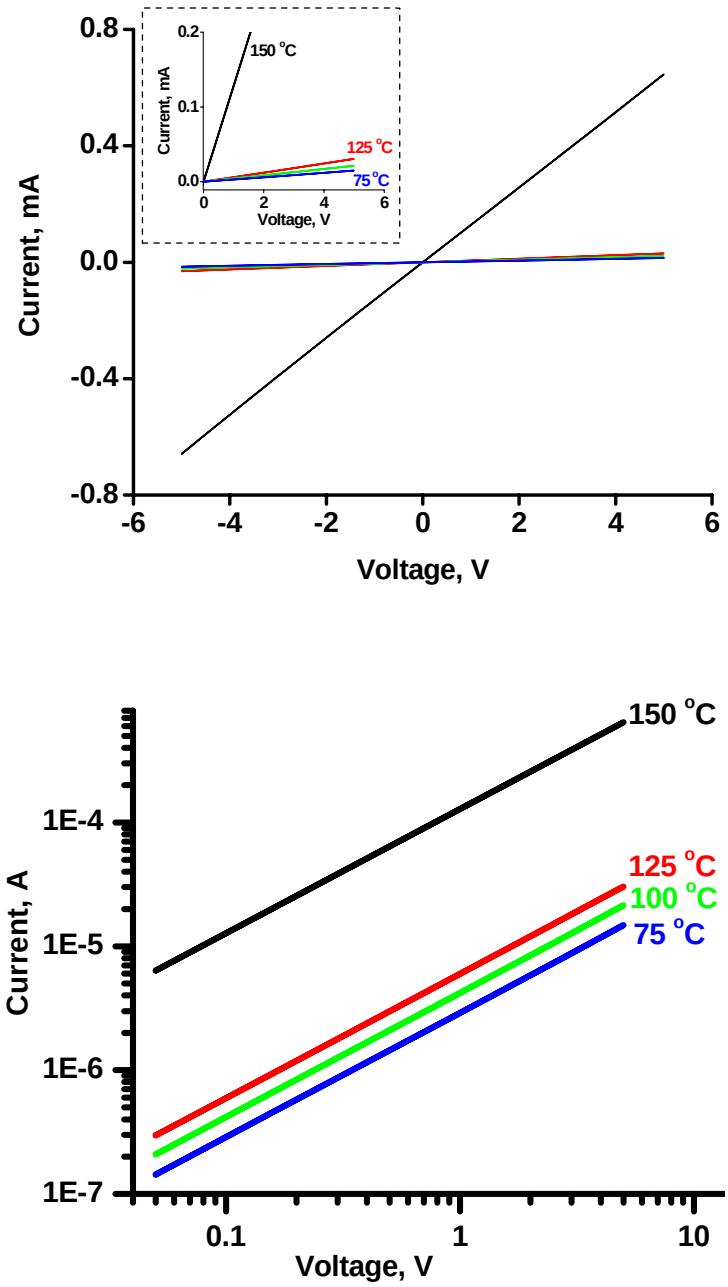

Figure 6.9: I-V plots of undoped tin oxide film at different temperatures. Bottom plot is the log-log plot of current and voltage (re-plotted from top plot). In this plot intercept is a direct measure of resistance.

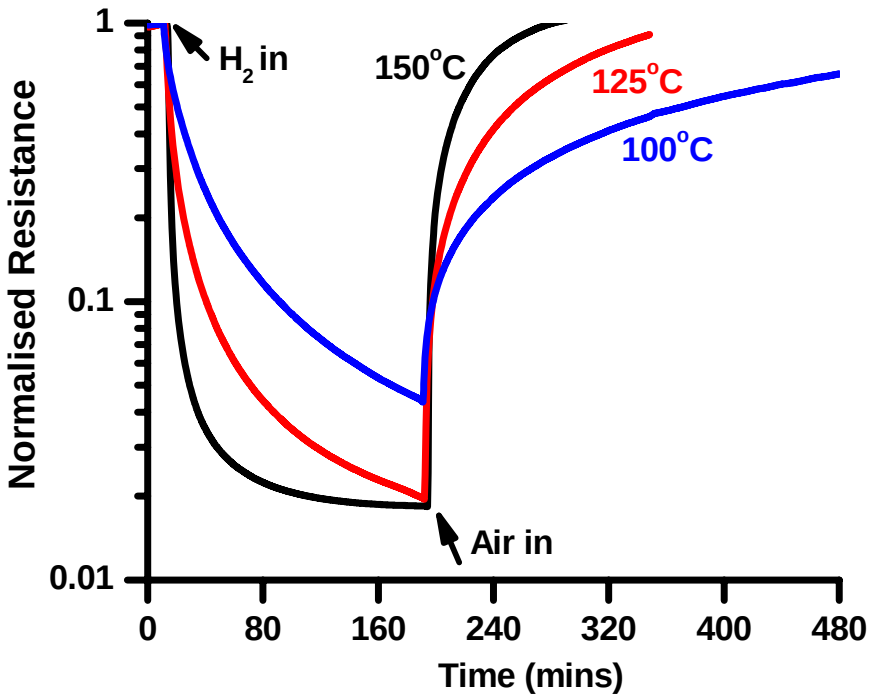

Figure 6.10: Response of undoped tin oxide films to 250 ppm of H_2 in N_2 at three different temperatures.

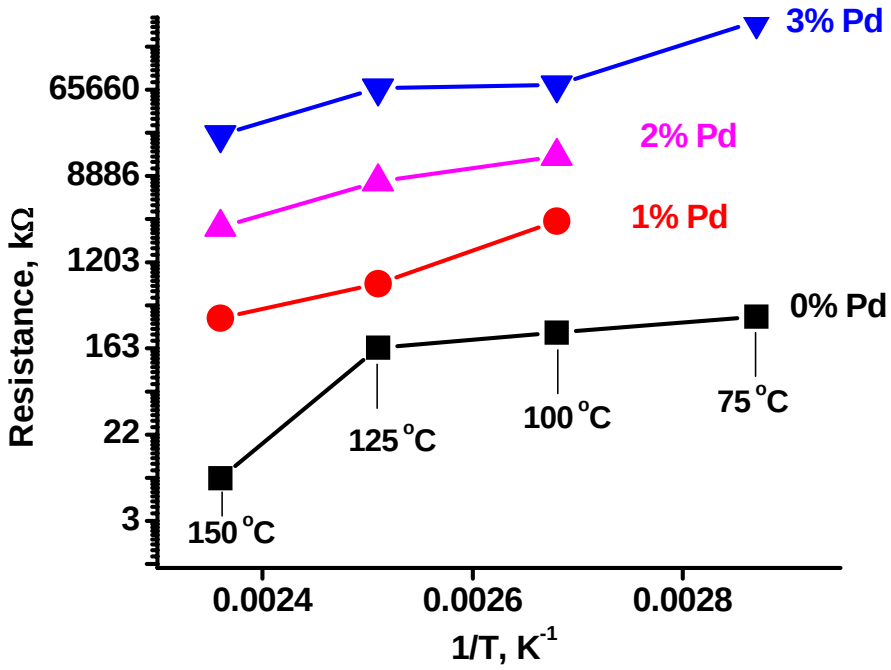

Figure 6.11a: Effect of Pd concentration on temperature dependent resistance of tin oxide thin films. Note that y-axis is in Ln (not Log) scale.

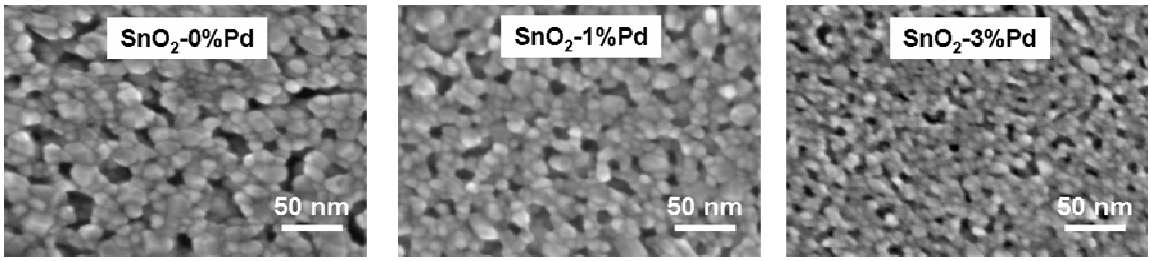

Figure 6.11b: SEM (SE) images of tin oxide thin films doped with different Pd concentration.

6.7.3 Pd doped tin oxide thin films

Tin oxide films with three different Pd concentrations (1%, 2% and 3%) were prepared. Compositions of these films were confirmed using XPS. I-V plots of all the doped samples at every temperature tested were also found to be linear, suggesting again that contacts were ohmic in case of doped samples too.

The temperature dependence of resistance in each case is shown in figure 6.11a. Again in each case the resistance decreases with increase in temperature. However, it is important to note in figure 6.11 that the resistance of thin film increases monotonically with Pd concentration at every temperature. Note that the electrode configuration and film thickness in each case is identical. The increase in resistance with Pd doping could be due to smaller grain size and higher porosity in doped samples. Based on XRD results in previous chapter, it was found that increasing Pd concentration monotonically decreased the grain size. Since grain boundaries and pores scatter electrons, smaller grains and higher porosity would result in higher resistance. The SEM images of doped and undoped thin films in figure 6.11b show that average grain and pore size decreases with increasing Pd concentration.

The response of Pd doped tin oxide films to 250 ppm of H_2 in N_2 are shown in figure 6.12. As expected the resistance decreases upon introduction of H_2 in every case. It is clear

that Pd has a significant effect on sensitivity and response times. For example, at 100 ^{o}C the undoped sample does not saturate even after exposing for 3 hr while 3% doped sample saturates in a little over 2 hr exposure. Furthermore the sensitivity of undoped film after 3 hr exposure is about 50 whereas 3% Pd doped sample shows a sensitivity of about 5000 for the same length of exposure. The effect of Pd concentration on sensitivity is shown in figure 6.13 and table 6.1. Note that in some samples, resistance did not saturate even after very long exposure times. For these samples, sensitivity is calculated by dividing the base resistance (R_a) in each case with the resistance of the film after 3 hr of exposure to analyte gas (250 ppm of H_2 in N_2).

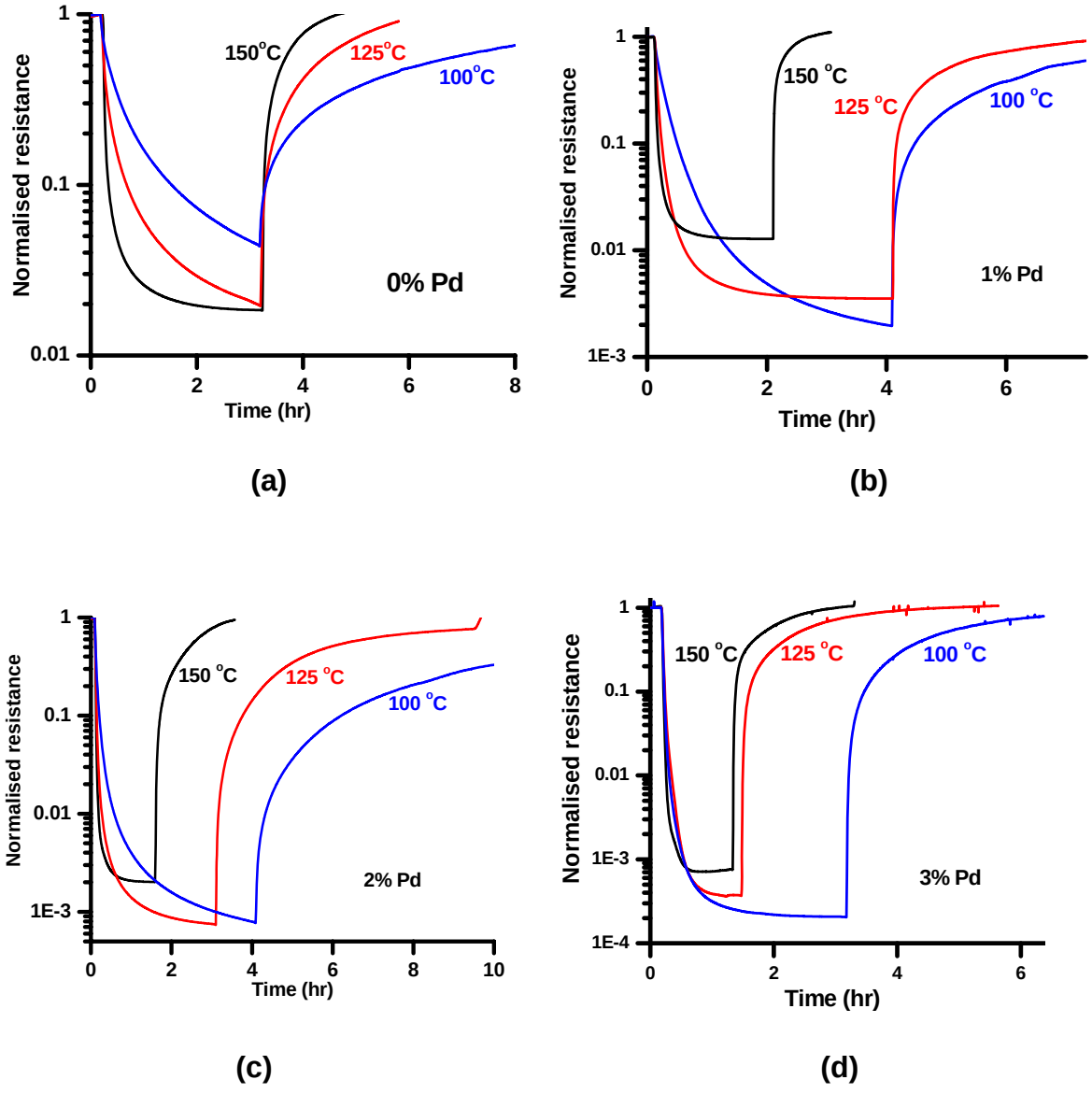

Figure 6.12: Response of tin oxide films doped with (a) 0%, (b) 1%, (c) 2% and (d) 3% Pd to 250 ppm of H_2 in N_2

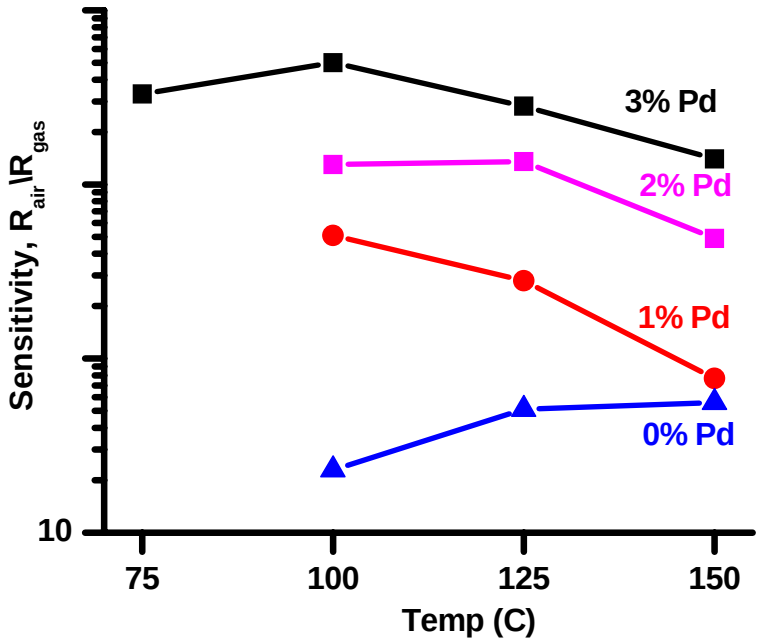

Figure 6.13: Sensitivity of tin oxide film doped with various Pd concentrations to 250 ppm of H_2 in N_2 at different temperatures. R_{air} is resistance in air before exposure to hydrogen and R_{gas} is the resistance of the film after 3 hr of exposure to 250 ppm H_2 in N_2

Table 6.1: Sensitivities measured in tin oxide films doped with different Pd concentrations. These values are used for the plot shown above.

% Pd Concentration → **Temperature ↓**	**0**	**1**	**2**	**3**
150 °C	56	77	490	1400
125°C	51	280	1350	2809
100 °C	23	510	1300	5000

The plot in figure 6.13 clearly shows that at every temperature tested, films with higher Pd concentration consistently gave higher sensitivities. Furthermore, the plot shows that the optimum temperature, in terms of sensitivity, for 3% Pd doped film is around 100 ^{o}C while the optimum temperature for undoped sample appears to be above 150 ^{o}C. While sensitivity is an important performance attribute, the other equally important variable is the response time. In a qualitative sense, this is the measure of how long it would take the sensor to respond upon exposure to analyte gas. Based on the definition given earlier, response times were measured at different temperatures for doped and undoped samples. These values are shown in figure 6.14 and table 6.2. The data in this table and figure clearly show that at every temperature, increasing Pd concentration results in shorter response times. For example 3% Pd doped film shows a response time of about 4 min at 100 ^{o}C, whereas undoped film at the same temperature shows response time of about 80 min. Even for a given Pd concentration increasing temperature results in shorter response times. Note that while figure 6.13 suggests an optimal temperature of about 100 ^{o}C for highest sensitivity in 3% Pd doped sample, figure 6.14 suggests that higher temperatures are better for quicker response. Therefore one has to oftentimes compromise between requirements of highest sensitivity and shortest response time as optimum temperatures for both of them could be different.

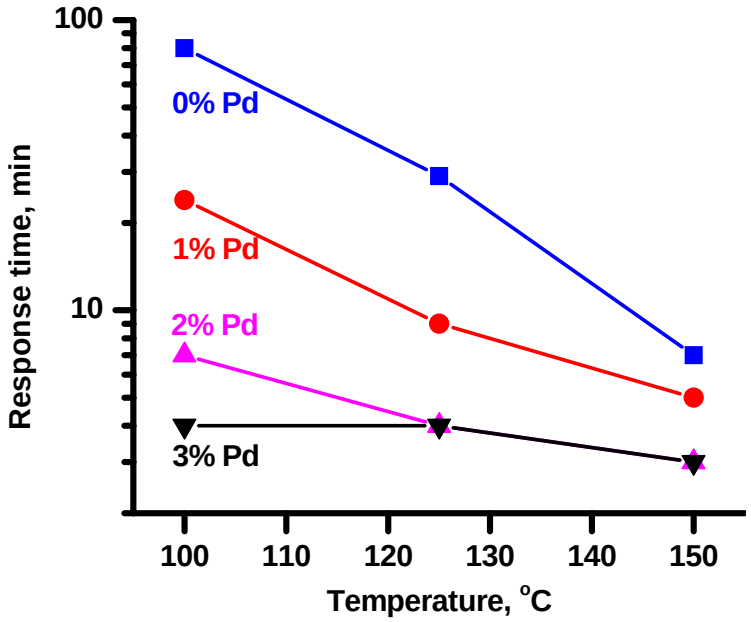

Figure 6.14: Response times of Pd doped and undoped tin oxide thin films to 250 ppm H_2 in N_2 measured at three different concentrations.

Table 6.2: Response times measured in tin oxide films doped with different Pd concentrations. These values are used for plot shown above.

% Pd Concentration → **Temperature ↓**	**0**	**1**	**2**	**3**
150 °C	7 min	5 min	3 min	3 min
125°C	29 min	9 min	4 min	4 min
100 °C	80 min	24 min	7 min	4 min

The effects of Pd observed in this work are consistent with many reports in literature that demonstrated the improved sensor performance of Pd doped tin oxide films over undoped tin oxide films. While the actual mechanism for this enhanced performance is still a matter of debate, it is often attributed to either "spill-over effect" [273, 274] or "fermi-energy control" [275]. Fermi-energy control refers to the fact that partial oxidation of Pd to PdO would alter the space-charge layer and modify the fermi-energy at the SnO_2 surface. On the other hand spill-over effect refers to the cleaving of molecular hydrogen bond to convert into its atomic form and the subsequent spill-over of atomic hydrogen onto SnO_2 substrate to react with surface oxygen ions. A third mechanism[276] oftentimes invoked mostly in case of sensors made from pure Pd metal is the volume expansion of Pd upon absorption of H_2. The volume expansion of Pd upon exposure to H_2 would control the spacing between grains and therefore act as a switch. However, this mechanism might not be relevant in case of Pd doped oxide films because of low Pd concentration used in these materials. Irrespective of what the real mechanism is, it is shown beyond reasonable doubt that Pd has significant effect on hydrogen sensing characteristics of tin oxide films.

6.8 GAS SENSING PROPERTIES OF SOFT-eBL NANOSTRUCTURES

6.8.1 undoped soft-eBL tin oxide nanostructures

The details of sample preparation are covered in experimental section earlier in the chapter. The slight difference in samples used for this particular section is in their contact electrodes. The electrodes were a bilayers of 10 nm Cr and 100 nm Au. The SEM images of soft-eBL lines together with their contact electrodes are shown in figure 6.15.

Prior to gas sensing experiments, I-V plots were taken at different temperatures and are shown in figure 6.16a. Linear I-V plots suggest that contacts are ohmic between 75 ^{o}C and 200 ^{o}C. Based on the measured dimensions of each tin oxide soft-eBL lines (height ≈ 80 nm, width ≈ 300 nm) and electrode spacing (≈ 6 μm), the resistance values were converted into resistivity values and are plotted in figure 6.16b. Note that since the measurements were performed in two-probe configuration, the values in plot 6.16b include contact resistance. One could eliminate contact resistance by taking measurements in four-probe configuration as shown in next section on doped tin oxide soft-eBL lines.

The hydrogen sensing properties of undoped tin oxide soft-eBL lines are measured at different temperatures and hydrogen concentrations. For example, figure 6.17 shows the response of 300 nm wide soft-eBL undoped tin oxide lines to various hydrogen

concentrations at 150 ^{o}C and 200 ^{o}C. It is clear that these lines are sensitive to hydrogen at concentrations as low as 250 ppm. The sensitivities for 250 ppm are about 3 and 5 at 150 ^{o}C and 200 ^{o}C. The sensitivity values of this sample measured at different temperature and H_2 concentration are shown in table 6.3. We have also fabricated electrodes without any tin oxide nanostructures on the same sample to confirm that the sensing behavior is not from substrate. The response of the substrate is shown as red-color plot in figures 6.17a and 6.17b. The substrate response was only measured for three different concentrations. The absence of any response to hydrogen from the substrate (silicon oxide) therefore confirms hydrogen sensitivity of soft-eBL tin oxide nanostructures.

The sensitivity values measured for lines are distinctly smaller than those measured for thin films (section 6.7.2). Undoped tin oxide films showed a sensitivity of about 50 when tested for 250 ppm of H_2 at 150 ^{o}C. However, note that thin films and lines were tested using different electrode configuration even though they were prepared from same sols and annealed at the same temperature. The electrode spacing in case of thin films was about 70 μm whereas for lines the electrode spacing is only 6 μm. In addition to the differences in the electrode configuration one must also realize that electric field distribution around contact electrodes in case of thin films and soft-eBL structures will be different. The width of the soft-eBL lines is smaller than electrodes whereas electrode width is significantly smaller than the film coverage (film covers the entire substrate). Until one understands the role of electric field distribution around the electrodes and the effect of ambient on this distribution

it is difficult to rationalize the differences in the performance of thin films and 1D nanostructures. The future work could involve masking the region near electrodes with an inert layer and probing the sensing behavior. In this way one could eliminate effects of the differences in electric field distribution in case of lines and thin films.

One of the other desirable attributes of a sensor is the stability and repeatability. As discussed in the previous chapter, grain growth kinetics in dimensionally constrained materials system, like the soft-eBL lines, is reduced. This could lead to stable grain structure and therefore repeatable sensing performance. Figure 6.18 shows the response of 300 nm wide undoped tin oxide soft-eBL lines upon repeated exposure to 250 ppm H_2 in N_2 over 2 days. These measurements were taken at 150 ^{o}C. The figure shows that sensitivity is quite repeatable and the drift in base line resistance is less than 1% over 2 days. This demonstrates the high stability of these structures as gas sensors.

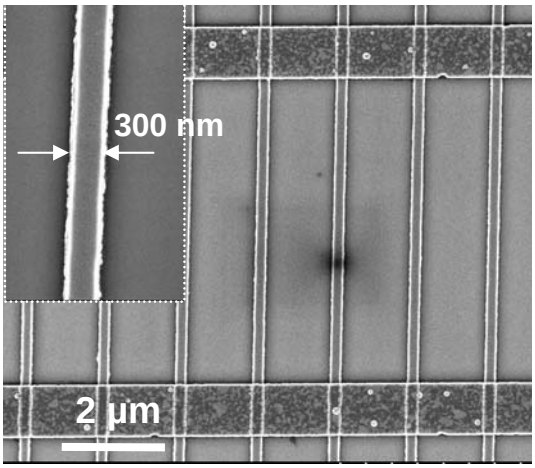

Figure 6.15: SEM image of soft-eBL undoped tin oxide nanostructures together with the Cr/Au electrodes.

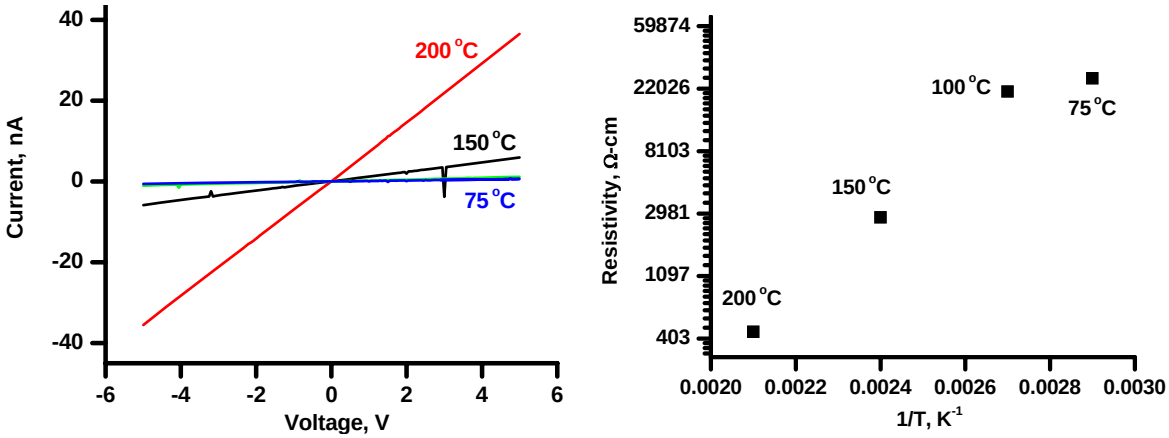

(a) **(b)**

Figure 6.16: (a) Linear I-V plots of undoped tin oxide soft-eBL lines at different temperatures and (b) plot of temperature dependence of resistivity of these lines. Note that y-axis is in Ln-scale (not Log-scale).

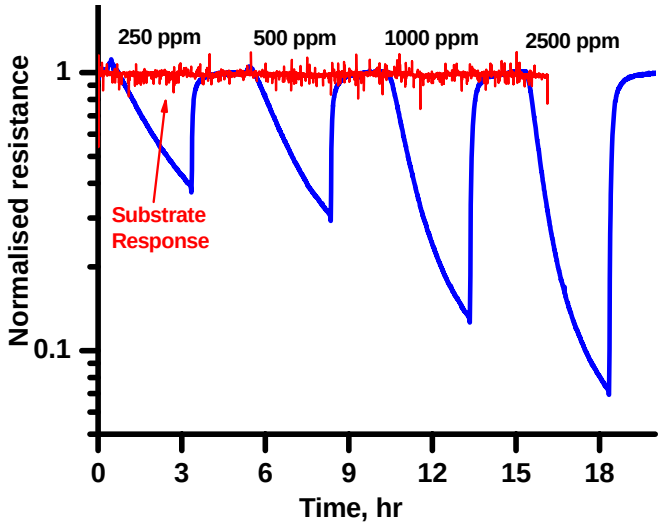

(a)

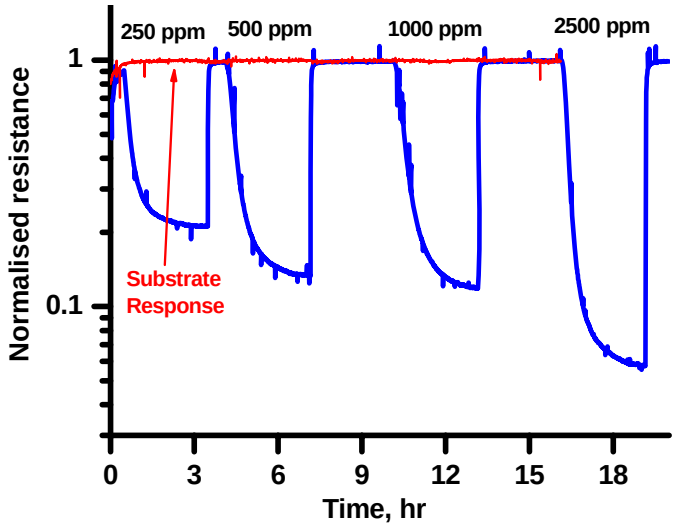

(b)

Figure 6.17: Response of 300 nm wide undoped tin oxide soft-eBL lines to different concentrations of hydrogen in nitrogen. Measurements were taken at (a) 150 ^{o}C and (b) 200 ^{o}C with a flow rate of 1000 sccm. Synthetic air is the purge gas. In each case plot in red shows the response of bare substrate tested under identical conditions and electrode configuration

Table 6.3: Sensitivity values measured at different temperatures and H_2 concentration for 300 nm wide soft-eBL undoped tin oxide lines

Temperature	Analyte Concentration (ppm)	300 nm-wide undoped lines
150 °C	250	3
	500	4
	1000	8
	2500	14
200 °C	250	5
	500	7
	1000	8
	2500	17

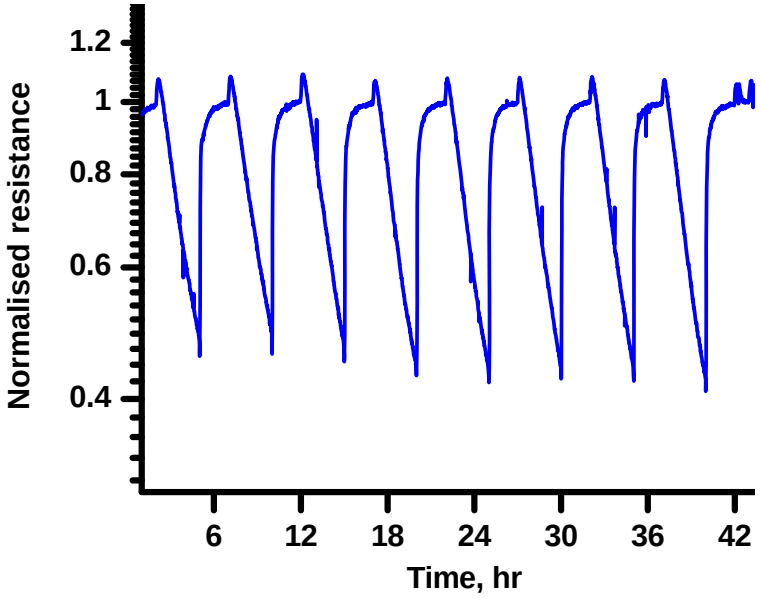

Figure 6.18: Response of undoped soft-eBL lines to 250 ppm H_2 in N_2 over two days of continuous testing. The measurements were done at 150 °C.

6.8.2 soft-eBL nanostructures of tin oxide 3%Pd doped

This section covers the H_2 sensing properties of soft-eBL lines of tin oxide doped with 3% Pd. Two different set of lines were fabricated as shown in figure 6.19. This figure shows the SEM and AFM images of two sets of soft-eBL lines. Figures 6.19a and 6.19b are AFM and SEM images of 200 nm wide lines respectively. There are 5 such lines in total. The AFM image was taken in tapping mode and the height profile shows that lines are about 65 nm in height. Figures 6.19c and 6.19d are the similar set of images of 85 nm wide lines. There are a total of 10 such lines and their height too is approximately 65 nm. These lines were designed such that their total line widths (5×200 nm, 10×85 nm) are approximately equal. Considering that they were fabricated on the same chip and therefore fabricated under identical conditions, the only difference between them is the surface to volume ratio. Narrower lines possess about 50% higher surface to volume ratio. The microstructural characterization using TEM showed that both set of lines possess similar grain size. These values were reported in table 5.2 in previous chapter. An average grain size of about 5.6 ± 1.7nm and 5.3 ± 1.6nm were measured in case of narrower and wider lines respectively. The similarity in every variable except the line width therefore suggests that the differences in their gas sensing performances would be a direct effect of the differences in their surface to volume ratio.

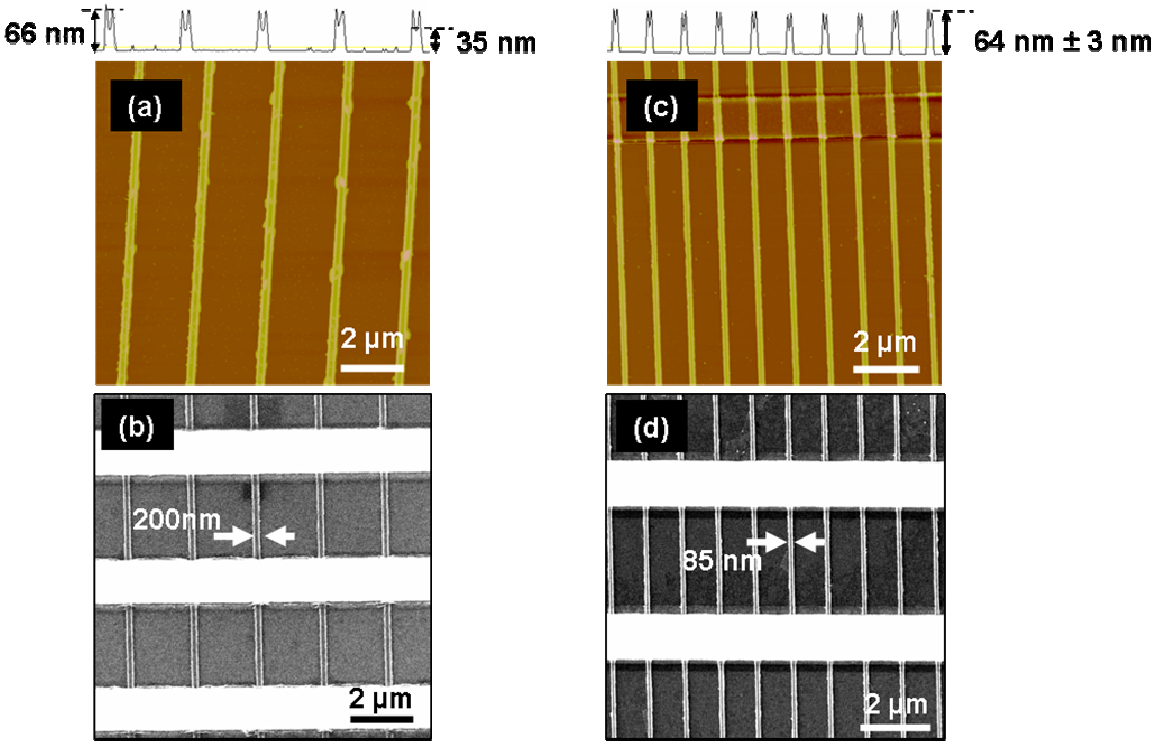

Figure 6.19: (a) AFM and (b) SEM images of 200 nm wide soft-eBL lines. (c) AFM and (d) SEM images of 85 nm wide soft-eBL lines. These are tin oxide lines doped with 3% Pd. AFM images were taken in tapping mode and the height profiles were used for measuring line heights whereas widths are measured from SEM images. The wide white horizontal patches are the electrodes.

Prior to gas sensing measurements, I-V plots were taken for both samples at various temperatures. The I-V plots were found to be linear at all temperatures in both samples. As an example, I-V plots at different temperatures measured on narrower lines are shown in figure 6.20a. Please note that these plots were taken in two-probe configuration. Based on the measured dimensions of the lines, the resistivity in case is calculated and plotted as shown in figure 6.20b and table 6.4. The decrease in resistivity with temperature is consistent with semiconducting behavior of the lines. Note that y-axis of plot is in natural logarithmic scale and x-axis is the inverse of temperature in degree Kelvin. The linearity of this plot shows that conductivity in these lines is thermally activated with a single activation energy value. The activation energy is measured to be 0.68 eV/atom, which is much smaller than bandgap energy of SnO_2 (3.6 eV). This suggests presence of a mid-bandgap defect state in these lines. Since tin oxide is often times found to be oxygen deficient, these mid-bandgap states are mostly to be oxygen vacancies.

It is interesting to note that both narrower and wider lines show the same activation energy though narrower lines consistently show lower resistivity at every temperature. On average, narrower lines are about 20% more conductive than wider lines. Narrower lines have about 50% higher surface to volume ratio and both lines are anticipated to have similar microstructure and therefore similar volume resistivity. The higher conductivity of narrower lines therefore could be due to higher surface conductivity compared to volume conductivity.

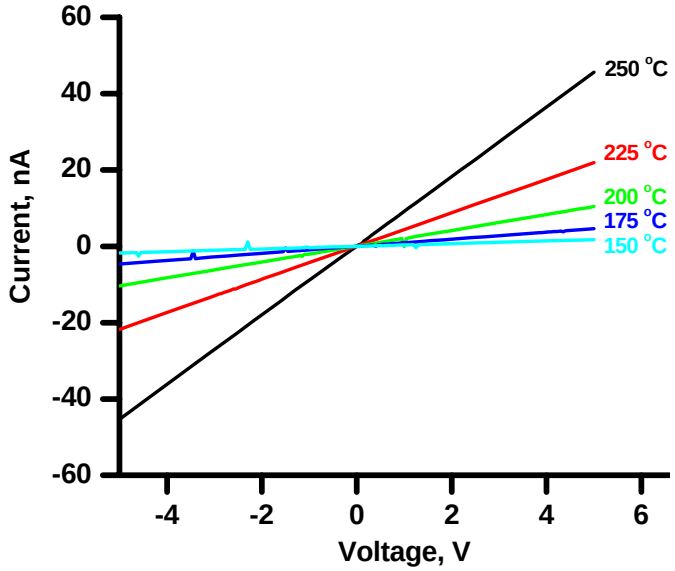

Figure 6.20a: I-V plots of 85 nm wide lines taken in two-probe configuration at different temperatures.

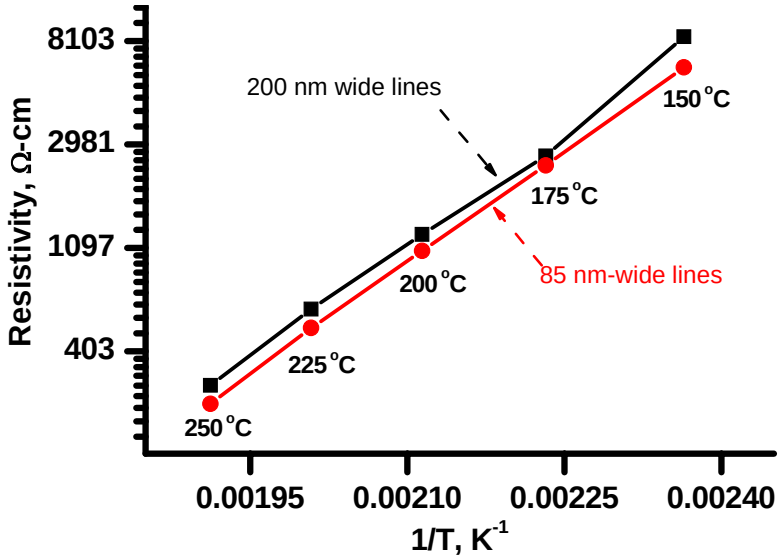

Figure 6.20b: Resistivity measured at different temperatures in lines of two line widths. Note that y-axis is in Ln-scale (not in Log-scale).

Table 6.4: Resistivity per line values used for plotting the above graph

Line width → **Temperature ↓**	**Narrower lines**	**Wider lines**
150 °C	6276 Ω-cm	8448 Ω-cm
175 °C	2431 Ω-cm	2666 Ω-cm
200 °C	1067 Ω-cm	1251 Ω-cm
225 °C	506 Ω-cm	607 Ω-cm
250 °C	243 Ω-cm	290 Ω-cm

The response of these lines to various concentrations of H_2 in N_2 is measured at different temperatures. Figure 6.21a shows the response to four different H_2 concentrations at 150 °C. At each concentration, sample is exposed to analyte gas for 3 hr while purged with air for only about an hour. Clearly, narrower lines show higher sensitivity especially at concentrations greater than 250 ppm. For example, sensitivity of narrower lines increases from about 210 at 500 ppm to about 930 at 2500 ppm. On the other hand, sensitivity of wider lines increases from 70 at 500 ppm to about 360 at 2500 ppm. The concentration dependent sensitivities of these lines at 150 °C and 200 °C are shown in figure 6.21b. The values used for these plots are shown in table 6.5. From these plots it can be seen that both sets of lines show higher sensitivity at 150 °C compared to 200 °C. The line-width effect appears to decrease with temperature. In other words, narrower lines are more sensitive than wider lines at lower temperatures and higher analyte concentrations.

It is important to note that the two sets of lines studied in this section had same total line-width and line height. Also the electrode spacing is the same in each case. Therefore the total volume in each case is the same and the only difference between them is the surface area. This experiment therefore evaluates the gas sensitivity of structures with different surface areas but having the same volume. Considering that both sets of lines have similar grain sizes too, the differences in their sensitivities are predominately due to dimensional effect. There were several reports in literature that have studied the effect of surface to volume ratio on sensitivity. However, in almost all of these cases neither the volume nor the surface area is fixed. In such cases it is hard to evaluate the effect of surface area on gas sensitivity.

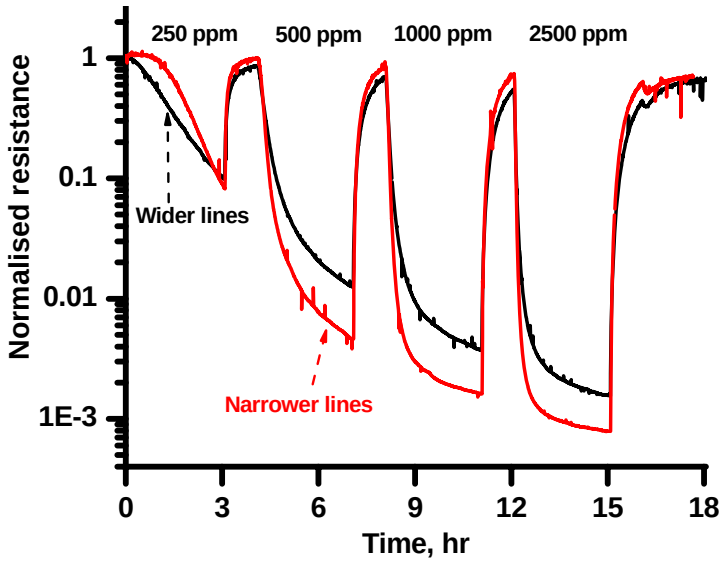

Figure 6.21a: Response of wider and narrower lines to four different H_2 concentrations measured at 150 ^{o}C. The measurements were taken by applying 1V bias. Based on the electrode spacing, this equals about 4×10^{5} V/m electric field.

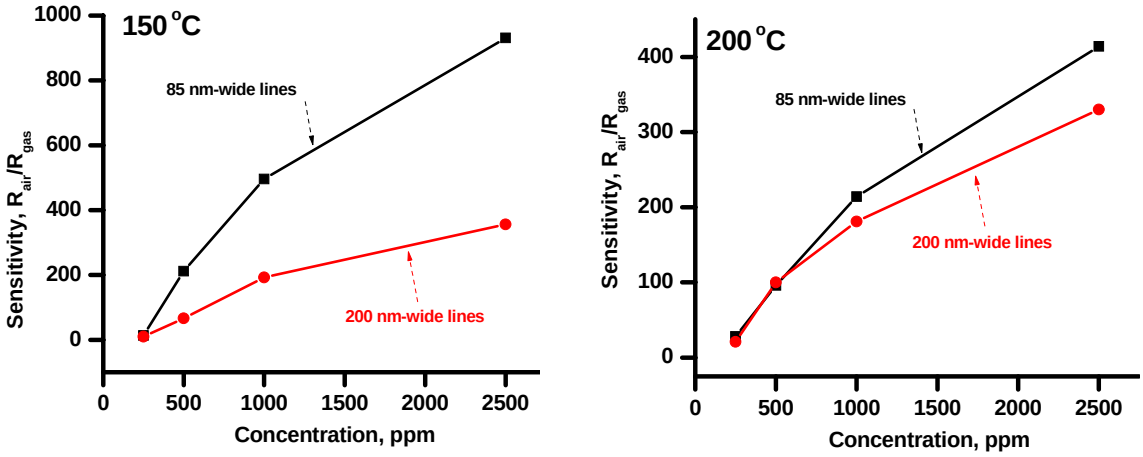

Figure 6.21b: Sensitivity dependence on analyte concentration at two different temperatures between wider and narrower lines

Table 6.5: Sensitivity values used for the plots in figure 6.21b

Temperature	Analyte Concentration (ppm)	85 nm-wide lines	200 nm-wide lines
150 ^{o}C	250	13	10
	500	212	66
	1000	496	192
	2500	931	356
200 ^{o}C	250	28	21
	500	96	100
	1000	214	181
	2500	414	330

6.8.3 Four-probe measurements of 3% Pd doped tin oxide soft-eBL nanostructures

In order to evaluate the role of contact resistance on overall resistivity and gas sensing performance, four-probe measurements were performed. The temperature dependence of resistivity is shown in figure 6.22. This plot also shows the values measured in two-probe configuration for comparison. The values used for this plot are shown in table 6.6. Comparison between four-probe and two-probe values shows that contact resistance in case of narrower lines is nearly 90% of the total resistance whereas it is nearly 80% in case of wider lines. Considering that both sets of lines have the same total electrode contact area, one might expect them to have the same amount of contact resistance. The absolute contact resistivity values calculated as a difference between two-probe and four-probe measurements are also in table 6.6. It is very interesting to see that the absolute contact resistivity values measured in 85 nm and 200 nm wide lines are quite comparable, especially

at higher temperatures. The comparable absolute contact resistivity values between narrower and wider lines suggest that the contacts between electrode and each line are nearly identical.

Based on four-probe measurements it can be inferred that narrower lines are more conductive suggesting that surface conductivity is higher than bulk conductivity. The resistivity values measured in our work are compared with values reported in literature. Not surprisingly, the resistivity of polycrystalline tin oxide was found to vary considerably depending on the processing conditions. Resistivities as low as 2×10^{-3} Ω-cm at room temperature have been reported[218, 277]. Wide range of values for the resistivities of even tin oxide nanowires, which are single crystalline, have been reported. Ramirez et.al[278] reported a value of about 2.2 Ω-cm while Arnold et.al[279] have reported a value of 6.7×10^{-2} Ω-cm for tin oxide nanowires at room temperature. The bulk single crystals of tin oxide were reported[280] to have resistivities between 10^6 and 10^2 Ω-cm in 700 - 900K temperature range. Therefore the resistivities of doped tin oxide soft-eBL patterns measured in this work appear to be reasonable values.

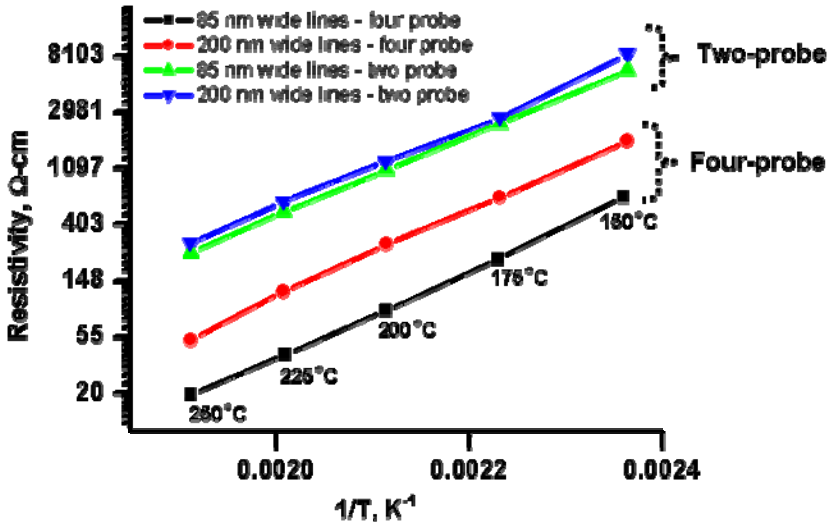

Figure 6.22: Comparison between resistivities of lines measured at different temperatures in four-probe and two-probe configuration.

Table 6.6: Resistivity per line values used for plotting the above graph

Configuration	Temperature, ^{o}C	85 nm-wide lines	200 nm-wide lines
Four-probe	250	20	52
	225	40	123
	200	87	285
	175	218	655
	150	658	1778
Two-probe	250	243	290
	225	506	607
	200	1067	1251
	175	2431	2666
	150	6276	8448
Difference	250	223	238
	225	466	484
	200	980	966
	175	2213	2011
	150	5618	6670

The temperature dependence of resistivity shown in figure 6.22 indicates the presence of single activation energy. Furthermore the similarities in activation energy measured in both two-probe and four-probe configuration shows the measured activation energy corresponds to lines and not contacts. The activation energy measured from these plots is about 0.7 eV/atom. The activation energies measured from temperature dependence of resistivity for undoped tin oxide in bulk form (pellets) as well as single crystals were reported to be between 0.6 and 1 eV/atom in literature depending on temperature range[281, 282].

6.9 BENCHMARKING GAS SENSING PROPERTIES OF SOFT-eBL NANOSTRUCTURES

One has to be very careful while comparing the gas sensing data from literature because of the reasons expounded in section 6.5. The large number of variables that can affect the sensitivity and the lack of any standards for gas sensing measurements make it almost futile to compare ones results with literature values. However, interested reader can easily access hundreds of articles on hydrogen sensing using palladium doped tin oxide.

Instead of comparing with the literature values, we benchmarked the performance of soft-eBL nanostructures with a commercial hydrogen sensor based on tin oxide. The commercial sensor (TGS 821) was bought from Figaro (Figaro USA Inc., Glenview, IL) and

tested under identical conditions using the same gas sensing measurement set-up. Figure 6.23 shows the response of Figaro TGS 821 sensor to four different H_2 concentrations at 150 ^{o}C. For comparison, response of 85 nm wide soft-eBL lines with 3% Pd (shown earlier in figure 6.21) is also shown in the same graph. Clearly, the soft-eBL lines respond quicker and show higher sensitivity at all four concentrations tested.

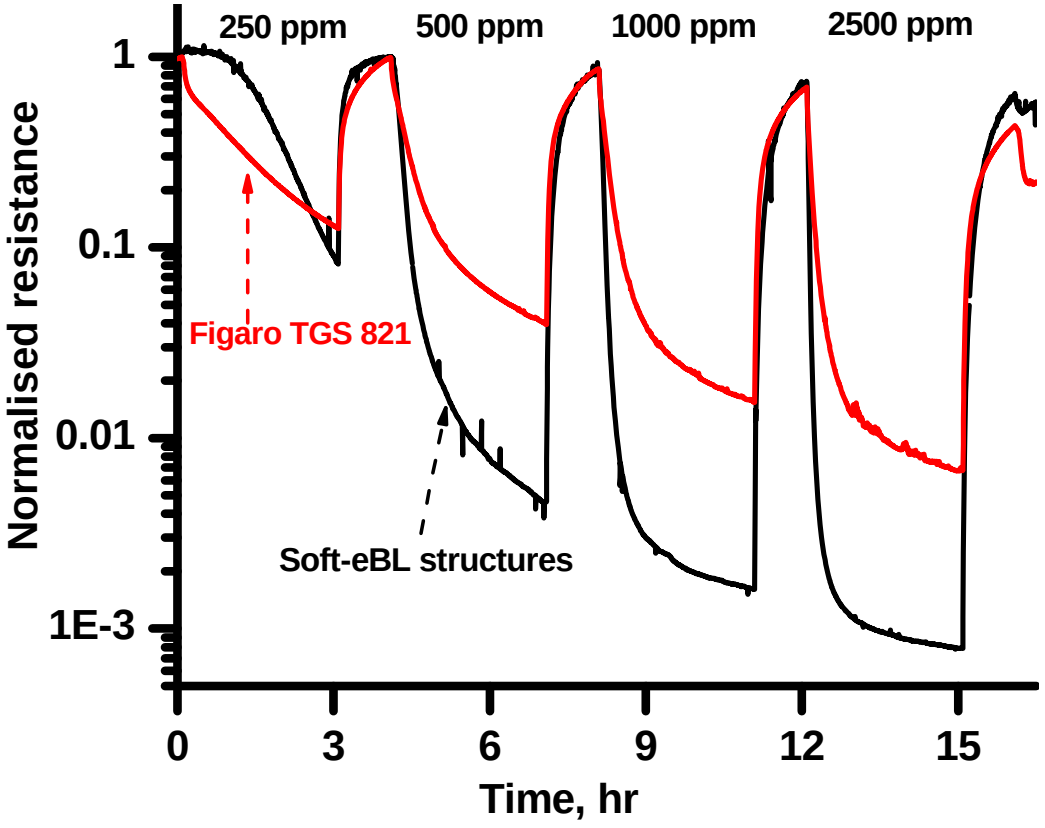

Figure 6.23: Response of Figaro TGS 821 hydrogen sensor to different H_2 concentrations tested in our in-house built gas sensing set-up. Response of 85 nm wide soft-eBL tin oxide lines with 3% Pd is shown for comparison.

Table 6.7: Sensitivities of soft-eBL lines and Figaro TGS 821 sensor measured from above plot

Temperature	Analyte Concentration (ppm)	85 nm-wide lines	Figaro TGS 821
150 ^{o}C	250	13	8
	500	212	25
	1000	496	65
	2500	931	148

We also tested the long term stability and repeatability of soft-eBL structures. Figure 6.24 shows the response of 85 nm wide soft-eBL lines to 2500 ppm of H_2 in N_2 at 200 ^{o}C. The sample was exposed to continuous cycles of 5 min exposure and 5 min purge steps. The drift in base line resistance is less than 4% after 240 cycles demonstrating that the soft-eBL structures are very stable. The drift is calculated as a percentage change in resistance between 50th and 240th cycle of exposure. The following equation is used to calculate the drift.

$$Drift(\%) = \frac{\left| R_{gas}^{50} - R_{gas}^{240} \right|}{R_{gas}^{50}} \times 100 \qquad (6.2)$$

For comparison we have also tested the Figaro sensor performance under similar testing-protocols and the measured response is shown in figure 6.25. The drift measured in Figaro sensor is about 40%. This large drift observed in commercial sensors is a common problem observed in bulk metal oxide semiconductor sensors. The drift is usually associated

with the microstructural instability or grain growth observed at sensor operating temperatures in bulk sensors. The slow grain growth kinetics in dimensionally constrained systems such as soft-eBL 1D nanostructures could be one reason for smaller drift observed in these structures.

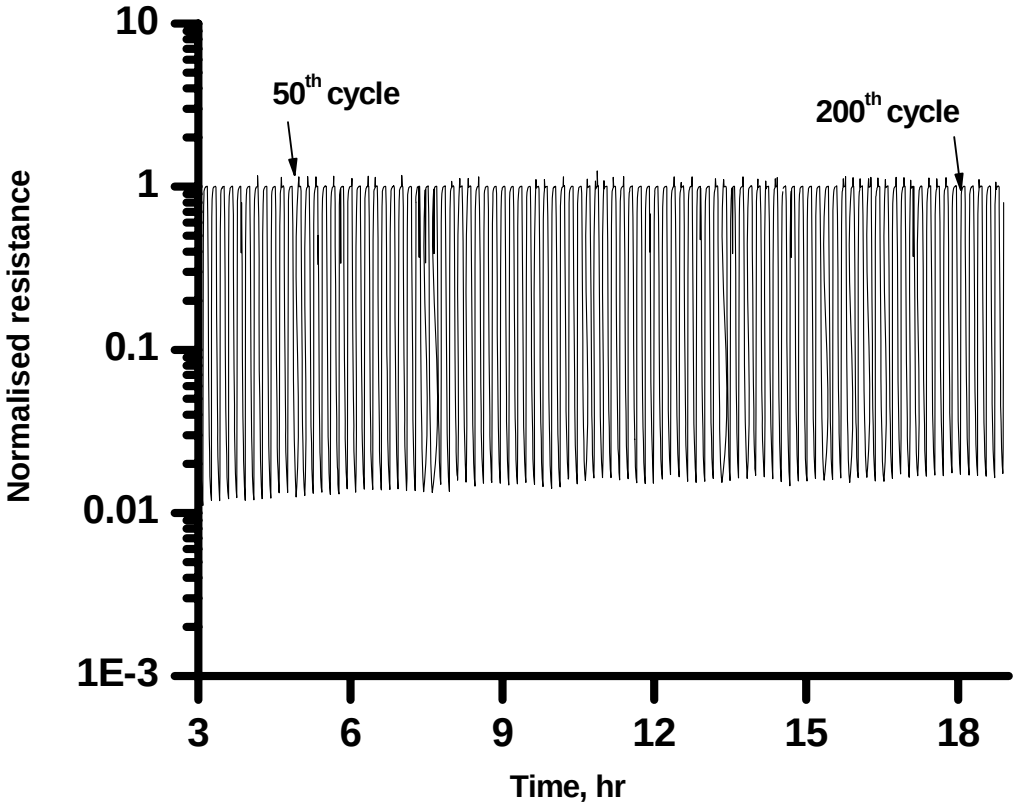

Figure 6.24: Response of Soft-eBL lines to over 200 continuous cycles of exposure-purge. Analyte gas is 2500 ppm H_2 in N_2 and purge gas is synthetic air. The measurements were performed at 200 ^oC

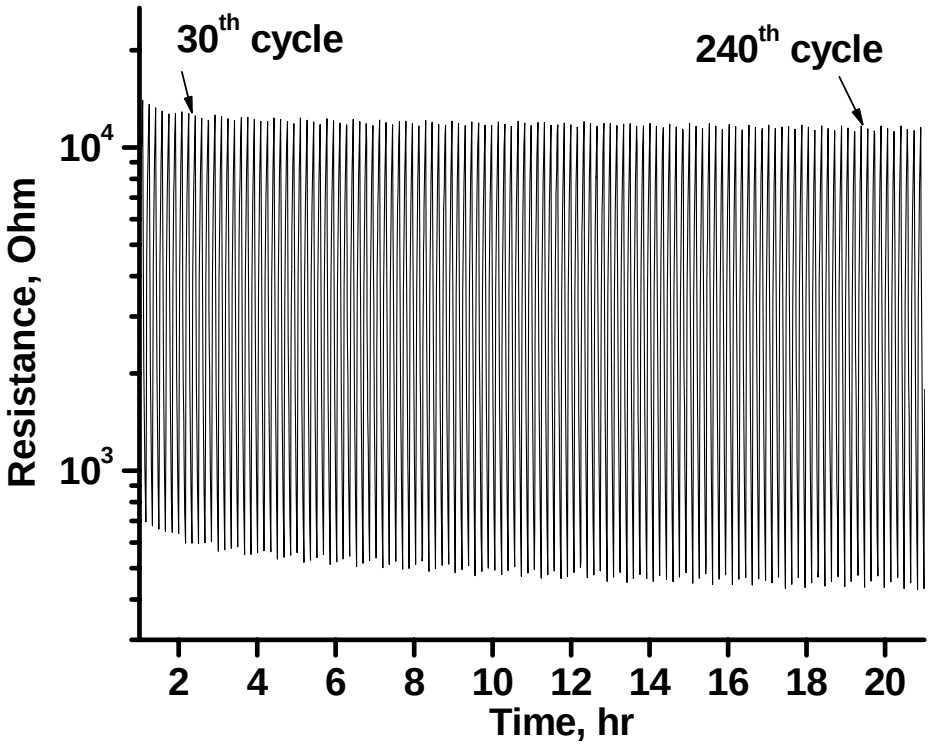

Figure 6.25: Response of Figaro sensor to over 200 continuous cycles of exposure-purge. Analyte gas is 2500 ppm H_2 in N_2 and purge gas is synthetic air. The measurements were performed at 200 ^oC

6.10 SUMMARY

The primary goal of this chapter is to demonstrate the application aspects of soft-eBL. Miniaturized gas sensors using soft-eBL nanostructures as active sensing elements was demonstrated. An in-house gas sensing set-up was described and the results obtained from the set-up are reported in this chapter. A detailed experimental protocol for fabricating gas sensing devices containing soft-eBL nanostructures is described. Some of the major conclusions from this chapter are:

1. Hydrogen sensing properties of tin oxide and Pd doped tin oxide films were measured. It was found that doping with Pd has significant effect on their hydrogen sensing properties. Increasing Pd concentration up to 3% was beneficial in increasing sensitivity and reducing the response time. Furthermore, doping with Pd decreased the optimal temperature to about 100 ^{o}C compared to undoped sample whose optimal temperature was above 150 ^{o}C

2. The hydrogen sensing properties of 3% Pd doped and undoped tin oxide soft-eBL nanostructures were measured. Even among lines, doping has a significant effect on sensitivity. The sensitivity has increased from about 4

in case undoped 300 nm wide tin oxide lines to about 210 in case of 3% Pd doped 85 nm wide lines when tested at 150 ^{o}C and 500 ppm H_2 in N_2.

3. Comparison between four-probe and two-probe measurements showed that contact resistance is nearly 90% of the total resistance of soft-eBL nanostructures measured.

4. Resistivity values measured on 85 nm and 200 nm wide lines in four-probe configuration indicated that narrower lines with higher surface to volume ratio are more conductive. This is inferred to be due to higher surface conductivity over bulk conductivity.

5. The H_2 sensing performance of 85 nm and 200 nm wide lines measured in two-probe configuration showed that narrower line are more sensitive. This is attributed to the higher surface to volume ratio of the narrower lines.

6. H_2 sensing performance of 85 nm wide soft-eBL lines was compared with Figaro TGS 821 commercial hydrogen sensor. The commercial sensor was also tested using the same in-house built gas sensing set-up. Soft-eBL

structures showed better sensor characteristics (higher sensitivity and faster response) compared to commercial sample.

7. Long term stability and repeatability tests showed that soft-eBL structures are very stable. The resistance was found to drift by less than at 4% when tested at 200 ^{o}C. These structures could be potential gas sensing elements.

CHAPTER 7

Fabrication of ceramic nanostructures through nanopatterning approach is challenging. However, patterning is a desirable approach because it enables "on-site" structural fabrication and provides a facile means of integrating them into device circuitry. One of the major contributions of this dissertation is the development of a nanopatterning approach, soft-eBL, that is especially well suited for ceramic nanostructure fabrication.

Soft-eBL synergistically combines the advantages of electron beam lithography and soft-chemistry routes for fabricating ceramic oxide nanostructures with excellent control on their size, shape and location on substrate. The technique is capable of fabricating ceramic lines with widths as small as 30 nm. These dimensions are comparable to grain sizes in these structures. The other contributions of this thesis work are:

1. The high resolution capability of soft-eBL is exploited to fabricate ceramic oxide lines with widths equal to their size. These are called as beaded structures. Through soft-eBL we have developed a protocol to fabricate beaded structures of variety of ceramic oxides. These structures would be ideal test-beds for some interesting "structure-property" evaluation experiments.

2. We have demonstrated that structural evolution or more specifically grain growth kinetics during crystallization are dependent on line-widths of ceramic lines. We have demonstrated the feasibility of using soft-eBL to fabricate ceramic nanostructures of different line-widths and to study the crystallization kinetics in these structures.

3. We have demonstrated the feasibility of fabricating ceramic nanostructures on fragile substrates such as 75 nm thick electron transparent membrane and microhotplates.

4. We have developed an experimental protocol for fabricating miniaturized devices containing polycrystalline ceramic nanostructures for gas sensing applications.

5. We have set-up in-house an experimental unit for performing gas sensing measurements.

7.1 SUGGESTIONS FOR FUTURE WORK

By its very nature scientific research is never complete. No matter how many experiments are done to do to plug-in the seemingly gaping holes in the work, every additional experiment only seems to make a case for ever more experiments. In some ways

the value of a work is judged more for the new questions it raises than the old ones it answers. In that spirit, the following suggestions are made for the future work:

a. Gas Sensing

1. All the gas sensing measurements in this work were performed in two probe configuration. Comparison of I-V measurements from two-probe and four-probe measurements clearly showed that contact resistance is significant (as high as 90% of the total resistance) though the contacts were found to be ohmic. It is not clear how the contact resistance responds to analyte gases and therefore what fraction of sensitivity measured in two-probe configuration is truly that of nanostructures. Therefore, the next stage of gas sensing measurements should be performed in four-probe configuration in order to eliminate the effect of contact resistance to overall gas sensing behavior.

2. The gas sensing measurements in this work were performed by monitoring resistance under a constant voltage bias (DC). In addition to these DC measurements, it would be interesting to perform these measurements at different voltage frequencies and monitor their impedance instead of DC resistance. Through impedance measurements one could decouple the contributions of grain boundaries, electrode contacts, surfaces and other interfaces.

3. In addition to operating at high temperatures, sensitivity could also be increased by using a background of UV light. It is possible to operate sensors at room temperature by continuously exposing the sensor to UV light. It is useful to perform UV assisted H_2 sensing measurements to explore the possibility of developing a room temperature H_2 sensor. This has a tremendous technological implication since hydrogen in explosive and lower temperature operation is desirable.

4. In addition to hydrogen sensing, it is only natural that one should test the sensing performance of soft-eBL structures for other gases. The current gas sensing set-up contains four mass flow meters and is therefore capable of studying at least three different analytes.

5. The current electrode design contains 4 sets of 8 electrodes on four sides. Through a series of multiple soft-eBL steps it is possible to fabricate ceramic nanopatterns of different compositions on a single chip. This multiplexing capability can be exploited for future work on "electronic-nose" project in the group.

6. The main focus of this thesis work has been ceramics. However, soft-eBL is capable of fabricating even polymer nanopatterns as shown for polypyrrole system. Since polymers are amorphous, they could be ideal material systems to study the size effect on sensing properties. Fabricating polypyrrole patterns of different line-widths and

measuring their gas sensing properties could help understand the role of dimension on sensing performance.

b. Structural Engineering of Patterns

7. One of the strengths of soft-eBL is the ability to fabricate very narrow ceramic oxide lines with widths approaching grain size. These beaded structures are very interesting test vehicles to understand the relative contributions of grain boundaries and surfaces to overall physical property, sensing for example. Beaded structures of two material systems, namely ZnO and $BiFeO_3$, were fabricated in this work. One could extent this to other material systems. Furthermore, following the device fabrication protocol developed in this work, one could fabricate probing electrodes onto the beaded structures and study their physical properties. For a start, one could study their gas sensing properties and compare them with those of single crystalline nanowires having similar line widths. This would provide an unambiguous evidence for the role of grain boundaries on sensing. AC Impedance measurements would particularly useful for the beaded structures as their microstructure is so well defined.

8. Soft-eBL was demonstrated for fabricating beaded structures and single crystalline patterns albeit in different material systems (ZnO beaded structures and $CoFe_2O_3$, $BaTiO_3$ single crystal patterns). The formation of beaded structure is a result of dimensional constraint while the single crystal conversion is primarily driven by low

lattice mismatch between pattern and substrate. By choosing an appropriate substrate and heat treatment protocol, one should be able to convert ZnO patterns into single crystalline structures. The idea is to fabricate either beaded structures or single crystalline structures of a single material system using soft-eBL depending on the substrate and other process conditions. The structures thus fabricated would be ideal samples to understand the structure-property correlations in ceramics.

c. Structural Characterization

9. The beneficial effects of Pd on gas sensing properties of tin oxide were demonstrated not only in this work but also through numerous reports in literature. Despite extensive property measurements, there is no single report that identifies, beyond doubt, the location of Pd in tin oxide. This is mainly due to the limitations of commonly used structural characterization tools such as TEM coupled with the very small grain size observed in this material system. However, recent developments in atom probe microscope (AP) enable this technique a very suitable tool. Versions such as 3D-AP and Local Electron Atom Probe (LEAP) have the spatial and chemical resolution (single atom resolution) that is ideally suited for investigating the location of Pd in tin oxide. This technique was recently used Kim et.al[283] for profiling Pd in nickel silicide thin films. It is worthwhile to adapt Kim et.al methodology to the current work.

REFERENCES

1. Castro, T.; Reifenberger, R.; Choi, E.; Andres, R. P., *Phys. Rev: B.* **1990,** 42, 8548.

2. Buffat, P.; Borel, J. P., *Phys. Rev: A.* **1976,** 13, 2287.

3. Ross, C., *Annu. Rev. Mate.r Res.* **2001,** 31, 203.

4. Mundra, M. K.; Donthu, S. K.; Dravid, V. P.; Torkelson, J. M., *Nano. Lett.* **2007,** 7, 713.

5. Kubo, R.; Kawabata, A.; Kobayashi, S., *Annu. Rev. Mater. Sci.* **1984,** 14, 49.

6. Ito, T.; Okazaki, S., *Nature.* **2000,** 406, 1027.

7. Wagner, R. S.; Ellis, W. C., *Appl. Phys. Lett.* **1964,** 4, 89.

8. Law, M.; Goldberger, J.; Yang, P. D., *Annu. Rev. Mate.r Res.* **2004,** 34, 83.

9. Givargizov, E. I., *Kristallografiya+.* **1975,** 20, 812.

10. Greene, L. E.; Law, M.; Goldberger, J.; Kim, F.; Johnson, J. C.; Zhang, Y. F.; Saykally, R. J.; Yang, P. D., *Angew. Chem. Int. Edit.* **2003,** 42, 3031.

11. Vayssieres, L.; Keis, K.; Lindquist, S. E.; Hagfeldt, A., *J. Phys. Chem. B.* **2001,** 105, 3350.

12. Xia, Y. N.; Yang, P. D.; Sun, Y. G.; Wu, Y. Y.; Mayers, B.; Gates, B.; Yin, Y. D.; Kim, F.; Yan, Y. Q., *Adv. Mater.* **2003,** 15, 353.

13. Whang, D.; Jin, S.; Wu, Y.; Lieber, C. M., *Nano. Lett.* **2003,** 3, 1255.

14. Whang, D.; Jin, S.; Lieber, C. M., *Nano. Lett.* **2003,** 3, 951.

15. Lieber, C. M., *MRS. Bull.* **2003,** 28, 486.

16. Seiyama, T.; Kato, A.; Fujiishi, K.; Nagatani, M., *Anal. Chem.* **1962,** 34, 1502.

17. Azad, A. M.; Akbar, S. A.; Mhaisalkar, S. G.; Birkefeld, L. D.; Goto, K. S., *J. Electrochem. Soc.* **1992,** 139, 3690.

18. Moseley, P. T., *Meas. Sci. Technol.* **1997,** 8, 223.

19. Gopel, W.; Schierbaum, K. D., *Sensor. Actuat. B-Chem.* **1995,** 26, 1.

20. Stetter, J. R.; Penrose, W. R., *Sensors. Update.* **2002,** 10, 189.

21. Gopel, W.; Reinhardt, G., *Sensors. Update.* **1996,** 1, 49.

22. Shaver, P. J., *Appl. Phys. Lett.* **1967,** 11, 255.

23. Law, M.; Kind, H.; Messer, B.; Kim, F.; Yang, P. D., *Angew. Chem. Int. Edit.* **2002,** 41, 2405.

24. Comini, E.; Faglia, G.; Sberveglieri, G.; Pan, Z. W.; Wang, Z. L., *Appl. Phys. Lett.* **2002,** 81, 1869.

25. Li, C.; Zhang, D. H.; Liu, X. L.; Han, S.; Tang, T.; Han, J.; Zhou, C. W., *Appl. Phys. Lett.* **2003,** 82, 1613.

26. Varghese, O. K.; Gong, D. W.; Paulose, M.; Ong, K. G.; Dickey, E. C.; Grimes, C. A., *Adv. Mater.* **2003,** 15, 624.

27. Bloomstein, T. M.; Horn, M. W.; Rothschild, M.; Kunz, R. R.; Palmacci, S. T.; Goodman, R. B., *J. Vac. Sci .Technol-B.* **1997,** 15, 2112.

28. Rothschild, M., *Mater. Today.* **2005,** 8, 18.

29. Gates, B. D.; Xu, Q. B.; Love, J. C.; Wolfe, D. B.; Whitesides, G. M., *Annu. Rev. Mate.r Res.* **2004,** 34, 339.

30. Geissler, M.; Xia, Y. N., *Adv. Mater.* **2004,** 16, 1249.

31. Kramer, S.; Fuierer, R. R.; Gorman, C. B., *Chem. Rev.* **2003,** 103, 4367.

32. Sotomayor Torres, C. M., *Alternative Lithography: Unleashing the Potentials of Nanotechnology*. Kluwer Academic: New York, 2003.

33. Tseng, A. A.; Notargiacomo, A.; Chen, T. P., *J. Vac. Sci .Technol-B.* **2005,** 23, 877.

34. Menzel, R.; Bachmann, T.; Machalett, F.; Wesch, W.; Lang, U.; Wendt, M.; Musil, C.; Muhle, R., *Appl. Surf. Sci.* **1998,** 136, 1.

35. Tseng, A. A., *J. Micromech. Microeng.* **2004,** 14, R15.

36. Hiramoto, T.; Hirakawa, K.; Ikoma, T., *J. Vac. Sci .Technol-B.* **1988,** 6, 1014.

37. Menzel, R.; Bachmann, T.; Wesch, W.; Hobert, H., *J. Vac. Sci .Technol-B.* **1998,** 16, 540.

38. Schmidt, B.; Bischoff, L.; Teichert, J., *Sensor. Actuat A-Phys.* **1997,** 61, 369.

39. Steckl, A. J.; Mogul, H. C.; Mogren, S., *Appl. Phys. Lett.* **1992,** 60, 1833.

40. Odagiri, T.; Hiramoto, T.; Hirakawa, K.; Ikoma, T., *J. Electrochem. Soc.* **1988,** 135, C375.

41. Young, R. J.; Cleaver, J. R. A.; Ahmed, H., *J. Vac. Sci .Technol-B.* **1993,** 11, 234.

42. Komuro, M.; Hiroshima, H., *J. Vac. Sci .Technol-B.* **1991,** 9, 2656.

43. Xu, Z.; Gamo, K.; Namba, S., *J. Vac. Sci .Technol-B.* **1988,** 6, 1039.

44. Langfischer, H.; Basnar, B.; Hutter, H.; Bertagnolli, E., *J. Vac. Sci .Technol-A.* **2002,** 20, 1408.

45. Schaffer, M.; Wagner, J.; Schaffer, B.; Schmied, M.; Mulders, H., *Ultramicroscopy.* **2007,** 107, 587.

46. Cairney, J. M.; Munroe, P. R.; Sordelet, D. J., *J. Microsc-Oxford.* **2001,** 201, 201.

47. Wu, H. Z.; Roberts, S. G.; Mobus, G.; Inkson, B. J., *Acta. Mater.* **2003,** 51, 149.

48. Iliescu, M.; Nelea, V.; Werckmann, J.; Mihailescu, I. N., *Surf. Coat. Tech.* **2004,** 187, 131.

49. Tseng, A. A., *Small.* **2005,** 1, 924.

50. Chou, S. Y.; Krauss, P. R.; Renstrom, P. J., *Appl. Phys. Lett.* **1995,** 67, 3114.

51. Chou, S. Y.; Krauss, P. R.; Renstrom, P. J., *J. Vac. Sci .Technol-B.* **1996,** 14, 4129.

52. Chou, S. Y.; Krauss, P. R., *Microelectron. Eng.* **1997,** 35, 237.

53. Byun, Y. H.; Hwang, E. C.; Lee, S. Y.; Lyu, Y. Y.; Yim, J. H.; Kim, J. Y.; Chang, S.; Pu, L. S.; Kim, J. M., *Mat. Sci. Eng. B-Solid.* **2005,** 117, 11.

54. Avey, A. A.; Hill, R. H., *J. Am. Chem. Soc.* **1996,** 118, 237.

55. Hill, R. H.; Avey, A. A.; Blair, S. L.; Gao, M.; Palmer, B. J., *Mater. Chem. Phys.* **1996,** 43, 233.

56. Lachish-Zalait, A.; Zbaida, D.; Klein, E.; Elbaum, M., *Adv. Funct. Mater.* **2001,** 11, 218.

57. Della Giustina, G.; Brusatin, G.; Guglielmi, M.; Romanato, F., *Mat. Sci. Eng. C-Bio. S.* **2007,** 27, 1382.

58. Chang, M. S.; Hou, T. W., *Opt. Commun.* **1978,** 24, 220.

59. Nagai, H.; Yoshikawa, A.; Toyoshima, Y.; Ochi, O.; Mizushima, Y., *Appl. Phys. Lett.* **1976,** 28, 145.

60. Subramanian, K. R. V.; Saifullah, M. S. M.; Tapley, E.; Kang, D. J.; Welland, M. E.; Butler, M., *Nanotechnology.* **2004,** 15, 158.

61. Saifullah, M. S. M.; Kang, D. J.; Subramanian, K. R. V.; Welland, M. E.; Yamazaki, K.; Kurihara, K., *J. Sol-Gel. Sci. Techn.* **2004,** 29, 5.

62. Saifullah, M. S. M.; Subramanian, K. R. V.; Kang, D. J.; Anderson, D.; Huck, W. T. S.; Jones, G. A. C.; Welland, M. E., *Adv. Mater.* **2005,** 17, 1757.

63. Saifullah, M. S. M.; Subramanian, K. R. V.; Anderson, D.; Kang, D. J.; Huck, W. T. S.; Jones, G. A. C.; Welland, M. E., *J. Vac. Sci .Technol-B.* **2006,** 24, 1215.

64. Voicu, N. E.; Saifullah, M. S. M.; Subramanian, K. R. V.; Welland, M. E.; Steiner, U., *Soft. Matter.* **2007,** 3, 554.

65. Passinger, S.; Saifullah, M. S. M.; Reinhardt, C.; Subramanian, K. R. V.; Chichkov, B. N.; Welland, M. E., *Adv. Mater.* **2007,** 19, 1218.

66. Saifullah, M. S. M.; Subramanian, K. R. V.; Tapley, E.; Kang, D. J.; Welland, M. E.; Butler, M., *Nano. Lett.* **2003,** 3, 1587.

67. Lewis, J. A.; Smay, J. E.; Stuecker, J.; Cesarano, J., *J. Am. Ceram. Soc.* **2006,** 89, 3599.

68. Tuttle, B. A.; Smay, J. E.; Cesarano, J.; Voigt, J. A.; Scofield, T. W.; Olson, W. R.; Lewis, J. A., *J. Am. Ceram. Soc.* **2001,** 84, 872.

69. Mott, M.; Song, J. H.; Evans, J. R. G., *J. Am. Ceram. Soc.* **1999,** 82, 1653.

70. Seerden, K. A. M.; Reis, N.; Evans, J. R. G.; Grant, P. S.; Halloran, J. W.; Derby, B., *J. Am. Ceram. Soc.* **2001,** 84, 2514.

71. Su, M.; Liu, X. G.; Li, S. Y.; Dravid, V. P.; Mirkin, C. A., *J. Am. Chem. Soc.* **2002,** 124, 1560.

72. Su, M.; Dravid, V. P.; Mirkin, C. A., *Abstr. Pap. Am. Chem. S.* **2002,** 224, U410.

73. Su, M.; Li, S. Y.; Dravid, V. P., *J. Am. Chem. Soc.* **2003,** 125, 9930.

74. Liu, X. G.; Fu, L.; Hong, S. H.; Dravid, V. P.; Mirkin, C. A., *Adv. Mater.* **2002,** 14, 231.

75. Lewis, J. A., *Curr. Opin. Solid. St. M.* **2002,** 6, 245.

76. Morissette, S. L.; Lewis, J. A.; Clem, P. G.; Cesarano, J.; Dimos, D. B., *J. Am. Ceram. Soc.* **2001,** 84, 2462.

77. Morissette, S. L.; Lewis, J. A.; Cesarano, J.; Dimos, D. B.; Baer, T. Y., *J. Am. Ceram. Soc.* **2000,** 83, 2409.

78. Bandyopadhyay, A.; Panda, R. K.; Janas, V. E.; Agarwala, M. K.; Danforth, S. C.; Safari, A., *J. Am. Ceram. Soc.* **1997,** 80, 1366.

79. Calvert, P., *Chem. Mater.* **2001,** 13, 3299.

80. Lewis, J. A., *Adv. Funct. Mater.* **2006,** 16, 2193.

81. Tohver, V.; Morissette, S. L.; Lewis, J. A.; Tuttle, B. A.; Voigt, J. A.; Dimos, D. B., *J. Am. Ceram. Soc.* **2002,** 85, 123.

82. Martinez, C. J.; Lewis, J. A., *J. Am. Ceram. Soc.* **2002,** 85, 2409.

83. Michna, S.; Wu, W.; Lewis, J. A., *Biomaterials.* **2005,** 26, 5632.

84. Jackman, R. J.; Wilbur, J. L.; Whitesides, G. M., *Science.* **1995,** 269, 664.

85. Kumar, A.; Whitesides, G. M., *Appl. Phys. Lett.* **1993,** 63, 2002.

86. Xia, Y. N.; Whitesides, G. M., *Annu. Rev. Mater. Sci.* **1998,** 28, 153.

87. Jeon, N. L.; Clem, P. G.; Nuzzo, R. G.; Payne, D. A., *J. Mater. Res.* **1995,** 10, 2996.

88. Liu, J. P.; He, P. S., *Chin. J. Chem. Phys.* **2004,** 17, 215.

89. Leung, W. Y.; Kang, H.; Constant, K.; Cann, D.; Kim, C. H.; Biswas, R.; Sigalas, M. M.; Ho, K. M., *J. Appl. Phys.* **2003,** 93, 5866.

90. Zhang, D.; Su, B.; Button, T. W., *J. Eur. Ceram. Soc.* **2004,** 24, 231.

91. Donthu, S. K.; Pan, Z.; Shekhawat, G. S.; Dravid, V. P.; Balakrisnan, B.; Tripathy, S., *J. Appl. Phys.* **2005,** 98.

92. Heule, M.; Schell, J.; Gauckler, L. J., *J. Am. Ceram. Soc.* **2003,** 86, 407.

93. Beh, W. S.; Xia, Y. N.; Qin, D., *J. Mater. Res.* **1999,** 14, 3995.

94. Heule, M.; Gauckler, L. J., *Adv. Mater.* **2001,** 13, 1790.

95. Heule, M.; Gauckler, L. J., *Sensor. Actuat. B-Chem.* **2003,** 93, 100.

96. Zhu, J.; Somorjai, G. A., *Nano. Lett.* **2001,** 1, 8.

97. Li, L. S.; Hu, J. T.; Yang, W. D.; Alivisatos, A. P., *Nano. Lett.* **2001,** 1, 349.

98. Alivisatos, A. P., *Science.* **1996,** 271, 933.

99. M.H. Huang, Y. W., H. Feick, N. Tran, E. Weber and P. Yang, *Adv. Mater.* **2001,** 13, 113.

100. Y. Dai, Y. Z., Q.K. Li and C.W. Nan, *Chem. Phys. Lett.* **2002,** 358, 83.

101. Bando, J. Q. H. a. Y., *Appl. Phys. Lett.* **2003,** 82, 1401.

102. I. Shalish, H. T. a. V. N., *Phys. Rev:B.* **2004,** 69, 245401.

103. Kim, E.; Xia, Y.; Whitesides, G. M., *J. Am. Chem. Soc.* **1996,** 118, 5722.

104. N.L. Jeon, I. S. C., B. Xu and G.M. Whitesides, *Adv. Mater.* **1999,** 11, 946.

105. Seraji, S.; Wu, Y.; Jewell-Larson, N. E.; Forbess, M. J.; Limmer, S. J.; Chou, T. P.; Cao, G. Z., *Adv. Mater.* **2000,** 12, 1421.

106. M. Heule, J. S., L.J. Gauckler, *J. Am. Ceram. Soc.* **2003,** 86, 407.

107. Kim, E.; Xia, Y. N.; Whitesides, G. M., *Nature* **1995,** 376, 581.

108. Brinker, C. J.; Scherer, G. W., "*Sol-Gel Science: The Physics and Chemistry of Sol-Gel Processing*", Academic Press: New York, 1990.

109. Dunn, B.; Zink, J. I., *Chem. Mater.* **1997,** 9, 2280.

110. Morris, C. A.; Anderson, M. L.; Stroud, R. M.; Merzbacher, C. I.; Rolison, D. R., *Science.* **1999,** 284, 622.

111. Tian, Z. R.; Tong, W.; Wang, J. Y.; Duan, N. G.; Krishnan, V. V.; Suib, S. L., *Science.* **1997,** 276, 926.

112. Wu, N. L.; Wang, S. Y.; Rusakova, I. A., *Science.* **1999,** 285, 1375.

113. Feng, X.; Fryxell, G. E.; Wang, L. Q.; Kim, A. Y.; Liu, J.; Kemner, K. M., *Science.* **1997,** 276, 923.

114. Fan, H. Y.; Lu, Y. F.; Stump, A.; Reed, S. T.; Baer, T.; Schunk, R.; Perez-Luna, V.; Lopez, G. P.; Brinker, C. J., *Nature.* **2000,** 405, 56.

115. Vioux, A., *Chem. Mater.* **1997,** 9, 2292.

116. Ben-Ami, U.; Nagar, R.; Ben-Ami, N.; Scheuer, J.; Orenstein, M.; Eisenstein, G.; Lewis, A.; Kapon, E.; Reinhardt, F.; Ils, P.; Gustafsson, A., *Applied Physics Letters* **1998,** 73, 1619.

117. B. Hecht, B. S., U.P. Wild, V. Deckert, R.Zenobi, O.J.F. Martin, D.W. Pohl, *J. Chem. Phys.* **2000,** 112, 7761.

118. Trautman, E. B. a. J. K., *Science.* **1992,** 257, 189.

119. M.J. Fasolka, L. S. G., J. Hwang, A.M. Urbas, P. DeRege, T. Swager and E.L. Thomas, *Phys. Rev. Lett.* **2003,** 90, 16107.

120. J.C. Johnson, H. Y., R.D. Schaller, P.B. Petersen, P.Yang and R.J. Saykally, *Nano. Lett.* **2002,** 2, 279.

121. O. Tikhomirov, H. J. a. J. L., *Appl. Phys. Lett.* **2000,** 77, 2048.

122. Ichinose, I.; Senzu, H.; Kunitake, T., *Chemistry of Materials* **1997,** 9, 1296.

123. B. Hecht, H. B., Y. Inouye, D.W. Pohl and L.Novotny, *J. Appl. Phys.* **1997,** 81, 2492.

124. R. Carminati, A. M., M. Nieto-Vesperinas and J.J. Greffet, *J. Appl. Phys.* **1997,** 82, 501.

125. K. Park, J. S. L., M.Y. Sung and S. Kim, *Jpn. J. Appl. Phys.* **2002,** 41, 7317.

126. Liu, X., Chemical Vapour Deposition and Characterization of Zinc Oxide thin films and Nanostructures. Ph.D, Northwestern University, Evanston, 2003.

127. S. Choopun, R. D. V., W. Noch, A. Balsamo, R.P. Sharma, T. Venkatesan, A. Lliadis and D.C. Look, *Appl. Phys. Lett.* **1999,** 75, 3947.

128. T. Aoki, Y. H. a. D. C. L., *Appl. Phys. Lett.* **2000,** 76, 3257.

129. Zhang, S. B.; Wei, S. H.; Zunger, A., *Physical Review B* **2001,** 6307, art. no.

130. K. Vanheusden, C. H. S., W.L. Warren, D.R. Tallant and J.A. Voigt, *Appl. Phys. Lett.* **1998,** 68, 403.

131. B. Lin, Z. F. a. Y. J., *Appl. Phys. Lett.* **2001,** 79, 943.

132. Zelikin, Y. M. G. a. Y. M., *Opt. Spectrosc+.* **1970,** 28, 521.

133. Lehmann, W., *J. Electrochem. Soc.* **1968,** 115, 538.

134. Lauer, R. B., *J. Phys. Chem. Solids.* **1973,** 34, 249.

135. Donthu, S.; Pan, Z. X.; Myers, B.; Shekhawat, G.; Wu, N. G.; Dravid, V., *Nano. Lett.* **2005,** 5, 1710.

136. Pan, Z. X.; Donthu, S. K.; Wu, N. Q.; Li, S. Y.; Dravid, V. P., *Small* **2006,** 2, 274.

137. Lakeman, C. D. E.; Payne, D. A., *Mater. Chem. Phys.* **1994,** 38, 305.

138. Martin, C. R.; Aksay, I. A., *J. Electroceram.* **2004,** 12, 53.

139. Kolmakov, A.; Moskovits, M., *Annu. Rev. Mater. Res.* **2004,** 34, 151.

140. Look, D. C., *Mat. Sci. Eng. B-Solid.* **2001,** 80, 383.

141. Yun, M. H.; Myung, N. V.; Vasquez, R. P.; Lee, C. S.; Menke, E.; Penner, R. M., *Nano. Lett.* **2004,** 4, 419.

142. Mohaddes-Ardabili, L.; Zheng, H.; Ogale, S. B.; Hannoyer, B.; Tian, W.; Wang, J.; Lofland, S. E.; Shinde, S. R.; Zhao, T.; Jia, Y.; Salamanca-Riba, L.; Schlom, D. G.; Wuttig, M.; Ramesh, R., *Nat. Mater.* **2004,** 3, 533.

143. Nagarajan, V.; Ganpule, C. S.; Ramesh, R., *Ferroelectric Random Access Memories Fundamentals and Applications* **2004,** 93, 47.

144. Chae, G. S., *Jpn. J. Appl. Phys. 1.* **2001,** 40, 1282.

145. Bagnall, D. M.; Chen, Y. F.; Zhu, Z.; Yao, T.; Koyama, S.; Shen, M. Y.; Goto, T., *Appl. Phys. Lett.* **1997,** 70, 2230.

146. Z.K. Tang, G. K. W., P. Yu, M. Kawasaki, A. Ohtomo, H. Koinuma and Y. Segawa, *Appl. Phys. Lett.* **1998,** 72, 3270.

147. Buhlmann, S.; Dwir, B.; Baborowski, J.; Muralt, P., *Appl. Phys. Lett.* **2002,** 80, 3195.

148. Alexe, M.; Harnagea, C.; Hesse, D., *J. Eelectroceram.* **2004,** 12, 69.

149. Zheng, H.; Wang, J.; Lofland, S. E.; Ma, Z.; Mohaddes-Ardabili, L.; Zhao, T.; Salamanca-Riba, L.; Shinde, S. R.; Ogale, S. B.; Bai, F.; Viehland, D.; Jia, Y.; Schlom, D. G.; Wuttig, M.; Roytburd, A.; Ramesh, R., *Science.* **2004,** 303, 661.

150. Moshnyaga, V.; Damaschke, B.; Shapoval, O.; Belenchuk, A.; Faupel, J.; Lebedev, O. I.; Verbeeck, J.; Van Tendeloo, G.; Mucksch, M.; Tsurkan, V.; Tidecks, R.; Samwer, K., *Nat. Mater.* **2003,** 2, 247.

151. Chou, S. Y.; Krauss, P. R.; Renstrom, P. J., *Science.* **1996,** 272, 85.

152. Piner, R. D.; Zhu, J.; Xu, F.; Hong, S. H.; Mirkin, C. A., *Science.* **1999,** 283, 661.

153. Tang, Q.; Shi, S. Q.; Zhou, L. M., *J. Nanosci. Nanotechno.* **2004,** 4, 948.

154. Zhang, L. B.; Shi, J. X.; Yuan, J. L.; Ji, S. M.; Chang, M., *Advances in Materials Manufacturing Science and Technology* **2004,** 471-472, 353.

155. Ginger, D. S.; Zhang, H.; Mirkin, C. A., *Angew. Chem. Int. Edit.* **2004,** 43, 30.

156. Payne, D. A.; Clem, P. G., *J. Eelectroceram.* **1999,** 3, 163.

157. Auger, M. A.; Schilardi, P. L.; Caretti, I.; Sanchez, O.; Benitez, G.; Albella, J. M.; Gugo, R.; Fonticelli, M.; Vazquez, L.; Salvarezza, R. C.; Azzaroni, O., *Small.* **2005,** 1, 300.

158. Cheong, W. C.; Yuan, X. C.; Koudriachov, V.; Yu, W. X., *Opt. Express.* **2002,** 10, 586.

159. Rantala, J. T.; Penner, R. S.; Honkanen, S.; Vahakangas, J.; Fallahi, M.; Peyghambarian, N., *Thin. Solid. Films.* **1999,** 345, 185.

160. Rantala, J. T.; Nordman, N.; Nordman, O.; Vahakangas, J.; Honkanen, S.; Peyghambarian, N., *Electron. Lett.* **1998,** 34, 455.

161. Saifullah, M. S. M.; Namatsu, H.; Yamaguchi, T.; Yamazaki, K.; Kurihara, K., *Jpn. J. Appl. Phys. 1.* **1999,** 38, 7052.

162. Gratson, G. M.; Xu, M. J.; Lewis, J. A., *Nature.* **2004,** 428, 386.

163. Lewis, J. A.; Gratson, G. M., *Mater. Today.* **2004**, 32.

164. Austin, M. D.; Zhang, W.; Ge, H. X.; Wasserman, D.; Lyon, S. A.; Chou, S. Y., *Nanotechnology.* **2005,** 16, 1058.

165. Chai, J. N.; Lu, F. Z.; Li, B. M.; Kwok, D. Y., *Langmuir.* **2004,** 20, 10919.

166. Schonholzer, U. P.; Hummel, R.; Gauckler, L. J., *Adv. Mater.* **2000,** 12, 1261.

167. Shimada, S.; Matsuu, M.; Miyazawa, K.; Kuwabara, M., *J. Am. Ceram. Soc.* **2002,** 110, 391.

168. Shimada, S.; Miyazawa, K.; Kuwabara, M., *Jpn. J. Appl. Phys. 2.* **2002,** 41, L291.

169. Carminati, R.; Madrazo, A.; NietoVesperinas, M.; Greffet, J. J., *J. Appl. Phys.* **1997,** 82, 501.

170. S.B. Zhang, S. H. W. a. A. Z., *Phys. Rev: B* **2001,** 63, 75205.

171. Kim, D. J.; Maria, J. P.; Kingon, A. I.; Streiffer, S. K., *J. Appl. Phys.* **2003,** 93, 5568.

172. Kim, S. H.; Kim, D. J.; Streiffer, S. K.; Kingon, A. I., *J. Mater. Res.* **1999,** 14, 2476.

173. Myers, B. D.; Dravid, V. P., *Nano. Lett.* **2006,** 6, 963.

174. Andeen, D.; Loeffler, L.; Padture, N.; Lange, F. F., *J. Cryst. Growth.* **2003,** 259, 103.

175. Lange, F. F.; Goh, G. K. L., *J. Ceram. Process. Res.* **2001,** 2, 4.

176. Lange, F. F., *Science.* **1996,** 273, 903.

177. Brinker, C. J., *Curr. Opin. Colloid. In.* **1998,** 3, 166.

178. Pan, Z. X.; Alem, N.; Sun, T.; Dravid, V. P., *Nano. Lett.* **2006,** 6, 2344.

179. Wan, Q.; Li, Q. H.; Chen, Y. J.; Wang, T. H.; He, X. L.; Li, J. P.; Lin, C. L., *Applied Physics Letters* **2004,** 84, 3654.

180. Park, Y. K.; Han, J. I.; Kwak, M. G.; Yang, H.; Ju, S. H.; Cho, W. S., *Appl. Phys. Lett.* **1998,** 72, 668.

181. Lima, S. A. M.; Sigoli, F. A.; Davolos, M. R.; Jafelicci, M., *J. Alloy. Compd.* **2002,** 344, 280.

182. Hayashi, Y.; Narahara, H.; Uchida, T.; Noguchi, T.; Ibuki, S., *Jpn. J. Appl. Phys. 1.* **1995,** 34, 1878.

183. Egerton, R. F.; Malac, M., *Ultramicroscopy* **2002,** 92, 47.

184. MacKenzie, M.; Craven, A. J.; Collins, C. L., *Scripta. Mater.* **2006,** 54, 1.

185. Thomas, J.; Gemming, T., *Appl. Surf. Sci.* **2005,** 252, 245.

186. Suehle, J. S.; Cavicchi, R. E.; Gaitan, M.; Semancik, S., *IEEE. Electr. Device. L.* **1993,** 14, 118.

187. Meier, D. C.; Taylor, C. J.; Cavicchi, R. E.; White, V. E.; Ellzy, M. W.; Sumpter, K. B.; Semancik, S., *IEEE. Sens. J.* **2005,** 5, 712.

188. Wang, C. H.; Chu, X. F.; Wu, M. W., *Sensor. Actuat. B-Chem.* **2006,** 113, 320.

189. Shimada, S.; Hirano, S.; Kuwabara, M., *Jpn. J. Appl. Phys 1.* **2003,** 42, 6721.

190. Xia, D. Y.; Biswas, A.; Li, D.; Brueck, S. R. J., *Adv. Mater.* **2004,** 16, 1427.

191. Xia, D. Y.; Brueck, S. R. J., *Nano. Lett.* **2004,** 4, 1295.

192. Fujikawa, S.; Takaki, R.; Kunitake, T., *Langmuir.* **2006,** 22, 9057.

193. Donthu, S.; Sun, T.; Dravid, V., *Adv. Mater.* **2007,** 19, 125.

194. Heule, M.; Vuillemin, S.; Gauckler, L. J., *Adv. Mater.* **2003,** 15, 1237.

195. Xia, Y. N.; Yang, P. D., *Adv. Mater.* **2003,** 15, 351.

196. Yang, P. D., *MRS. Bull.* **2005,** 30, 85.

197. Spanier, J. E.; Kolpak, A. M.; Urban, J. J.; Grinberg, I.; Lian, O. Y.; Yun, W. S.; Rappe, A. M.; Park, H., *Nano. Lett.* **2006,** 6, 735.

198. Fang, X. S.; Zhang, L. D., *J. Mater. Sci. Technol.* **2006,** 22, 1.

199. Sawicka, K. M.; Prasad, A. K.; Gouma, P. I., *Sens. Lett.* **2005,** 3, 31.

200. Xu, J. Q.; Pan, Q. Y.; Shun, Y. A.; Tian, Z. Z., *Sensor. Actuat. B-Chem.* **2000,** 66, 277.

201. Shukla, S.; Seal, S., *Sens. Lett.* **2004,** 2, 73.

202. Xu, C.; Tamaki, J.; Miura, N.; Yamazoe, N., *Sensor. Actuat. B-Chem.* **1991,** 3, 147.

203. Geatches, R. M.; Chadwick, A. V.; Wright, J. D., *Sensors and Actuators B: Chemical* **1991,** 4, 467.

204. Steele, J. M., Metal oxide single crystals as gas sensors. University of Kent at Canterbury, 1988.

205. Egashira, M.; Matsumoto, T.; Shimizu, Y.; Iwanaga, H., *Sensor. Acuator.* **1988,** 14, 205.

206. Sakai, G.; Baik, N. S.; Miura, N.; Yamazoe, N., *Sensor. Actuat. B-Chem.* **2001,** 77, 116.

207. Mulla, I. S.; Ramgir, N. S.; Hwang, Y. K.; Chang, J. S., *J. Ind. Eng. Chem.* **2004,** 10, 1242.

208. Mishra, S.; Ghanshyam, C.; Ram, N.; Singh, S.; Bajpai, R. P.; Bedi, R. K., *B. Mater. Sci.* **2002,** 25, 231.

209. Chen, Y. J.; Nie, L.; Xue, X. Y.; Wang, Y. G.; Wang, T. H., *Appl. Phys. Lett.* **2006,** 88, 83105.

210. Kolmakov, A.; Zhang, Y. X.; Cheng, G. S.; Moskovits, M., *Adv. Mater.* **2003,** 15, 997.

211. Stein, R. S.; Powers, J., *J. Polym. Sci.* **1962,** 56, S9.

212. Schultz, J. M., *Macromolecules.* **1996,** 29, 3022.

213. Escleine, J. M.; Monasse, B.; Wey, E.; Haudin, J. M., *Colloid. Polym. Sci.* **1984,** 262, 366.

214. Safarik, D. J.; Mullins, C. B., *J. Chem. Phys.* **2002,** 117, 8110.

215. Billon, N.; Escleine, J. M.; Haudin, J. M., *Colloid. Polym. Sci.* **1989,** 267, 668.

216. Gautheron, B.; Labeau, M.; Delabouglise, G.; Schmatz, U., *Sens. Actuators, B* **1993,** 16, 357.

217. Epifani, M.; Alvisi, M.; Mirenghi, L.; Leo, G.; Siciliano, P.; Vasanelli, L., *J Am Ceram Soc* **2001,** 84, 48.

218. Kim, I. H.; Ko, J. H.; Kim, D.; Lee, K. S.; Lee, T. S.; Jeong, J. H.; Cheong, B.; Baik, Y. J.; Kim, W. M., *Thin. Solid. Films.* **2006,** 515, 2475.

219. Jain, K.; Pant, R. P.; Lakshmikumar, S. T., *Sens. Actuators, B* **2006,** 113, 823.

220. Qi, X. D.; Dho, J.; Tomov, R.; Blamire, M. G.; MacManus-Driscoll, J. L., *Appl. Phys. Lett.* **2005,** 86, 62903.

221. Zang, G. Z.; Wang, J. F.; Chen, H. C.; Su, W. B.; Wang, C. M.; Qi, P.; Ming, B. Q., *High-Performance Ceramics Iii, Pts 1 and 2* **2005,** 280-283, 271.

222. Galatsis, K.; Cukrov, L.; Wlodarski, W.; McCormick, P.; Kalantar-zadeh, K.; Comini, E.; Sberveglieri, G., *Sens. Actuators, B* **2003,** 93, 562.

223. Cabot, A.; Dieguez, A.; Romano-Rodriguez, A.; Morante, J. R.; Barsan, N., *Sens. Actuators, B* **2001,** 79, 98.

224. Cabot, A.; Arbiol, J.; Morante, J. R.; Weimar, U.; Barsan, N.; Gopel, W., *Sensor. Actuat. B-Chem.* **2000,** 70, 87.

225. Bittencourt, C.; Llobet, E.; Silva, M. A. P.; Landers, R.; Nieto, L.; Vicaro, K. O.; Sueiras, J. E.; Calderer, J.; Correig, X., *Sensor. Actuat. B-Chem.* **2003,** 92, 67.

226. Calderer, J.; Molinas, P.; Sueiras, J.; Llobet, E.; Vilanova, X.; Correig, X.; Masana, F.; Rodriguez, A., *Microelectron. Reliab.* **2000,** 40, 807.

227. Martin, C. R.; Aksay, I. A., *J Phys Chem B* **2003,** 107, 4261.

228. d'Heurle, F., *J. Mater. Res.* **1998,** 3, 167.

229. Yonenaga, I.; Suzuki, T., *Phil. Mag. Lett.* **2002,** 82, 535.

230. Senda, T.; Bradt, R. C., *J. Am. Ceram. Soc.* **1991,** 74, 1296.

231. Schmelzer, J.; Pascova, R.; Moller, J.; Gutzow, I., *J. Non-Cryst. Solids.* **1993,** 162, 26.

232. Schmelzer, J.; Moller, J.; Gutzow, I.; Pascova, R.; Muller, R.; Pannhorst, W., *J. Non-Cryst. Solids.* **1995,** 183, 215.

233. Hau-Riege, C. S.; Thompson, C. V., *Appl. Phys. Lett.* **2001,** 78, 3451.

234. Klinger, L.; Rabkin, E., *Acta. Mater.* **2006,** 54, 305.

235. *World Industrial Gas Sensors Detectors and Analyzers Markets.* Market Engineering Research, Frost and Sulliuvan: Aug, 2006.

236. M. Madou; Morrison, S. R., "*Chemical Sensing with Solid State Devices*", Academic Press: Boston, 1989.

237. Baller, M. K.; Lang, H. P.; Fritz, J.; Gerber, C.; Gimzewski, J. K.; Drechsler, U.; Rothuizen, H.; Despont, M.; Vettiger, P.; Battiston, F. M.; Ramseyer, J. P.; Fornaro, P.; Meyer, E.; Guntherodt, H. J., *Ultramicroscopy.* **2000,** 82, 1.

238. Battiston, F. M.; Ramseyer, J. P.; Lang, H. P.; Baller, M. K.; Gerber, C.; Gimzewski, J. K.; Meyer, E.; Guntherodt, H. J., *Sensor. Actuat. B-Chem.* **2001,** 77, 122.

239. Eranna, G.; Joshi, B. C.; Runthala, D. P.; Gupta, R. P., *Crit. Rev. Solid. State.* **2004,** 29, 111.

240. Heule, M., Shaping Ceramics in Small Scale - from Microcomponents to Gas Sensors. Ph.D thesis, Swiss Federal Institute of Technology, Zurich, 2003.

241. Simon, T.; Barsan, N.; Bauer, M.; Weimar, U., *Sensor. Actuat. B-Chem.* **2001,** 73, 1.

242. Singh, S., *J. Hazard. Mater.* **2007,** 144, 15.

243. Park, C. O.; Akbar, S. A.; Weppner, W., *J. Mater. Sci.* **2003,** 38, 4639.

244. Di Bartolomeo, E.; Grilli, M. L.; Traversa, E., *J. Electrochem. Soc.* **2004,** 151, H133.

245. Dutta, A.; Ishihara, T.; Nishiguchi, H.; Takita, Y., *J. Electrochem. Soc.* **2004,** 151, H122.

246. Schmitt, R. F.; Allen, J. W.; Vetelino, J. F.; Parks, J.; Zhang, C., *Sensor. Actuat. B-Chem.* **2001,** 76, 95.

247. Nieuwenhuizen, M. S.; Barendsz, A. W.; Nieuwkoop, E.; Vellekoop, M. J.; Venema, A., *Electron. Lett.* **1986,** 22, 184.

248. Ali, Z., *J. Therm. Anal. Calorim.* **1999,** 55, 397.

249. Si, P.; Mortensen, J.; Kornolov, A.; Denborg, J.; Moller, P. J., *Anal. Chim. Acta.* **2007,** 597, 223.

250. Nakamura, K.; Nakamoto, T.; Moriizumi, T., *Sensor. Actuat. B-Chem.* **2000,** 69, 295.

251. Goka, S.; Okabe, K.; Watanabe, Y.; Sekimoto, H., *Jpn. J. Appl. Phys. 1.* **2000,** 39, 3073.

252. Wang, X. H.; Zhang, J.; Zhu, Z. Q., *Appl. Surf. Sci.* **2006,** 252, 2404.

253. Korotcenkov, G., *Sensor. Actuat. B-Chem.* **2007,** 121, 664.

254. Bartlett, P. N.; Guerin, S., *Anal. Chem.* **2003,** 75, 126.

255. Christie, S.; Scorsone, E.; Persaud, K.; Kvasnik, F., *Sensor. Actuat. B-Chem.* **2003,** 90, 163.

256. Cho, E. J.; Bright, F. V., *Anal. Chem.* **2001,** 73, 3289.

257. Aguirre, N. M.; Perez, L. M.; Colin, J. A.; Buenrostro-Gonzalez, E., *Sensors.* **2007,** 7, 1954.

258. Wong, C. I.; Ho, H. P.; Chan, K. S.; Wu, S. Y.; Lin, C. L., *Opt. Eng.* **2005,** 44.

259. Wang, Y. J.; Coti, K. K.; Jun, W.; Alam, M. M.; Shyue, J. J.; Lu, W. X.; Padture, N. P.; Tseng, H. R., *Nanotechnology.* **2007,** 18.

260. Bai, H.; Shi, G. Q., *Sensors.* **2007,** 7, 267.

261. Lang, S. B.; Muensit, S., *Appl. Phys. A-Mater.* **2006,** 85, 125.

262. Barsan, N.; Weimar, U., *J. Eelectroceram.* **2001,** 7, 143.

263. Lenaerts, S.; Roggen, J.; Maes, G., *Spectrochim. Acta. A-M.* **1995,** 51, 883.

264. Yamazoe, N.; Fuchigami, J.; Kishikawa, M.; Seiyama, T., *Surf. Sci.* **1979,** 86, 335.

265. Llobet, E.; Rubio, J.; Vilanova, X.; Brezmes, J.; Correig, X.; Gardner, J. W.; Hines, E. L., *Sensor. Actuat. B-Chem.* **2001,** 76, 419.

266. Martin, M. A.; Santos, J. P.; Agapito, J. A., *Sensor. Actuat. B-Chem.* **2001,** 77, 468.

267. Massart. D.L.; and Vandeginste. B.G.M., "*Chemometrics: a text book*", Elsevier: Amsterdam, 1988.

268. Gardner, J. W., *Sensor. Actuat. B-Chem.* **1995,** 27, 261.

269. Vilanova, X.; Llobet, E.; Brezmes, J.; Calderer, J.; Correig, X., *Sensor. Actuat. B-Chem.* **1998,** 48, 425.

270. Hoefer, U.; Bottner, H.; Felske, A.; Kuhner, G.; Steiner, K.; Sulz, G., *Sensor. Actuat. B-Chem.* **1997,** 44, 429.

271. Gardner, J. W.; Iskandarani, M. Z.; Bott, B., *Sensor. Actuat. B-Chem.* **1992,** 9, 133.

272. Toohey, M. J., *Sensor. Actuat. B-Chem.* **2005,** 105, 232.

273. Grass, K.; Lintz, H. G., *J. Catal.* **1997,** 172, 446.

274. Cabot, A.; Vila, A.; Morante, J. R., *Sensor. Actuat. B-Chem.* **2002,** 84, 12.

275. Yamazoe, N., *Sensor. Actuat. B-Chem.* **1991,** 5, 7.

276. Favier, F.; Walter, E. C.; Zach, M. P.; Benter, T.; Penner, R. M., *Science.* **2001,** 293, 2227.

277. Park, H. H.; Park, H. H.; Hill, R. H., *Sensor. Actuat A-Phys.* **2006,** 132, 429.

278. Hernandez-Ramirez, F.; Tarancon, A.; Casals, O.; Rodriguez, J.; Romano-Rodriguez, A.; Morante, J. R.; Barth, S.; Mathur, S.; Choi, T. Y.; Poulikakos, D.; Callegari, V.; Nellen, P. M., *Nanotechnology.* **2006,** 17, 5577.

279. Arnold, M. S.; Avouris, P.; Pan, Z. W.; Wang, Z. L., *J. Phys. Chem. B.* **2003,** 107, 659.

280. Geatches, R. M.; Chadwick, A. V.; Wright, J. D., *Sensor. Actuat. B-Chem.* **1991,** 4, 467.

281. Kim, M. C.; Song, K. H.; Park, S. J., *J. Mater. Res.* **1993,** 8, 1368.

282. Zarzebski, Z. M., "*Oxide Semiconductors*", Pergamon Press, Oxford: 1988.

283. Kim, Y. C.; Adusumilli, P.; Lauhon, L. J.; Seidman, D. N.; Jung, S. Y.; Lee, H. D.; Alvis, R. L.; Ulfig, R. M.; Olson, J. D., *Appl. Phys. Lett.* **2007,** 91.